Loughborough University

This item was submitted to Loughborough's Research Repository by the author.
Items in Figshare are protected by copyright, with all rights reserved, unless otherwise indicated.

Development of a measurement base for static secondary ion mass spectrometry

PLEASE CITE THE PUBLISHED VERSION

PUBLISHER

© Ian Stuart Gilmore

LICENCE

CC BY-NC-ND 4.0

REPOSITORY RECORD

Gilmore, Ian S.. 2019. “Development of a Measurement Base for Static Secondary Ion Mass Spectrometry”. figshare. https://hdl.handle.net/2134/11110.

Loughborough University

This item was submitted to Loughborough University as a PhD thesis by the author and is made available in the Institutional Repository (https://dspace.lboro.ac.uk/) under the following Creative Commons Licence conditions.

creative commons

COMMONS DEED

Attribution-NonCommercial-NoDerivs 2.5

You are free:

- to copy, distribute, display, and perform the work

Under the following conditions:

Attribution. You must attribute the work in the manner specified by the author or licensor.

Noncommercial. You may not use this work for commercial purposes.

No Derivative Works. You may not alter, transform, or build upon this work.

- For any reuse or distribution, you must make clear to others the license terms of this work.
- Any of these conditions can be waived if you get permission from the copyright holder.

Your fair use and other rights are in no way affected by the above.

This is a human-readable summary of the Legal Code (the full license).

Disclaimer

For the full text of this licence, please go to:
http://creativecommons.org/licenses/by-nc-nd/2.5/

Loughborough University

Pilkington Library

Author/Filing Title .....GILMORE.....

.....

Vol. No. ..... Class Mark .....T.....

Please note that fines are charged on ALL overdue items.

~~NOA~~
OPEN SHELF COPY

0402292723

DEVELOPMENT OF A MEASUREMENT BASE FOR STATIC SECONDARY ION MASS SPECTROMETRY

by

Ian Stuart Gilmore

A Doctoral Thesis

Submitted in partial fulfilment of the requirements for the award of

Doctor of Philosophy of Loughborough University

28 March 2000

© by Ian Stuart Gilmore 2000

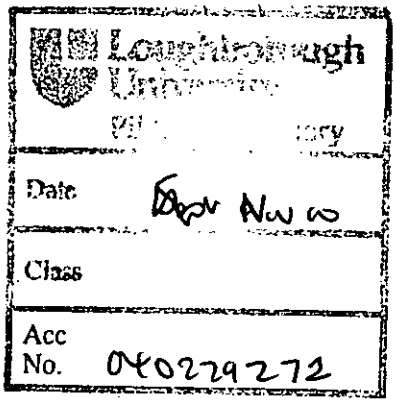

M0002544LB

To Jeannie, Jade and Phoebe

Preface

This thesis describes the research carried out independtly by this author at the National Physical Laboratory, since April 1995. The results presented are original and no part of the thesis has been submitted for any degree in this or any other University. Appropriate references are given where the work of others has been used.

The author wishes to thank :

Dr M P Seah for his inspiration, valuable comments and careful supervision;
Dr M Crapper and Dr D E Sykes for their supervision of the work and valuable comments.
Dr A Chew for her encouragment and advice;
Professor D Briggs for his general advice and encouragment and for providing the PET reference material;
All of the respondees involved in the inter-laboratory study, listed in chapter 7;
Dr E Niehuis for helpful discussions for chapter 8;
The National Physical Laboratory for providing enrolement funds;
Mrs B Miller and Mrs L Nelhams for their careful typing of the manuscript;
My family for their support and encouragment over the years.

This work forms part of the Valid Analytical Measurement programme of the National Measurement System Policy Unit of the Department of Trade and Industry.

Abstract

This work sets out a framework to provide a metrological basis for static SIMS measurements. This surface analytical technique has been is use for over thirty years but, because of the lack of an infrastructure, has not achieved its full potential in industry. To build this basis, the measurement chain is studied from the sample through to the detector and data processing. By understanding the effects of each link in the chain, repeatabilities are reduced by orders of magnitude to below 1%, the ion beam current and flux density are calibrated to better than 2%, ion beam damage in polymers is controlled and detection efficiencies calculated. Utilising these developments, a characterised and calibrated SIMS spectrometer is used to establish reference materials. An inter-laboratory study to assess the extent of spectrum variability between spectrometers was conducted involving over twenty laboratories worldwide. Analysis of the data gives the level of repeatability and reproducibility using current procedures. Repeatabilities for some laboratories are as good as 1% but many are at 10% and a few as poor as 80%. A Relative Instrument Spectral Response, RISR, is developed to facilitate the comparison of spectra from one instrument to another or library data. For most instruments reproducibilities of 14% are achievable.

Additionally, the wide variety of ion beam sources and energies, presently in use, result in spectra that are only broadly comparable. A detailed study of these effects provides, for the first time, a unified method to relate the behaviour for all ion species and energies. A development of this work gives a totally new spectroscopy, known as G-SIMS or gentle-SIMS. Here, the static SIMS spectrum for a low surface plasma temperature is calculated which promotes those spectral intensities truly representative of the analysed material and reduces those caused by additional fragmentation and rearrangement mechanisms. The resulting G-SIMS spectra are easier to identify and are interpreted more directly.

This work provides the essential basis for the development of static SIMS. Future work will improve the consistency of library data so that the valid data for molecular identification can be uniquely extracted. The measurement base will be developed to meet the growing requirements for static SIMS analysis of complex organic and biomaterials.

CONTENTS

	Preface	i
	Abstract	ii
	Contents	iii
Chapter 1	Introduction	1
Chapter 2	Fluence, Flux, Current and Current Density Measurement in Faraday cups for Surface Analysis	10
Chapter 3	Surface Charge Stabilisation of Insulators for Highly Repeatable Spectra when using a Quadrupole Mass Spectrometer	32
Chapter 4	A Study of Damage in Polymers	59
Chapter 5	Ion Detection Efficiency in SIMS: Energy, Mass and Composition Dependencies for Microchannel Plates used in Mass Spectrometies	101
Chapter 6	A Conductive Reference Material for the Evaluation of Instrument Response Functions for Static SIMS	127
Chapter 7	A Static SIMS Inter-laboraty Study	138
Chapter 8	Towards Unfragmented Spectra : the G-SIMS Procedure	168
Chapter 9	Conclusion and Outlook	194

CHAPTER ONE

Introduction

1	SURFACE ANALYSIS	2
2	HISTORICAL DEVELOPMENT	3
3	THE SIMS PROCESS	4
3.1	SPUTTER YIELD	5
3.2	IONIZATION PROBABILITY	6
4	A MEASUREMENT BASE	6
REFERENCES		8

1 SURFACE ANALYSIS

Surfaces are where bulk material interacts with the surrounding environment. For material performance these characteristics often dominate those of the bulk. Examples of the importance of surfaces are found in all industrial sectors. In the electronics industry, semiconductor devices continue to reduce in size to meet requirements. Surface contamination is now a significant problem which can result in the output of a whole production line being scrapped; Adhesives are used in a diverse range of modern products, being much quicker, lighter and cost effective than other traditional joining methods. Performance is critical as many applications are in the automobile and aerospace industries. Surface properties control the effectiveness of bonding. A monolayer of contaminant may cause bonding failure or delamination; The packaging industry is an important sector, particularly for food. Here the packaging must protect and extend the product shelf life, by reducing oxygen permeability and additionally must not poison the food through the leaching of plasticizers or low molecular weight compounds. More recently the bio-materials and pharmaceutical sectors have developed strongly. Biomedical implants must have resistance to the body environment and also not be rejected by the body, the material surface may be engineering to reduce protein adsorption. Modern drug delivery systems are based on a pharmaceutical drug seeded around a silicate particle. The drug is enclosed within a polymer coating layer which only allows the drug to be delivered in certain environments, for example the alkaline environment of the duodenum. Properties of the surface polymer layer define the dose and dose rate given to the patient.

There are three techniques used to provide the surface chemical analysis necessary in industry. Auger Electron Spectroscopy (AES) provides elemental composition with a spatial resolution below 20 nm, X-ray Photoelectron Spectroscopy additionally provides simple chemical state information but with a spatial resolution of approximately 3 μm. Only Secondary Ion Mass Spectroscopy gives the high specificity required to analyse complex molecules and materials on the top-most surface. It is this ability together with femptomole detection limits and spatial resolution below 100 nm that has provided industry with the most useful analytical tool for the study of complex surfaces.

2 HISTORICAL DEVELOPMENT

The origins of SIMS begin with the studies by J.J. Thomson[1] and co-workers at the beginning of the last century. He observed the effects of ions on a metal plate in a discharge tube and deduced that secondary particles were emitted in all directions. For the most part these particles were neutrals but a small fraction were positively charged. It was not until the 1930s that further progress was made by Woodcock[2] and Arnot and Milligan[3] with their studies of negative ions using a magnetic deflection field. Instrument development was boosted in the late 50s by the rapidly growing space programme. NASA wanted to study the spatial and isotopic distribution of all elements from hydrogen to uranium in samples brought back from the Moon. This analytical capability is unique to SIMS and a contract was placed with Herzog[4,5] and co-workers at the RCA laboratories where the first commercial SIMS instrument was built.

The high sensitivity and speciation of SIMS led to a strong growth and instrumentation developed rapidly along two different fundamental designs. Firstly, the ion microscope developed by Castang and Slodzian[6] utilizes an unfocused ion beam for illumination coupled with a double focusing stigmatic imaging mass analyser. The principle of this system is essentially that of the traditional optical microscope where a magnified image is projected onto a detector. Sub-micron resolution is typically achieved. This configuration is particularly well suited to depth profiling and the CAMECA range of magnetic sector instruments are the work horse of the semiconductor industry.

The second approach uses the method of the scanning electron microprobe. Here a focused ion beam is rastered across the sample in registration with an ion detector to form an image of the selected mass. This arrangement decouples the design constraints of transmission and spatial resolution from the mass analyser. A wide range of focused ion beams are available and together with cheaper quadrupole mass analysers greatly expanded the use of SIMS.

The technique used so far consumed material which was either used to give a bulk analysis or by monitoring intensities against time to give a concentration profile through the material. In 1969, at the University of Münster, Benninghoven[7,8] developed a completely new approach. He reduced the ion beam flux density so that the chance of one impact site being struck again was low. Instruments of that time had sufficient sensitivity that a mass

spectrum could be acquired before a whole monolayer was consumed. He distinguished this "none destructive" surface analytical technique with the term static SIMS. A mass spectrometry of the surface opened up a new area. In the early eighties Briggs[9,10] realised the potential of the technique for the study of polymer systems. He found the spectra were rich with detail containing information simply not available in the electron spectroscopies. The team at ICI began a systematic investigation of polymers which lead to the first library of Static SIMS spectra[11].

More recently, time-of-flight, TOF, spectrometers have been developed[12,13]. These measure the intensities of all the mass peaks quasi-simultaneously instead of subsequently as in a scanned mass filter. Parallel mass detection and the inherent uniform high transmission gives far greater efficiencies, making this the system of choice for most applications. Further advantages occur because the extraction field may be reduced to zero during primary ion pulses allowing low energy electrons to neutralise insulating samples and also low energy ion beams for profiling giving low atomic mixing.

3 THE SIMS PROCESS

A brief introduction to the processes involved in the production of secondary ions is given here, readers interested in more detail are referred to refs (14) and (15). The processes leading to the emission of a charged particle or fragment from the surface are not well understood. For both AES and XPS, simple expressions may be written allowing peak intensities to be calculated theoretically. Indeed, recent work by Seah and Gilmore[16,17,18] show that there is excellent agreement between theory and experiment for both AES and XPS. Such is not the case for SIMS. A simple equation may be written which encompasses the general terms to describe emission. However, the terms themselves are not simple and may behave in a strongly non-linear way. The ion yield, $Y_{i,m}$, of a species, i, in a matrix, m, may be written,

$$Y_{i,m} = S_{i,m} P_{i,m} C_{i,m}$$

where S is the matrix dependent sputter yield, P is the ionisation probability and C is the fractional surface coverage. We shall now briefly outline the sputter yield and ionisation probability terms.

3.1 SPUTTER YIELD

The most successful model so far to quantitatively explain sputtering is the Collision Cascade Model of Sigmund[19]. In this theory momentum and energy are transferred through binary collisions between primary ion and target particles and between recoil and stationary target particles. The whole set of particles set in motion is called a cascade. Molecules or atoms are liberated from the top atom layers where a cascade meets the surface. For the successful ejection of large molecules two or more cascades are required to correlate in both space and time. The theory is quantitatively successful at explaining total yields and energy distributions of ejected particles and the effect of primary ion mass, energy and angle of incidence on the yield. However, the theory is restricted to amorphous targets and does not simply transfer to organic systems.

Another approach to model sputtering is to use Monte Carlo simulations[20,21]. In this method a computer algorithm is used to follow each impacting ion and the subsequent collisions. Each collision is modelled using classical or quantum mechanical treatments combined with a randomisation process. After following many events, the statistics are sufficiently good to give reliable values for sputter yields. The cascade calculated by Ishitani and Shimizu[20] is shown in Fig 1 for 4 keV argon ions impacting a copper substrate. This illustrates the shallow sampling depth for static SIMS even though the cascade may extend as deep as 10 nm. These models have been enormously helpful to dynamic SIMS but cannot fully describe the complex nature of linked organic materials on surfaces.

Molecular dynamic simulations have been used for around a decade but the method is still in its infancy. Here each atom in the target is described by its own potential, every atom is monitored for each collision. This requires a huge amount of computing resource and so model systems have been extremely simple. So simple that they have had very little in common with experimental results. Computer power has increased dramatically over this time and is allowing more complex systems to be studied. Recent work by Delcorte[22] modelling benzene tetramers is closing the gap between the computational models and experimental results.

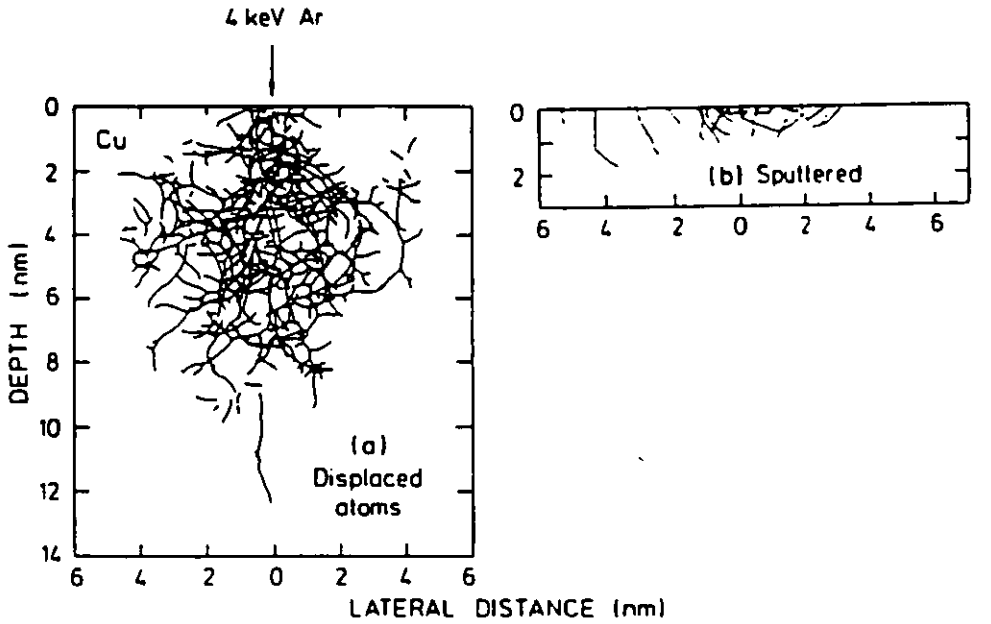

Fig 1 Cascade produced from Ishitani and Shimizu's[20] Monte Carlo simulation of 4 keV Ar^+ ions impacting a copper substrate, (a) displaced substrate atoms and (b) trajectory of atoms that are sputtered.

3.2 IONIZATION PROBABILITY

Most of the sputtered particles are neutral with around 1% carrying a charge. The probability that an emitted particle is ionised is sensitive to the electronic environment at the surface. For example the presence of electronegative species may enhance yields for positive ions by four orders of magnitude. This is a great complication to quantification as the ion yield for any species is strongly dependent on the matrix it is in and the presence of contamination. General sensitivity factors like those used in AES[16] and XPS[18] cannot be defined.

4 A MEASUREMENT BASE

A measurement base is essential for valid analytical measurements in surface analysis. Without this framework, results cannot be transferred from one laboratory to another, data libraries will not achieve their full impact, uptake of the technique will be slow. To establish a measurement infrastructure, a detailed knowledge of the measurement system is required

and standards need to be in place. There are two distinct classes of standards[23], reference or measurement standards, known as *étalons* and documentary standards, called *normes*. *Étalons* extend the SI measurement system and have a wholly scientific basis whereas *normes* are established by consensus[23]. The work developed in this thesis will lead into *étalons* which will feed the developement of *normes*.

AES and XPS are now considered quantitative techniques with an accuracy of around 1%. This has not always been the case, reproducibility was poor, energy scales uncalibrated and intensities varied over orders of magnitude between different instruments. In 1979, the ASTM E-42 survey for XPS[24] showed that peak ratios varied by a scatter factor $\times/\div$ 243% from one instrument to another. Similarly in 1982, the same committee conducted a round robin for AES intensity measurements[25] which showed scatter factors of relative intensities of $\times/\div$ 356%. Yet, for a given instrument, the repeatability could be as good as 1%. Seah[26,27], at the National Physical Laboratory, developed a precise understanding of the electron optics transmission and the detection efficiency, enabling the development of a system for the intensity calibration of electron spectrometers[28]. Reproducibility was improved enormously to below 2% for AES and 4% for XPS[27]. Energy scales had also been poorly calibrated for both techniques causing difficulties for XPS where chemical state identification needs an energy scale accuracy of ±0.1 eV. A calibration scheme developed at the NPL[29,30] improved typical errors from ±0.4 to ±0.04 eV for XPS and a separate scheme[31] for AES improved the standard uncertainty of ±2.0 to ±0.1 eV. This work is now being embodied in ISO standards enabling quantitative analysis using AES and XPS with high reproducibilty and repeatability in laboratories throughout the world.

The evolution of AES, XPS and SSIMS is shown in Fig 2 as a Kondratieff plot, after Seah[23]. The diagram shows the growth of each technique from the original concept to innovation and development through maturity and eventually decline. The development of standards should be at the innovation and development stage. This timing is critical. *A standard developed too early will embody obsolete concepts and a standard developed too late will have to unite the ad hoc standards that individuals or groups have had to develop for their own purposes*[23]. It is therefore surprising that there are no static SIMS standards. Work items for SIMS are progressed through subcommittee SC6 (Secondary Ion Mass Spectrometry) of ISO technical committee TC201 (Surface Chemical Analysis). The second strategic policy statement for SC6 now includes static SIMS. A new work item has now been initiated[32] to develop a standard data

transfer format for static SIMS, complementing ISO 14976[33]. It is hoped that the work in the following chapters will nurture the development of standards for static SIMS.

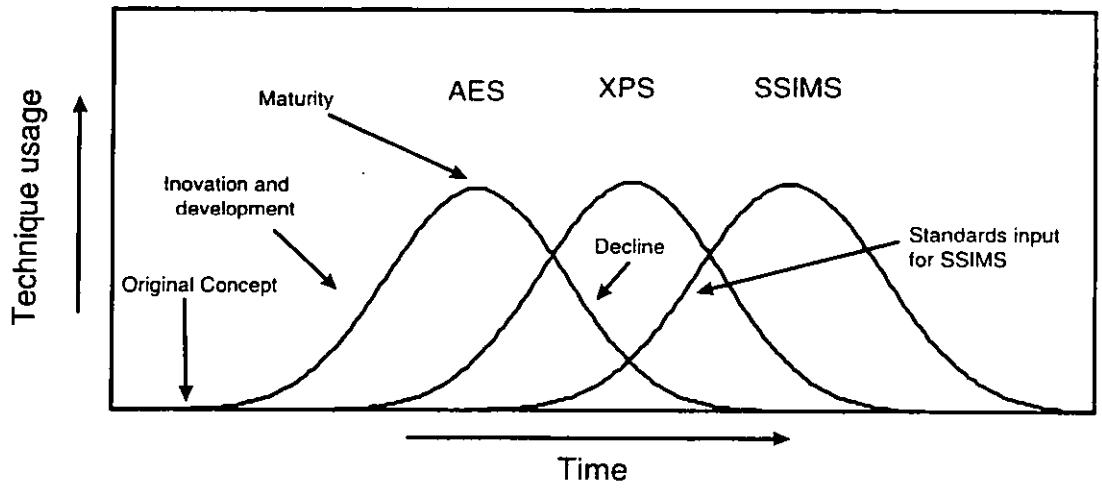

Fig 2 Kondratieff cycles showing the evolution of AES, XPS and SSIMS, after Seah[23].

REFERENCES

(1) J J Thomson, *Phil. Mag.*, **20** 252 (1910).

(2) K S Woodcock, *Phys. Rev.*, **38** 1696 (1931).

(3) F L Arnot and J C Milligan, *Proc. Roy. Soc.* A, **156** 538 (1936).

(4) R F K Herzog, W P Poschenrieder and F G Satkiewicz, NASA, Contract No. NAS5-9254, final report GCA-TR-67-3N (1967).

(5) H J Liebl and R F K Herzog, *J. Appl. Phys.*, **34** 2893 (1963).

(6) R Castaing and G Slodzian, *J. Microscopie*, **1** 395 (1962).

(7) A Benninghoven, *Phys. Status Solidi*, **34** k169 (1969).

(8) A Benninghoven, Z. *Physik*, **230** 403 (1970).

(9) D Briggs, *Surf. Interface Anal.*, **4** 151 (1982).

(10) D Briggs and A B Wooton, *Surf. Interface Anal.*, **4** 109 (1982).

(11) D Briggs, A Brown and J C Vickerman, *Handbook of Static Secondary Ion Mass Spectrometry* (SIMS), Wiley, Chichester (1989).

(12) E Niehuis, T Heller, H Feld and A Benninghoven, in *Secondary Ion Mass Spectrometry*, SIMS V, Springer Series in Chemical Physics Vol. 36, p404, Springer, Berlin (1984).

(13) B Schueler, P Sander and D A Reed, in *Secondary Ion Mass Spectrometry*, SIMS VII, p447, Wiley, Chichester (1990).

(14) *Secondary Ion Mass Spectrometry*, A Benninghoven, F G Rüdenauer and H W Werner, Wiley, Chichester (1987).

(15) *Practical Surface Analysis Second Edn. Vol. 2 Ion and Neutral Spectroscopy*, eds. D Briggs and M P Seah, Wiley, Chichester (1992).

(16) M P Seah and I S Gilmore, *Surf. Interface Anal.*, **26** 908 (1998).

(17) M P Seah, I S Gilmore and S J Spencer, to be published.

(18) M P Seah, I S Gilmore and S J Spencer, to be published.

(19) P Sigmund, in *Sputtering by Particle Bombardment I*, Springer Series Topics in Applied Physics, Ed R. Behrisch, p47, Springer Verlag, Berlin, (1981).

(20) T Ishitaii and R Shimizu, *Phys. Lett.*, **46A** 487 (1974).

(21) J F Ziegler and J P Biersack, Stopping and Range of Ions in Matter (SRIM), (1996).

(22) A Delcorte, P Bertrand, J C Vickerman and B J Garrison, SIMS XII, to be published.

(23) M P Seah, *Phil. Trans.*, **354A** 2765 (1996)

(24) C J Powell, N E Erickson and T E Madey, J. Electron Spectrosc. Relat. Phenom., **17** 361 (1979)

(25) C J Powell, N E Erickson and T E Madey, J. Electron Spectrosc. Relat. Phenom., **25** 87 (1982)

(26) M P Seah, M E Jones and M T Anthony, *Surf. Interface Anal.*, **6** 5 (1984).

(27) M P Seah and G C Smith, *Surf. Interface Anal.*, **15** 751 (1990).

(28) M P Seah, J. Electron Spectrosc. Relat. Phenom., **25** 87 (1982).

(29) M T Anthony and M P Seah, *Surf. Interface Anal.*, **6** 95 (1984).

(30) M P Seah, I S Gilmore, G Beamson, *Surf. Interface Anal.*, **26** 642 (1998).

(31) M P Seah and G C Smith, *Surf. Interface Anal.*, **15** 309 (1990).

(32) I S Gilmore and M P Seah, Draft ISO Standard, *"Surface chemical analysis - Inforamtion format - Static Secondary Ion Mass Spectrometry"*, (1999).

(33) ISO 14976: *"Surface chemical analysis - Data transfer format"* (1998).

CHAPTER TWO

Fluence, Flux, Current and Current Density Measurement in Faraday Cups for Surface Analysis

1	INTRODUCTION	11
2	THE FARADAY CUP DESIGNS	12
2.1	CUPS FOR BEAM CURRENT MEASUREMENT	12
2.2	CUPS FOR CURRENT DENSITY MEASUREMENT	15
2.3	ASTM Standard Practice for Approximate Determination of Current Density of Large Diameter Ion Beams for Sputter Depth Profiling of Solid Surfaces, E684-93	17
3	EXPERIMENTAL	17
4	RESULTS AND DISCUSSION	19
4.1	ELECTRON BEAM CURRENTS	19
4.2	ION BEAM CURRENTS	20
4.3	ELECTRON BEAM CURRENT DENSITIES	23
4.4	ION BEAM CURRENT DENSITIES	26
4.5	ION BEAM CURRENT DENSITIES USING THE STANDARD PRACTICE ASTM E 684-93	28
5	CONCLUSIONS	30
REFERENCES		31

1 INTRODUCTION

The measurement of fluence, flux, beam currents and current densities in surface analysis systems is commonplace. For the majority of work it is sufficient to know that during an analysis the beam current has been stable. In depth-profiling studies, however, where one material is to be compared with another, or where materials are to be compared with a prior set of results, one needs to be able to make repeatable measurements. For reference to, (i) measurements in the literature, (ii) absolute parameters such as cross sections, sputtering yields etc and (iii) for instrument specification, any measurements of currents or current densities must not only be repeatable but also be accurate. By accurate here we mean traceable to measurements of current in amps and current density in amps per square metre within a specified uncertainty. This is readily achieved by using a Faraday cup of known aperture. How to make such cups is well-established technology[1,2] and yet, in surface analysis systems we still have considerable problems today[3].

In order to be clear about the terms used in this work, we use the current in a beam as amps or the number of appropriately charged particles passing per second. The current density in the beam is the current per unit area at right angles to the beam and the fluence is the integral of the beam current density over time (or the number of particles per unit area normal to the beam passing in a defined time interval - these particles may or may not be charged). The flux of particles is the number passing per second per unit area normal to the beam and is similar to the current density but may also be applied to neutral particles[4]. These terms and in this work it is assumed that the particle beams are neither convergent nor divergent. Both current density[4] and flux[5] may be referred to a unit area on a surface that is not normal to the beam, however such is not the case for fluence[4] which is always referred to the beam. To avoid confusion the term dose rate[6] is used for the current density on a surface and the term dose then becomes the counterpart of fluence for that surface. In this work all parameters are referred to the beam and, where appropriate, unit areas normal to that beam.

In nuclear beam systems, Faraday cups have defining apertures with knife edges, skimmer plates, secondary electron suppressors etc which all lead to effective current and current density measurements[1,2]. In surface analysis systems such cups have been used[7] but are rather bulky and are not generally compatible with modern systems which have sample

changers and airlocks. In the present work we seek to evaluate the simplest possible cups and to define the accuracy with which they may be used. Typical structures for Faraday cups are discussed by Kuyatt[8] and by Ballu[9] and detailed calculations are presented by Ingram and Seah[10]. In the present work we shall provide data for the simplest designs as well as recommendations for practical analysts. We shall also consider the ASTM Standard Practice for Approximate Determination of current Density of Large Diameter Ion Beams[11].

2 THE FARADAY CUP DESIGNS

2.1 CUPS FOR BEAM CURRENT MEASUREMENT

The simplest Faraday cup is a drilled hole in a sample stub. For a given beam size we need to consider the effects of the hole diameter, d, the hole depth, D, and the voltage of the cup (commonly known as the cup bias, V_B). When these are optimised we may determine the effectiveness as a function of the beam species and its energy. The arrangement is shown in Fig 1, where the hole is shown tilted to be aligned with the beam direction. In our first experiments a set of holes is drilled with increasing values of the depth, D, as shown to the left in Fig 1.

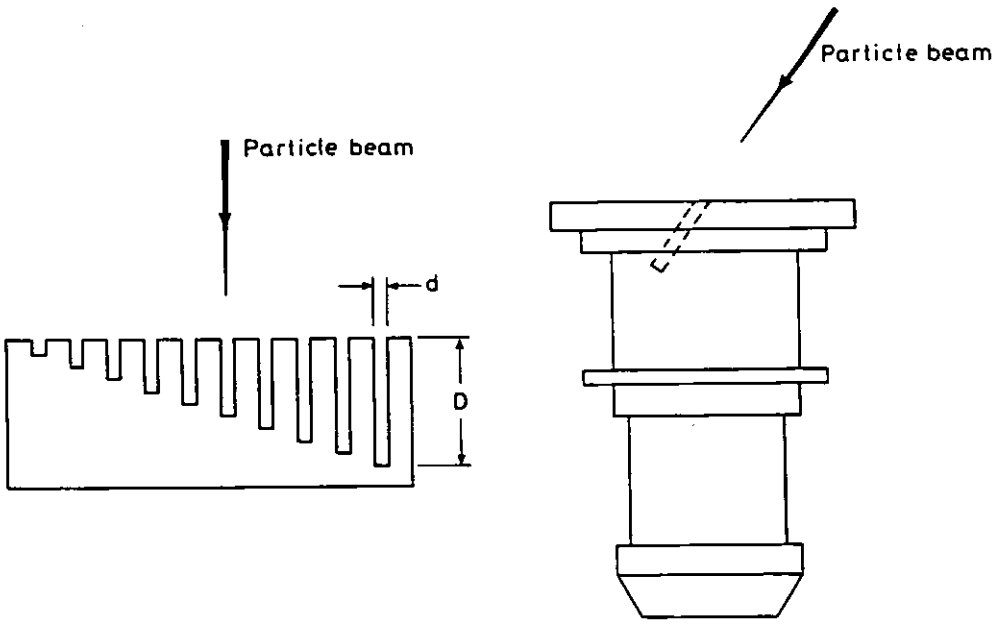

Fig 1 Schematic of the simple Faraday cup for electron and ion beam current measurements made from stainless steel. The multiple test structure is shown to the left and the practical cup to the right.

For a Gaussian beam profile, of standard deviation σ, described by a current density J(r,σ) at a radial distance, r, where

$$J\ (r,\sigma) = \frac{I_0}{2\pi\sigma^2} \exp(-r^2\ /\sigma^2) \tag{1}$$

the total current within a radius R, I(R), is

$$I(R) = I_0\ [1 - \exp(-R^2/2\sigma^2)] \tag{2}$$

so that for greater than 99.9% of the beam to enter the hole of diameter d we require:

$$d \geq 7.4\,\sigma \tag{3}$$

$$d \geq 3.2 \text{ FWHM of beam} \tag{4}$$

To allow a margin of error one should always use d ≥ 5 FWHM of the beam.

If this beam strikes the flat bottom of the cup in Fig 1 and if we assume the secondary electron emission coefficient is δ with a cosine angular emission dependence, it is easy to show that a fraction of the electrons emitted do not strike the cup walls at all and are directly emitted. This emission current, ε, is given by

$$\varepsilon = 0.5\ \delta\ (1 - \cos 2\alpha) \tag{5}$$

where α is given by

$$\tan\ \alpha = d\ /2D \tag{6}$$

Thus

$$\varepsilon = \delta d^2/(4D^2 + d^2) \tag{7}$$

$$\approx \delta d^2/4D^2 \qquad \text{if } d^2 << D^2 \tag{8}$$

If the drill leaves the base sloping at an angle β (say 30°) to the electron beam we find

$$\varepsilon = \delta \cos\beta(1-\cos\alpha) \tag{9}$$

$$\approx 0.866\ \delta\, d^2/4D^2 \tag{10}$$

which is very similar to Eq (8). The fraction of emission, δ - ε, strikes the wall of the Faraday cup liberating further electrons which may only be emitted if they are aligned to the aperture. Most of the electrons striking the wall of the cup have energies of less than 30 eV and hence have secondary electron emission coefficients of less than 0.1. Bearing in mind that the tertiary electrons are emitted with a cosθ distribution about the surface normal, we see that few of these tertiary electrons will be emitted. We therefore ignore these electrons.

We describe the secondary electron emission δ as a sum of the emission of low energy electrons, δ_o, and that of the high energy electrons, η:

$$\delta = \delta_o + \eta \tag{11}$$

The energy spectrum of the low energy secondary electrons may be described by the spectrum shape[12], n(E), where

$$n(E) = W\delta_o/(E + W)^2 \tag{12}$$

and W is a small energy term. If we now apply a bias voltage, V_B, to the drilled-hole Faraday cup we shall retain all electrons that would be emitted with energies, E, less than eV_B. Thus, from Eq (8)

$$\varepsilon(V_B) = \frac{d^2}{4D^2}\left(\frac{W\delta_0}{W+V_B} + \eta\right) \tag{13}$$

If we write

$$\eta = k\,\delta_0 \tag{14}$$

then

$$\varepsilon(V_B) = \frac{d^2\delta}{4D^2}\left(\frac{W}{W+V_B} + k\right)\frac{1}{1+k} \tag{15}$$

and hence

$$\varepsilon(V_B) = \frac{\varepsilon(0)}{1+k}\left(\frac{W}{W+V_B} + k\right) \tag{16}$$

Thus, as V_B increases, the fractional emission lost, $\varepsilon(V_B)$, will be reduced considerably over the value at zero bias. In the experiments that follow, therefore, we measure the overall efficiency of cups made from 1 mm drilled holes of up to 10 mm depth with biases, V_B, between 0 and 50 volts for (i) electron beams of energies between 1 and 3.5 keV and (ii) a focused gallium ion beam of energies between 4 and 7 keV.

2.2 CUPS FOR CURRENT DENSITY MEASUREMENT

The simple cups noted above, of one electrode to capture the charged particles, will not work for defining current densities accurately. Now we need a separate defining aperture as well as a collector, as shown in Fig 2. Note that normally the potential of the aperture and shield, V_S, is zero. For SIMS studies a target bias is often used to ensure that the emitted ions have the correct energy for mass analysis. For these systems V_S emulates the target bias.

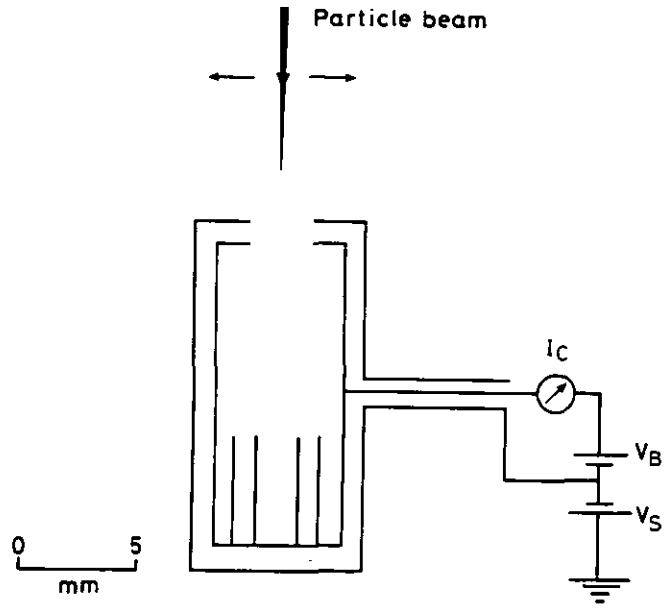

Fig 2 Schematic of a simple Faraday cup for electron and ion beam current density measurements. The vertical baffles inside the cup are a spiral electron absorbing structure coated with colloidal graphite.

To test the effectiveness of the cup we need a beam of known current density and this is achieved by rastering a known current, I, over a known raster area, A_R, covering the cup entrance aperture of area A_A. Note, as above, that the height and width of the raster must exceed the aperture diameter by five times the beam width at each side to cover the tails of

the beam distribution. The true current density, J_T, is thus given by

$$J_T = \frac{I}{A_R} \tag{17}$$

and the measured current density, J_M is deduced from the measured Faraday cup current, I_C, with the beam rastering the area A_R

$$J_M = \frac{I_C}{A_A} \tag{18}$$

The efficiency of the cup is then given by

$$\text{Efficiency} = J_M/J_T \tag{19}$$

The calculations of Ingram and Seah[10] describe the effects of the bias inside the cup, V_B, on (i) the effective aperture and (ii) the reduction in the secondary electron emission from the cup. In those calculations the effect of emission from the outside of the defining aperture of the cup shield, which is also important, was ignored. This is exacerbated by excessively positive values of V_B which attract the electrons inwards. It may, however, be reduced by biasing the whole cup negatively with respect to ground such that the stray electrons move to other electrodes rather than being attracted into the cup shown in Fig 2.

To test the system we therefore need to measure I, I_C, A_A and A_R. It should be noted, however, that A_R will depend on V_S, the potential of the cup outer shield. If it is assumed that the electrons or ions of energy E_o emerge from the deflector system of the gun which is forming the raster through a grounded electrode, then an increase in the area of the raster occurs due to the particle trajectories spreading in the retarding field due to V_S. The fractional increase, Δ, in the rastered area is given by:

$$\Delta = \frac{V_S}{2\,E_0} \tag{20}$$

where the 2 is valid for an ideal flat field between the Faraday cup shield and the end of the gun and may, in a practical environment, be somewhat higher or lower. Note that if V_S is positive, Δ is an increase in area for positive ions and a reduction for electrons.

2.3 ASTM Standard Practice for Approximate Determination of Current Density of Large Diameter Ion Beams for Sputter Depth Profiling of Solid Surfaces, E684-93[11]

This practice is designed as a simple method to define the approximate current density distribution of ion beams, of diameter greater than 0.5 mm, in which the density distribution is symmetrical about the beam axis. A 25 μm diameter tungsten wire is set to protrude from the side of a sample holder, normal to the ion beam axis. The total ion beam current, I, is measured by centering the holder and applying a + 30 V d.c. bias. The full width at half maximum (FWHM) of the distribution is determined by mechanically scanning the 25 μm wire across the beam. For a Gaussian beam the standard gives the current density at the centre of the beam, J_M as

$$J_M = \frac{0.88\ I}{(\mathrm{FWHM})^2} \tag{21}$$

If the distribution is formed by a raster, the wire needs to be aligned with the raster sides to determine the raster area A_R. In this case

$$J_M = \frac{I}{A_R} \tag{22}$$

In practice it is not possible to produce a true Gaussian beam and so to test the method we use the rastered focused beam and Eq (19). The standard notes that the errors of measurement of the method have not been investigated and that a Faraday cup detector should be used to obtain more accurate measurements of I. It is therefore difficult to know when this standard should be applied.

3 EXPERIMENTAL

The experiments were all conducted in a VG Microlab using VG electron and ion guns. For electron current and current density measurements an LEG 32 electron gun, capable of producing an electron beam of less than 100 μm diameter, was used for energies between 1 and 5 keV. The ion beam for current and current density measurements was from a liquid gallium sourced MIG 100. This gave beams of less than 10 μm diameter for energies between 4 and 7 keV. The ion beam for testing the ASTM standard was an argon ion beam from an EX05 capable of producing a 400 μm beam between 1 and 5 keV.

The Faraday cups were all set to be aligned to the relevant electron and ion beams. Raster sizes were determined from a calibrated grid imaged by the scanned beams at the Faraday cup position. A problem that occurred with the raster, which is non-trivial, occurred in our use of a TV raster scanning system. The VG microlab has two rasters available (i) a digital raster that is well defined and operates at up to 1024 by 1024 points with a frame time of 20s or with fewer points at frame times down to 1.25s and (ii) a standard TV scanning system. For much of our work in static SIMS we need many frames per channel in scanning the mass spectrum. A typical spectrum of 500 amu with 0.2 amu channel separation and 0.2s per channel would need TV rate imaging or different parts of the spectrum will come from different regions of the sample. The TV image extends some 31% beyond the screen image in the X direction and 29% in the Y direction compared with the area viewable and so the precise area of scan was calibrated by separate observation of the individual TV rate linescans in the image of the grid. Thus, the raster area was found to be 69% bigger than suggested by the area viewed on the screen. Such a factor was not found for the slow digital raster, but care has still to be taken if the number of pixels in the frame is changed. A change from 1024 pixels per line to 64 reduces the line length by 15 parts in 1024 etc, as will all digital rasters of this type.

Note also that for evenness in current densities, the points in the raster or lines in the TV display should not be separated by more than 0.7 times the full width at half maximum (FWHM) of the beam focal size. The value of 0.7 is deduced for a maximum of 0.5% intensity variation using Gaussian shaped beams. To be safe, a figure of 0.5 times the FWHM is recommended. In all of this work this criterion was observed.

The Faraday cups for beam current measurement were made as a set of 1 mm diameter holes drilled to depths from 1 mm to 10 mm at 1 mm increments in a stainless steel sample holder. The holes were separated by 2 mm. These were nominal sizes. The actual sizes were measured by optical microscopy and by using micrometers.

The Faraday cup for current density measurements is as shown in Fig 2 with a 2.5 mm diameter knife edge aperture, a shield to define A_A and vertical baffles inside the cup, coated with graphite, to reduce the scattered ions and secondary electrons. The cup inner aperture is 3.0 mm diameter and the cup depth 12.7 mm. Figure 2 is approximately to scale.

The experiments to test the ASTM standard practice to determine approximate current densities in ion beams could not be undertaken on unknown ion beams as one would then have no estimate of error. We, therefore, tested it on a rastered beam. The current was measured by biasing the sample holder by the recommended + 30 volts. The size was determined by tracing the recommended 25 μm wide tungsten wire across the beam. To do this effectively the wire is aligned exactly parallel to one side of the raster and the current to the wire, biased to + 30 volts, is monitored as a function of the wire position.

4 RESULTS AND DISCUSSION

4.1 ELECTRON BEAM CURRENTS

The effects of the depth of the simple cup on the measured current for a 3 keV electron beam with zero bias voltage is shown by the curve with $V_B = 0$ in Fig 3. The plotted curve represents

$$\varepsilon(0) = 4.2 \frac{d^2}{4D^2} \tag{23}$$

where, as before, ε is the fraction of the current lost. This plot is in close agreement with Eq (8). For over 95% efficiency D ≥ 5d, and for over 99% efficiency D > 12d.

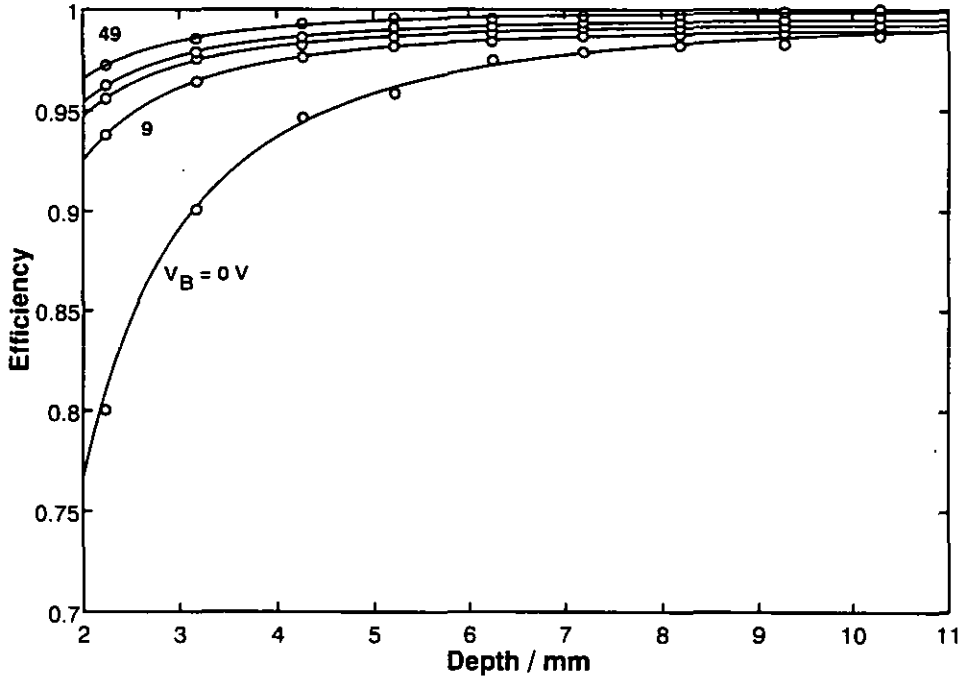

Fig 3 The efficiency of the Faraday cup formed by a 1 mm diameter hole drilled in stainless steel to various depths for a 3 keV electron beam at biases from zero up to 49 volts.

Applying a positive bias voltage, V_B, clearly improves the behaviour, as described in Eq (16). Figure 3 shows curves for four values of V_B in the range up to 49 volts. It is clear that a small bias raises the efficiency so that ε is reduced by a factor of 4 or so. Figure 4 shows the results replotted as a function of V_B with an expansion of the efficiency from 90 to 100%. The bias of 16.5 volts represents a 3-fold reduction in ε whereas at 49 volts the improvement increases 9-fold. Thus, we may write:

$$\varepsilon\,(49) \;=\; 0.615\;\frac{d^2}{4D^2} \tag{24}$$

In fact, the curves drawn in Figs 3 and 4 are for the function

$$\varepsilon(V_B) \;=\; \frac{d^2 4.20}{4D^2}\left(\frac{2.25}{2.25+V_B}\;+0.12\right)\frac{1}{1.12} \tag{25}$$

which is exactly of the form of Eq (16) with W = 2.25 eV and k = 0.12. These are values of the magnitude expected. The results of Figs 3 or 4 thus confirm our predictions very precisely. The form of Eq (25) is shown most clearly in the plot of Fig 5 where $\varepsilon(V_B)$ is plotted versus $(d/D)^2$.

It is useful to require that $\varepsilon(V_B)$ is less than say 1%, then one can solve Eq (25) for D/d versus V_B. For practical reasons, however, it is useful to keep V_B to the range 15 to 30 volts. We would therefore recommend a minimum bias of 30 volts with a minimum depth, D, of 5d. The above results are all for a beam energy of 3 keV. At other energies both δ_o and η will change. As the beam energy falls, δ_o and η will rise[10] slowly. We therefore expect a small deterioration in efficiency at lower beam energies, as shown in Fig 6.

4.2 ION BEAM CURRENTS

The above experiment was repeated for the gallium focused ion beam for energies of 4, 5, 6 and 7 keV and the same bias potentials as for the electron beam. The results for the 5 keV ion beam are shown in Fig 7. The results show that a small bias of 9 volts is sufficient to reduce errors to less than 0.25%. The results are described again by Eqns (15) and (16) except that, of course, the loss of secondary electrons leads to an overestimate rather than underestimate of the positive ion beam current. Furthermore, for ions, k is zero and the secondary electron emission from ions is much less than that for electrons[14,15]. Here δ has been reduced by a factor of 5 compared with the case for electrons.

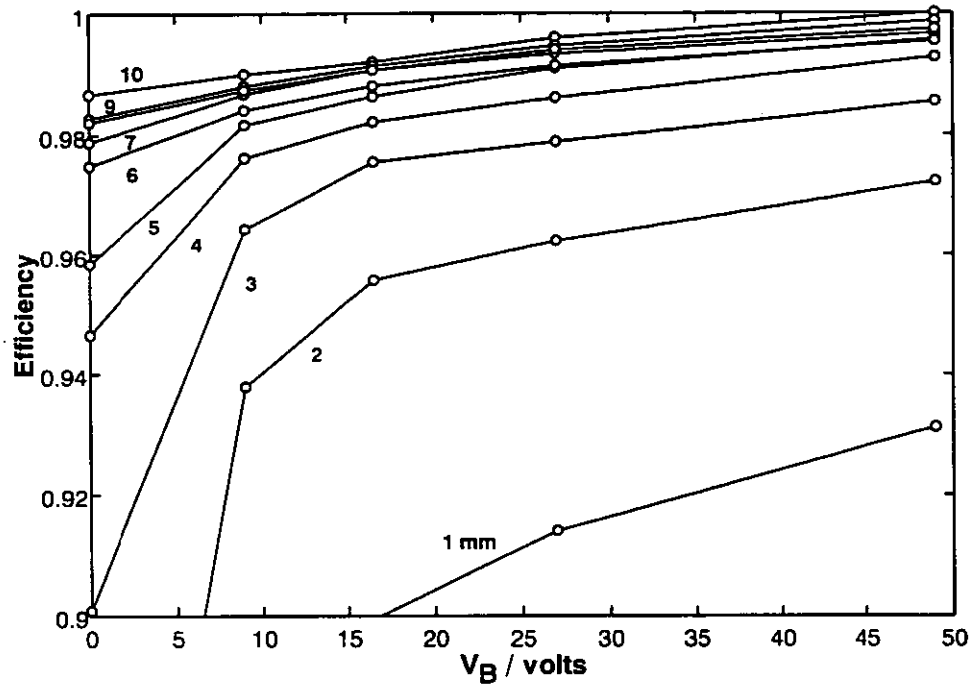

Fig 4 The data of Fig 3 replotted to show efficiencies above 90% as a function of the value of V_B for the cups of different depths, D.

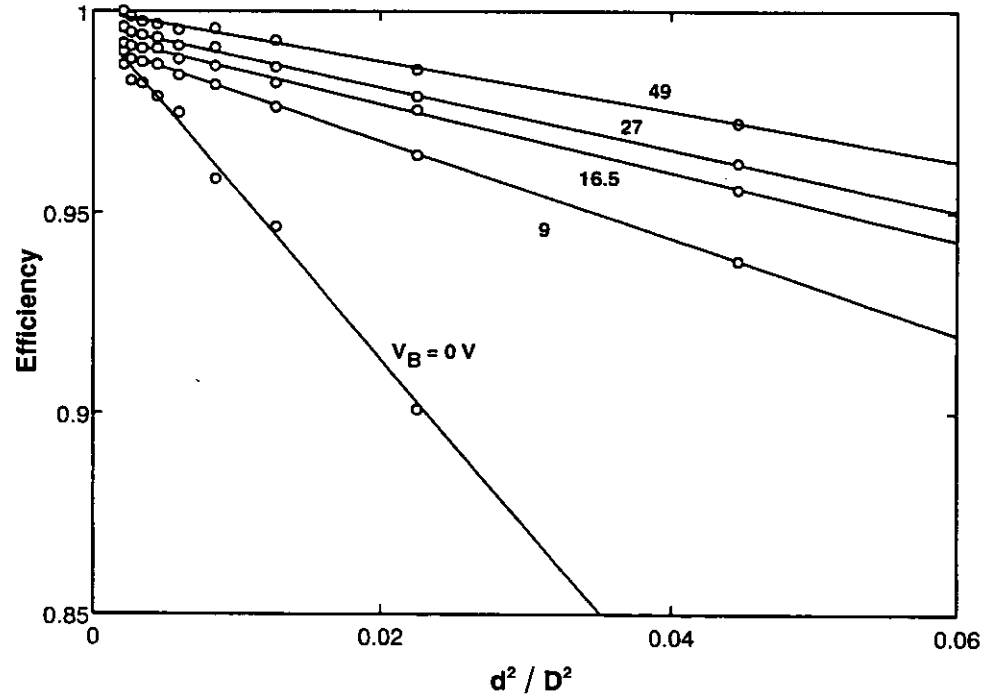

Fig 5 The data in Fig 3 replotted versus $(d/D)^2$.

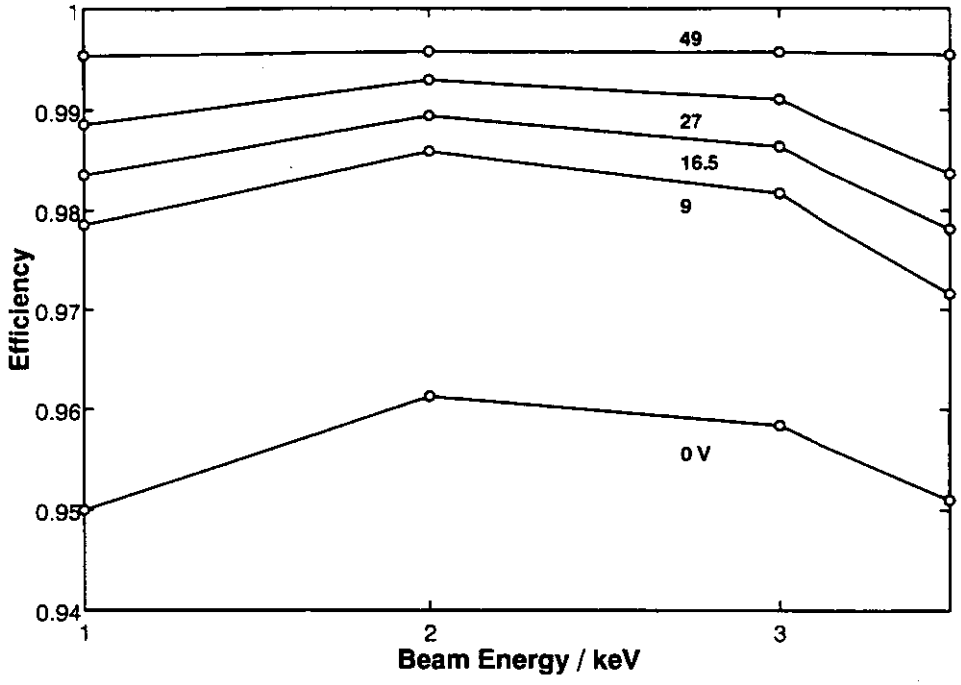

Fig 6 The efficiency of the 5 mm deep cup for various biases as a function of the electron beam energy.

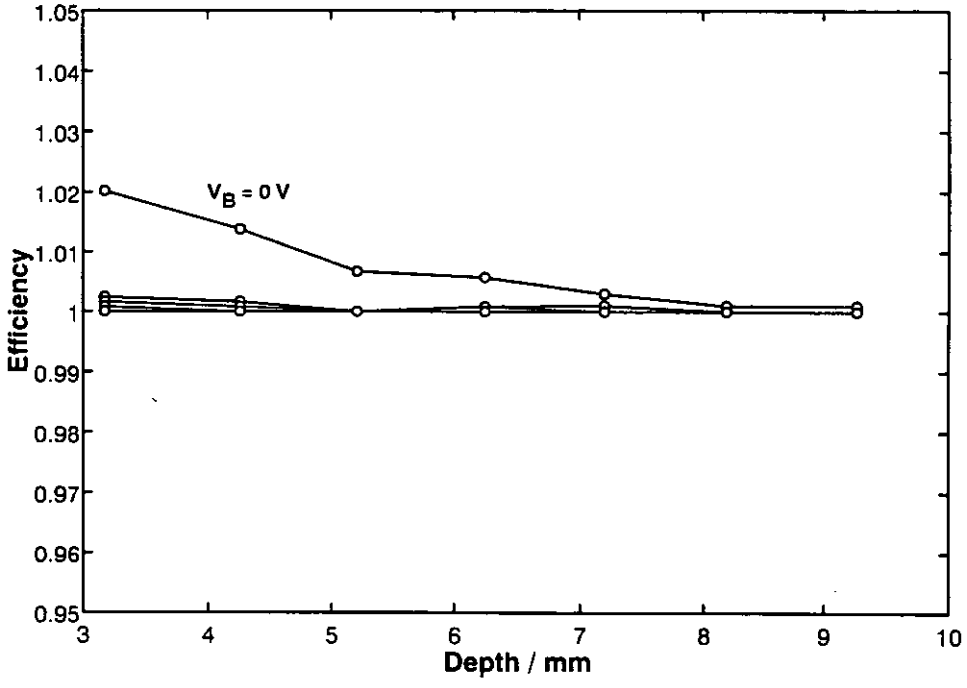

Fig 7 As for Fig 3 but using a 5 keV Ga^+ ion beam.

For ions the secondary electron emission rises with the beam energy in this range[16]. In general the rise will be roughly proportional to energy. The divergence from 100% efficiency for the ions would be difficult to measure (it is so small!) except at zero bias and so, in Fig 8, the cup efficiency measurements are given for the 5 mm deep cup at zero bias only. It is clear that the above recommendation for electrons, of a cup with D ≥ 5d and with + 30 volts bias would be more than satisfactory for ions, even for beams of up to 25 keV.

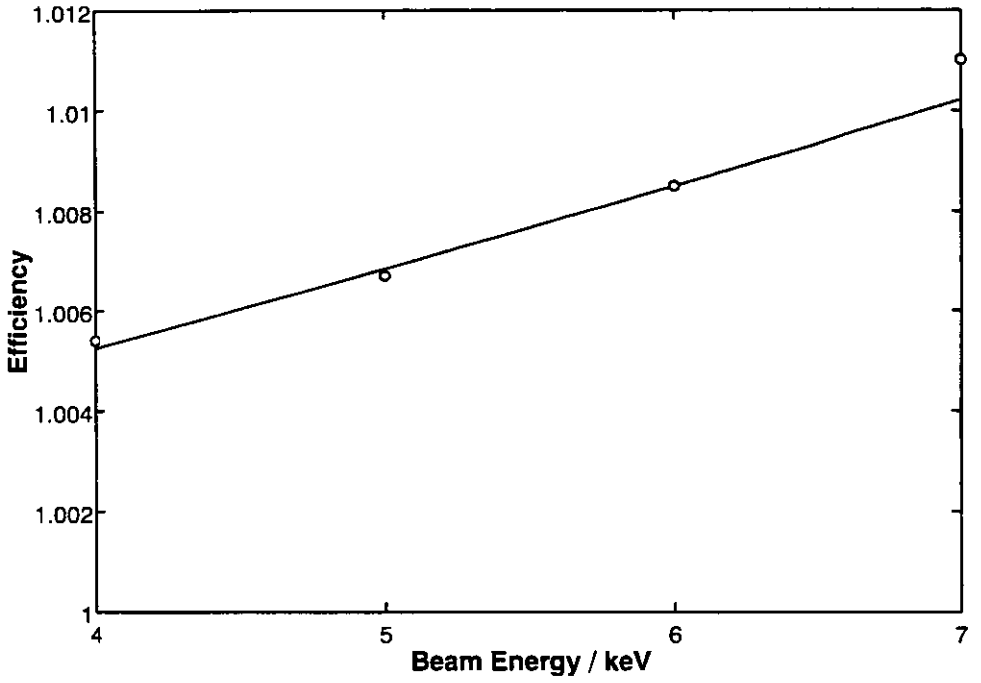

Fig 8 As for Fig 4 but using 4 to 7 keV Ga^+ ion beams and the 5 mm deep cup at zero bias.

4.3 ELECTRON BEAM CURRENT DENSITIES

Current densities may be needed in a stationary broad beam or in a raster scanned beam. Here we use an electron beam of 13 μA rastered over an area of 4.36 mm by 3.99 mm about the 2.5 mm diameter aperture with the inner cup potential, V_C (= V_B + V_S), set at fixed values and V_S variable over a wide range. The effect of scanning on the magnitude of the electron beam current was confirmed to be negligible. For V_C positive with respect to V_S, the secondary electrons should be retained in the cup. Thus, in Fig 9, we show how the collected current alters with the value of V_C-V_S for V_C = - 16.5 volts. For V_C-V_S > 10 volts the current is within 0.5% of its maximum. As V_S becomes more positive, electrons are repelled from the

cup and the efficiency falls.

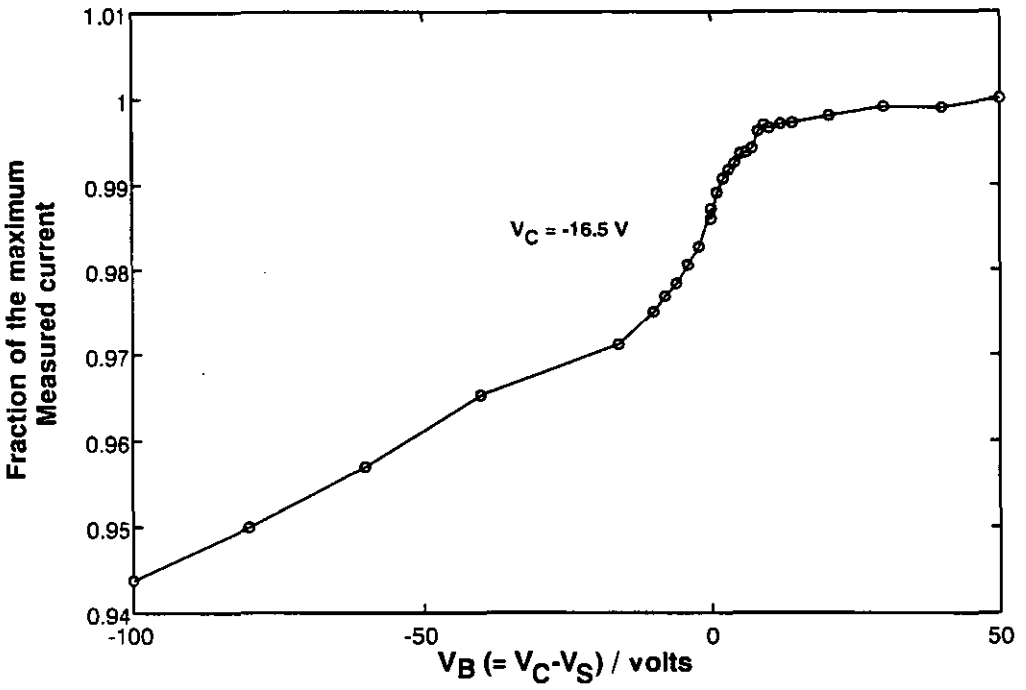

Fig 9 The fraction of the maximum current measured for a 3 keV rastered electron beam, by the Faraday cup of Fig 2, as a function of V_C-V_S for V_C = - 16.5 volts.

The reason for altering V_S is that, for convenience in the rest of the experiment one may either wish for the local field-free environment in front of the cup to be at a potential other than ground or alternatively one may require the electrometer, and therefore the cup, to be at ground.

If V_S is altered one needs to recalibrate the deflector system as suggested by Eq (20). In this work, by using grids attached to the shield electrode we find

$$\Delta = (0.884 \pm 0.034) \frac{V_S}{2E_0} \tag{26}$$

for V_S values up to 150 volts and electron beam energies between 1 and 5 keV. The slight reduction compared with Eq (20) arises because parts of the equipment at fixed potentials screen the fields arising from V_S. With the above correction and with the raster size calibrations described in section 3 we then determine the efficiency of the Faraday cup using Eqs (17), (18) and (19). In this way we deduce the efficiencies of Fig 10 for beams with energies between 1 and 3.5 keV.

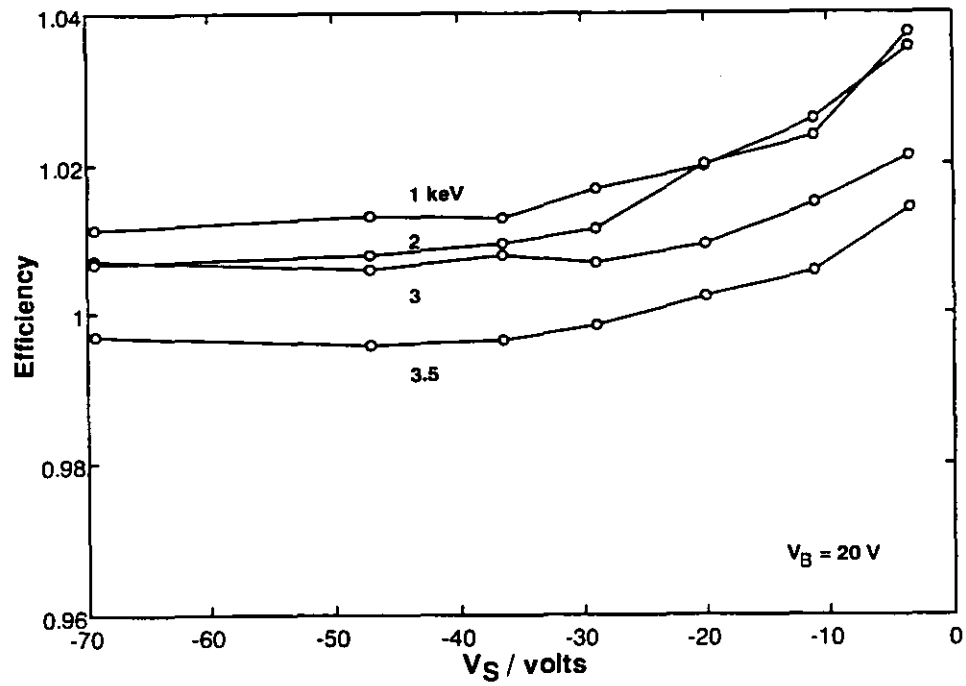

Fig 10 The efficiencies of the Faraday cup of Fig 2 for measuring the current densities of electron beams of different energies.

At low shield potentials a few of the electrons emitted from the front of the outer aperture, which should be excluded from the cup, may be attracted round and into the cup by the potential difference between the shield and cup. As the shield potential becomes more negative these are rejected more in the forward direction so that the efficiency, originally in excess of 100% in Fig 10 falls to be more closely 100%. As the beam energy rises the secondary electron emission coefficient of the cup surfaces falls and the efficiency converges more closely to 100%. Thus, from Fig 10, we recommend that the cup be 20 volts more positive than the shield but also the shield should be at least 40 volts negative with respect to ground. A convenient setting is with the cup at ground and the shield at - 40 volts.

In this work, the electron lensing effect of the potential difference between the cup and shield calculated by Ingram and Seah[10], shows the efficiency to be in excess of unity by γ, where

$$\gamma = \frac{0.144\ e\ (V_C - V_S)}{E_0} \qquad (28)$$

which, for V_C-V_S = 20 volts is less than 0.3% in Fig 10. The above choice of V_C = 0 and

V_S = -40 volts is thus a useful compromise with better than 1% accuracy for electron beams in the 1 to 4 keV range.

4.4 ION BEAM CURRENT DENSITIES

This part parallels that for the electrons except that, as we have already noted, the secondary electron emission for ion beams is generally lower than for electron beams. Figure 11 shows the effects of the shield and cup potentials as in Fig 9. Providing the cup potential is 10 V more positive than that of the shield, the measured current is within 0.3% of its saturation value. Using this bias we show, in Fig 12, the effects of varying the shield potential. This time the attraction of the stray electrons from the outer aperture outer surface for low shield values, reduces the cup efficiency instead of increasing it as in Fig 10. This arises as the gallium ion beam is of the opposite charge to that for the electron beam.

For a shield potential of - 40 volts, the efficiencies are within 2% of the target value of unity for beam energies in the range 3 to 7 keV. Unlike the electron case, the higher the ion beam energy, the more the secondary electron emission and so the most error occurs at the higher energies rather than the low.

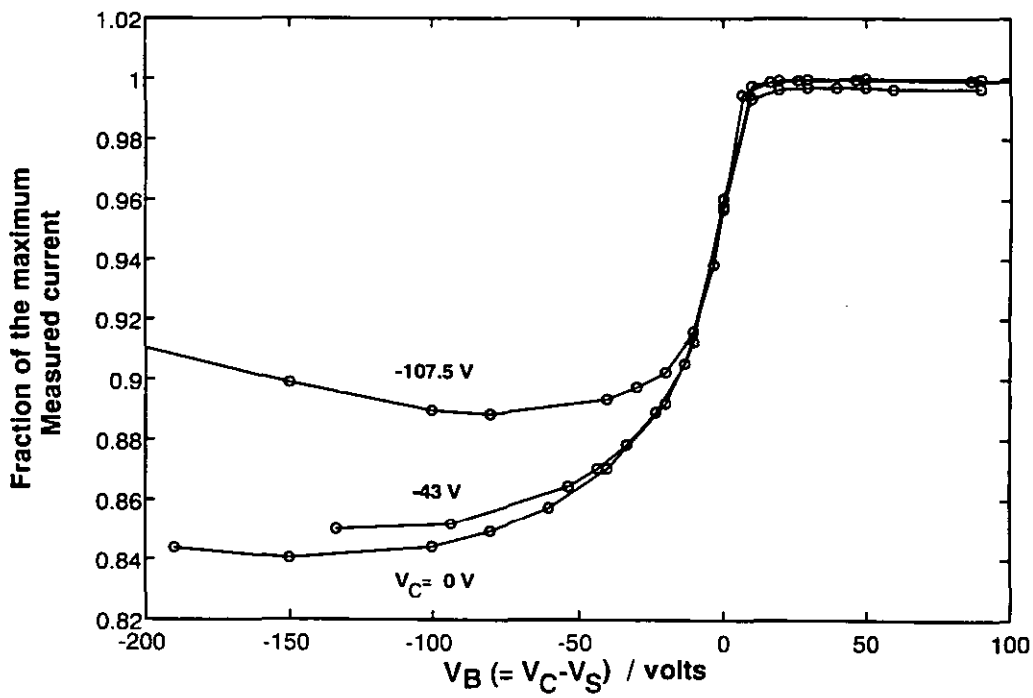

Fig 11 As in Fig 9 but for 3 values of V_C using a 5 keV rastered gallium ion beam.

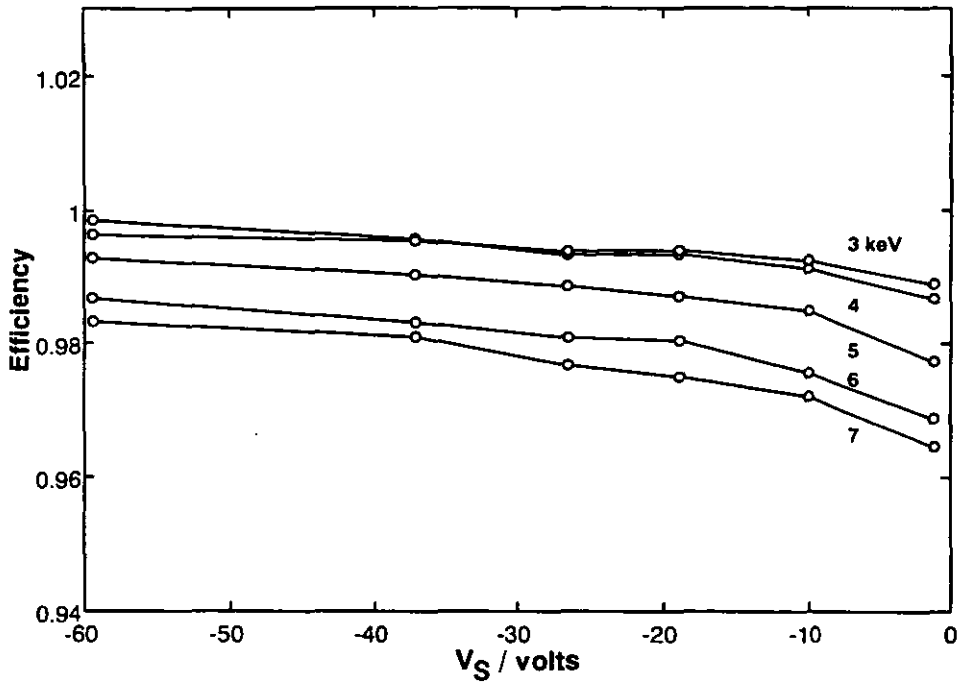

Fig 12 As in Fig 10 but for rastered gallium ion beams of 3 to 7 keV.

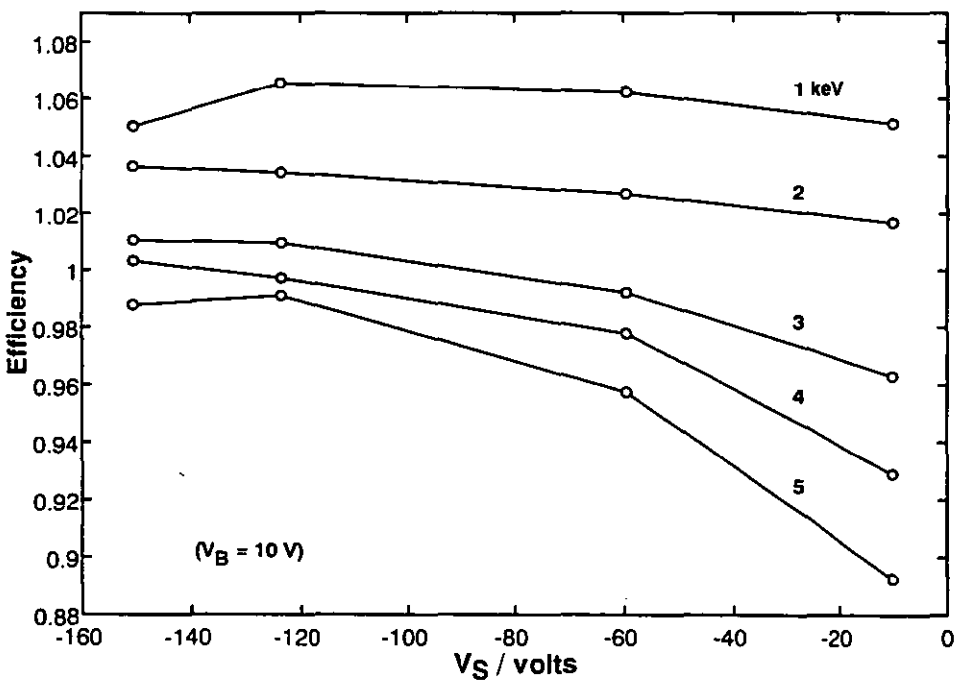

Fig 13 As for Fig 12 but with the internal aperture of the cup in Fig 2 removed.

In a simpler design where the inner aperture of the cup was omitted, electrons emitted from the back of the outer aperture were also collected when $V_C > V_S$. This caused the results shown in Fig 13 which show errors of 5% or so. The inner aperture in Fig 2 reduced the area of the outer aperture, viewed by the cup, by a factor of 8 so that the final errors in Fig 12 are less than 2%.

4.5 ION BEAM CURRENT DENSITIES USING THE STANDARD PRACTICE ASTM E 684-93

The method described in section 3 gave excellent results. The bias of + 30 volts gives the current in the ion beam to within 5% *provided that the sample holder fully intercepts the ion beam.* The current as a function of bias is shown in Fig 14. The ordinate here shows the ratio of the measured current to that defined by a Faraday cup.

The dimensions of the rastered square are also well established by this method, as shown in Fig 15. In this ideal situation of a square, flat-topped current distribution the accuracy of the FWHM will be around 5% leading to current densities accurate to 10%.

It is clear, however, without doing any experiments, that scans taken in two orthogonal directions, even if in the plane normal to the ion beam, will lead to errors for arbitrary current density distributions. If the distribution is Gaussian and symmetric or if it is Gaussian but elliptical with its major and minor axes parallel to wires for scanning, the results could still be valid. However, if the distribution is elliptical, but at an arbitrary angle to the wires, the current density deduced at the beam centre could be overestimated by a factor of up to:

$$(1 + m^2)/2m$$

where m is the ratio of the major and minor ellipse axes. For m values of 2 and 5 this error reaches 25% and 160%, respectively. The standard is stated to be relevant to a beam with a symmetrical density distribution, i.e. m = 1. For this case the standard can be accurate to better than 5%. The main problem is that, in general, one has no way of knowing if the ion beam conforms to the standard or not.

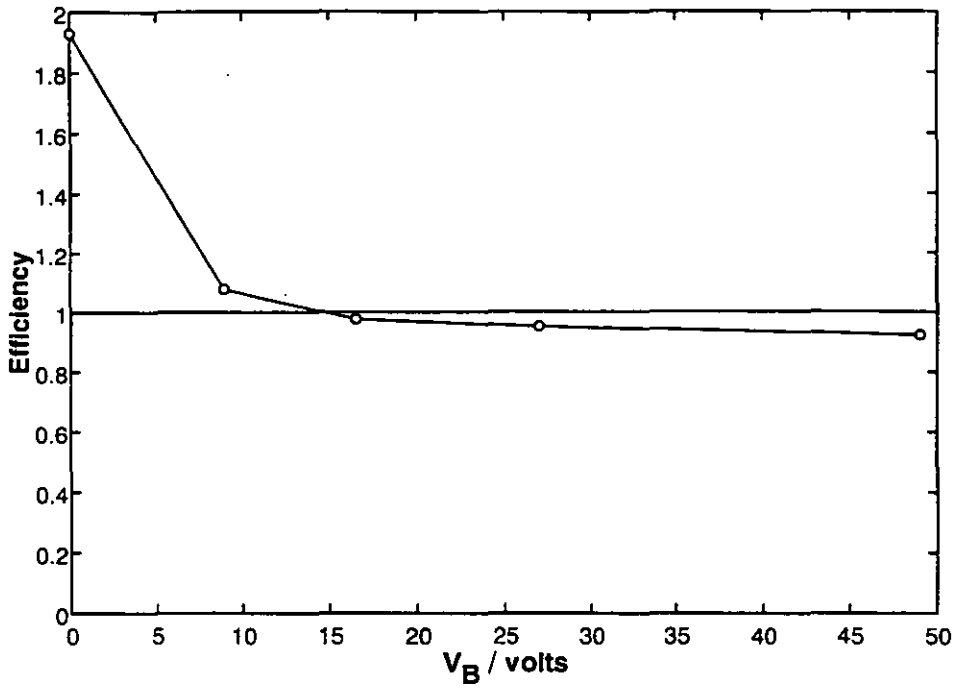

Fig 14 The ratio of the current measured by the sample holder for a 4 keV argon ion beam of 2 mm^2 rastered area to the beam current for a Faraday cup, as a function of the holder bias potential.

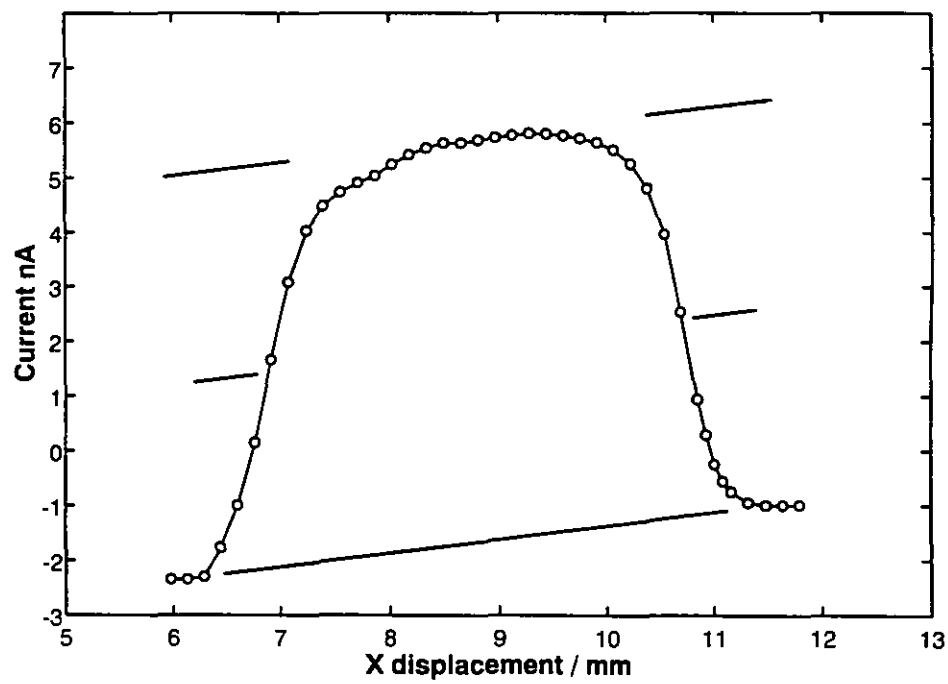

Fig 15 Trace of the current to the 25 μm tungsten wire across the beam used in Fig 14 as a function of position.

5 CONCLUSIONS

Electron and ion beam currents may be accurately measured by means of a biased sample holder with a simple drilled hole aligned to the beam. The hole diameter should be greater than 5 times the beam size and with a depth more than 5 times the hole diameter. The bias should be at least + 30 volts for electrons and + 15 volts for ions.

Electron and ion beam current densities may be measured using a simple shielded cup of the design shown in Fig 2 with appropriate dimensions. The entrance aperture must be chosen to be appropriate to the distribution required. Accurate results may be obtained with cup potentials 20 volts more positive than the shield and the shield - 40 volts with respect to ground.

The above conclusions relate to the conditions in instruments used for surface analysis and give accuracies better than ± 2% and often better than ± 1%. At these levels it is important to ensure that ancillary equipment, such as ammeters and calibration grids, have proper calibration certificates with up-to-date validity.

REFERENCES

(1) H L Bay, H H Andersen, W O Hofer and O Nielsen, Nucl. Instrum. Methods **132**, 301 (1976).

(2) H L Bay, H H Andersen, W O Hofer and O Nielsen, Appl. Phys. **11**, 289 (1976)

(3) J A Bevolo, Surf. Interface Anal. **3**, 240 (1981).

(4) ISO Standards Handbook 2, *Units of Measurement*, 2nd Edn., ISO Central Secretariat, Geneva, 1982.

(5) I Mills, T Cvitas, K Homann, N Kallay and K Kuchitsu, *Quantities, Units and Symbols in Physical Chemistry*, IUPAC, Blackwell, Oxford (1993).

(6) E673-93 *Standard Terminology Relating to Surface Analysis*, 1994 Annual Book of ASTM Standards, Vol 03.06, ASTM, Philadelphia (1994).

(7) C P Hunt and M P Seah Surf. Interface Anal. **5**, 199 (1983).

(8) C E Kuyatt, Methods of Exp. Phys. **7A**, 1 (1968).

(9) Y Ballu, Adv. Electron Electron Phys. Suppl. **13B**, 257 (1980).

(10) G D Ingram and M P Seah, J. Phys. E. Sci. Instrum. **22**, 242 (1989).

(11) E684-93 *Standard Practice for Approximate Determination of Current Density of Large Diameter Ion Beams for Sputter Depth Profiling of Solid Surfaces*, 1994 Annual Book of ASTM Standards, Volume 03.06, ASTM, Philadelphia (1994).

(12) M P Seah, Surf. Sci. **17**, 132 (1969).

(13) K Kanaya and S Ono, in *Electron Beam Interactions with Solids*, Proc 1st Pfefferkorn Conference, Asilomar 1982, SEM Inc., AMF O' Hare, Illinois (1984) p 69.

(14) S Y Lai, D Briggs, A Brown and J C Vickerman, Surf. Interface Anal. **8**, 93 (1986).

(15) W O Hofer, Scanning Microscopy Suppl. **4**, 265 (1990).

(16) M Kaminsky, *Atomic and Ionic Impact Phenomena on Metal Surfaces*, Springer (Berlin) 1965.

CHAPTER THREE

Surface Charge Stabilisation of Insulators for Highly Repeatable Spectra when using a Quadrupole Mass Spectrometer

1	INTRODUCTION	33
2	DESIGNS OF THE STABILISING SYSTEMS	34
3	OPERATION OF THE STABILISING SYSTEMS	35
3.1	THE ENERGY RESPONSE OF THE MODIFIED SIMS OPTICS	35
3.2	THE LOW ENERGY FLOOD GUN	36
3.3	THE 500 eV ELECTRON BEAM NEUTRALISATION	40
3.4	THE EMISSION PLATE ELECTRON NEUTRALISER	41
4	EXPERIMENTS	43
5	RESULTS AND DISCUSSIONS	44
6	CONCLUSIONS	57
REFERENCES		58

1 INTRODUCTION

A considerable proportion of the analysis of solid surfaces using static SIMS is of insulating samples. For these samples the surface potential must be stabilised in order that the emitted ions have the correct energy for analysis by the mass spectrometer. The quality needed for this stabilisation depends on the width of the energy band pass of the mass spectrometer. For quadrupole-based systems this is given typically as 10 eV[1,2] whereas, for time-of-flight systems, it ranges from 20 to 100 eV[1,3,4] depending on the mass resolution. Unfortunately, the range of ion emission energies and the band-passes are not rectangular functions which encompass each other so that some potential variation may be easily tolerated, but are peaked functions with their own particular structure. For instance, the Ni^+ and Ni_2^+ ion spectra from an oxidised Ni foil[5] show energy spectra which comprise a sharp rise at zero eV followed by a decay from the peak at 3 eV with full widths at half-maxima of 10 and 8 eV, respectively. The compound peaks NiO^+ and Ni_2O^+, however, have widths of only 4 eV. This variation in energy spectral widths between the species[5,6] means (i) that their relative intensities will depend on the range of energies accepted by the quadrupole and (ii) that those relative intensities will again change as the surface potential of the sample changes. In static SIMS, where these relative intensities are important, these effects need to be controlled.

Many methods have been used to stabilise the surface potential of insulators in SIMS[7], including low energy electrons from a flood gun[5], the deposition of a conducting grid[8], secondary electrons generated by a 700 eV electron beam striking the sample[9,10] or its support[11] and the use of uncharged atom beams[12,13]. The use of the grid is not popular for static SIMS studies because the deposition will contaminate even the areas supposedly left clear. The use of neutral beams also leads to charging since there is still emission of charged ions and emitted electrons. The use of flood electrons or electron beams are the most practical and popular methods of stabilising and so these are studied and developed here. This work only covers the use of positive ion beams; negative beams may need further consideration.

It is most important that the neutralisation is even over the sample surface or the fields developed may cause (i) a loss in intensity through a mismatch to the mass spectrometer energy window, (ii) a loss in intensity through deflection of the ions in the lateral field and

(iii) a migration of mobile ions[14] such as K^+ or Na^+.

2 DESIGNS OF THE STABILISING SYSTEMS

The electron neutralising systems are shown in Fig 1. At the top is the entrance system to the lens optics for the quadrupole mass spectrometer. The lens was originally a VG Scientific HTO100 which transported ions to an MM12-12 large rod, quadrupole mass spectrometer. This lens has been modified by the addition of an extra lens element and changes in the lens aperture sizes leading to a considerable increase in its sensitivity for large area, low fluence, static SIMS. This appears to be achieved without any change to the mass resolution settings of the instrument. The front element of this lens may be set at ground or any relevant potential to increase the SIMS sensitivity. In front of the lens is an electron emission plate whose potential, V_p, may also be set as required.

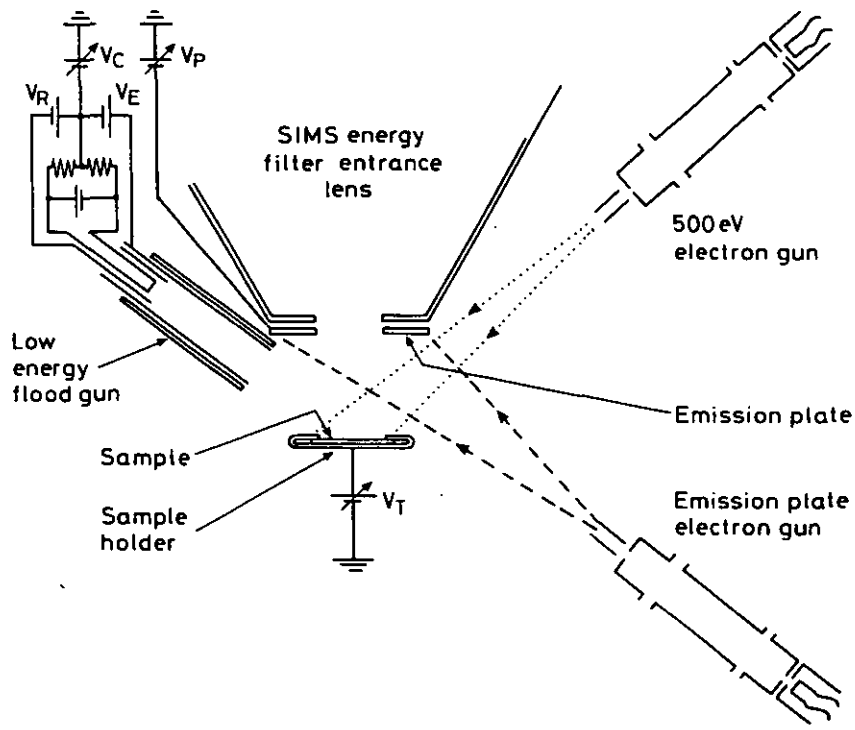

Fig 1 Schematic of the three electron source neutralising systems and other electrodes used in this work.

The sample is set in a sample holder which wraps around the sides of the sample. The potential of this holder, V_T, may be fixed or scanned. The sample surface may be charge

stabilised by electrons from any of the three guns. The low energy flood gun has a large area ribbon filament with an extraction drift tube, at V_E with respect to the filament centre tap, generally as discussed earlier[5]. This gun has a repeller at the back to increase efficiency and a shielding tube at ground so that the drift tube does not affect the ion trajectories from the sample in the SIMS analysis. The 500 eV electron gun is a VG Scientific LEG 32 gun which can deliver up to 40 μA of current into a focused or defocused spot which may be rastered over the sample. The emission plate electron gun is arranged behind the sample so that 1000 eV electrons may be focused onto a point on the stainless steel emission plate or rastered to cover its full area. Secondary emitted electrons from this plate illuminate the sample fairly evenly. The argon ion gun is a VG Scientific EX05 pointing at the sample and set at 56° to the mass spectrometer.

3 OPERATION OF THE STABILISING SYSTEMS

3.1 THE ENERGY RESPONSE OF THE MODIFIED SIMS OPTICS

For maximum efficiency the sample holder potential, V_T, is not set at zero but at +20V for positive ions and -20V for negative ions. Figure 2 shows the intensity transmitted as V_T is scanned for ions of both polarity from a sample of tantalum pentoxide grown on tantalum[15] sputtered by 4 keV argon ions. The scanning of the sample holder potential produces an approximation to the true energy spectrum of the emitted ions. There is no charge neutralisation problem here as this oxide film, 100 nm thick, does not charge under the beam current conditions used and hence the sample potential may be taken to be the same as the sample holder potential.

In this application, to keep the sample in a field-free region and for reasons that will become clear later, the emission plate is tied electrically to the sample, i.e. $V_p = V_T$.

Several points may be noted from Fig 2. Firstly, the energy resolution of the spectrum is not as good as previously[5]. The reason for this is that the opening up of the apertures in the HTO 100 lens degrades its resolution as an energy filter. This does not, however, affect the mass resolution to the limits of our measurements. This is a desired result since one would ideally like the system to be totally insensitive to the emitted ion energies. Secondly the zero energy positive ions are measured when they are accelerated away from the sample by 25

eV and similarly for the negative ions so that the SIMS optics is most efficient for ions being passed at 25 eV. Since the peak intensities occur around 5 eV, the target bias is usually set to add 20 eV of energy. The top abscissa in Fig 2 gives the ion energy scales. It is clear in Fig 2 that the relative intensities of the peaks depends sensitively on the sample potential. For less than a 2% change, the potential must not change more than 0.8 volts. With the undegraded energy resolution in a similar system, Briggs[7] shows that such a change in the target bias can lead to changes of 25% or more! This criticality does not appear to have been addressed by manufacturers and has remained a problem for analysts using quadrupole mass spectrometer based SIMS systems.

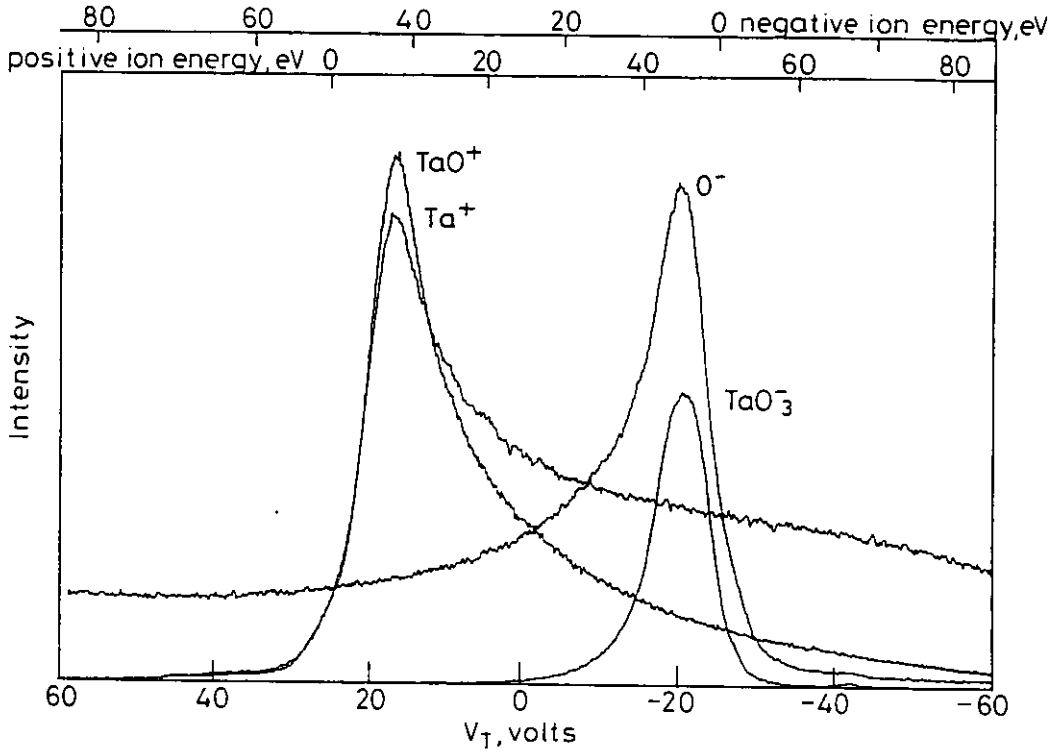

Fig 2 The intensities of the TaO^+, Ta^+, O^- and TaO_3^- peaks from sputtered tantalum pentoxide using 4 keV argon ions, as a function of the sample and emission plate potentials.

In order to define the behaviour of the neutralising systems for insulating samples we may produce plots, as in Fig 2, either for conducting samples, with the sample not connected to V_T but left open circuit, or for insulating samples.

3.2 THE LOW ENERGY FLOOD GUN

In the absence of an incident ion beam we may readily consider the sample behaviour by

using Fig 3[5]. The hatched zones show the potentials for the Fermi levels of ground (earth), the sample (here a conductor left floating) and the gun cathode. The cathode emits an energy distribution, ΔE, above its work function, ϕ_c. These electrons will be attracted to the sample and, since low energy electrons have a secondary electron emission coefficient of less than unity, will charge it negatively until the potential has risen so that the sample vacuum level at S reaches close to the top of the energy distribution of the cathode electrons and no more charging can occur. Thus, at equilibrium:

$$V_T = V_c + V_1 \tag{1}$$

where V_c is the cathode potential and V_1 is a constant given by:

$$V_1 = \phi_T - \phi_c - \Delta E \tag{2}$$

If we now switch on an ion beam, secondary electrons and ions are emitted from the sample. These secondary currents are less intense than the primary ion beam so that the sample starts to change positively. The point S then fails to reach the top of the cathode energy distribution. If there is a high flux of electrons and if ΔE is very narrow, as soon as S falls below this point, the electrons are attracted back to the sample surface and balance the ion beam current. The higher the ratio of the electron to ion beam currents and the narrower ΔE, the more effectively the point S is stabilised at the cathode surface potential.

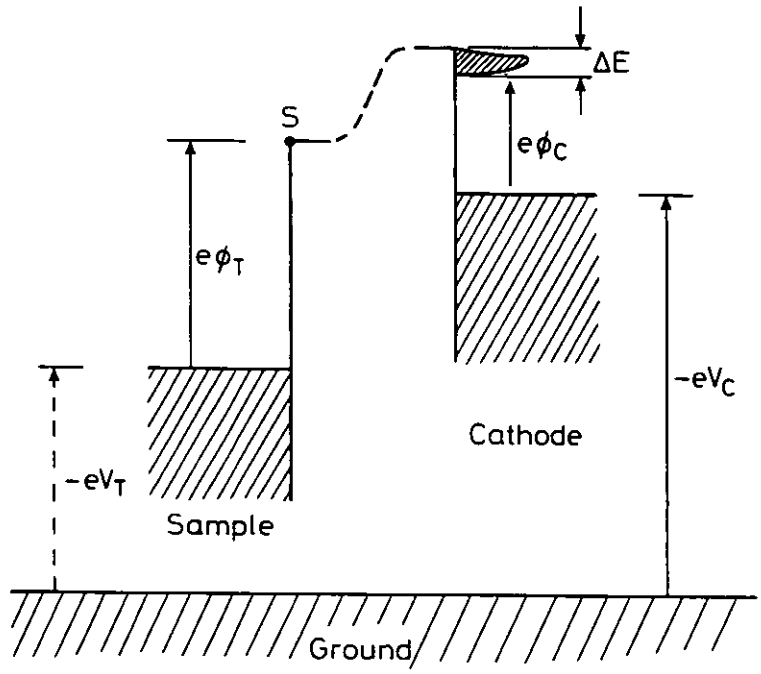

Fig 3 Potential energy diagram for the sample and simple neutralising gun cathode, after Hunt et al[5].

Thus, from Eq (1) we may scan V_T by scanning V_c for the case in which the sample is either floating or an insulator and try to replicate energy spectra such as those in Fig 2. If we can replicate such spectra we may be confident that the gun is usable and evaluate its robustness to changes in the gun settings, the ion beam parameters, the sample properties and geometry.

The above model is described in terms of a conductor for simplicity. For insulators part of the discussion is much the same. The sample Fermi level is effectively in the band gap above the valence band and its position will depend on defects and damage; the surface potential at S, however, is stabilised in exactly the same way as for conductors. One point of difference with an insulator is the lack of lateral conductivity. This causes the surface potential in the centre of the ion beam to be more positive than elsewhere.

Using the SIMION ray tracing program we have calculated this focusing effect, and hence the increase in solid angle of the transmitted ions as a function of (i) the surface potential, (ii) the area that is charging (assumed to be the area of the positive ion beam) and (iii) the charge sign of the emitted ion. The focusing effect for positive ions turns out to be very small for small areas, irrespective of the charging of the surface (assuming it to be positive) since the focusing field that is formed has spherical equipotentials. In order to neutralise a given incident beam current, flood electrons must be attracted from a certain volume of the surrounding space. We assume, here, an ambient environment of very low energy electrons for neutralising the surface. Since the spherical potentials follow an inverse square law with distance, it turns out that the charging of the surface must also follow this law, approximately, in relation to the beam diameter. Thus, as the beam size increases, the charging of the surface decreases, the area that is charging increases and the equipotentials begin to flatten and provide an enhancement of the solid angle. As the beam size increases further, the charging of the surface becomes insignificant and the focusing effect is lost. For a spectrometer able to accept ions of all energies, therefore, we have the efficiency as a function of beam size, all other parameters being constant, shown by the upper curve in Fig 4. For small beams the surface charges strongly and, in our system, the ion energies would be beyond the transmission range of the equipment. The dotted line shows an estimate of the reduction caused by this effect that is appropriate to a quadrupole instrument.

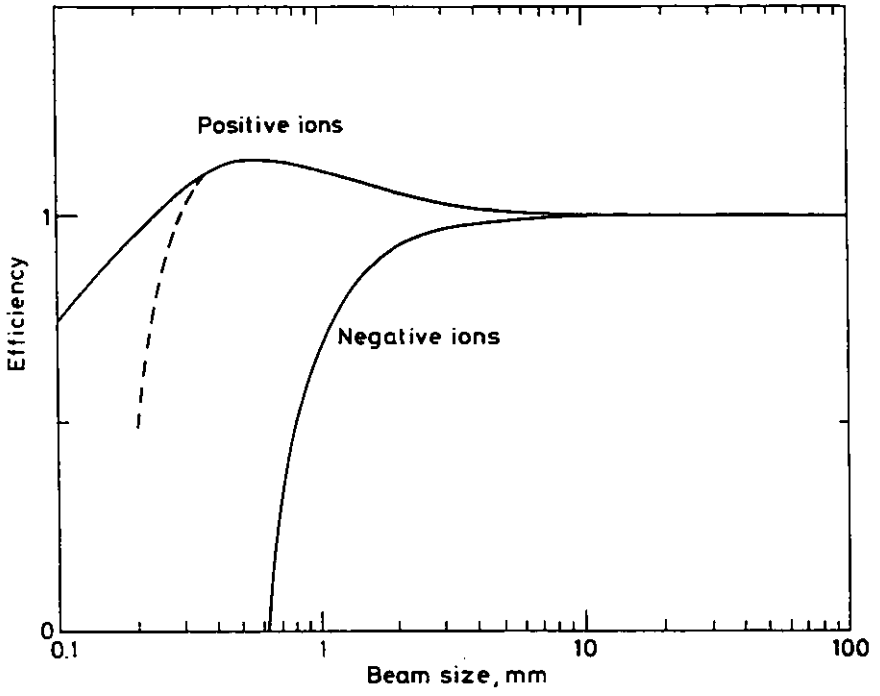

Fig 4 The efficiency of ion collection as a function of the size of a positive ion beam for an insulating sample surrounded by an environmental of very low energy flood electrons. The dotted position shows the loss of efficiency which would arise due to the increase in the ion energy and the failure of the mass spectrometer to detect these ions.

For negative ions the behaviour is different since the surface charging instead of ejecting the ions tends to retain them. Thus, until the beam size is large enough for the surface charging to be less than, say, 5 volts, the emitted flux of negative ions is small. As the beam size increases the potential hill to emission is reduced and the measured flux rises. The behaviour in Fig 4 assumes a certain flux of neutralising electrons and a certain ion beam current. For a given beam size we would move to the right in Fig 4 as the ratio of the electron and ion currents increases and to the left as it reduces. The peak in the curve for positive ions may mislead analysts to matching the electron current to "tune" their system for maximum efficiency and so doing find that they have lost the negative ions completely. In this case they have used the sample to form a small lens which works to their advantage only with the positive ions. It would appear to be best to work as far to the right in Fig 4 since then all potentials are properly controlled even though the positive ion intensity may not be at its maximum. Note that rastering the ion beam is not the same as defocusing since the instantaneous current density remains unaltered.

3.3 THE 500 eV ELECTRON BEAM NEUTRALISATION

With this general method, either the sample holder close to the sample is struck by the focused 500 eV electron beam or the beam is used to flood the surface by defocussing or by raster scanning. The focused beam impacting the holder at the side is a simple variant of the next method and so will be discussed there. The raster scanned electron beam is not the same as the defocused beam since the charging rates are effectively instantaneous and we therefore have a very much higher electron current density than in the defocused unrastered mode. In concept, the 500 eV beam energy-level diagram is similar to Fig 3 except that the ΔE part is much more complex, comprising a positive peak at 500 eV due to the incoming electrons and a negative energy spectrum of the outgoing electrons which, if the secondary electron emission is around unity, will be dominated by the low energy secondaries in the range 0 to 20 eV. The fraction of these that escape depends on the relative potential at S and the surrounding electrodes which are usually at ground.

In this method we start with our positive ion beam, I_p. This will charge the surface positively. With the whole sample illuminated by a beam, I_e, of 500 eV electrons, low energy secondaries are emitted from the whole sample and are attracted to the region of the ion beam. Providing $I_e > I_p$, they will start to neutralise the charge. As the potential reaches zero the attraction reduces so that the surface area struck by the ion beam should naturally equilibrate at a potential close to that of the neighbouring electrodes. If the potentials of these electrodes are scanned we should be able to replicate the spectra as in Fig 2 as if we were scanning the sample holder potential V_T. It may well be that regions not struck by the ion beam charge negatively to potentials up to -500 volts. The large potential gradient around the emission area of the sample will cause larger focusing effects than those mentioned above and therefore significant intensity changes in the measured ions that are difficult to predict and may produce an unwanted source of uncertainty. The use of a focused rastered electron beam may lead to further uncertainties if the charging is very rapid since there are then, at any given time, three identifiable regions: (i) both electron and ion beams, (ii) ion beam only and (iii) electron beam only which may lead to irreproducibility in the ion energies and the ion trajectories so that poor intensity repeatability results.

3.4 THE EMISSION PLATE ELECTRON NEUTRALISER

This method was originally devised to provide an even flux of low energy electrons which would strike the sample from many incident angles from the forward direction. It also provides the electrons in this rather cramped space without the need for a UHV port with access to the front of the sample. A 1000 eV electron beam strikes the stainless steel electrode, known as the emission plate, which is held at the same potential as the sample holder. The spectrum of secondary electrons emitted from the plate, as measured in an Auger electron spectrometer, is shown in Fig 5. Figure 5(a) shows approximately the whole En(E) spectrum, where E is the emitted electron energy and n(E) is the true spectrum. Most of the emitted electrons are in the low energy peak with energies below 5 eV but a few percent have energies of up to 1000 eV. Figure 5(b) shows a detail of the low energy peak from 0 to 20 eV and 0 to 4 eV in the n(E) format.

With this electron flux incident on the sample and in the absence of an ion beam we would expect that the sample could in principle, charge to -1000 volts, i.e. the maximum energy shown in Fig 5(a) so that eventually no electrons are absorbed by the sample. If the ion beam is now switched on, the surface potential will become more positive until the electrons attracted to the region struck by the ion beam just balance the effect of the ion beam current, I_p. In terms of the energy spectrum n(E) from the emission plate the sample surface potential, V_T, will be given approximately by:

$$\int_{eV_T}^{1000\ eV} n(E)\ dE = I_p \qquad (3)$$

It is clear that, as most of n(E) is distributed over the energy range 1 to 3 eV, for a large range the ratio of I_p to the electron beam current, I_e, the surface potential, V_T, will settle 1 to 3 volts negative with respect to the emission plate. As I_p is increased or I_e reduced this potential will reduce until eventually I_e is insufficient and the surface charges to a high positive potential.

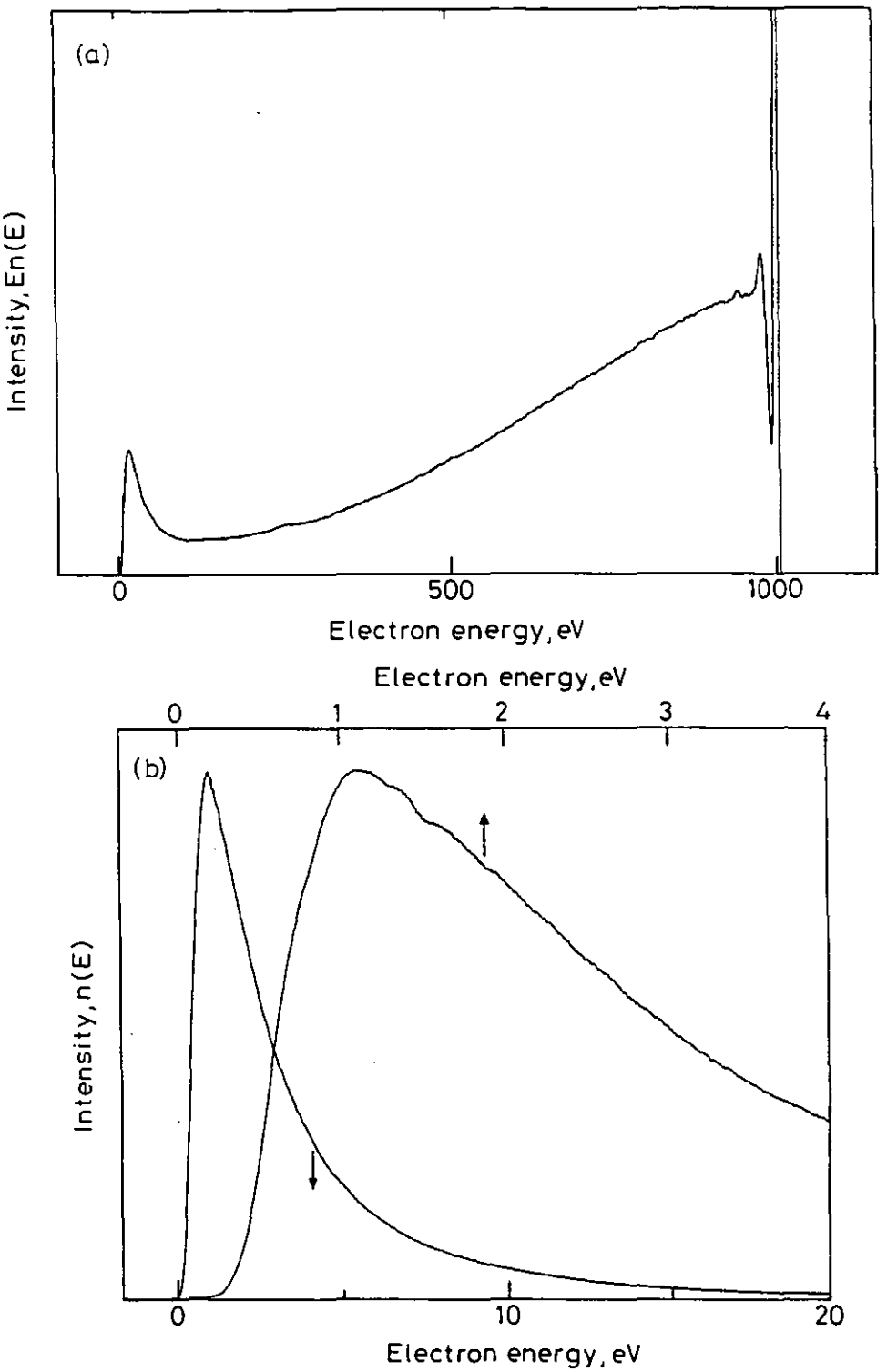

Fig 5 Energy spectra from the stainless steel emission plate bombarded by 1 keV electrons, (a) whole spectrum in the En(E) format, (b) detail of the low energy secondaries in n(E) format from 0 to 20 and 0 to 4 eV.

As with the 500 eV beam method, the region not struck by the ion beam will tend to charge negatively towards the cathode potential of the electron gun. The extent to which this occurs

should be much weaker here since the current of high energy electrons is only of the order of 1% of those for the direct beam. As with the previous cases, by scanning the sample holder and emission plate potentials we should be able to produce energy spectra as in Fig 2.

It is important to note in all of these methods that stray electrodes intruding into the space between the sample and the emission plate will affect the quality of the stabilisation and of the secondary ion trajectories to the SIMS analyser.

4 EXPERIMENTS

In order to achieve the high quality of repeatability presented here it was found necessary to replace the valves in the RF power circuits with semiconductor diodes and to improve the thermal stability of the quadrupole electronics generally. In this work we use a 4 keV argon ion beam to study the positive and negative ions from tantalum pentoxide films 100 nm thick, grown on polycrystalline foil[15], potassium bromide cleaved single crystals and PTFE tape of the type used for domestic plumbing work, purchased locally. All of the samples are selected to provide a good range of elemental and polyatomic species across the mass range, so that different width energy distributions (which are likely to cause relative spectral intensity changes in SIMS as the surface potential alters) may be studied. The tantalum pentoxide is used as a conductor or, by disconnecting the holder, as an insulator in which there are no lateral surface potential changes, whereas the other materials represent true insulators. To produce repeatable spectra, the tantalum pentoxide is always sputtered with 100 Cm^{-2}, an amount sufficient to remove more than 10 nm and to reach sputtering equilibrium, the KBr is also sputtered to equilibrium, whereas the PTFE is kept in the static SIMS regime with a fluence in the beam of less than 10^{17} ions/m^2[16]. In all cases the sputtering beam is of 4 kV argon ions set at 56° to the surface normal. For the samples sputtered to equilibrium, the beam is focused to a spot of 100 μm and is set to raster an area 2 mm by 2 mm on the sample at TV rates whereas, for those studied in the static mode, approximately 7 mm by 7 mm is analysed with the beam defocused to 1.5 mm diameter. This latter mode is best for static conditions to keep the fluence low but led to very long sputtering times for equilibrium conditions. Hence the former conditions were also used in this work.

The SIMS spectra for these three samples are shown in Figs 6, 7 and 8, respectively. In all of this work the mass resolution in the spectra is set to unity. The data are acquired at channel intervals of 0.2 amu and are then allocated to a defined mass by a separate software programme. As can be seen from Figs 6, 7 and 8, the overlap from one peak into the channel at 0.6 amu from the peak is well below 1% across the mass range. The Ta_2O_5 spectrum shows clear atomic and polyatomic species but differs strongly from the handbook spectra[17] as the latter are for contaminated Ta_2O_5 and are in the static SIMS regime. The KBr has peaks in both the positive and negative spectra extending to over 800 amu and again differs from the Handbook of Static SIMS[17] where the data are again for the static regime and where Na appears as a strong impurity. For PTFE, the data here in Fig 7 are for the static regime. It is difficult to compare these spectra with those of Briggs[16] since damage effects were being studied in that work and the fluence for those spectra are well beyond the static regime. The results, however, are in fair agreement with the above Handbook of Static SIMS[17], the more recent ToF SIMS spectra of Briggs et al[18] and in moderate agreement with the Static SIMS Handbook of Polymer Analysis[19].

5 RESULTS AND DISCUSSIONS

The simplest system to study was the low energy flood gun. With an insulating sample the emission plate voltage, V_p, the sample holder potential, V_T, and the gun cathode voltage, V_c, are all set equal and are slowly scanned from -60V to +60V. Here it was found that energy spectra precisely as in Fig 2 were obtained. Great care was needed or the flood electrons were repelled by the grounded vacuum vessel and other metal parts of the system so that no electrons could strike the sample to charge stabilise for $V_c > 1$ volt. This difficulty was found earlier[5] but was overcome here by mounting the gun close to the sample, as shown in Fig 1. A disadvantage of this design is that now radiant heat from the filament has direct impact on the sample and may cause (i) unwanted thermal degradation problems and (ii) contamination from the filament. A further disadvantage appeared, as discussed later in this section.

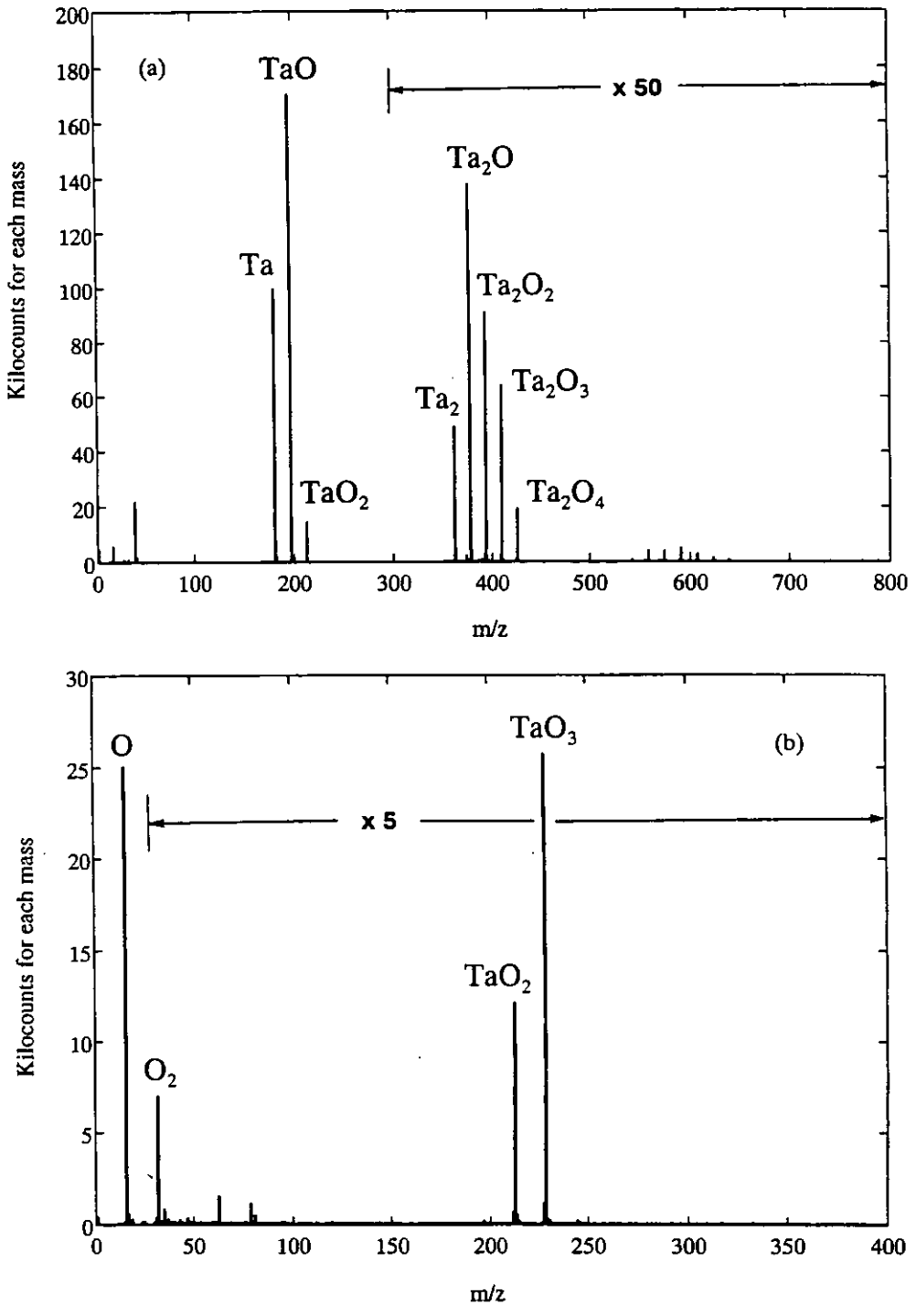

Fig 6 SIMS mass spectra from sputtered tantalum pentoxide at equilibrium after sputtering with 4 keV argon ions, at 56° to the surface normal (a) positive spectrum using a 2.5 nA beam (b) negative spectrum using a 2.5 nA beam. The beam rasters an area of 4 mm^2 on the sample. The spectra, acquired at 5 channels per amu with 200 msec channel dwell time, are presented as the total counts in each amu.

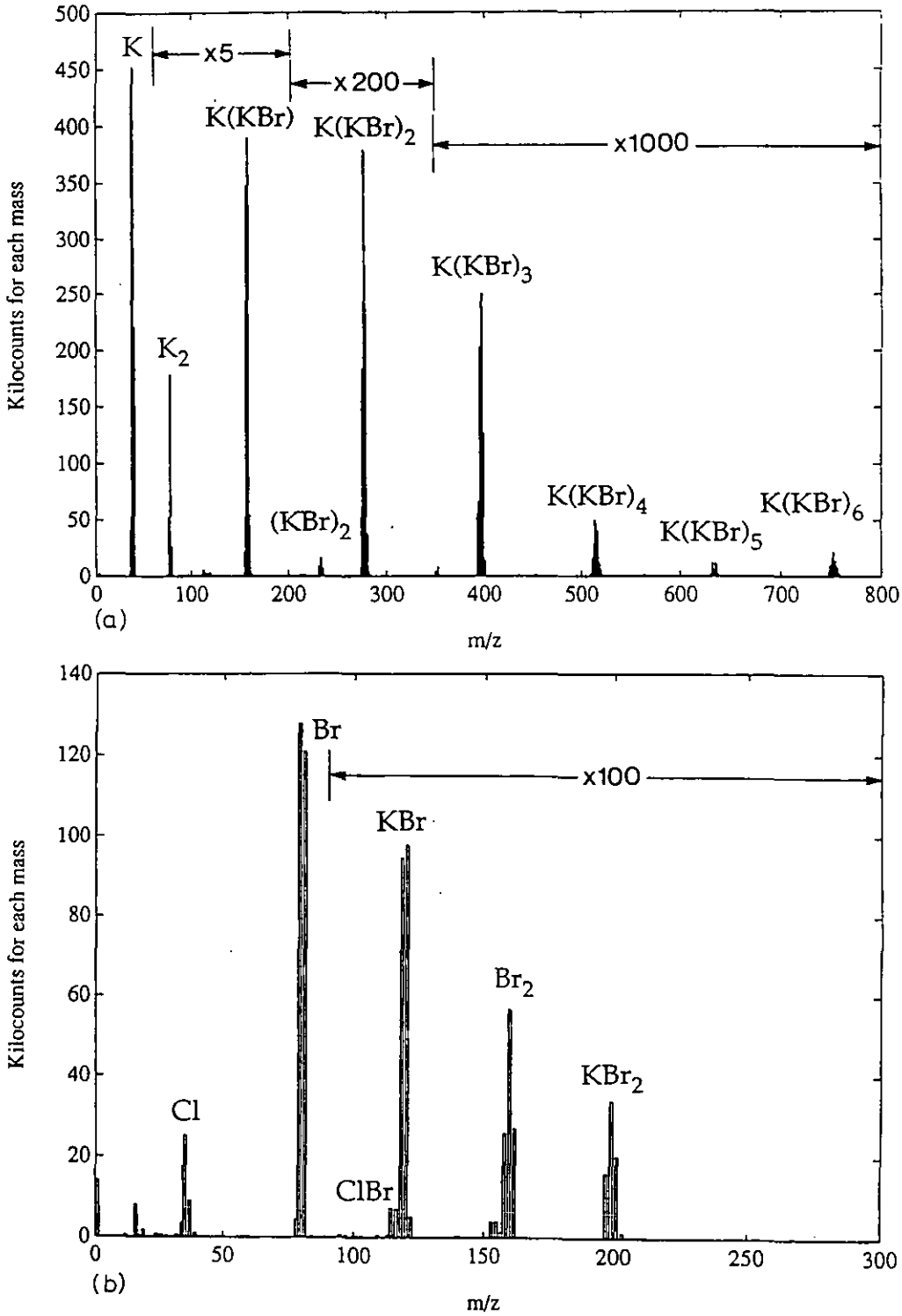

Fig 7 As for Fig 6 but for KBr but with beam currents of 0.5 nA (the charge stabilisation uses the emission plate method with currents of 0.18 and 8.6 μA, respectively).

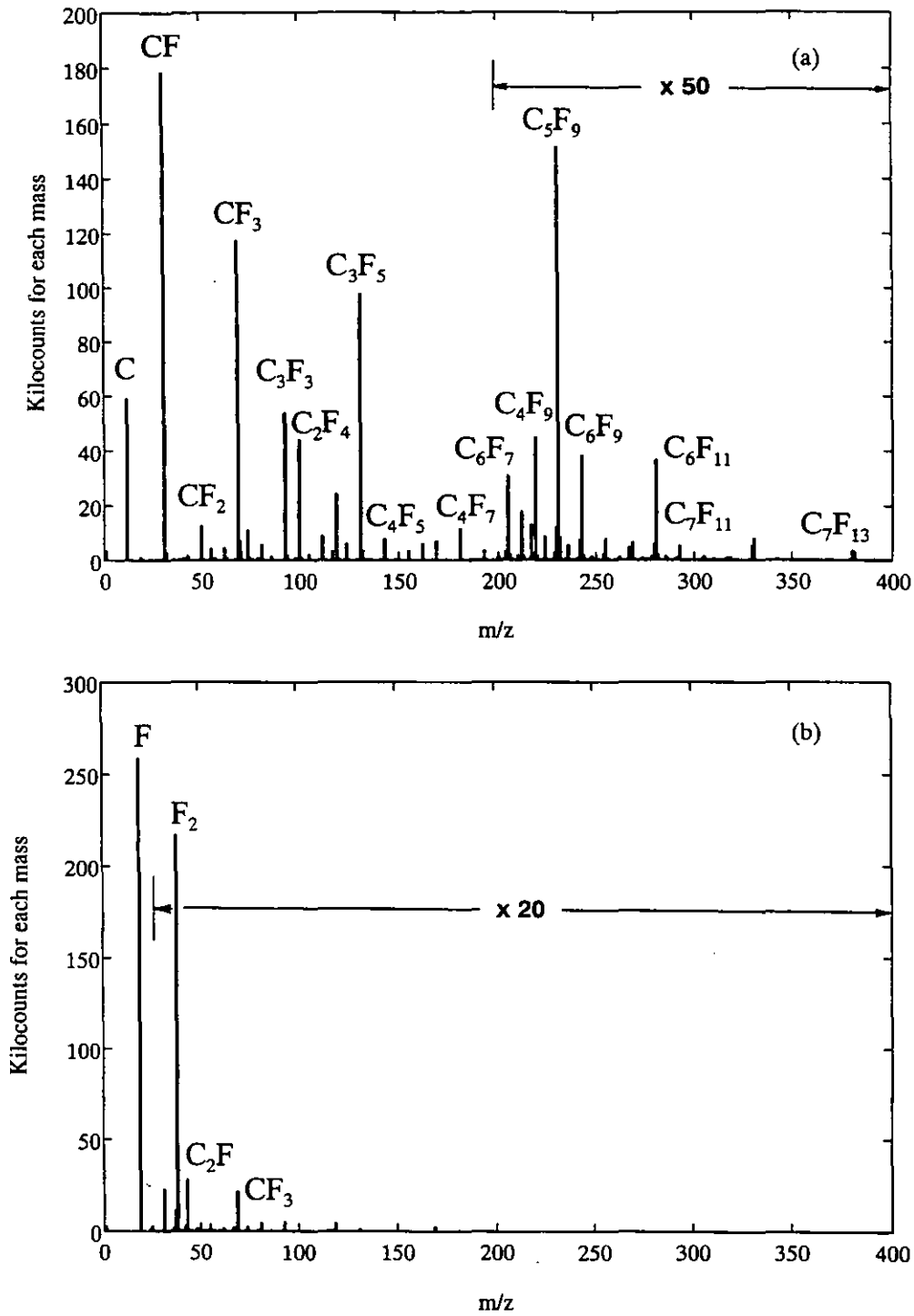

Fig 8 As for Fig 6 but for PTFE using a 0.5 nA beam scanned over 50 mm^2 on the sample (the ion dose on the sample is 0.5 x 10^{17} ions/cm^2). The dose increases through the positive and negative spectra as the mass increases so that by mass 60 in the positive spectrum the dose is 0.1 x 10^{17} ions/cm^2.

Bearing in mind that, to produce a robust system, the relative strengths of the ion and electron neutralisation beams should not be too critical, a comparison of the 500 eV beam and the emission plate methods were made using the 131 amu positive SIMS peak from PTFE shown in Fig 8(a). Here, V_c and V_T are set at +20V and the intensity of the peak per nA of ion beam current monitored as a function of that beam current. The results for the two methods are shown in Fig 9. It is clear that for a drop of intensity from the optimum by, say, 10% the 500 eV beam current must be set three times more precisely than that of the emission plate gun - i.e. the latter method is the more robust. In general use, the setting of the 500 eV gun was found to be quite critical and, as noted earlier[16] fluorine fragments, F^-, could be observed from PTFE by electron stimulated desorption.

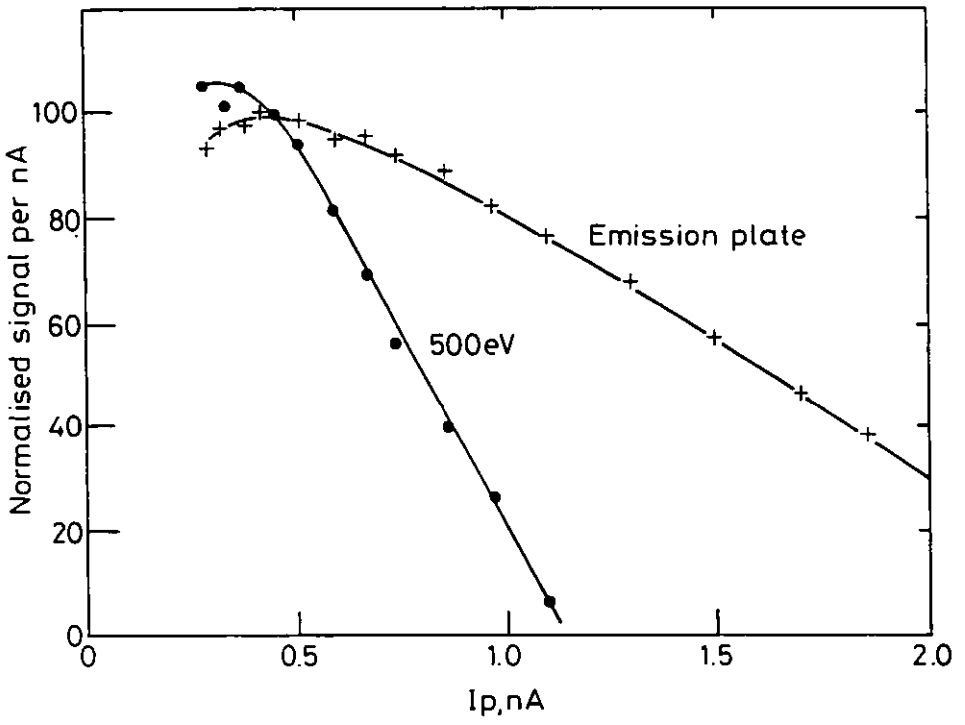

Fig 9 The normalised intensity of the $C_3F_5^{131}$ peak from PTFE per nA of beam as a function of the 4 keV argon ion beam current for given settings of the 500 eV electron gun (●) and of the 1 keV emission plate electron gun (+).

The emission plate method overcomes the above points and is convenient for use and so forms the focus of the rest of this paper. The results shown in Fig 2 are recorded by scanning with the sample potential. The same results for Ta_2O_5, with the peaks typically within 0.5 eV, are also obtained by using a floating sample and the emission plate method. In order to define the range of emission plate gun currents necessary to provide neutralisations, studies of the K $(KBr)^+$ and Br^- intensities were made from KBr. KBr is now used since the Ta_2O_5,

being a conductor, can never show a non-uniform charge distribution and cannot show all the faults of an inadequate charge neutralisation system. However, like Ta_2O_5 the KBr may be sputtered for a long time once equilibrium is established so that considerable work is accomplished with one sample. The energy spectra have the narrowness of TaO_3^-, as shown in Fig 2, being typically of half widths of 10 eV and 15 eV for $K(KBr)^+$ and Br^-, respectively. The effect of increasing the total emission plate current on these spectra was to increase or reduce the overall signal whilst essentially retaining the same spectral shape and peak position. The dependence of the peak intensity on the total emission plate current is shown in Fig 10 for an ion beam of 0.5 nA focused to a beam size of 100 μm and rastered over 4 mm^2 on the sample. If the beam current is increased, the value of I_e is scaled accordingly. The results are interesting. Over the current range shown in Fig 9 the majority of the KBr surface is controlled by the emission plate potential. At the low emission plate currents the region of the ion beam spot charges a little more positively than the surrounding region so enhancing the positive secondary ions and reducing the negative ones, precisely as shown in Fig 4 and as discussed in section 3.2. As the emission plate current increases this effect is reduced as shown in Fig 10. Note that the "optimum" conditions for positive SIMS gives a yield that is higher than expected for a conductor and may, as shown in Fig 4, coincide with the full suppression of negative ion spectra. Defocusing the ion beam also reduces these effects and so, for all of the static SIMS work, an instantaneous current density below 1% of the above values was used.

To test the emission plate more fully, a set of freshly unrolled PTFE samples was mounted on separate sample holders. The PTFE is simply wrapped around a stainless steel plate and tied behind. This forms a flat surface exposing only PTFE without the need for adhesives or spincasting, both of which can lead to contaminations unless care is taken with the choice of adhesive or solvent. As each sample is to be treated as a completely new sample, the emission plate voltage was reset each time to maximise the 93 amu peak. The energy spectra for both the positive and negative ions are shown in Fig 11 as a counterpart to the similar plot for a conductor in Fig 2. This shows that the surface potential follows the emission plate and the sample holder bias potentials over the full relevant range. Each sample of PTFE was analysed with a total fluence of approximately 0.02×10^{17} ions/m^2 and gave essentially the same energy and mass spectra with strong peaks at C^{12}, CF^{31}, CF_3^{69}, $C_3F_3^{93}$, $C_3F_5^{131}$ and $C_5F_9^{231}$, as shown in Fig 8.

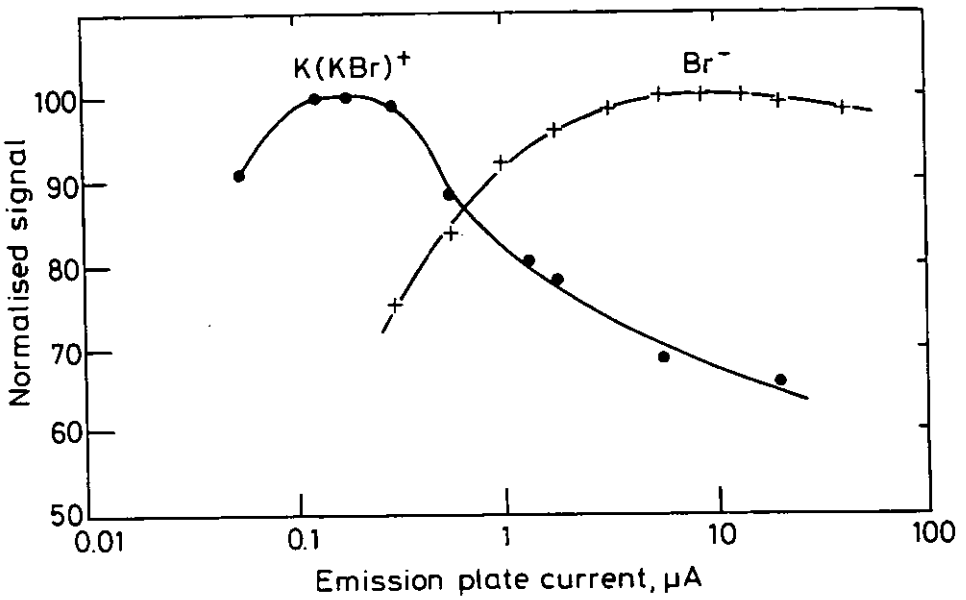

Fig 10 The intensities of $K(KBr)^+$ and Br^- as a function of the emission current (the emission plate current is 2.25 times the 1 keV electron beam current). The 4 keV argon ion beam is 0.5 nA rastered to cover 4 mm^2 on the sample.

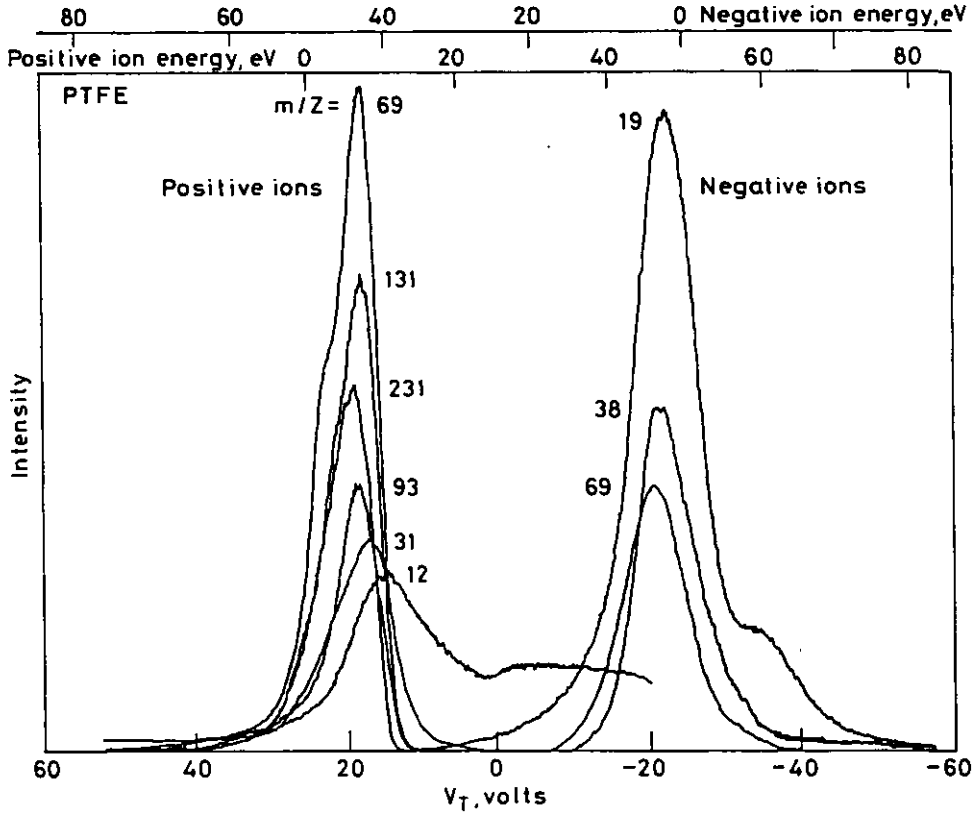

Fig 11 Energy spectra of the positive and negative ion peaks from PTFE using the emission plate stabiliser and a 0.5 nA, 4 keV argon ion beam covering 50 mm^2 of the sample.

We consider the statistical scatter of the PTFE data, as follows, to remove the relative intensities of the different peaks, i, and any drifts in beam current etc between the different spectra j. If the intensities of j_0 spectra each containing i_0 peaks are denoted I_{ij}, then the average intensity of the i th peak is

$$\bar{I}_i = \sum_j I_{ij} / j_0 \tag{4}$$

We divide each intensity I_{ij} by the relevant average $\bar{I}_i$ to evaluate the power, P_{ij}, in each peak:

$$P_{ij} = I_{ij} / \bar{I}_i \tag{5}$$

The average power $\bar{P}_j$ in the spectrum, which depends on the beam current etc, is given by:

$$\bar{P}_j = \sum_i P_{ij} / i_0 \tag{6}$$

This average power is now removed from the spectrum by forming the normalised intensities N_{ij}:

$$N_{ij} = P_{ij} / \bar{P}_j \tag{7}$$

The N_{ij} will all be around unity with an average value in each spectrum of unity. The scatter in the relative intensities of the peaks is now given by the standard deviation of the N_{ij} for any given mass, i. If all of the spectra were identical in relative intensities but merely changed in absolute magnitude, the N_{ij} would be identically unity.

Using this analysis for the PTFE data we find that the percentage scatters, σ, for the peaks at mass 12, 31, 69, 93, 131 and 231 are, respectively, 23, 13, 10, 8, 7 and 21% with an average of 13.8%. These scatters are reasonably acceptable for the current state of static SIMS but an analysis of the relative intensities of the peaks for each set shows a systematic variation from sample-to-sample whose source could easily be misinterpreted. Figure 12 shows typical, N_{ij}, ratio plots as a function of mass for 4 of the 10 data sets in this experiment. The slope on each plot could be misinterpreted as a real effect due to either changes in mass spectrometer transmission functions or changes in the SIMS fragmentation process if the series were not simply repeats and were, say, acquired whilst some other parameter were varying.

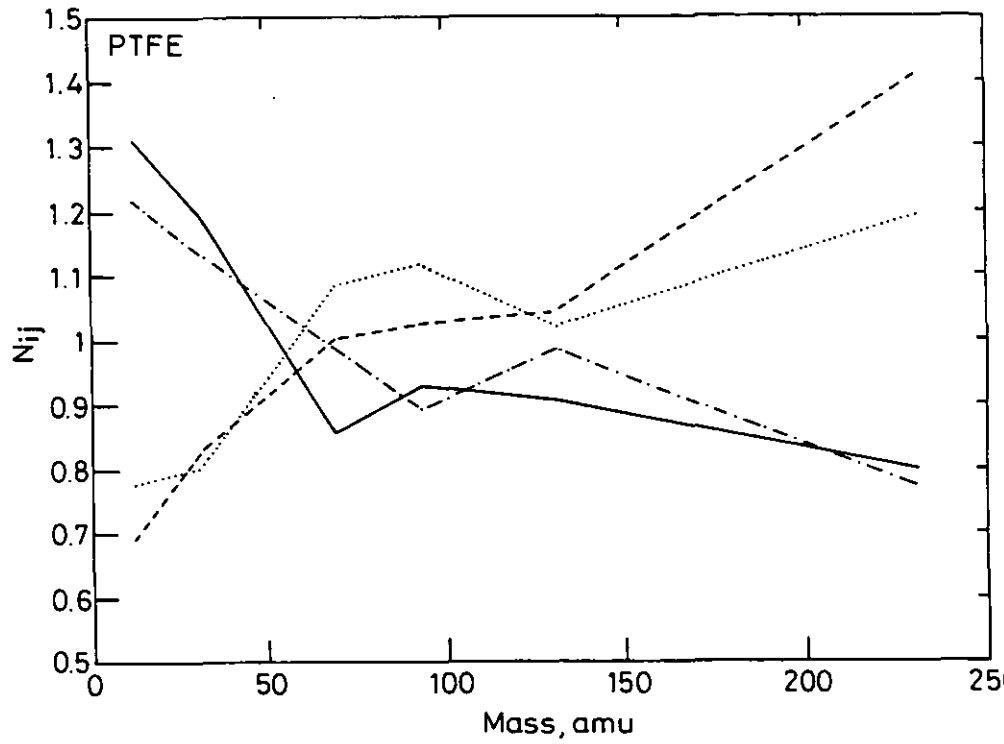

Fig 12 Plots of the normalised intensity N_{ij} for each peak from PTFE as a function of the mass of the detected species (data points occur at masses 12, 31, 69, 93, 131 and 231 amu). The lines join points for each of four data sets. Ten were recorded but the rest, similar to these four, are omitted for clarity.

In the above set the emission plate potential settings varied from 16 to 19 volts. Figure 11, on the left hand side, shows the energy spectra for the positive ion peaks concerned. Similar effects have been published by Briggs and Wootton[8] for paraffin wax. It is clear that the small shifts in the surface potential could have very significant effects. At a sample and emission plate potential of 17V the C peak is very strong whereas at 21V the $C_5F_9^{231}$ peak is strong. The ratio of these peak intensities would change by a factor of 30 for this 4V change in the sample potential. The effects in Fig 12 would only need changes of 2V. The precise voltages for the peaks unfortunately varied from sample holder to sample holder. For different samples with different surface roughnesses, emission characteristics etc, it is not possible to guarantee a very close setting of the surface potential so we sought a way of reducing this overall sensitivity. One way, of course, would be to increase the energy width acceptable to the SIMS analyser. Unfortunately, this is not possible with the quadrupole systems without degrading the mass resolution significantly. Instead we broaden the apparent energy spectra of Fig 2 by scanning the emission plate and sample holder potentials at an even rate up and down from the median position. This is easily done with a triangular

wave-form signal generator feeding the target bias through a capacitor. As the amplitude of this modulation increases, the peaks in the energy spectra attenuate and flatten, as shown for the 131 amu peak in Fig 13(a). At 32 volts peak-to-peak the spectra are flat over the central 18V range. SIMS intensities are not now sensitive to the exact average surface potential.

Two clear points should be made concerning the result. Firstly, the resultant SIMS mass spectra will appear similar to those for a mass spectrometer with a 32 eV wide energy window. From Figs 2 and 10 we see that this will satisfactorily cover the total peak width for all polyatomic ions. Secondly this is only achieved at the cost of a loss of about a factor of 3 in the optimal signal intensities measured. Note that scanning the sample potential up and down is no different from scanning the whole SIMS spectrometer up and down in potential.

For analysing the SIMS spectra, the widescan analyses are made here at 200 msec channel integration times. In order that we do not find different parts of the modulation cycle operating in different channels it is necessary to ensure 100 cycles in each channel, i.e. the modulation frequency should exceed 500 Hz. We expected the modulation to work well at low frequencies but to fail as the frequency is increased, however, as shown in Fig 13(b), no measurable changes occur until the frequencies exceeded 15 kHz. In all of the work that follows the sample holder and emission plate are modulated at 6.5 kHz with a triangular waveform of 32 volts peak-to-peak. The choice of 6.5 kHz was found by ensuring that the TV scan generator for rastering the ion beam over the sample surface did not synchronise with the modulation. If this were to happen the beam may not sample all of the area to be analysed at all potentials. It should be noted that large samples of dielectrics may require lower frequencies.

After the above modifications a fixed mean sample holder potential of 20 volts was used for all samples but it was found that the scatters had not improved as much as had been hoped. The scatters for the peaks at mass 12, 31, 69, 93, 131 and 231 were, respectively, 19, 10, 8, 5, 6 and 14% with an average of 10.2%. Much of this scatter was attributed to one sample holder and if the data for that holder were eliminated the scatter fell to 5.3%. It appeared that differences in the frame of the exposed part of the sample holder defining the potential around the perimeter of the sample were important for defining the fields around the sample

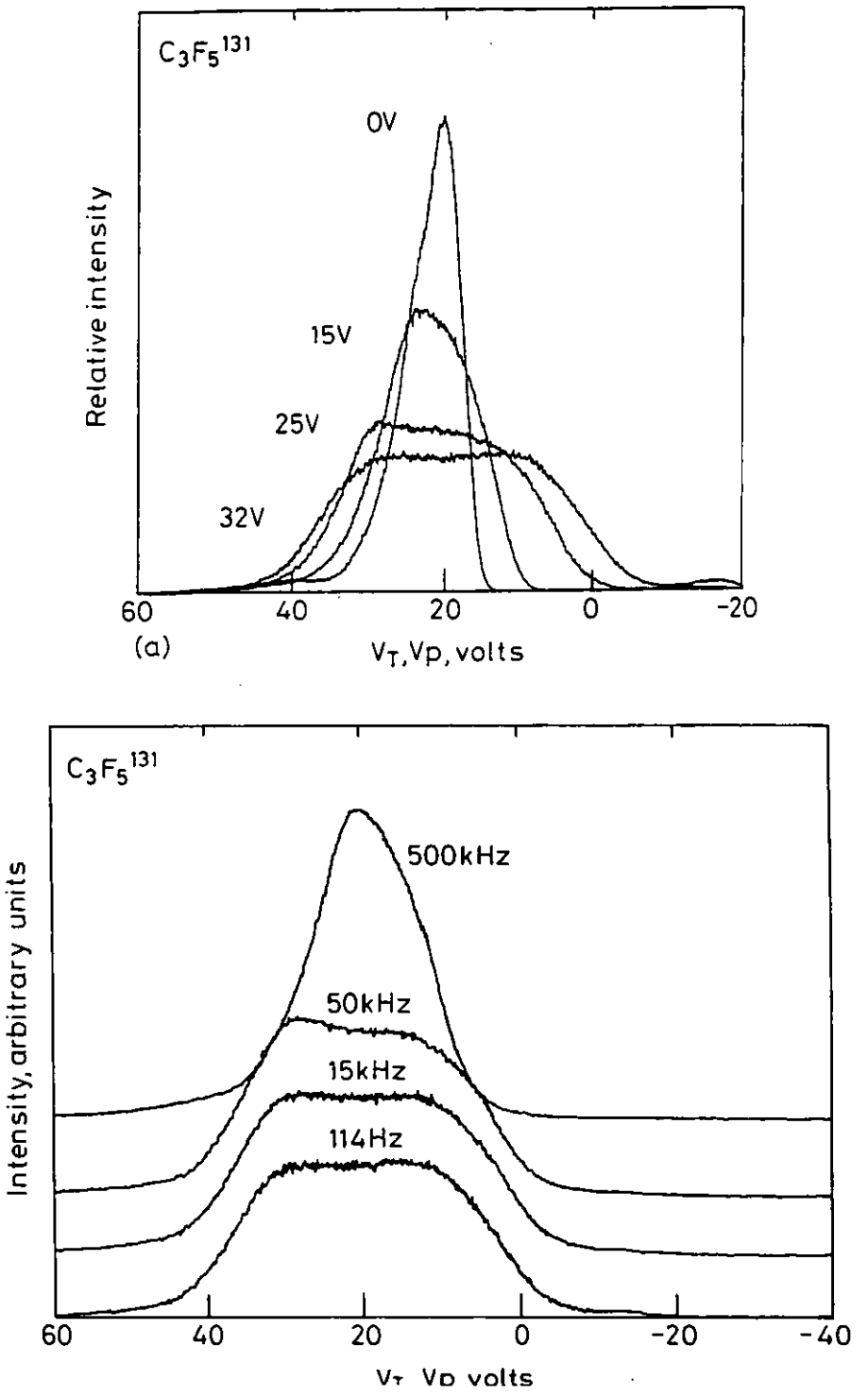

Fig 13 The energy spectra of $C_3F_5^{131}$ from PTFE as a function of (a) the modulation amplitude at 6.5 kHz and (b) the modulation frequency at 32 volts peak-to-peak, using a 0.5 nA, 4 keV argon ion beam covering 50 mm^2 of the sample. Note that in (b) the spectra are displaced vertically for clarity of presentation.

and so a stainless steel frame with a 10 mm by 10 mm aperture was added covering the PTFE samples. This now reduced the scatters so that for the 12, 31, 69, 93, 131 and 231 amu peaks the standard deviations from 16 samples in 16 separate sample mounts were 4, 2, 2, 1, 2 and 3%, respectively with an average of 2.4%. Much of the scatter was caused by variations in the C^{12} peak as would be expected from Fig 14. If this peak is removed the scatters reduce to 3, 1, 1, 1 and 3%, respectively with an average of 1.8%. The data for the 231 peak only have 1100 total counts. The standard deviation for this peak is therefore expected to be 3%, from the counting statistics alone. If this peak is deleted the scatters for the 31, 69, 93 and 131 mass peaks average only 1.5%. This is probably a true reflection of the overall repeatability of the system except for the C^{12} peak. This value is excellent and so this mode was used to generate Figs 6, 7 and 8 shown earlier.

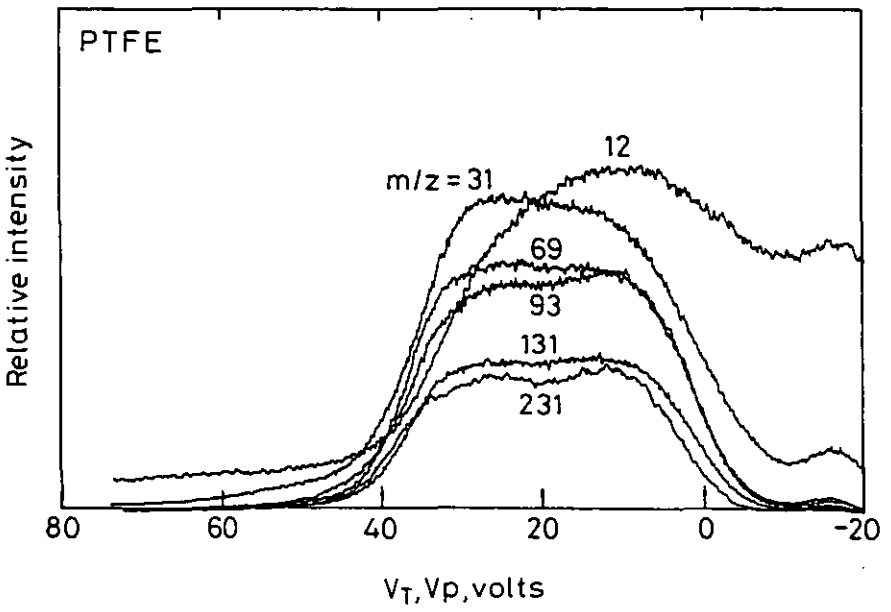

Fig 14 The energy spectra of the peaks as in Fig 12 but using a 32V peak-to-peak triangular modulation at 6.5 kHz on the sample and emission plate.

In order to check the efficiency of the emission plate system we show in Fig 15 repeated measurements on the same sample with different settings of $V_T(=V_p)$. The dose per measurement cycle here is 0.02×10^{17} ions/m^2 on the sample. This is sufficient to cause damage which alters the intensities a few percent[16,20]. This small change has been removed from the data. The first 4 points are at the standard bias, the next 4 at 2 volts lower bias, the next 4 at 2 volts raised bias and the last 4 at the standard bias. These data only include masses 31, 69, 93 and 131, as above, and show an rms scatter of only 0.6% for the whole set.

Clearly, the modulated emission plate system is insensitive to the precise surface potential of insulating or other samples. The success of this method is not easy to transfer to the simple low energy electron gun discussed at the start of this section although that gun performed as well as the emission plate without modulation. The problem arises from the need to modulate the whole of the gun electrode structure and filament supply, in phase with V_T. This can be done but not at the frequency chosen if the gun's electronic supplies have large smoothing capacitors.

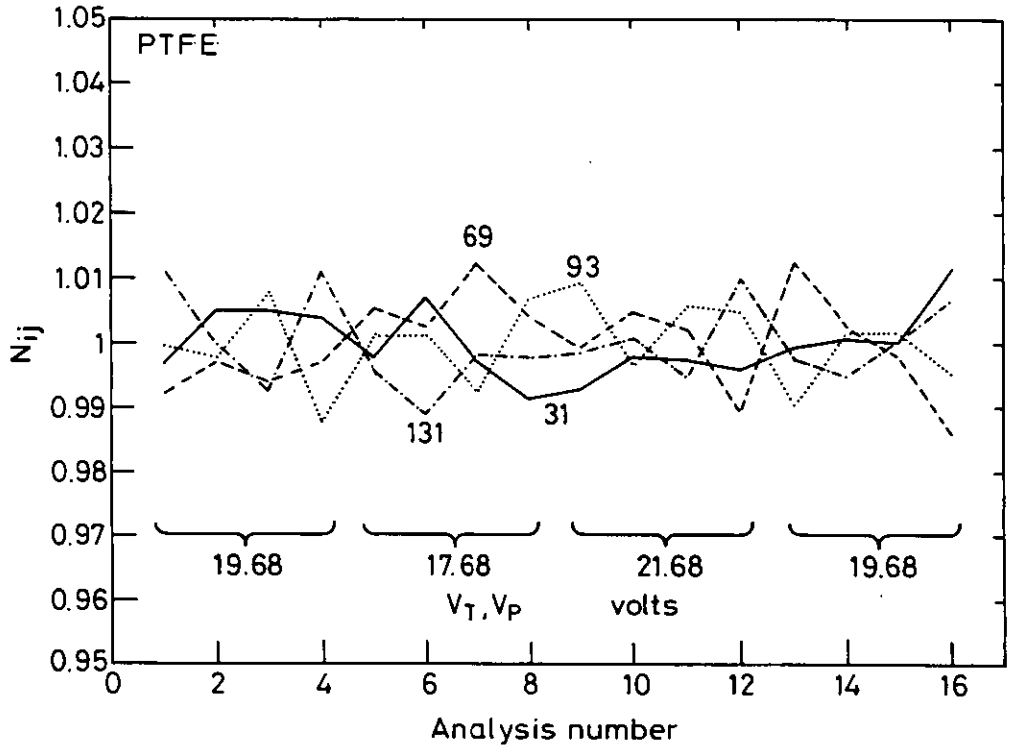

Fig 15 Plots of the normalised intensity N_{ij} for the four peaks 31, 69, 93 and 131 amu from PTFE as a function of the mean potential of the modulated emission plate and sample potential system. The N_{ij} have been corrected for the initial onset of damage[20].

It is clear that, for static SIMS studies using quadrupole mass spectrometers, a greater degree of control is needed of the charge compensation schemes than has been generally available. Shifts in the surface potential affect the absolute and relative intensities of peaks. These make analyses uncertain and will also affect damage estimates[16,20,21].

6 CONCLUSIONS

The different energy spectra for the different peaks in quadrupole-based SIMS analysers causes uncertainties in the relative intensities of peaks from insulating samples through the inability to define the surface potential accurately. Several charge neutralisation systems have been studied and it is found that an emission plate fixed at the sample holder potential is a convenient and effective system. Electrons, emitted from this plate by the action of a 1 keV electron beam with a current of 10^3 to 10^4 times that of a defocused ion beam, bathe the sample and stabilise its surface potential very close to those of the plate and the sample holder. The effectiveness of this system is enhanced further by the application of a 32V peak-to-peak triangular wave modulation at 6.5 kHz to the plate and the sample holder. With carefully designed sample holders this reduces the scatter of the relative peak intensities of all species except C^{12} from 16 PTFE samples by an order of magnitude to below ±2% standard deviation.

REFERENCES

(1) A Benninghoven, F G Rüdenauer and H Werner, *Secondary Ion Mass Spectrometry*, Wiley-Interscience, New York (1987).

(2) P H Dawson, *Quadrupole Mass Spectrometry and its Applications*, Elsevier, New York (1976).

(3) W P Poschenrieder, Int. J. Mass Spectrom. Ion Phys. **9**, 357 (1972).

(4) E Niehuis, T Heller, H Feld and A Benninghoven, in *SIMS V*, Springer Series in Chemical Physics 44, Springer, Berlin (1986), p 188.

(5) C P Hunt, C T H Stoddart and M P Seah, Surf. Interface Anal. **3**, 157 (1981).

(6) G Slodzian, Surf. Sci. **48**, 161 (1975).

(7) D Briggs in *Practical Surface Analysis: Vol 2, Ion and Neutral Spectroscopy*, Eds D Briggs and M P Seah, Wiley, Chichester (1992), Chapter 7 p 367.

(8) D V McCaughan and R A Kushner, *Characterisation of Solid Surfaces*, Eds R F Kane and G B Larrabee, Plenum, New York (1974) p 627.

(9) D Briggs and A B Wootton, Surf. Interface Anal. **4**, 109 (1982).

(10) D Briggs and M J Hearn, Int. J. Mass Spectrom. Ion Proc. **67**, 47 (1985).

(11) D Briggs, V G Scientific Newsletter 2, Spring 1986, p 5.

(12) D J Surman, J A van den Berg and J C Vickerman, Surf. Interface Anal. **4**, 160 (1982).

(13) A Brown, J A van den Berg and J C Vickerman, Spectrochim. Acta **40B**, 871 (1985).

(14) J Cazaux and P Lehude, J. Electron Spectrosc. **59**, 49 (1992).

(15) C P Hunt and M P Seah, Surf. Interface Anal. **5**, 199 (1983).

(16) D Briggs, Surf. Interface Anal. **14**, 209 (1989).

(17) D Briggs, A Brown and J C Vickerman, *Handbook of Static Secondary Ion Mass Spectrometry (SIMS)*, Wiley, Chichester (1989).

(18) D Briggs, M J Hearn, I W Fletcher, A R Wangh and B J McIntosh, Surf. Interface Anal. **15**, 62 (1990).

(19) J G Newman, B A Carlson, R S Michael, J F Moulder and T A Hohlt, *Static SIMS Handbook of Polymer Analysis*, Perkin Elmer, Eden Prairie MN (1991).

(20) I S Gilmore and M P Seah, Surf. Interface Anal. **24**, 746 (1996).

(21) G J Leggett and J C Vickerman, Anal. Chem. **63**, 561 (1991).

CHAPTER FOUR

A Study of Damage in Polymers

1	INTRODUCTION	60
2	THEORY OF THE DAMAGE PROCESS	62
2.1	THE SIMPLE MODEL	65
2.2	AN EXTENSION OF THE MODEL TO A FRAGMENT WITH SEVERAL INTERNAL BONDS	68
2.3	AN EXTENSION OF THE MODEL TO SIDE CHAINS	70
2.4	A FRAGMENT REQUIRING THREE BROKEN BONDS	71
2.5	THE END BONDS A AND B UNEQUAL	72
2.6	BONDS THAT RAPIDLY RE-COMBINE	73
2.7	SUMMARY	73
3	EXPERIMENTAL	75
4	RESULTS	76
4.1	PTFE	76
4.1.1	FRAGMENT DAMAGE PHENOMENA WITH 4 KEV ARGON IONS	76
4.1.2	RELATIVE DAMAGE RESPONSES FOR 4 KEV ARGON AND XENON IONS	83
4.2	PET	87
4.2.1	FRAGMENT DAMAGE PHENOMENA WITH 4 KEV ARGON IONS	87
4.2.2	THE EFFECT OF ARGON BEAM ENERGY	90
4.2.3	RELATIVE DAMAGE RESPONSES FOR 4 KEV ARGON AND XENON IONS	92
4.3	CONTAMINATION LAYER ON A SILICON WAFER	95
4.4	CONTAMINATION LAYER ON TANTALUM PENTOXIDE	96
5	CONCLUSIONS	97
REFERENCES		100

1 INTRODUCTION

In the study of polymers and organic material surfaces, static secondary ion mass spectrometry is extremely powerful. The high sensitivity, detailed speciation and availability of equipment make its contribution unique. The importance of the method may be understood by the prolific output from researchers both in industry and university departments[1-13]. In recent years an important shift in research has occurred as groups have invested in time-of-flight (ToF) instruments to replace the older quadrupoles. These newer instruments allow a higher sensitivity and higher mass resolution. The higher mass resolution allows the precise mass of species to be determined, rather than the nominal amu, so that ambiguities of molecular fragment assignment are greatly reduced[9].

The higher sensitivity of the ToF instruments is important for working in the static regime although, as higher spatial resolutions are demanded, severe damage may still occur. The notional maximum dose of ions incident on the sample is typically taken as† 0.5×10^{17} ions/m^2 [4,14,15], beyond which significant damage has occurred so that the spectra are altered. The publications dealing with damage are few. In 1986 Briggs and Hearn[16] showed that the higher mass fragments of several bulk polymers would reduce significantly after 5.10^{17} ions/m^2 of exposure. Studying the oxygen loss from poly(methyl methacrylate) (PMMA) they show that the rate of damage increases with both the bombarding ion beam energy and the bombarding ion mass. In 1989, Briggs[1] showed how, in poly(tetrafluoroethylene) (PTFE), six of the fragments with masses in the range 31 to 231 amu increased in intensity to a peak at around 2×10^{17} ions/m^2, for 4 keV xenon, before slowly decaying again. More recently Leggett and Vickermann[17] have studied PTFE and poly(ethylene terephthalate) (PET) using both argon and xenon as both ions and neutrals. Their results show signals rising from zero to a very sharp peak followed by a rapid decay. For PET the peaks occurred at around 0.2×10^{17} ions/m^2 for ions and 0.5×10^{17} particles/m^2 for atoms although they note that a dose of 0.5×10^{17} ions/m^2 was needed to stabilise the surface potential in their equipment and hence the data at lower doses may be in error. The data show that the damage caused by 2 keV

† We shall express all doses as a number times 10^{17} ions or particles per m^2. In converting from the traditional per cm^2 we hope the reader will be less confused if we keep at least the decade order constant. It is also useful to remember that 1% of a monolayer has around 10^{17} atoms/m^2.

xenon is about twice that for 2 keV argon and that ions were more damaging than neutrals. They measure a half life of the signal decay for Ar°, Xe°, Ar^{+} and Xe^{+} as 5.0, 2.6, 0.9 and 0.6 in units of 10^{17} particles/m^2. Measurements for PTFE showed the rise to a peak, as in Briggs' study[1], at similar doses as for the PET, followed by similar decays. The initial rise is again ascribed to surface charge instabilities in the early stages of sputtering. In more recent studies on poly(vinyl chloride) (PVC) and poly(methyl methacrylate) (PMMA), Leggett and Vickerman[18] reinforce the above conclusions. The decays are always faster for ions than for atoms and the initial peak probably occurs through surface charge instability. For PMMA the half lives of peaks 41 to 133 amu are in the ranges 2.6 to 4.3 and 19 to 100 times 10^{17} particles/m^2 for 2 keV argon ions and neutrals, respectively. In both cases the intensities of the higher mass fragments generally decayed most rapidly.

This rise and decay is also seen in the careful studies of Delcorte, Weng and Bertrand[19]. Data for polypropylene analysed for doses up to 8×10^{17}, 4 keV Xe^{+} ions/m^2, show that C_8H_{17} decayed rapidly whilst the series C_8H_{15}, C_8H_{13}, C_8H_{11}, C_8H_9 and C_8H_7 developed slower decays leading to an initial rise and then a rise with a peak moving to higher and higher doses. This set is interpreted rather nicely as a series of daughter products following a similar behaviour to that of radioactive series.

The above studies were all conducted using traditional quadrupole-based static SIMS systems. These are excellent for such studies as it is easy to calibrate and provide the necessary doses. A major problem can be the stabilisation of the surface potential. This is important as the energy window of the quadrupole is rather narrow so that a surface potential shift of 2 volts may give a 100% intensity change[20]. In a recent development of a quadrupole system the present author[21] has modified the equipment so that any surface potential changes of up to 15 volts have a negligible effect on most peaks. With such a system a scatter of less than 2% is seen for different samples of PTFE from a single batch studied sequentially with preset conditions, ie there was no setting up or optimisation on any of the samples. We are, therefore, able to define intensities from zero dose with confidence.

In the present work the effects of dose are found to be quite repeatable from sample to sample. We, therefore, seek to model the damage seen in polymers so that basic parameters may be measured and the damage process characterised. From the results of the earlier studies we may pose a series of questions. (1) Is the peak in the damage curve real? (2) Are

the damage curves described by a single exponential? (3) Is argon more damaging than xenon? (4) Is argon more damaging per unit of ion yield than xenon? (5) Are low energies more damaging per unit of ion yield than high energies? These and similar questions should be answered in order to optimise instruments for measurements and so that standard and meaningful conditions may be used.

In the past, considerable excellent work has been done in studying the fragmentation routes[7,22,23]. This has its origins in the considerable volume of organic mass spectrometry research. Here, we shall not comment on these aspects but seek instead to see what information may be extracted from the damage curves as a function of the ion dose (ions/m^2 of sample surface). Note that, in the present work, all dose areas are related to the sample surface and not the plane normal to the ion beam.

2 THEORY OF THE DAMAGE PROCESS

Very few equations are available in the literature and so we shall not review previous work. Leggett and Vickerman[23] review some of the aspects of sputtering and of ion formation in polymers but, here, we wish to consider just the change in the ion yield of the fragment species. We are not concerned with the different intensities of different fragments which involve ionisation probabilities etc, but only with the relative changes of the intensity for any given fragment from a given sample.

We assume that the intensity of a given fragment, as a function of dose, measures the quantity of a particular structure present in the sample and that changes in the sample, at doses less than $10x10^{17}$ ions/m^2, do not alter the ion-to-neutral branching ratio.

For polymers, the simplest model one may consider for the overall SIMS process is that the incident ion first enters undamaged material and, through internal collisions brings about a certain probability per ion of breaking a bond A in the surface layer, that does not subsequently heal, of P_A. Thus, the probability of emitting a fragment of a linear polymer lying in the plane of the surface and requiring a bond A at one end and a bond B at the other, both to be broken is P_AP_B. If there is a bond C in the middle that may also be broken the probability of seeing the given fragment is $P_AP_B(1-P_C)$. If the bond heals slowly with time

any measured effects of damage with dose will vary with the beam current density. This may occur but is not seen in general. If the bond heals very rapidly, we ignore the event completely.

Note that the probability of breaking a particular bond involves a whole series of mechanisms. It is likely that the action of the lower energy recoils returning to the surface are more important than the direct action of the primary ion. These recoils are moving in the correct direction to eject the ionised clusters measured in SIMS. The sputtering yield Y(E) is a measure of the intensity of the recoils in any given sample and since Y(E) increases with the incident ion energy, E, we would expect P_A, etc, also to increase with E. Furthermore, although a certain atom may become excited or ionised, that event may then be passed along the molecule to some other point where a second atom becomes sufficiently unstable that a bond breaks. The value of P, the probability per incident ion, involves all of these parts of the process.

If the above permanent damage occurs in a zone of area θ, then the fraction of whole unbroken A bonds decays as:

$$\exp(-NP_A\theta t)$$

where N is the incident ion dose rate on the sample and t is time. This decay is of the form $\exp(-N\sigma_A t)$ where σ_A is a cross section for damage of the A bonds. Actually, of course σ_A here is $P_A\theta$, i.e. if the cascade of ion damage covers a surface area of 100 atoms (say, 10^{-17} m^2) with reasonable intensity and if P_A is 0.25, then σ_A or $P_A\theta$ will be approximately 2.5 x 10^{-18} m^2. In a full description of this model, the zone of area θ would, of course, not be an area with a constant effect within that area and zero outside but would be represented by some Gaussian or other probability distribution with a characteristic radius of, say, $(\theta/\pi)^{0.5}$. We do not need this detail here but will return to it later. For simplicity in the algebra we shall now use the reduced units:

$$N\theta t = \tau \qquad (1)$$

Note that both P_A and θ will increase with the ion energy, E. The probability of emission of our fragment at reduced time τ is then the probability that we have C unbroken and the sum of the events for (i) breaking unbroken A and B bonds by the incident ion, (ii) breaking an A bond by the incident ion when B is already broken and (iii) breaking a B bond by the

incident ion when A is already broken. Thus, the intensity $I(\tau)$ is given by

$$I(\tau) = \exp(-P_C\tau)\{P_A \exp(-P_A\tau)\ P_B \exp(-P_B\tau) + P_A \exp(-P_A\tau)\ [1-\exp(-P_B\tau)] + P_B \exp(-P_B\tau)\ [1-\exp(-P_A\tau)]\} \quad (2)$$

which, rearranged, becomes

$$I(\tau) = P_A \exp\{-(P_A+P_C)\tau\} + P_B \exp\{-(P_B+P_C)\tau\} - (P_A+P_B-P_AP_B) \exp\{-(P_A+P_B+P_C)\tau\} \quad (3)$$

which is of the form

$$I(t) = Qe^{-Nqt} + Re^{-Nrt} - Se^{-Nst} \quad (4)$$

ie the sum and difference of simple exponentials involving q, r and s, the composite damage cross sections. Note that in Eq (2) we have only considered the mechanical bond breaking so that the equation relates to neutrals. If the bond-breaking is caused by an energetic particle it may also simultaneously be associated with the creation of a locally ionised species. If we include this effect, as is necessary for studying emitted ions, the first term in which the two bonds are broken has twice the probability for ionisation compared with the remaining terms for the breaking of one bond. In Eq (3) this has the effect of multiplying the P_AP_B term in the first brackets by a factor of 2. If the bonds that are "already broken" are originally ionised and retain that charge stably for more than milliseconds, each term may have the same multiplying factor and so the relative effect of the factor of 2 may be removed. Furthermore, the bond breaking will involve momentum transfer from the closely moving energetic particle. In this case, the first term in the brackets of Eq (2) should include a further factor of two to allow for there being twice the probability of the fragment having sufficient energy to escape from the surface. Finally, we should note that Eq (2) is derived assuming that all events are uncorrelated and purely random. Correlation effects will further modify the first term in the brackets. Thus, we should write S as $P_A + P_B - \alpha P_AP_B$ where α, previously 1, may lie approximately in the range 1 to 4.

It is difficult to visualise the properties of Eq (3) with three independent variables as well as time and so, to simplify matters, we first reduce the model further. In these equations a constant intensity scaling parameter involving the beam current, spectrometer efficiency, ionisation efficiency etc is assumed to be constant with time and so is ignored.

2.1 THE SIMPLE MODEL

We now consider the polymer bonds A and B to be the same as each other but different from C. Since the fragmentation of large molecules is very likely, we shall write, for convenience:

$$\beta P = \beta P_A = \beta P_B = P_C \tag{5}$$

Thus,

$$\begin{aligned} I(\tau) &= 2P_A \exp\{-(P_A+P_C)\tau\} - (2-\alpha P_A)P_A \exp\{-(2P_A+P_C)\tau\} \\ &= 2P \exp\{-(1+\beta)P\tau\} - (2-\alpha P)P \exp\{-(2+\beta)P\tau\} \end{aligned} \tag{6}$$

which is of the form:

$$I(t) = Re^{-Nrt} - Se^{-Nst} \tag{7}$$

Figure 1 shows a plot of Eq (6) for a normalised ordinate. Here we have chosen P=0.1, α=1 and values of β representing C bonds both stronger and weaker than the A bonds. If these curves are plotted for a normalised abscissa of $P\tau/P\tau_{max}$, where τ_{max} is the value of τ at which $I(\tau)$ maximises, we would see that the curves roughly overlap and the shapes are similar, irrespective of the β value.

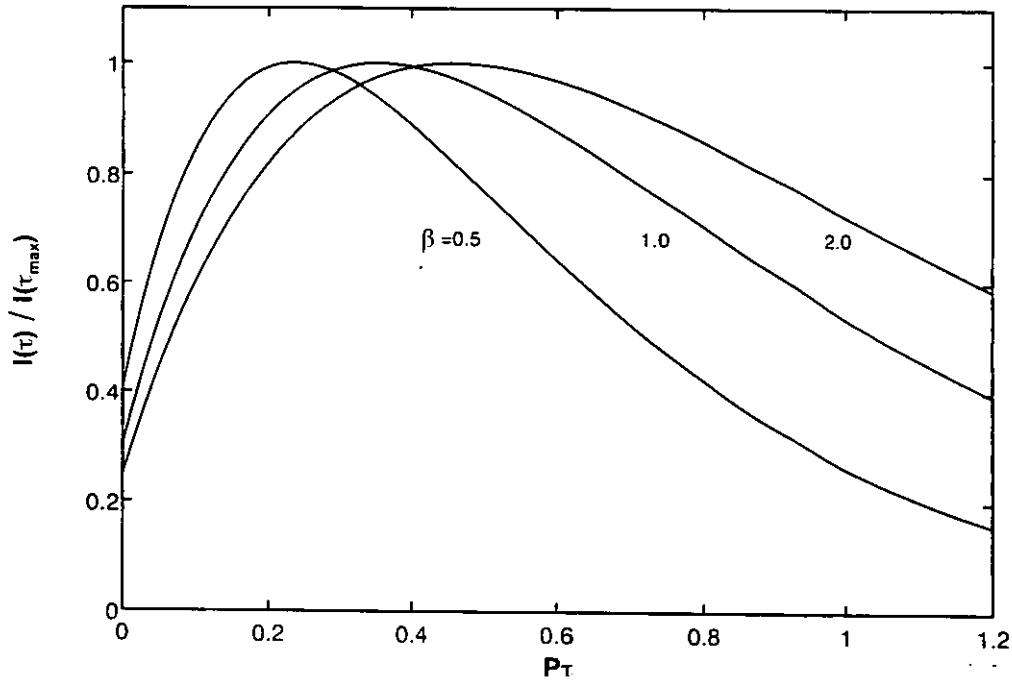

Fig 1 The predicted dependence of the fragment yield as a function of the delivered dose in $P\tau$ units. The curves have all been normalised on the ordinate axis. This model assumes that the A and B bonds are the same and that the probability of their breaking, P_A and P_B, is 0.1 whereas, for the C bonds, P_C is β times this value.

The effect of P for $\beta=1$ is seen in Fig 2. Here the axes are not normalised. We see directly that, for $P\tau>2$, the curves are close to simple exponential decays described by:

$$I(\tau) \approx 2P \exp\{-(1+\beta)P\tau\}, \quad P\tau>2 \tag{8}$$

Also, note that by differentiating Eq (6) at $\tau = 0$, a peak exists in the curve describing the peak intensity as a function of the damage dose if

$$\alpha P < \frac{1}{1+0.5\beta} \tag{9}$$

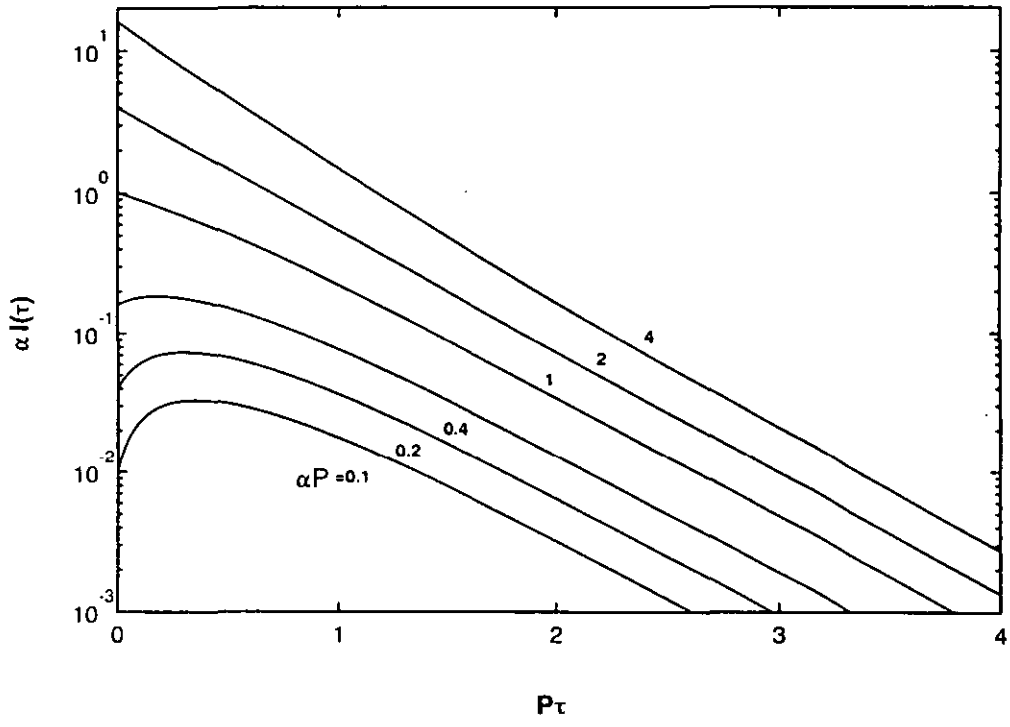

Fig 2 The predicted dependence of the fragment yield as a function of $P\tau$ for αP values up to 4 where the probabilities of breaking the A, B and C bonds are all the same.

Useful parameters to measure are the relative height of the maximum value, $I(\tau_{max})$, to that of the starting value, I(0), as well as R, S, r and s from Eq (7) by fitting. By differentiation of Eq (6)

$$P\tau_{max} = \ln\left\{\frac{(2-\alpha P)(2+\beta)}{2(1+\beta)}\right\} \tag{10}$$

and hence

$$I(\tau_{max}) = \frac{2P}{2+\beta}\left\{\frac{2(1+\beta)}{(2-\alpha P)(2+\beta)}\right\}^{(1+\beta)} \tag{11}$$

and, since

$$I(0) = \alpha P^2$$

then

$$\frac{I(\tau_{max})}{I(0)} = \frac{2}{\alpha(2+\beta)P}\left\{\frac{2(1+\beta)}{(2-\alpha P)(2+\beta)}\right\}^{(1+\beta)} \tag{12}$$

A plot of this function for three values of β is shown in Fig 3. It is clear that if αP is small a large rise may occur in the fragment intensity as a function of dose.

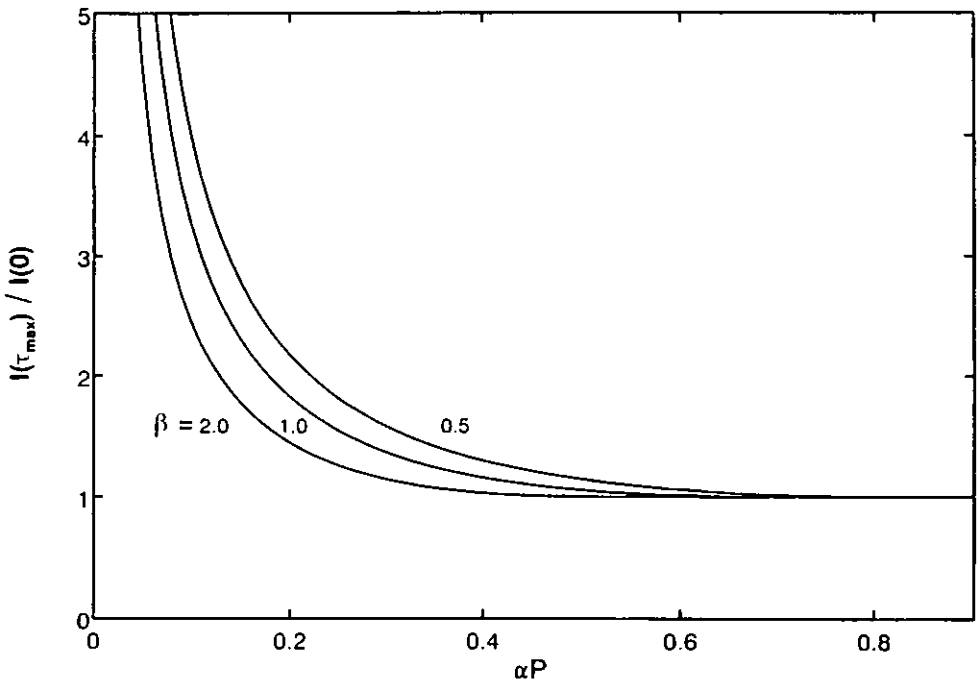

Fig 3 The magnitude of the maximum fragment yield divided by the initial yield as a function of αP for three values of β.

As noted above, by fitting the plots to the data, we may derive R, S, r and s. Since the absolute intensities we measure have an unknown scaling term we may only use the intensity ratio of R and S and not their absolute values. From Eq (6) directly

$$\frac{S}{R} = 1-0.5\alpha P \tag{13}$$

$$r = (1+\beta)P\tau/Nt \tag{14}$$

$$s = (2+\beta)P\tau/Nt \tag{15}$$

Hence, from Eqs (14) and (15),

$$\beta = \frac{2r-s}{s-r} \tag{16}$$

and from Eq (13)

$$\alpha P = 2\left(\frac{R-S}{R}\right) \tag{17}$$

We may obtain θ from Eqs (14), (16) and (17)

$$\theta = \frac{\tau}{Nt} = \left(\frac{R}{R-S}\right)\left(\frac{s-r}{2}\right)\alpha \tag{18}$$

Thus, from the fits of the experimental data to functions of the form of Eq (7) we may derive $\alpha P_{A,B}$, P_C and θ. The values of these parameters should not be interpreted too strictly since the model is very simple. However, as, we shall see, it is a good description of the behaviour. A fuller description will simply increase the number of parameters. Since the values of these parameters cannot yet be independently predicted, they become fitting parameters and the quality of any fit will always improve with model complexity. We therefore keep the model simple to see what information may be extracted from the experimental data.

2.2 AN EXTENSION OF THE MODEL TO A FRAGMENT WITH SEVERAL INTERNAL BONDS

In many of the detected species there are several of the bonds of type C. In these cases the factor, $\exp(-P_C\tau)$, before the large brackets in Eq (2) is replaced by

$$\prod_i \exp(-P_{Ci}\tau)$$

so that, in effect, in Eq (6) we may replace P_C by $\sum_i P_{Ci}$. If all of the P_{Ci} are the same bond

and there are n of these bonds within a fragment, then Eq (6) becomes

$$I(\tau) = 2P\exp\{-(1+n\beta)P\tau\}-(2-\alpha P)P\exp\{-(2+n\beta)P\tau\} \quad (19)$$

and similarly we obtain Eq (7) where

$$r = (1+n\beta)P\tau\ /Nt \quad (20)$$

$$s = (2+n\beta)P\tau\ /Nt \quad (21)$$

Thus, we see that β, in the previous equations, is simply replaced by $n\beta$. In terms of the final exponential decays for $P\tau>2$, Eq (8) reduces to

$$I(\tau) \approx 2P\ \exp\{-(1+n\beta)P\tau\}$$

ie as the chain length of a polymer increases, the rate of damage of the total chain also increases. This is exactly what we would expect as the total cross section for damage must be roughly proportional to the molecular area or the fragment length.

The initial signal at zero dose I(0), however, remains unchanged:

$$I(0) = \alpha P^2 \quad (22)$$

Note, that these equations only hold for our model of the polymer lying in the surface plane with the bonds A, B and C all within a molecular area of the order of θ. For very large molecules, unless there is essentially only one strong bond (polymers that are not fully polymerised may have chain ends preferentially in the surface) to the substrate, the two bonds to be broken may be sufficiently far apart that they exceed the range of the damage from any individual ion and then I(0) must fall to zero. In the spirit of Eq (2) for large molecular groups we may thus not be able to break the A and B bonds simultaneously and then

$$\begin{aligned} I(\tau) &= 2\ \exp(-n\beta P\tau)\{P\exp(-P\tau)\}\{1-\exp(-P\tau)\} \\ &= 2P\ \exp\{-(1+n\beta)P\tau\}\ -2P\ \exp\{-(2+n\beta)P\tau\} \end{aligned} \quad (23)$$

We now have the interesting prospect that this model predicts that some large molecular fragments may actually be more intense at doses beyond the static SIMS limit since the

intensity in Eq (23) starts from zero and peaks at a time given by:

$$P\tau_{max} = \ln\{(2+n\beta)/(1+n\beta)\} \qquad (24)$$

If n is large, we may rewrite Eq (24) in terms of the dose, Nt_{max}

$$Nt_{max} = \frac{1}{P\theta(1+n\beta)}$$

and hence see that Nt_{max} will be of the order of 10^{17} ions/m^2.

The transition from Eq (19) and Eq (23) occurs when the separation of the A and B bonds approximates the diameter of θ. At higher energies, as the angle of incidence of the ion beam increases, θ will increase and the high mass fragments become more intense. This effect arises simply because the sputtering yield is rising and so, in each event following an incident ion impact, the area of surface for a given density of energetic collisions to emit fragments must also rise. Additionally, a fragment with the A and B bonds physically close together will provide a greater intensity than a similar fragment where the backbone is more linear.

Of course, when we say I(0) will fall to zero for physically separated events, it must be remembered that SIMS has sensitivities over 5 or so orders of magnitude. I(0) will be zero for the present model, which is the model for the most intense peaks. There will be additional specific low probability events, such as a primary recoil with high energy travelling outwards at an acute angle to the surface, which will produce high mass fragments so that I(0) for a full model is never, in fact, identically zero.

2.3 AN EXTENSION OF THE MODEL TO SIDE CHAINS

For a side chain linked to the main backbone by one bond, Eq (6) becomes simplified to

$$\begin{aligned} I(\tau) &= \exp(-\textstyle\sum_i P_{Ci}\tau)\{P_A \exp(-P_A\tau)\} \\ &= P \exp\{-(P+\textstyle\sum_i P_{Ci})\tau\} \\ &= P \exp\{-(1+n\beta)P\tau\} \end{aligned} \qquad (25)$$

For different fragments these form simple exponential decays with the decay rate increasing as the number of bonds increases or as the bonds weaken in the fragment.

It is clear that the fragments that grow in intensity are those which require bonds broken at two or more points. The prior damage is helpful to these provided their internal structure is not too weak. A peak exists in the linear model of section 2(b) if

$$\alpha P < \frac{1}{1+0.5n\beta} \tag{26}$$

ie

$$n\beta <= \frac{2(1-\alpha P)}{\alpha P} \tag{27}$$

The product nβ is a measure of the fragility of the internal structure of any fragment.

2.4 A FRAGMENT REQUIRING THREE BROKEN BONDS

Following the above approaches

$$\begin{aligned} I(\tau) = \exp(-\sum_i P_{Ci}\tau)\{\alpha^2[P_A\exp(-P_A\tau)]^3 + 3\alpha[P_A\exp(-P_A\tau)]^2[1-\exp(-P_A\tau)] \\ + 3P_A\exp(-P_A\tau)[1-\exp(-P_A\tau)]^2\} \end{aligned} \tag{28}$$

$$\begin{aligned} &= (\alpha^2P^3-3\alpha P^2+3P)\exp\{-(3+n\beta)P\tau\} \\ &+ (3\alpha P^2-6P)\exp\{-(2+n\beta)P\tau\} \\ &+ 3P\exp\{-(1+n\beta)P\tau\} \end{aligned} \tag{29}$$

Whereas the single bond fragment starts with an intensity P_A, the double bond starts at αP_A^2 and the triple at $\alpha^2 P_A^3$. Similarly the single bond fragments initially decay whereas the double bond intensities may grow and the multiple bond functions start progressively weaker but grow more and more strongly. This is intuitively what one would expect. The interesting changes will all occur at doses much less than that required to sputter remove one monolayer.

2.5 THE END BONDS A AND B UNEQUAL

Here we may modify the earlier symbols and write

$$P_B = \gamma P_A = \gamma P \tag{30}$$

Then

$$\begin{aligned} I(\tau) = {} & P \exp\{-(1+n\beta)P\tau\} + \gamma P \exp\{-(\gamma+n\beta)P\tau\} \\ & - (\gamma+1-\alpha\gamma P)P \exp\{-(1+\gamma+n\beta)P\tau\} \end{aligned} \tag{31}$$

This reflects the form of Eq (4). If the A and B bonds are not too different they may be equated to give Eq (7). Thus, in splitting the experimental data into two exponentials using Eq (7), providing R and S are positive, as shown, the functions are meaningful. If S is negative we must be dealing with Eq (4) and it is the first two terms that have been determined. In principle, the data may just have sufficient accuracy to fit six independent parameters but it is doubtful if these simple models are sufficiently adequate to make such a determination fully meaningful. We therefore seek to find ways of reducing the complexity when we come to the section dealing with the data analysis. If we know that s is small or that the data are essentially described by the first two terms in Eq (4):

$$\frac{R}{Q} = \gamma \tag{32}$$

$$r = (\gamma+n\beta)P\tau/Nt \tag{33}$$

and

$$q = (1+n\beta)P\tau/Nt \tag{34}$$

Hence

$$n\beta = \frac{\gamma q - r}{r - q} \tag{35}$$

Unfortunately we cannot derive P and τ/t separately here, but only their product:

$$PN\theta = \frac{P\tau}{t} = \frac{r-q}{\gamma-1} \tag{36}$$

2.6 BONDS THAT RAPIDLY RE-COMBINE

In the spirit of Eq (2) for the general basic model if, for instance, the B bond rapidly re-heals we find for the A bond at one end and nC bonds in the middle:

$$\begin{aligned} I(\tau) &= \exp(-n\beta P\tau)\{\alpha P\exp(-P\tau)\gamma P+\gamma P[1-\exp(P\tau)]\} \\ &= \gamma P\exp(-n\beta P\tau)-\gamma P(1-\alpha P)\exp\{-(1+n\beta)P\tau\} \end{aligned} \tag{37}$$

which is similar to the behaviour of Eq (7).

If both A and B recombine Eq (2) reduces to

$$I(\tau) = \alpha\gamma P^2 \exp(-n\beta P\tau) \tag{38}$$

2.7 SUMMARY

A simple bond-breaking model of damage in polymers is presented. The model is very simple and allows the easy addition of particular boundary conditions. A number of these are developed. Many others may be easily added. Thus, the curves describing I(τ) or I(t) will be a sum of time-dependent exponentials whose rates of decay involve damage cross sections whose sum is raised as the fragment contains more and more bonds which may be disrupted. The more that prior disruption of bonds assists the release of the fragment, the more the fragment intensity will grow with dose (although starting from lower and lower initial intensities) generally as shown in fig 4. All important changes will occur long before the first monolayer is sputtered away (remember our doses are expressed in 10^{17} ions/m^2 which, at a sputtering yield of unity, would remove 1% of a monolayer of atoms).

The basic concept of a zone of area θ around the point of impact, in which large fragments may be both emitted and damaged, is essentially the same as that described by Benninghoven[24,25] in his discussion of the damage of adsorbed monolayers. His analysis is similar to that in section 2(c) leading to Eq (25) with a single exponential decay characterised by a disappearance cross sections around 10^{-18} m^2.

A simple test of this overall model may be made from the observation of spectra in the Static SIMS Handbook of Polymer Analysis[15]. According to the present model, the intensities of

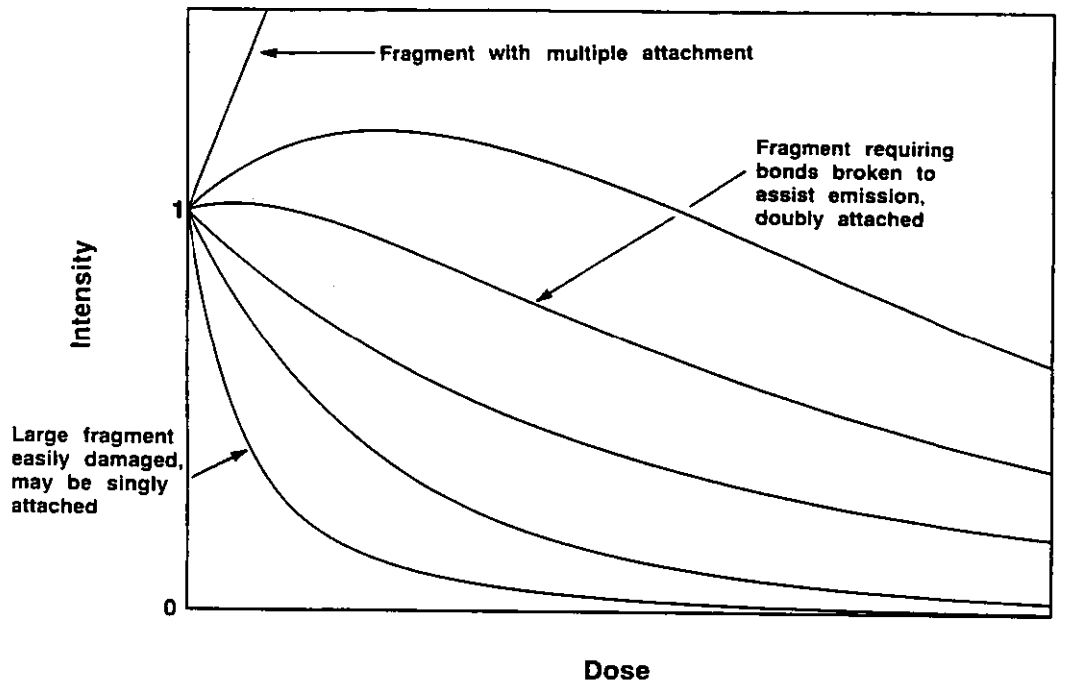

Fig 4 Summary damage plot showing the general behaviours.

fragments from a polymer with a certain repeat unit should decline rapidly at a mass where the A and B bonds are separated by a given fraction of the diameter of θ, rather than at a given mass. The masses at which this occurs in polyethylene, polypropylene, polyisobutylene and polybutadiene are 55, 69, 97 and 91, involving 4, 5, 7 and 7 carbon atoms, respectively. However, in each case this only involves 4, 3, 3 and 3 carbon atoms of the backbone, the increase in mass arising from the increased number of carbon atoms in side groups. This constancy in distance rather than mass is a property of this model for the condition where the bonds broken remain those of the initial damage event, i.e. there is no mobility in the bond scission process.

If our polymer chains do not lie in the surface plane but are intimately tangled in a 3-dimensional volume, fragments with a length significantly greater than any exposed lengths are highly unlikely to be detected. If the polymer is not fully polymerised but is composed of groups with long chains and is deposited on a substrate to which it is very weakly bonded, a high yield of high mass fragments may then be observed.

3 EXPERIMENTAL

The equipment used in this study is the VG Scientific quadrupole-based static SIMS system described before[21]. The ion optics are a modified HTO 100 lens system transporting ions to an MM 12-12 large rod quadrupole mass analyser. The ion gun is a VG Scientific EX05 set at 56° to the SIMS optics axis. The delivered ion dose is determined by measuring the beam current into the 300 μm focused spot with a 2 mm diameter aperture Faraday cup and then by defocusing this to 2 mm and by rastering this beam over an area of 7.98 mm by 7.53 mm on the sample surface at TV rates. This is achieved by rastering over an area of 4.21 mm by 7.98 mm in the plane normal to the ion beam. The deflection plates of the ion gun are sufficiently far from the sample (60 mm) that any non-linearities in the deflections may be ignored.

The electron neutralising system uses the emission plate method[21] with the emission plate and sample holder both modulated by a triangular waveform of 32 volts peak-to-peak at 6.5 kHz. The emission plate, at the front of the SIMS optics, is illuminated by 1 keV electrons and the low energy secondary electrons from that plate flood the sample to provide charge neutralisation. The modulation system reduces the measured signal by a factor of 3 but effectively broadens the energy window of the SIMS system so that the precise surface potential is unimportant. In this way sample-to-sample repeatabilities are reduced to better than 2%[21]. The factor of 3 loss is more than countered by the modification to the HTO 100 lens, noted above, so that the overall system is very efficient.

The quadrupole system is operated at a mass resolution better than unity so that the intensity between peaks at unit mass separation is very small. The mass scan is set at channel intervals of 0.2 amu and, subsequent to a mass scan, the counts in each single amu are summed to give a spectrum with data points at each amu. This method is used for detailed analyses. For studying the effects of dose the system may be operated to switch the electronics sequentially from mass peak to mass peak so that, for instance, up to ten masses may be followed as a function of time. This uses the standard depth profiling software available with the instrument. It was noticed prior to this work that the mass scale and resolution at high masses would drift with time as the radio frequency power unit delivered the extra power needed for the high masses. The electronic unit was thus rebuilt, eliminating such drifts before the work started.

The materials used in this study were obtained from a variety of sources. The first sample, PTFE, is part of a commercially prepared batch of tape as used domestically for water systems. The batch is a reference batch checked for homogeneity. The second sample, PET, is a sample from a set of 0.1 mm thick sheets of Melinex "O" supplied by M Hearn and D Briggs of ICI and is cleaned, as they suggested, by washing for 5 minutes in n-hexane[††] with ultrasonic agitation followed by an ethanol wash. The third sample is simply a silicon slice with adventitious laboratory contamination of around a year from containment in a plastic bag. The fourth sample is of tantalum pentoxide which has become contaminated in a plastic box. These latter two samples should exhibit surfaces with adsorbed hydrocarbon molecules of varying length but with contamination thicknesses of only one or two atom layers i.e. the molecules essentially lie in the surface plane. The damage effects may or may not, therefore, be similar to those of the bulk polymers. We show these data to show their essential similarities.

4 RESULTS

4.1 PTFE

4.1.1 FRAGMENT DAMAGE PHENOMENA WITH 4 KEV ARGON IONS

Static SIMS mass spectra for PTFE have been presented elsewhere[1,5,14,15,21]. They are broadly similar, but vary by factors of two in the relative intensities, to the spectra measured here in Figs 5(a) and (b). First we show the dose dependence of 6 of the masses in Fig 6(a) which is presented in a format to be similar to the measurement of Briggs[1]. These results are for 4 keV argon rather than 4 keV xenon but are broadly similar. However, the further results in Fig 6(b) bear little in common with the results of Leggett and Vickerman for 2 keV argon ions[16].

A comparison with Figs 1 to 4 shows all of the effects expected. The mass 12 (C^+) peak intensity is high to start with and falls a little, not because of the damage terms of the theory but because the damage alters the electronic environment slightly which affects the ion yields. The peak for mass 31 (CF^+) requires some damage but this is an intrinsic building block of

[††]Since this work the n-hexane exposure limit has been reduced to 20 ppm in the UK Health and Safety Occupational Exposure Limits, iso-hexane is now recommended.

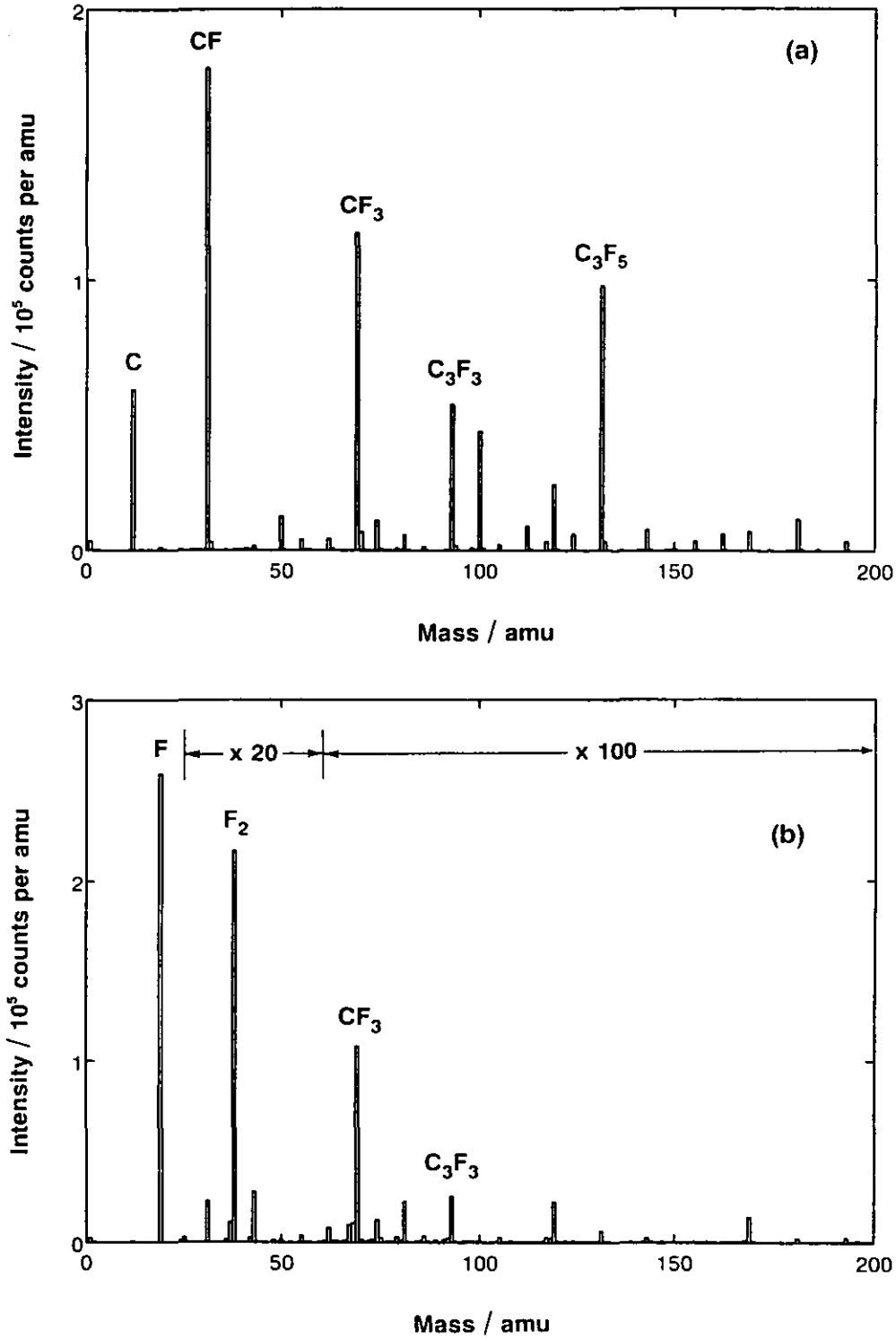

Fig 5 SIMS spectrum from PTFE using 4 keV argon ions at a total dose of 0.10×10^{17} ions/m^2, (a) positive ions, (b) negative ions.

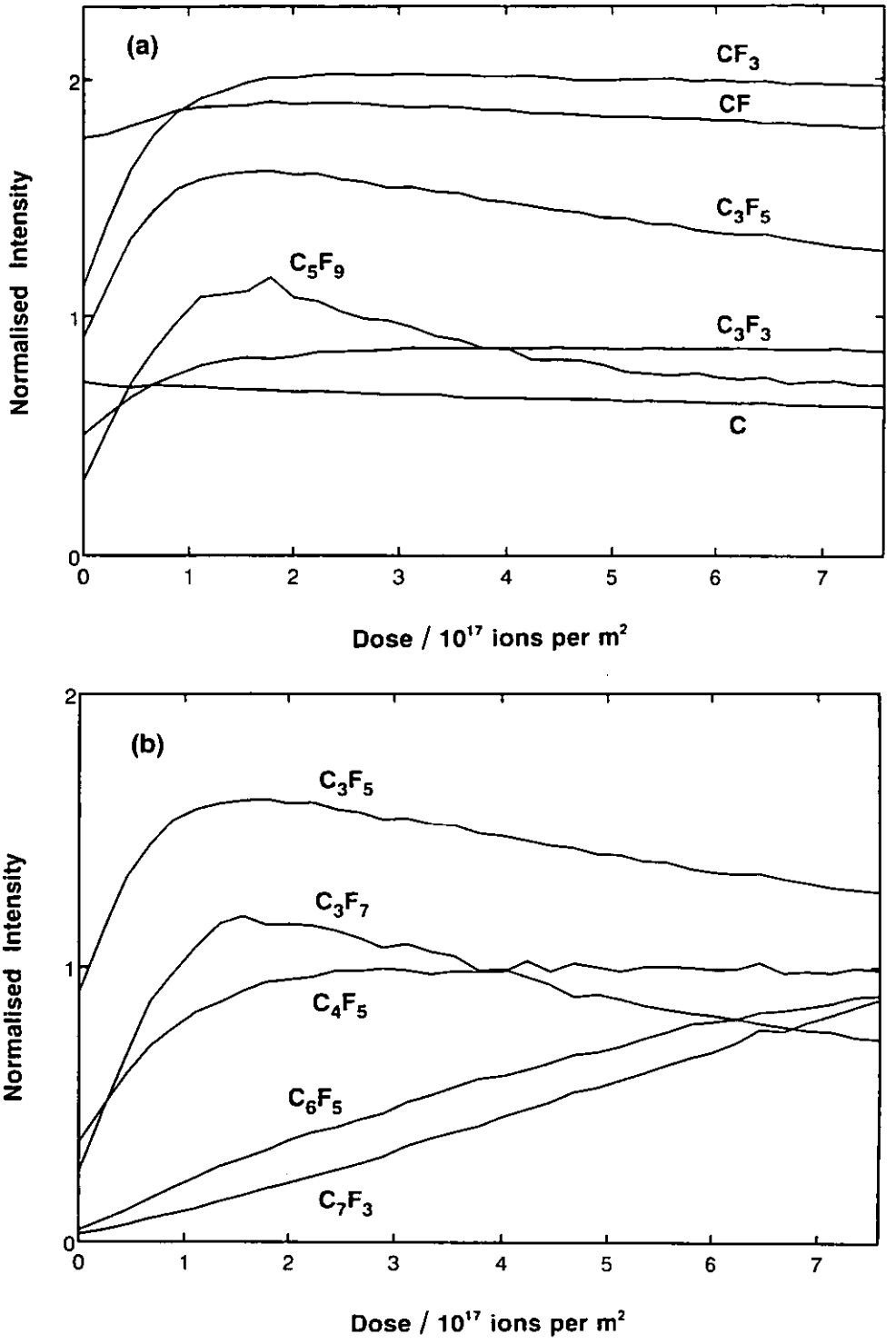

Fig 6 The dose dependence of peaks from Fig 5 for 4 keV argon ions for (a) the six masses measured by Briggs[1] (b) the five masses measured by Leggett and Vickerman[17]. These curves have all been scaled in intensity for presentation purposes.

PTFE and so is of high intensity with only weak damage effects. The peaks for masses 69(CF_3^+) and 93 ($C_3F_3^+$) require reconstruction and significant numbers of bonds to be broken and so rise strongly as the damage progresses. The peak for mass 131 ($C_3F_5^+$) rises very similarly but has rather weaker internal bonds and so decays rather more strongly. The peak for mass 231 ($C_5F_9^+$) should behave like the peak for mass 131 since the number of broken bonds is similar. The stronger decay is expected as there is approximately double the probability for internal damage, however the stronger rise is of particular interest. For convenience of reference, the peak masses and their attributions are given in Table 1.

Table 1 Peak masses and attributions used

Positive ions

Mass	Attribution	Mass	Attribution	Mass	Attribution
12	C	141	C_7F_3	51	C_4H_3
31	CF	143	C_4F_5	76	C_6H_4
69	CF_3	167	C_6F_5	91	C_7H_7
93	C_3F_3	169	C_3F_7	104	C_7H_4O
131	C_3F_5	231	C_5F_9	149	$C_8H_5O_3$
				193	$C_{10}H_9O_4$

Negative ions

Mass	Attribution	Mass	Attribution
19	F	16	O
38	F_2	76	C_6H_4
69	CF_3	121	$C_7H_5O_2$
93	C_3F_3		

It is likely that the stronger rise here is covered by the discussion for large molecules at the end of section 2(b) leading to Eq (23). If a single impact cannot easily breach two of the strong C-F bonds at 5 atom distances from each other, the intensity at zero dose will be low. Equation (19) is valid if the bonds at either end of the fragment are spatially close whereas Eq (23) is valid if they are far apart. The data for the peak for mass 231 appear to be an

intermediate case and so this fragment must have a size of the order of the radius of the damage area θ. For the C-F bond in PTFE we may thus expect the damage area to have a radius of 1.2 nm and hence an area, θ, of about 0.5×10^{-17} m^2 (ie 500Å^2). Rather more weakly bonded materials will, of course, show higher values of θ.

Figures 7(a) to (j) show the fits of functions of the form of Eq (7) to the data of Fig 6. It is clear that the algebraic description is excellent for the lower mass peaks but is not too good for masses 169 and 231. We shall return to these two peaks later. It is clear that most damage terms follow exponential functions accurately. For many of the fragments, the bond breaking is rather more complex than our simple theory and so a detailed interpretation of the values of R, S, r and s, given in Table 2 may not be too meaningful.

Table 2 Values of R, S, r and s for the PTFE data of Fig 6 using 4 keV argon ions

Mass amu	S counts	s x 10^{-17} m^2	R counts	r x 10^{-17} m^2
12	-1330	10.510	70634	0.018
31	22852	1.136	197146	0.013
69	95150	1.772	206392	0.006
93	37672	1.296	86926	0.002
131	87722	1.918	175545	0.046
231	20880	1.781	25900	0.092

The rise for mass 131 has characteristic damage cross sections of 0.05 x 10^{-17} m^2 and 1.9 x 10^{-17} m^2 for the decay and rise exponentials, respectively. These are equal to $(1+\beta)P\theta$ and $(2+\beta)P\theta$, respectively. If P is of the order of 0.5 these damage cross sections are consistent with our previous value of θ, the damage area for the single ion impact. Remember θ is the area for significant damage, not the area in which any damage occurs. Bearing this in mind we would not expect to see any significant intensity for masses much higher than 231 in PTFE at low doses and, indeed, in ToF SIMS spectra where the high masses are more readily detected this is, in fact, the case for bulk PTFE[5].

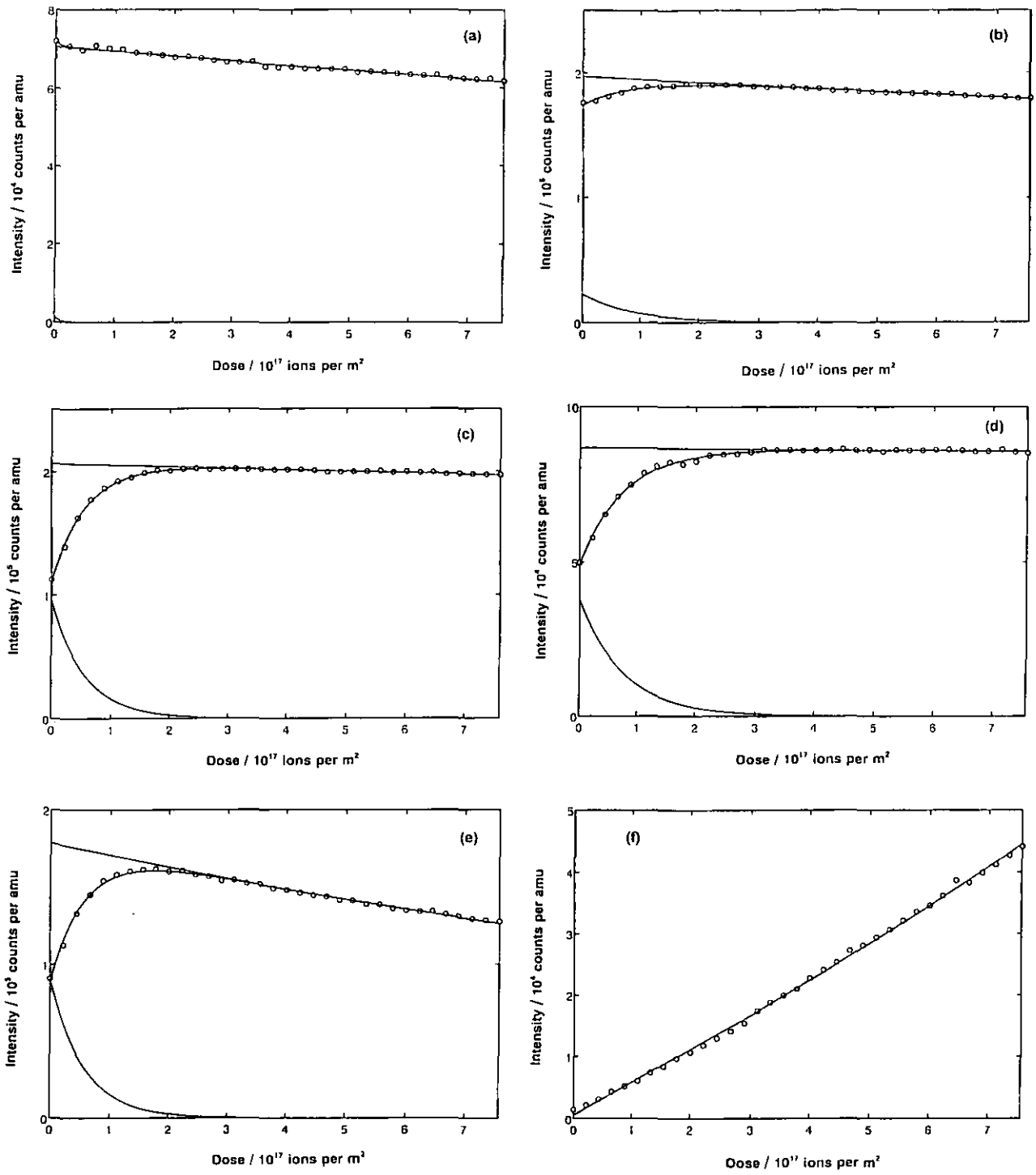

Fig 7 Fits of Eq (7) to the data of Figs 6(a) and 6(b) with the modulus of the constituent exponentials for the following positive ions, (a) 12, (b) 31, (c) 69, (d) 93, (e) 131, (f) 141, (g) 143, (h) 167, (i) 169, and (j) 231 amu. Fits of Eq (39) to (k) 169 and (l) 231 amu; the dashed curves represents the modulus of the constituent parts.

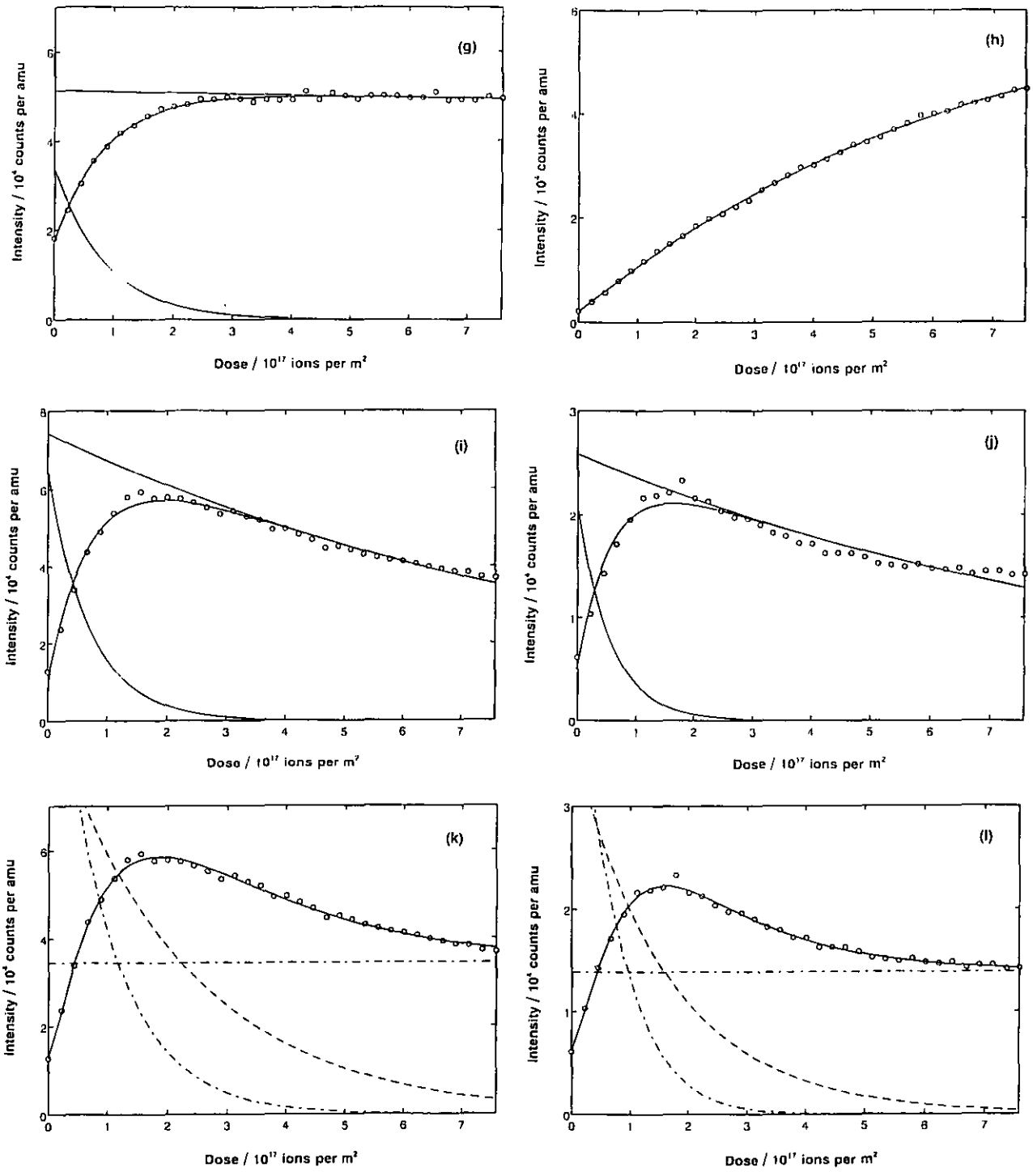

Fig 7 Fits of Eq (7) to the data of Figs 6(a) and 6(b) with the modulus of the constituent exponentials for the following positive ions, (a) 12, (b) 31, (c) 69, (d) 93, (e) 131, (f) 141, (g) 143, (h) 167, (i) 169, and (j) 231 amu. Fits of Eq (39) to (k) 169 and (l) 231 amu; the dashed curves represents the modulus of the constituent parts.

Note that, from the shape of the curve for the peak for mass 231 we could define a static SIMS dose limit. If we permit a 10% change in intensity the limit would be 0.035×10^{17} ions/m^2 and for 1% only 0.0035×10^{17} ions/m^2. At the conventional limit of 0.5×10^{17} ions/m^2 this peak has changed by 100%. Further data for PTFE are shown in Fig 6(b) to compare with the data of Leggett and Vickerman[17]. Their data show the intensities for masses 141 ($C_7F_3^+$) and 167 (C_6F_5) already decaying at a few percent of the present doses. It appears from the shape of their curves that the perennial problem that they identified, of surface charge neutralisation, does indeed dominate their results. In Fig 6(b) the curve for mass 131 (C_3F_5) has already been discussed. The curve for mass 169 ($C_3F_7^+$) should be very similar to that for mass 131 as the fragment is similar. However, the fragments of masses 143 ($C_4F_5^+$), 167 ($C_6F_5^+$) and 141 ($C_7F_3^+$) represent a series in which more and more bonds must be ruptured to obtain the fragment. We thus see, in this series, a progression of a lower and lower initial intensity and a raising of the power of the initial dose dependence, as described in section 2(d).

We return now to the fits for the masses at 169 and 231 amu shown in Figs 7(i) and (j). The simple theory that we have developed applies to a model of the sample as a fixed structure with bonds being broken. For bulk polymers it could be that the recoil of energy exposes additional amounts of the polymer chain out of the surface so increasing the overall yield as the dose increases with an additional source function proportional to {1-exp(-Nut)}. If this is added to Eq (7) we arrive at Eq (4) with an added constant:

$$I(t) = Qe^{-Nqt} + Re^{-Nrt} - Se^{-Nst} + U \qquad (39)$$

This function fits the data for masses 169 and 231 excellently, as shown in Figs 7(k) and (l). From this we conclude that the intensity of fragments from polymers may remain higher than those for singly attached adsorbed hydrocarbon layers, even when the total ion dose is beyond 1×10^{17} ions/m^2.

4.1.2 RELATIVE DAMAGE RESPONSES FOR 4 KEV ARGON AND XENON IONS

The effects of xenon were studied as it is a popular view that higher mass ions lead to better yields of the high mass fragments[2,3,7]. Using xenon, the spectra and damage plots look broadly similar to Figs 5 and 6.

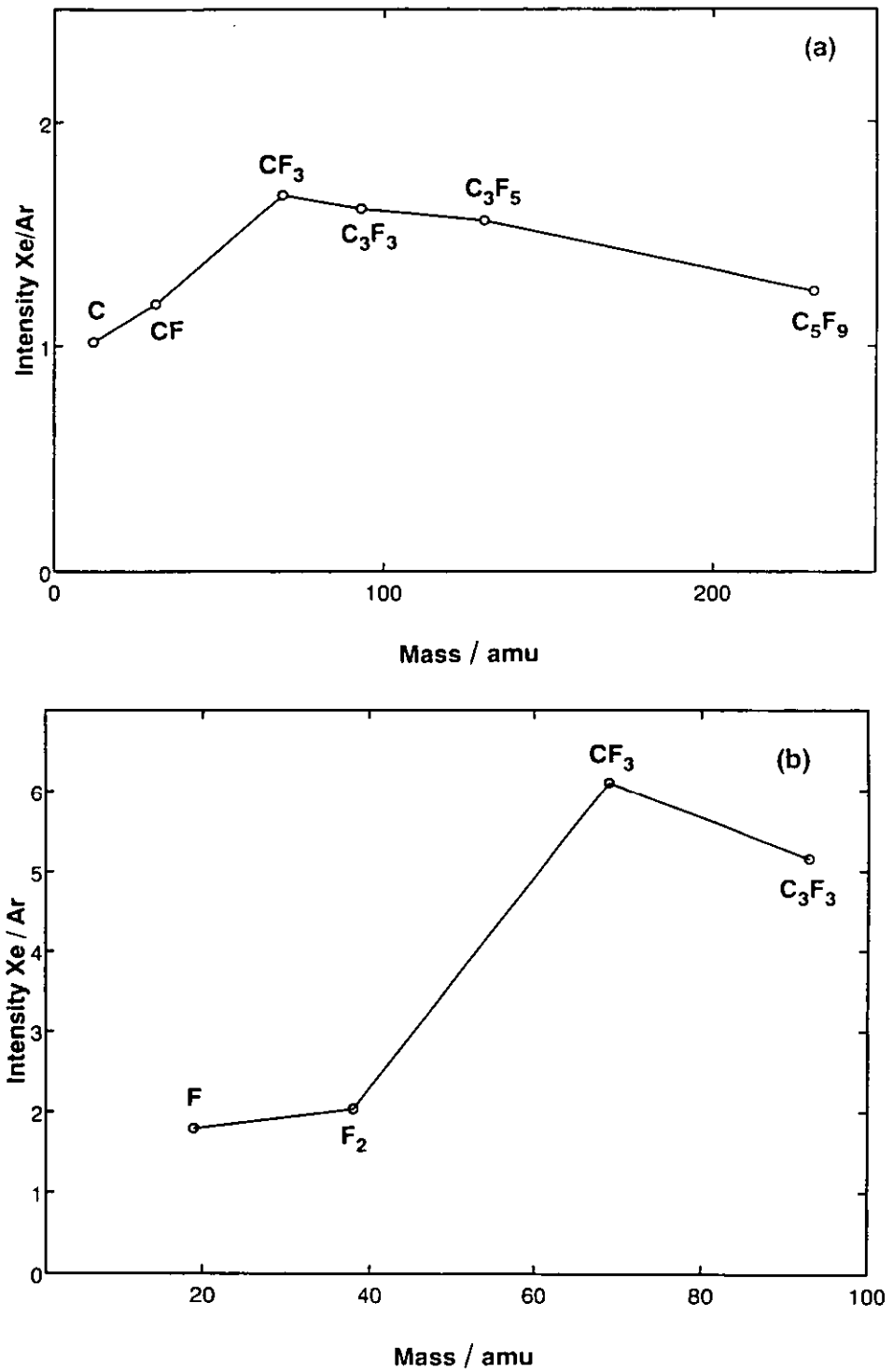

Fig 8 Ratio of the absolute intensities of the mass fragments shown in Fig 6(a) obtained with 4 keV xenon to the absolute intensities for 4 keV argon at the same beam current and beam current density, (a) positive ions, (b) negative ions.

To compare the effects, the first item of interest is the ratio of the absolute yields for various fragments. The result, normalised for the same beam current and operating conditions, is shown for positive ions in Fig 8(a). The xenon is more efficient than argon, with increases of up to 70% in the yields. It is interesting that in the mass range from 69 to 250 amu the curve seems to be falling so that for higher mass fragments from PTFE there may be little real advantage.

The gain in yield is of no use if there is a concomitant increase in the rate of damage. Really, the important parameter is a figure of merit, F, given by

$$F = I(0)/W(0) \tag{40}$$

where I(0) is the absolute yield at zero time and W(0) is the fractional rate of change of I(0) with the dose, D, at zero dose. This means that if the rate of damage is doubled then one needs double the yield to achieve the same figure of merit. In practice we could halve the beam current and we are back where we started. In Fig 9 we plot F(Xe)/F(Ar) for the same peaks as in Fig 8(a). In order to do this in a repeatable way we define W(0) from the gradient of the damage plots over the dose range from zero to 0.2 x 10^{17} ions/m^2. The remarkable result in Fig 9 shows that the higher yield for xenon is overshadowed by a significantly higher rate of damage so that the final effect is a small loss in the average figure of merit on moving to xenon!

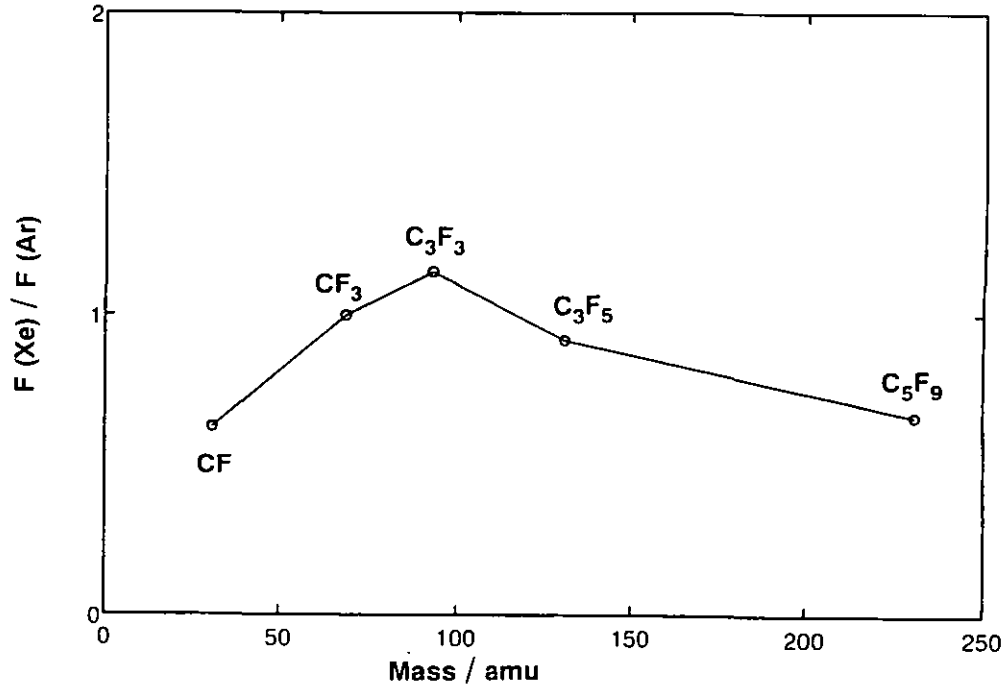

Fig 9 Ratio of the xenon and argon figures of merit, F, for PTFE at 4 keV.

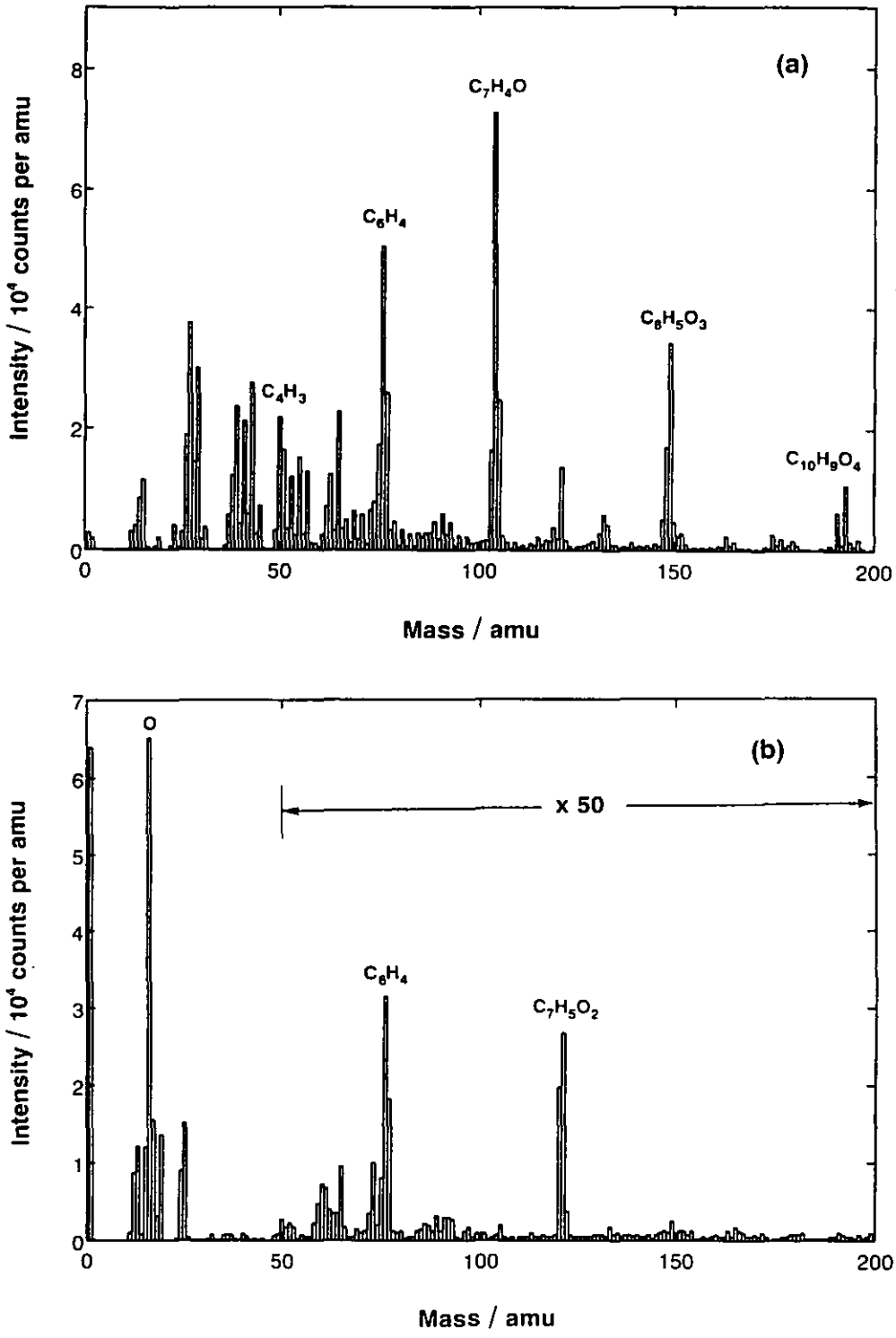

Fig 10 SIMS spectrum from PET using 4 keV argon ions at a total dose of 0.10×10^{17} ions/m^2, (a) positive ions, (b) negative ions.

In contrast to the above result for positive ions, we show, in Fig 8(b), that there is a significant intensity improvement for the negative ions. It is not clear why the improvement occurs but these results, as with all of the present studies, are quite repeatable.

4.2 PET

Positive and negative SIMS spectra for 4 keV argon from PET are shown in Figs 10(a) and (b) respectively.

4.2.1 FRAGMENT DAMAGE PHENOMENA WITH 4 KEV ARGON IONS

Figure 11 shows the compilation of the damage data for PET intensities normalised to unity at zero time as a function of the argon ion dose at 4 keV. We see from this directly how the rate of damage rises as the fragment size increases. Figure 12(a) to (f) show the fits to these data using Eq (7). It is clear that this description is excellent. However, it is unfortunate that, even within the typical uncertainty of 1% in the data points, unless the values of s and r are very well separated, any fit has a strongly correlated error between the two terms so that, at this stage, the individual values of r and s are not too meaningful.

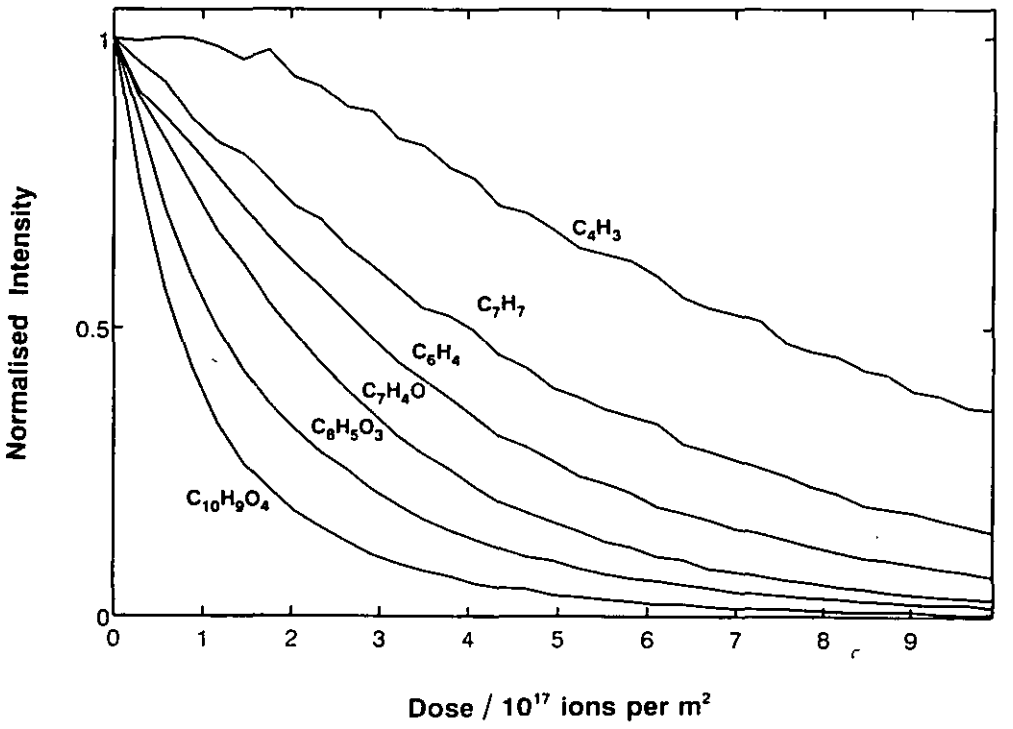

Fig 11 Normalised damage curves for selected masses from PET analysed with 4 keV Ar^+.

The curves show a behaviour broadly in line with our predictions. The mass 51 peak requires damage to the benzene ring as well as the breaking of the bonds in the polymer backbone and so, in the set of data, this curve is initially constant with dose and then decays least. The peaks at masses 76 and 91 require less damage and so grow less and generally decay faster. The peaks at masses 104, 149 and 193 progressively require less damage for their emission and consequently are more easily lost and so do not rise in intensity relative to their main decay. The peak at mass 104 essentially shows a single exponential decay and those at masses 149 and 193 show exponentials speeding the decay even faster, as discussed above.

Fitting the data to Eq (7) gives the values of R, S, r and s shown in Table 3. We shall discuss these values below. As we saw in the PTFE data, some of the peaks show the effects of damage very quickly. For a 10% change in the peak for mass 193 the dose limit is 0.11×10^{17} ions/m^2 and for a change of 1% the limit is reduced to 0.011×10^{17} ions/m^2. These values are three times those for PTFE. Again, at the conventional limit of 0.5×10^{17} ions/m^2, the 193 amu peak has fallen by 38% compared with, say, the 51 amu peak which has remained unchanged.

Table 3 Values of R, S, r and s for PET using 4 keV argon ions

Mass amu	S counts	s $\times 10^{-17}$ m^2	R counts	r $\times 10^{-17}$ m^2
51	3525	0.72	13609	0.13
76	8681	0.88	64969	0.29
91	1938	0.57	12433	0.21
104	2553	1.44	41941	0.38
149	-21538	0.94	22216	0.35
193	-12414	1.36	6351	0.44

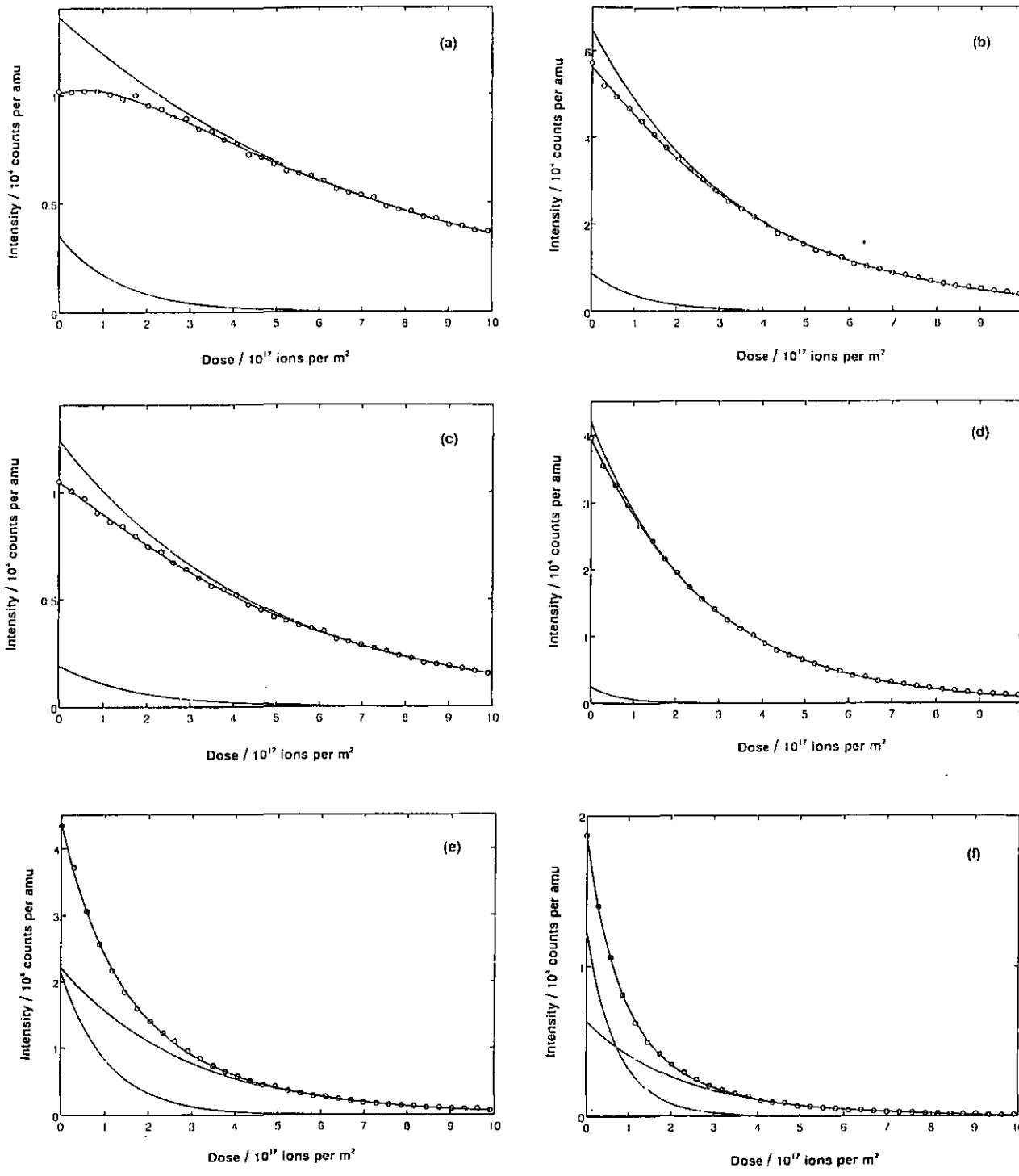

Fig 12 The fits of Eq (7) to the PET data of Fig 11 using 4 keV argon ions, with the moduli of the two components plotted separately, (a) 51, (b) 76, (c) 91, (d) 104, (e) 149 and (f) 193 amu.

4.2.2 THE EFFECT OF ARGON BEAM ENERGY

The data have been recorded for argon ion energies of 1, 2, 3, 4 and 5 keV to study the effect of beam energy on ion yields, damage and whether the ion yield per unit damage is highest at low or high beam energy. First we shall analyse the behaviour of R, S, r and s with the argon ion energy. Figure 13 shows the average value of r for the 6 mass peaks of Fig 12 as a function of energy. The fitted line shows the function

$$\bar{r} = 1.69 \times 10^{-18} E^{0.4} \; m^2 \qquad (41)$$

where E is the argon ion energy in keV. The values of s are prone to error if s is close to r, if S and R are of similar magnitudes or if S << R. Ignoring the data which show such errors, the average value of $\bar{s}$ appears to be independent of energy and is approximately 9.4×10^{-18} m^2. From Eqs (14) and (15), where r and s shown to be proportional to P, we would, in fact, expect both to increase with E.

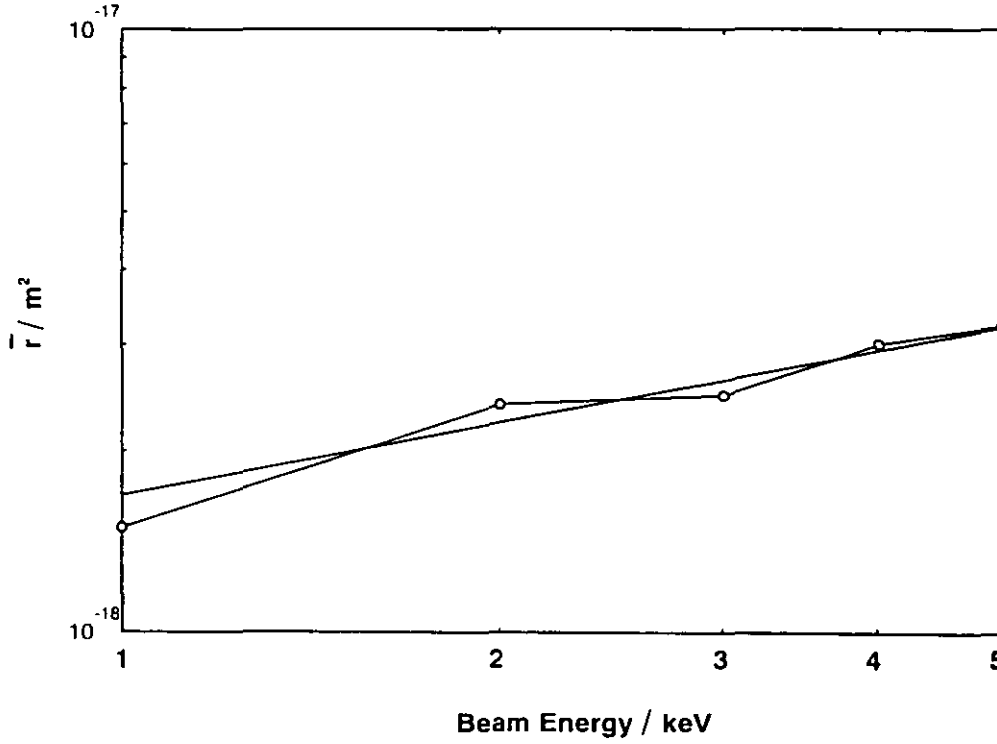

Fig 13 The energy dependence of $\bar{r}$, the average value of r, for the peaks at masses 51, 76, 91, 104, 149 and 193 amu, for 4 keV argon ions incident on PET.

The absolute values of R and S are prone to some error, however, the ratio S/R does not show a significant dependence on energy, is in the range 0.1 to 0.3 for the 51, 76, 91 and

104 amu peaks and is -1 at 149 amu and -2 at 193 amu. From Eq (17) this shows that αP is somewhat higher for PET than for PTFE but in both cases is above unity.

The largeness of $\bar{s}$ compared with $\bar{r}$ deserves a comment. From the simple theory a figure of 1 to 2 is expected rather than the approximate value of 3. The reason for this probably lies in the fact that most bonds are not left totally broken or totally unchanged by the increase of the damage dose but are left in weakened intermediate states with a local charge.

For each mass peak we first determine the absolute intensity at zero damage, I(0,E), as a function of the beam energy. This is then normalised by dividing by the average intensity over the energies 1 to 5 keV. This normalised intensity is then averaged over the peaks for masses 76, 91, 104, 149 and 193 to show the intensity dependence at unit beam current and fixed analytical area as a function of the argon ion beam energy. This is shown in Fig 14 with an $E^{1.0}$ function plotted to guide the eye. It may be expected that the yield of neutrals would increase as the sputtering yield or as $E^{0.65}$, say. This somewhat higher dependence may be due to a weak energy dependence of the ion-to-neutral partition function. In Fig 15(a) we plot the figure of merit F factor (the ratio of the absolute intensity to the fractional rate of change of that intensity) for each mass as a function of the beam energy. Here we plot the results on log/log scales to show the power dependence for each mass. The curves have been displaced vertically for the convenience of display. This result shows clearly that the information content per unit damage is roughly proportional to energy, i.e. the constant is highest at 5 keV and lowest at 1 keV. This arises mainly through the ion yield being roughly proportional to energy and the damage rates being only weakly dependent on energy.

In terms of the earlier simple model where the ionisation effects are ignored, the damage terms are exactly what permits the bond breaking to provide the signal. One would therefore expect the information content per unit damage to be fairly independent of energy. However, one would also expect that, as the energy rises, the area of the damage rises so that θ rises and the probability of seeing large fragments requiring more than one bond to break would therefore rise faster than that for small fragments. We thus see, in Fig 15(b), a plot of the power dependence of the data in Fig 15(a) as a function of the fragment mass or size. We see that the power dependence does rise with mass confirming that the figure of merit F factor improves more for the high mass fragments on increasing the energy from 1 to 5 keV, as predicted by the theory.

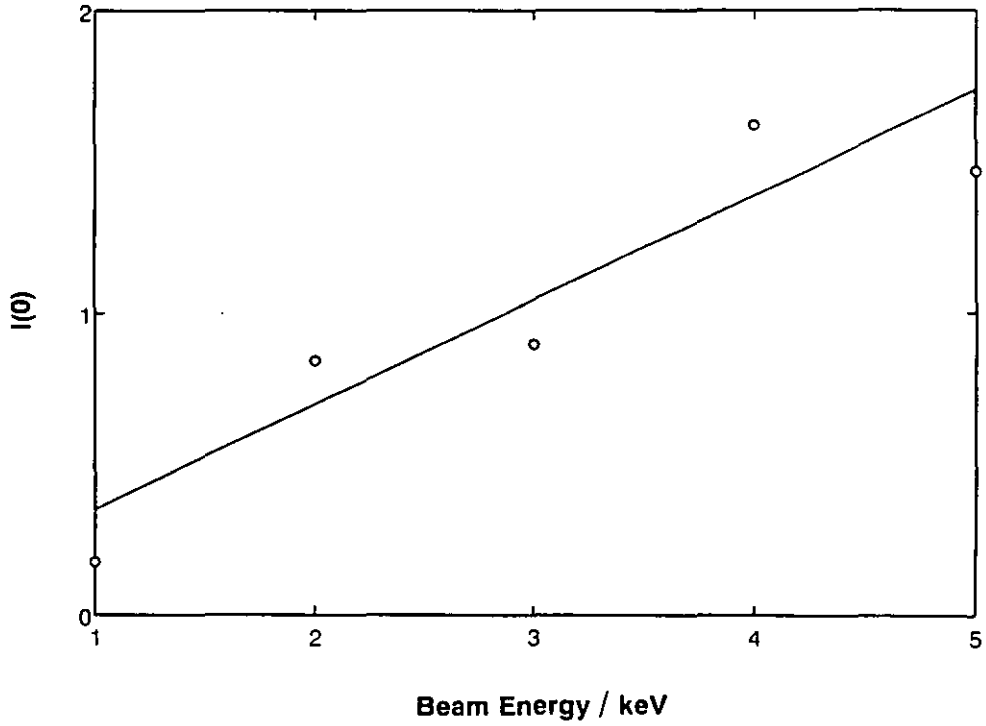

Fig 14 The argon ion energy dependence of the average of the normalised intensities at zero dose for the peaks at mass 76, 91, 104, 149 and 193 from PET. The plotted line has an $E^{1.0}$ dependence.

4.2.3 RELATIVE DAMAGE RESPONSES FOR 4 KEV ARGON AND XENON IONS

The ratio of the absolute intensities using xenon and argon for the masses 51, 76, 91, 104, 149 and 193 amu is plotted in Fig 16 as an analogue of Fig 7 for PTFE. Here we see that a gain of a factor of 3 has been achieved with an overall gain increasing with the fragment mass. This gain is carried over to our figure of merit factor, F, as shown in Fig 17. As we can see, F, the ratio of the absolute intensity to the initial damage gradient is three to five times as high for xenon as it is for argon. This mainly arises from the change in sign of S from negative for argon, as given in Table 3, to positive for xenon. We see, this time, a general increase in F(Xe)/F(Ar) for the high mass fragments.

From these data it appears that the 4 keV xenon data would be equivalent in F factor to a significantly higher beam energy for argon. For PTFE this increase would appear to be less. The precise equivalence clearly depends in detail on the type of mechanisms involved in the fragmentation process.

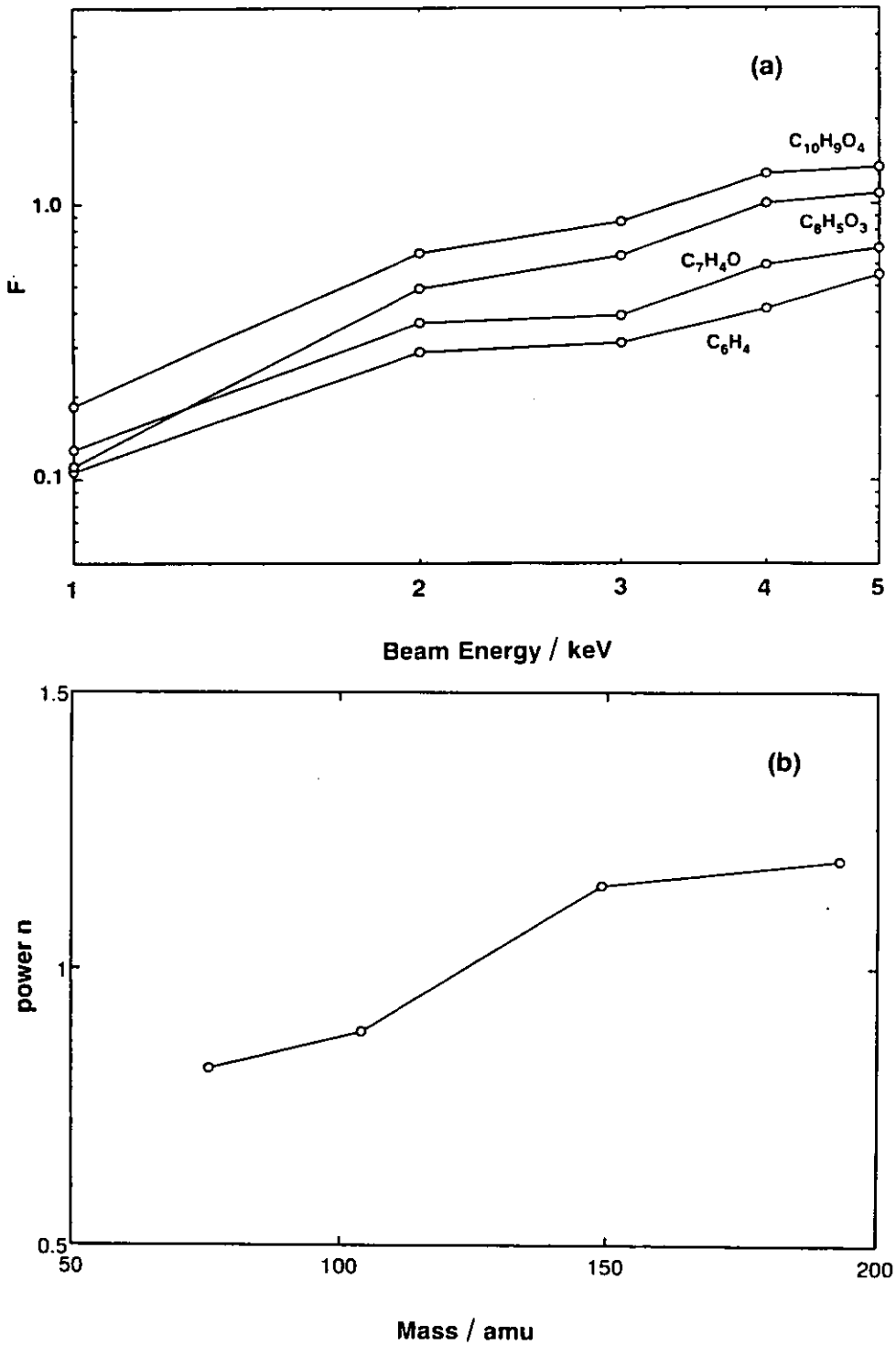

Fig 15 The argon ion energy dependence of the figure of merit F factor (the ratio of the absolute intensity to the fractional rate of change of that intensity at zero dose) for the peaks of mass 76, 104, 149 and 193 from PET, (a) plot on log/log axes to show a power dependence of the form $F \propto E_o^n$, individual data sets have been displaced vertically for display purposes, (b) plot of n from (a) versus mass.

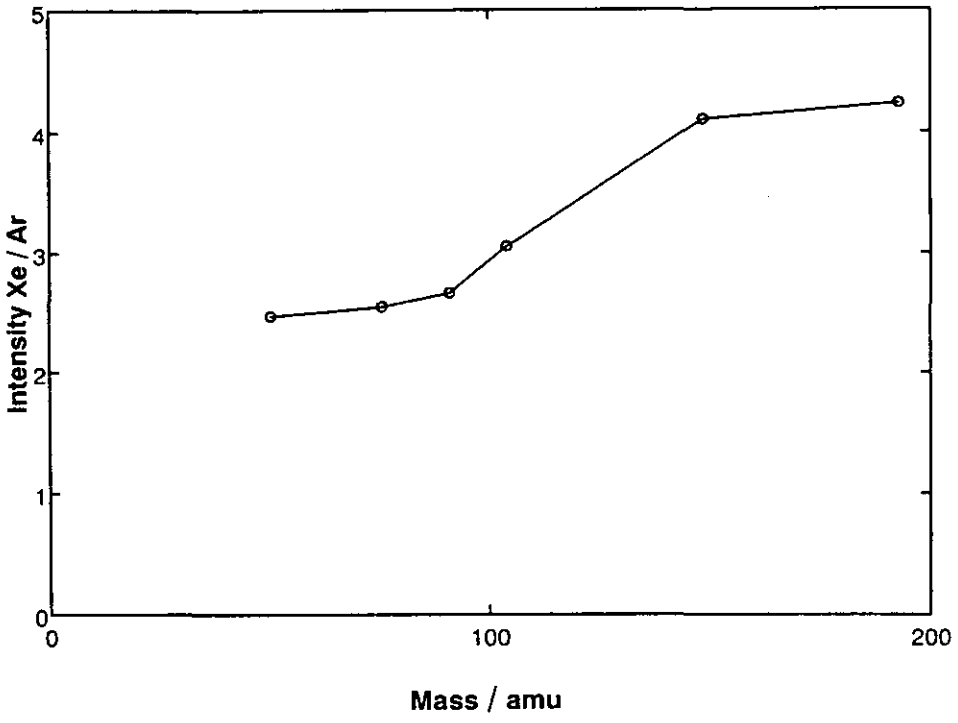

Fig 16 The ratio of the absolute intensities for the peaks for masses 51, 76, 91, 104, 149 and 193 amu for 4 keV xenon and argon ions incident on PET.

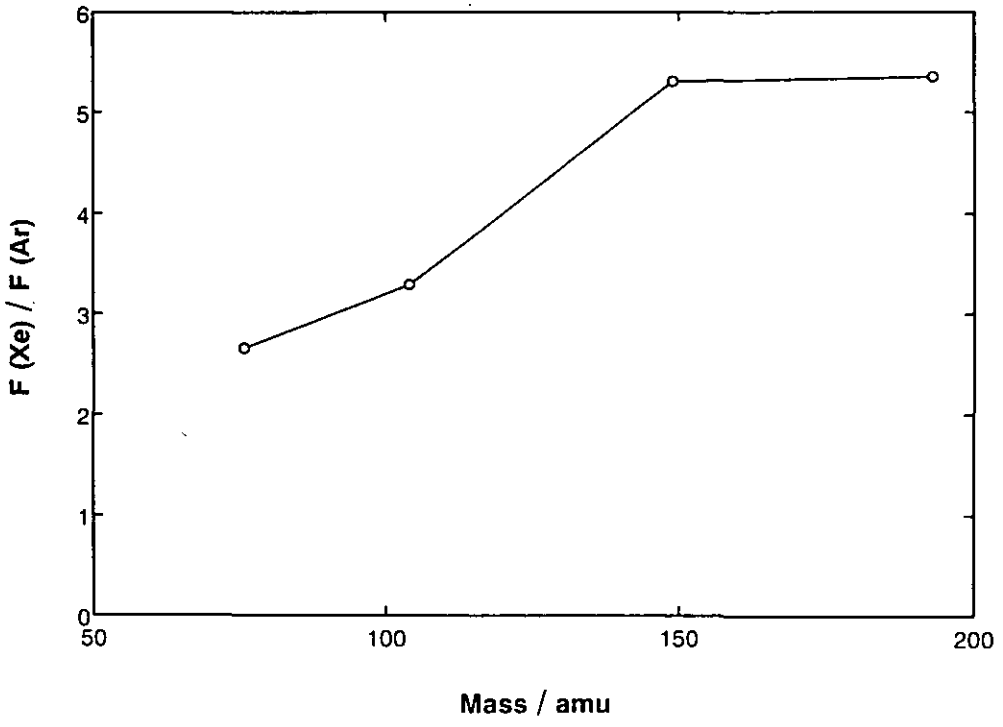

Fig 17 The ratio of the xenon and argon figures of merit for PET at 4 keV.

4.3 CONTAMINATION LAYER ON A SILICON WAFER

The positive SIMS spectrum from a contaminated silicon wafer kept for one year in a polyethylene bag and then washed in analar ethanol and sputtered using 4 keV argon ions, is shown in Fig 18. An intense peak at 149 amu identifies the contamination as a phthalate, a common plasticizer and lubricant with high mobility. This sample differs from the PET and PTFE in that the low molecular weight molecules reside as a thin film, maybe a monolayer or so thick, on the surface. Figure 19 shows how the peaks change with dose. The silicon peak rises, as expected, and all the contaminants decay. Basically, the higher mass fragments decay fastest, not due to sputter removal, but due to sputtering damage. For a 10% fall in the peak at mass 149 the dose should not exceed 0.09×10^{17} ions/m^2. This static SIMS limit is similar to the equivalent limits for PET but is 15 times faster than would be deduced from the data for $CH_2 = CHCOO^-$ from a silver catalyst, given by Benninghoven[22]. Note, in Fig 18, as predicted for thin layers of hydrocarbons, none of the high mass fragments retain significant intensities. Here there is no need to invoke the U term of Eq (39).

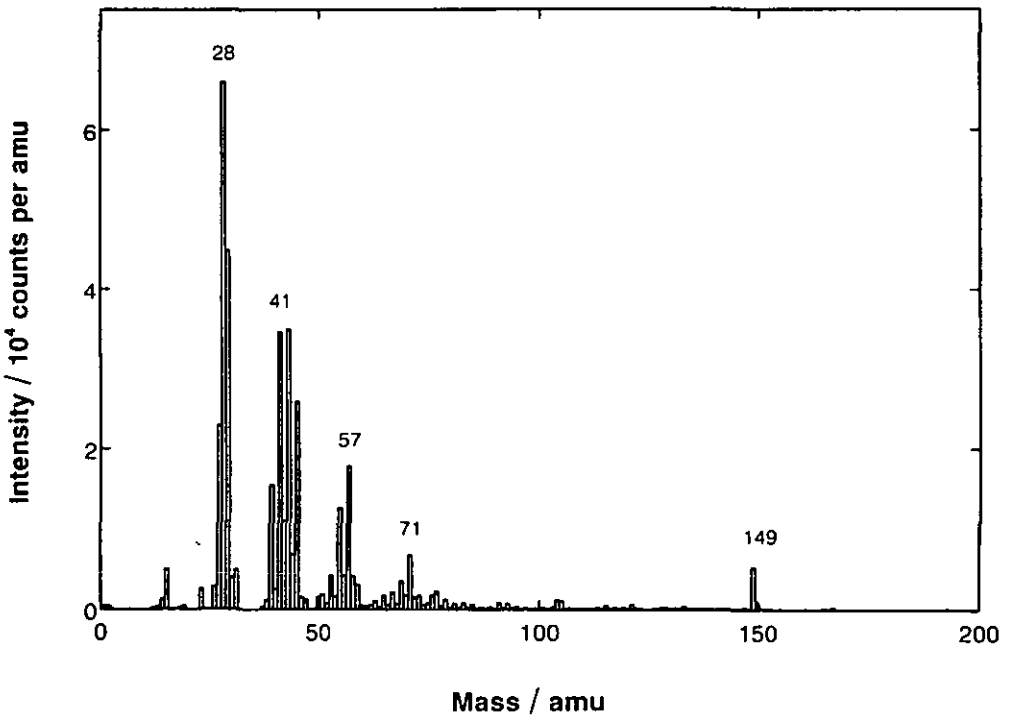

Fig 18 Positive SIMS spectrum from a contaminated silicon wafer washed in analar ethanol using 4 keV argon.

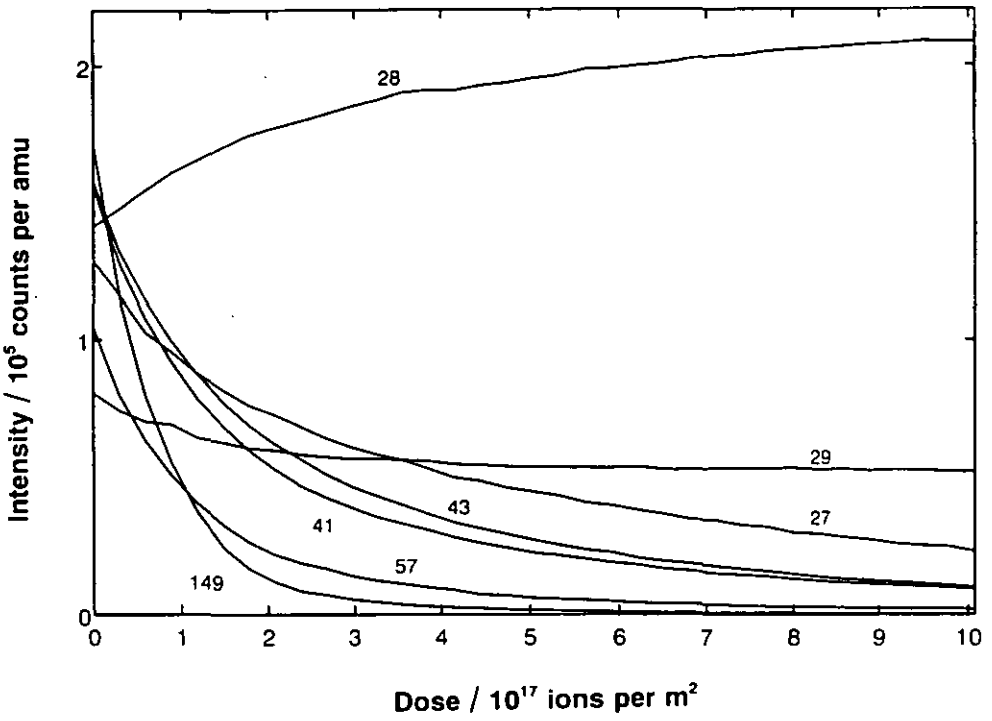

Fig 19 The effect of the dose of 4 keV argon ions on the peaks at masses 27, 28, 29, 41, 43, 57 and 149 amu from the contaminated silicon wafer of Fig 18.

4.4 CONTAMINATION LAYER ON TANTALUM PENTOXIDE

The positive SIMS spectrum from a sheet of tantalum with anodically oxidised surfaces, which had been stored in a plastic box, is shown in Fig 20. The intense tropylium ion at 91 amu indicates aromatic hydrocarbon contamination. In Fig 21(a) we show the effects of the damage dose on nine of the mass peaks up to a dose of 10.0×10^{17} ions/m^2 and in Fig 21(b) the extension to 131×10^{17} ions/m^2. The latter plot is of sufficient time to remove about one monolayer of hydrocarbon contamination. This is evidenced by the rise of the Ta and TaO peaks at 181 and 197 amu. The brief rise between the first two data points for the hydrocarbon peaks followed by a fall at a dose of 0.38×10^{17} ions/m^2 is quite reproducible and may be associated with the effects of the chemisorption interaction with the oxide. Again we see no generally rising peaks for the contaminant or high remaining levels but, unlike the earlier examples, a 20% change in intensities now survives even a dose of 10^{17} ions/m^2.

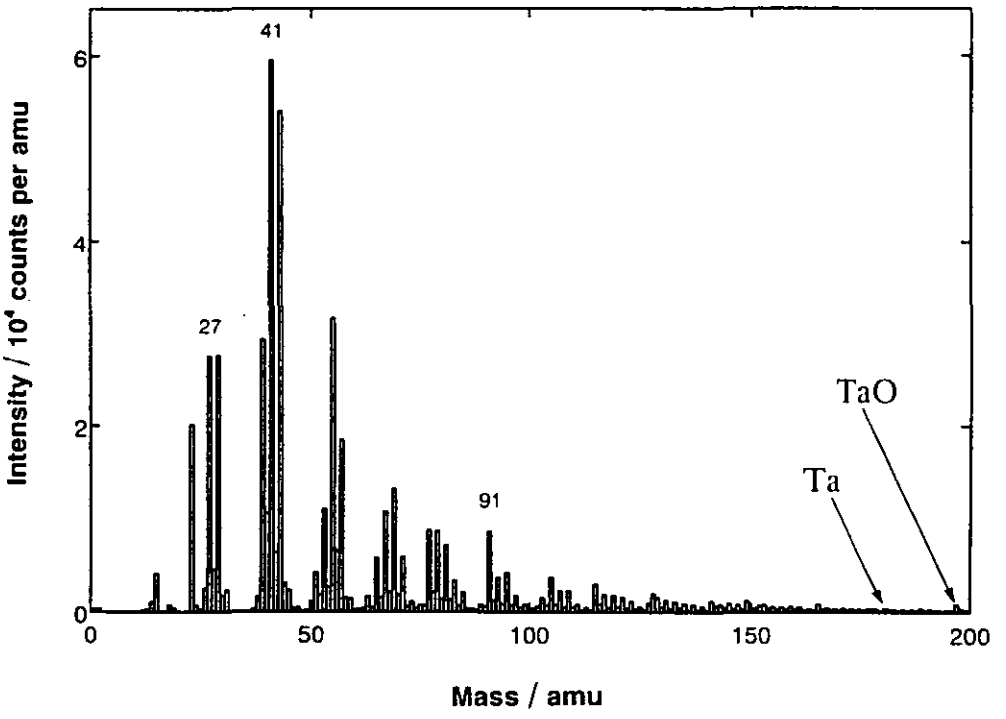

Fig 20 Positive SIMS spectrum from tantalum with anodically oxidised surfaces after storage in a plastic box, using 4 keV argon ions.

5 CONCLUSIONS

A number of effects derived from a simple bond-breaking model are summarised in Fig 4. It is simple to see how, from this figure, two possible models for any fragmentation group could be discriminated in a way not possible from the regular static SIMS spectrum. Additional specific conclusions may be made from this work based on these studies of bulk PTFE, PET and contamination layers using argon and xenon ion beams as follows.

(1) This work shows that all damage effects may be described by a simple linear sum of exponential damage functions containing damage cross sections.

(2) The intensities of the larger, more complex fragments decay most rapidly as they have a large cross-section for internal damage.

(3) Species that require prior bond breaking for their observation, either because their release involves a number of bonds or because their bonds are well separated in space may not decay as rapidly in time and may, indeed, grow in intensity.

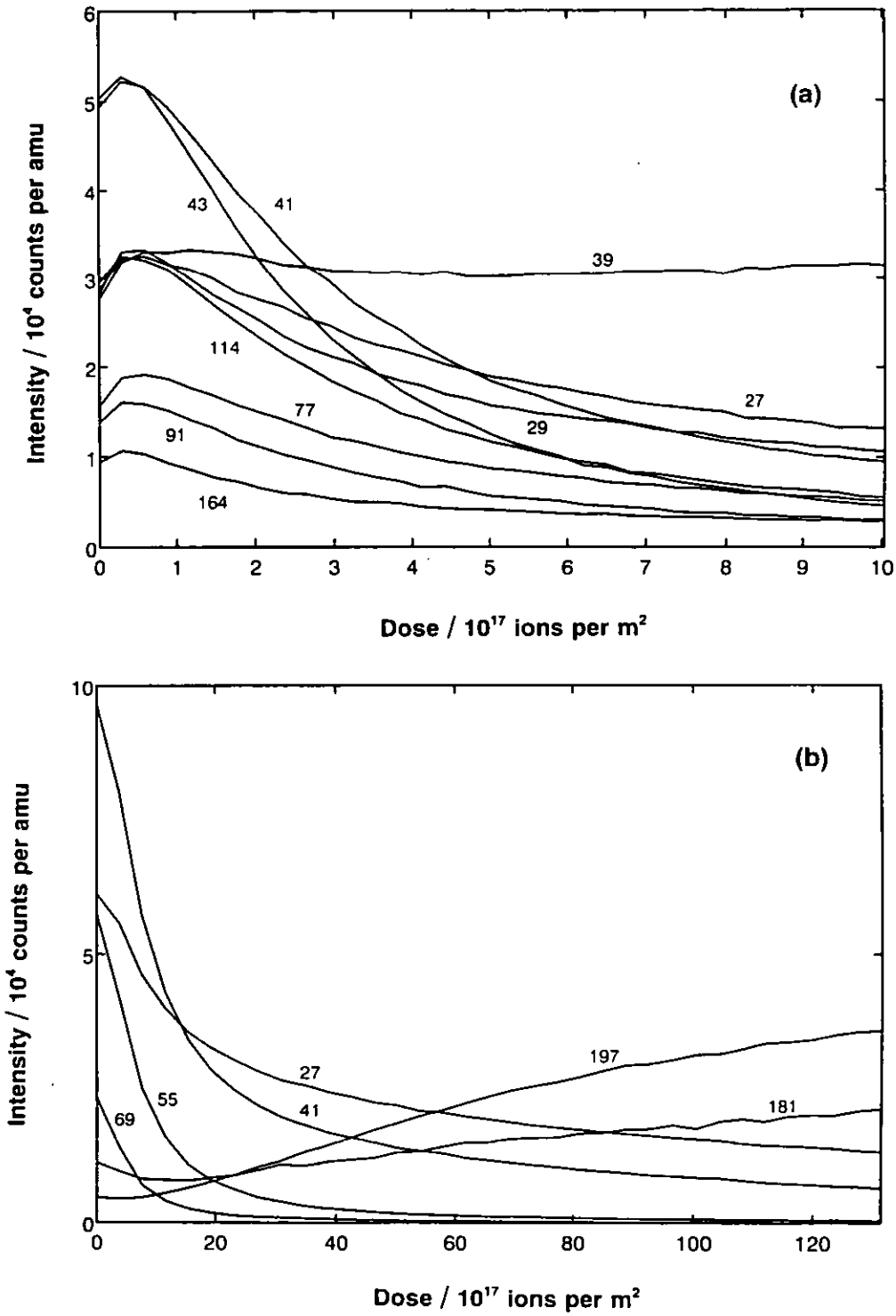

Fig 21 The effect of the dose of 4 keV argon ions on the peaks from the contaminated tantalum pentoxide, up to a dose of (a) 10.0×10^{17} and (b) 131×10^{17} 4 keV argon ions per m^2 of sample.

(4) Very large fragments are only seen if there is either no bond or only one major bond to the substrate.

(5) Static SIMS dose limits for 10% changes in intensity may be as low as 0.03×10^{17} ions/m^2 but depend strongly on the material and the fragment being studied. If the limit is defined for peaks which need extra damage for their appearance, the limit may be very small, however, if it is defined using clusters up to 300 amu *which decay and which are characteristic of undamaged material,* 0.1×10^{17} ions/m^2 may be used. As Delcorte et al[19] note, there is of course, no real "static" regime.

(6) A figure of merit factor, F, defined as the ratio of the absolute intensity of a given mass peak at zero dose divided by the fractional rate of change of that intensity with dose, is the best parameter to optimise the measurement conditions. This allows the highest signal for any given extent of damage to be obtained.

(7) Higher energy beams allow the damage zone, θ, to be increased so that larger fragments may be emitted in the primary impact before too much internal damage occurs to the fragment.

(8) Xenon appears to be two or more times as efficient as argon per unit of damage although this value varies from sample to sample.

(9) These conclusions do not apply to adsorbed layers on, for instance, a silver surface where the molecules are more weakly bonded to the substrate, and are all in the surface layer. Conclusions for these materials require the higher sensitivity of ToF mass analysis.

REFERENCES

(1) D Briggs, Surf. Interface Anal. **14**, 209 (1989).

(2) D Briggs and M J Hearn, Spectrochim Acta **40B**, 707 (1985).

(3) D Briggs and M J Hearn, Int. J. Mass Spec. Ion Proc. **67**, 47 (1985).

(4) D Briggs and M J Hearn, Surf. Interface Anal. **13**, 181 (1988).

(5) D Briggs, M J Hearn, I W Fletcher, A R Waugh and B J McIntosh, Surf. Interface Anal. **15**, 62 (1990).

(6) M J Hearn and D Briggs, Surf. Interface Anal. **17**, 421 (1991).

(7) D Briggs in *Practical Surface Analysis: Vol 2 - Ion and Neutral Spectroscopy*, Eds D Briggs and M P Seah, Wiley (Chichester), 1992, p367.

(8) A Benninghoven, J. Vac. Sci. Technol **A3**, 451 (1985).

(9) A Benninghoven, Surface Sci. **299/ 300**, 246 (1994).

(10) R D Short, A P Ameen, S T Jackson, D J Pawson, L O'Toole and A J Ward, Vacuum **44**, 1143 (1993).

(11) W J van Ooij and A Sabata, Surf. Interface Anal. **20**, 475 (1993).

(12) A Sabata, W J van Ooij and H K Yasuda, Surf. Interface Anal. **20**, 845 (1993).

(13) V A Brown, D A Barrett, P N Shaw, M C Davies, H J Ritchie, P Ross, A J Paul and J F Watts, Surf. Interface Anal. **21**, 263 (1994).

(14) D Briggs, A Brown and J C Vickerman, *Handbook of Static Secondary Ion Mass Spectrometry (SIMS)*, Wiley, Chichester (1989).

(15) J G Newman, B A Carlson, R S Michael, J F Moulder and T A Hohlt, *Static SIMS Handbook of Polymer Analysis*, Perkin Elmer, Eden Prairie MN (1991).

(16) D Briggs and M Hearn, Vacuum **36**, 1005 (1986).

(17) G J Leggett and J C Vickerman, Anal. Chem. **63**, 561 (1991).

(18) G J Leggett and J C Vickerman, Appl. Surface Sci. **55**, 105 (1992).

(19) A Delcorte, L T Weng and P Bertrand, Nucl. Ins. Meth. B **100**, 213 (1995).

(20) C P Hunt, C T H Stoddart and M P Seah, Surf. Interface anal. **3**, 157 (1981).

(21) I S Gilmore and M P Seah, Surf. Interface Anal. **23**, 1914 (1995).

(22) M J Hearn and D Briggs, Surf. Interface Anal. **11**, 198 (1988).

(23) G J Leggett and J C Vickerman, Int. J. Mass Spec. Ion Proc. **122**, 281 (1992).

(24) A Benninghoven in *Ion Formation from Organic Solids*, Ed A Benninghoven, Springer Series in Chemical Physics 25 (Springer, Berlin 1982) p65.

(25) A Benninghoven, Z Physik **230**, 403 (1970).

CHAPTER FIVE

Ion Detection Efficiency in SIMS: Energy, Mass and Composition Dependencies for Microchannel Plates used in Mass Spectrometries

1	INTRODUCTION	102
2	EXPERIMENTAL	105
3	RESULTS	107
3.1	EFFECT OF MCP GAIN VOLTAGE	107
3.2	EFFECT OF ION MASS, ENERGY AND COMPOSITION	111
4	CONCLUSIONS	122
REFERENCES		124

1 INTRODUCTION

Microchannel Plate Detectors (MCPs)[1] are used widely for ion detection in time-of-flight mass spectrometry. MCPs are compact, flat and have sub-nanosecond response times making them ideal for time-of-flight (TOF) applications. Channel Electron Multipliers (CEMs), which have been used for many years for both electron and ion detection, are not suitable for these systems. CEMs have conical entrance horns which, for ions of the same mass, would lead to a spread in arrival times across the detector, leading to a loss in mass resolution in a TOF analyser. However, the importance of the CEM in techniques such as Auger Electron Spectroscopy (AES) and X-ray Electron Spectroscopy (XPS) has led to a detailed understanding of the electron detection efficiency of CEMs[2-6] and hence of their optimal use in practice. Essentially, an MCP is an array of continuous channels, similar to those used in a CEM, but straight, so that much of the theoretical understanding for the CEM can be simply transferred. A recent study of the ion detection efficiency using CEMs[7,8] has shown that the established theories for electron detection are applicable, but with the first event replaced by he emission of electrons generated by the incident ions.

In mass spectrometry, the general relationship between the measured intensity, $I(c,m,E)$, and the true spectral intensity, $n(c,m,E)$, for a cluster, c, at a mass, m, and with energy, E, of those secondary ions which survive to the detector, is given approximately by;

$$I(c,m,E,E_D) = T(m,E)\ D(c,m,E_D)\ F(m,E)\ n(c,m,E) \qquad (1)$$

In this equation, $T(m,E)$ is the spectrometer transmission efficiency, $D(c,m,E_D)$ is the detector efficiency for ions impacting at energy E_D and $F(m,E)$ is the transfer characteristic of the electronic counting system. In Eq (1) we ignore any fragments arising from the decay of metastable ions. In the present work we study the term $D(c,m,E_D)$ for ions of masses up to 10,000 amu, for impact energies at the detector, E_D, between 0 and 20 keV and for clusters with a range of compositions.

The variation of $D(c,m,E_D)$ from one spectrometer to another, and also for one spectrometer with time, is a significant contribution to the poor reproducibility of spectra in static SIMS. In the past, these effects have been overshadowed by poor instrument repeatability, but now many instruments can achieve excellent repeatabilities of 2%[9] or better. A knowledge of the

behaviour of the term $D(c,m,E_D)$ is required to establish procedures which reduce the variations as much as possible. For some quantitative work, such as concentration measurement, spectral intensities need to be corrected using $D(c,m,E_D)$. Early studies by Rudat and Morisson[10] showed how the detection efficiency varied with atomic mass for single ions. They observed a periodic behaviour with broad maxima corresponding to F, K, Rb and Ba and minima at Mg, Ga, Cd and Pt, superimposed on a gradual decline in efficiency with mass, m, approximately as $m^{-0.1}$. The importance of mass spectrometry for elemental analysis has led to a detailed characterisation of detectors, particularly the discrete dynode types. However, these measurements are time consuming and so schemes are used to predict the behaviour from a restricted measurement set[11]. It would be much simpler for analysts if the detector gave unity efficiency, with no variations, in their required mass range.

The advent of time-of-flight mass analysers for SIMS, which are able to access a mass range up to 10,000 amu, has required an improved knowledge of the detection efficiency for large polyatomic ions. The detection efficiency of these heavy ions is low and sensitive to the precise operating conditions. Niehuis[12] used the electron yield measured for chromium clusters to estimate the effect of mass on detection efficiency for different values of the post-acceleration energy, E_D. This shows the efficiency falling away with mass. Hagenhoff[13] has used these curves to correct static SIMS spectra to improve the accuracy in the calculation of molecular weight distributions of PDMS oligomers. However, the detection efficiency is largely ignored in other static SIMS analyses.

Matrix Assisted Laser Desorption Ionisation (MALDI) has further increased the accessible mass range, providing ions with masses of 300,000 amu or more. The number of secondary electrons emitted by the detector surface at the initial impact is so low that the design of the detection system is critical. This has led to a number of studies of electron emission generated by large biological ions such as trypsin and albumin[14]. More recently, the interest in polyatomic primary ions for use in SIMS, and understanding the processes of ion emission, has led to more detailed studies of their secondary electron yields[20].

The ion induced electron emission yield is composed of two processes, potential and kinetic emission[21]. Potential emission occurs if the ionisation potential of the impact ion is greater than double the work function of the target. Following neutralisation of the incoming ion, the

excess energy liberates electrons via resonant Auger processes, providing a small constant yield as a function of energy[22]. Kinetic emission is caused directly by the interaction of the primary ion with target atoms as it moves through the material. A number of theories have been developed to account for the complex functionality of the emission yield. Some of these are reviewed in ref (21). One of the first models was that developed by Parilis and Kishinevski[23]. Here, the generation of secondary electrons is described by a complex mechanism involving the cross section for electron hole pair creation, in the valence or conduction bands, followed by an Auger recombination process. The cross section used has an implicit energy threshold for emission which is equivalent to an ion impact velocity, v, of approximately 6×10^4 m/s, dependent on the ion and target. The emission yield, γ, is calculated by integration over the attenuating electron path to the surface. A term is introduced called the "straight line threshold" velocity, v_o, which gives the intersection, on the velocity axis, of the extrapolated linear part of the γ dependence on v. This model predicts the functionality of the secondary electron emission yield, γ, to have three regions:

(i) $\gamma \propto v^4$ for velocities below v_o;
(ii) $\gamma \propto v^2$ for velocities at around v_o;
(iii) $\gamma \propto v$ for velocities above v_o.

This model has been shown to fit to data of Arivov and Rakhimov[24] for singly charged argon ions impacting a molybdenum target with velocities between 0.6×10^5 m/s to 1.2×10^5 m/s. However, Beuhler and Friedman[25] have found that this model does not fit well, with reasonable values of the parameters, for their work studying high molecular weight ions.

Beuhler and Friedman[25] have extended the concepts of Sternglass[26] for energies in the range to above 100 keV. In that model, the energy available for ionisation is proportional to the rate of energy loss, i.e. the sum of the nuclear and electronic stopping powers. Similarly to the theory of Parilis and Kishinevski, the emission yield is calculated by integration with the electron attenuation over the range of the ion. The nuclear stopping power they use is independent of the ion energy but the electron stopping power is proportional to ion velocity. At low velocity, where the range of the ion is within the secondary electron escape depth, the electron emission rises with a high power dependence on velocity. At high energies, the theory reduces to that of Sternglass, with the yield proportional to velocity. There is no velocity threshold in this model below which no emission occurs. This is in agreement with

recent sensitive experiments with large biomolecules at velocities below $1x10^4$ m/s. This model provide a good fit with data for H_2O clusters[27,28] extending up to masses of 50,000 amu. In this work[27], they find that the electron emission yield produced by polyatomic ions on a copper target is simply the sum of the yields from the constituent atoms. Additivity was found to be obeyed for clusters with velocities below $1x10^5$ m/s. However, for an insulating target, Al_2O_3, the yield was less than the summed yield. An empirical relationship between the electron emission yield and mass, for a given impact velocity, has shown the electron emission yield to exhibit a power dependent on the ion mass. The index of this power has been found in a number of studies[16,18,20] to be approximately 0.7.

2 EXPERIMENTAL

The instrument used in this study, a CAMECA TOF SIMS IV, is of an open structure, single stage reflectron design[29]. The instrument is equipped with a high resolution Ga^+ focused liquid metal ion gun with an energy range between 12 keV and 25 keV, mounted at 45° to the sample surface normal. The equipment is described in more detail in ref (30). In the present study, 15 keV gallium primary ions were digitally rastered with a 128 by 128 array over an area of 200 μm by 200 μm on the surface using a pulsed beam current of 0.5 pA. The time between each primary ion pulse was set to 300 μs, giving a mass range up to 3900 amu. Each spectrum was acquired for 60s giving a total ion surface dose of $5x10^{15}$ ions/m^2. To ensure the ion dose was uniform over the entire raster area, the spot size was defocused to be greater than 3 μm. Spectra were acquired from a fresh area of a square array for each condition. The centre to centre separation of the array was 700 μm and all of the analysis areas were at least 2.5 mm from the edge of the holder aperture.

The material analysed in this study is a thin polystyrene (PS) film, with a molecular weight of 2500, deposited on etched silver. Samples were prepared from a 1mg/ml toluene solution using the procedure developed for the preparation of Irganox 1010 used in an inter-laboratory study[9]. This method provided an evenly coated substrate which gave a good repeatability from area to area.

The ion detector arrangement for this system is shown in Fig 1. A single MCP is located after the last post-acceleration electrode. The surface is electrically connected to the final post-

acceleration electrode at a detector post acceleration voltage, V_D, which defines the impact energy, E_D. The MCP gain voltage across the channel plate, V_C, is variable between 0 and 1000 V. Following amplification by the cascades in the microchannels, the emitted plume of electrons is accelerated by nearly 10 kV to a scintillator with a thin surface film of aluminium. The resulting flashes of light are reflected by a mirror to a photomultiplier situated externally to the vacuum system. The advantage of using a method involving light is that it decouples the sensitive counting electronics from the high voltages present in the detector. This allows the use of accelerating voltages, for both positive and negative ions, to generate impact energies between 0 and 20 keV. This system can give shorter dead times than those which capacitatively decouple the high voltage.

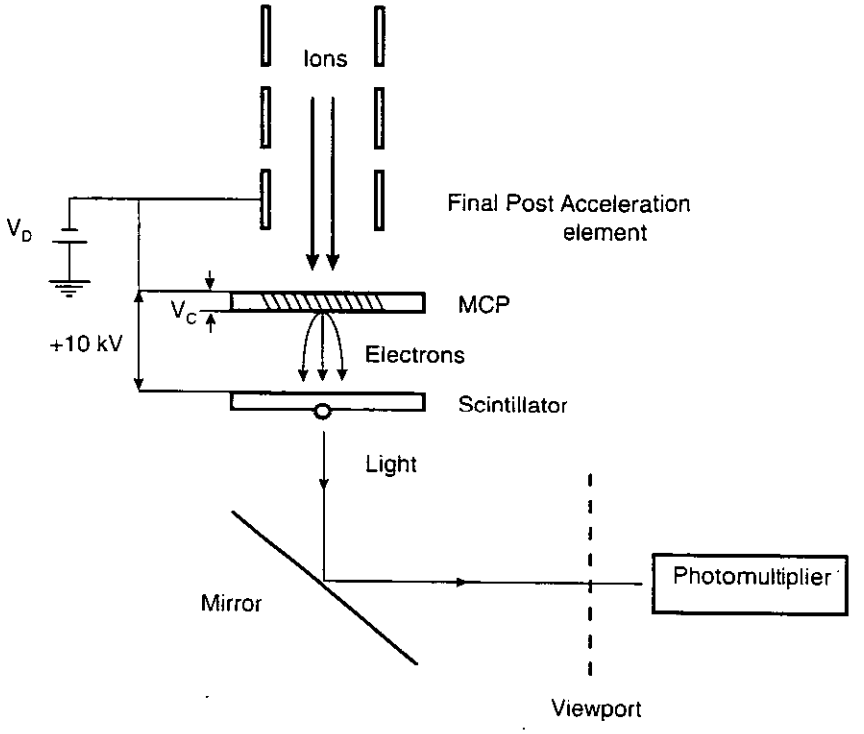

Fig 1 Schematic of the ion detection system used in this TOF SIMS spectrometer.

The MCP used in this study, supplied by Galileo, has an active area with diameter 18mm, channel size of 10 μm, a channel centre to channel centre spacing of 12 μm and a channel length to diameter ratio of 40:1. Each channel is inclined at an angle of 5 degrees to the surface normal to maximise the electron yield for the incoming particle. The detection efficiency is limited to the fractional area presented by the channel, known as the open area ratio. For this MCP the open area ratio is determined as 54.5%. In the rest of this work the efficiencies analysed only relate to this open area.

3 RESULTS

3.1 EFFECT OF MCP GAIN VOLTAGE

For an electron amplification cascade to develop along a microchannel, enough energy must be gained by emitted secondary electrons, so that the yield in the next event is sufficiently high to maintain the cascade. The gain[1,2], G, of an MCP with a secondary electron yield, δ, is simply given by

$$G = \delta_1 \delta^p \qquad (2)$$

where δ_1 is the ion-induced electron yield of the first event followed by p electron induced events. Of course, p is not a unique value for each event but is a statistical average. The secondary electron yield from the channel surface, δ, maximises at an energy above 400 eV. This energy is provided by a potential difference V_C applied across the front and rear faces of the MCP. The semi-conducting surface of the channel acts as a continuous dynode with the potential becoming more positive towards the end of the channel. For this MCP, the applied MCP gain voltage V_C is about 1000 V. The exact value of V_C will depend on the aspect ratio of the channels and so varies from one design to another. If m is approximately 10, δ is in a range where, approximately $\delta \propto V_C$, since the electron energies only reach some 100 eV for each impact in the amplification down a channel. As the applied voltage is increased further the gain rises to a plateau, probably due to depletion of the channel wall current at the output end of the device.

The positive ion SIMS spectrum of PS for low and high values of the MCP gain voltage, V_C, are shown in Fig 2. At a V_C value of 650 V, the high mass cationised PS oligomer distribution is only weak. The full distribution is revealed at the higher voltage. The effect of V_C on the detection efficiency for ions of different mass is shown in Fig 3. Efficiencies rise steeply before reaching a plateau, as expected. The voltage necessary to reach the plateau increases with mass. It is evident that relative ion intensities along the mass scale will vary sensitively with the value of V_C. A method is therefore required to allow users to set the MCP gain voltage to give a known efficiency and reduce spectrum variability. A very simple procedure, developed by Seah[31] for CEMs, may be applied here. The transition voltage, V_T which gives 50% of the plateau efficiency may be quickly and accurately determined, because

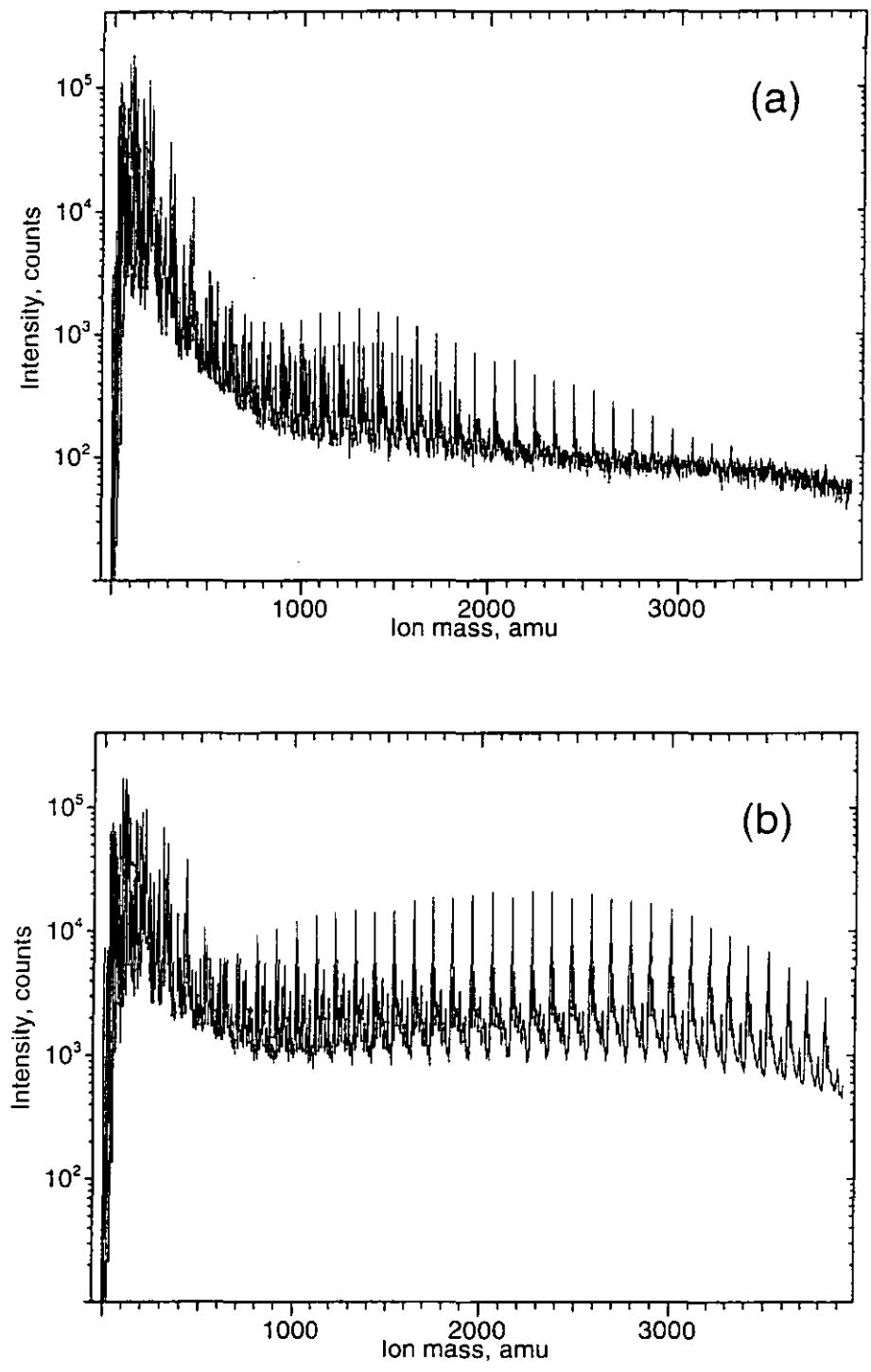

Fig 2 Positive ion SIMS spectra of Ag cationised PS oligomers at 20 kV post-acceleration voltage with detector voltages, V_C, of (a) 650 V and (b) 950 V.

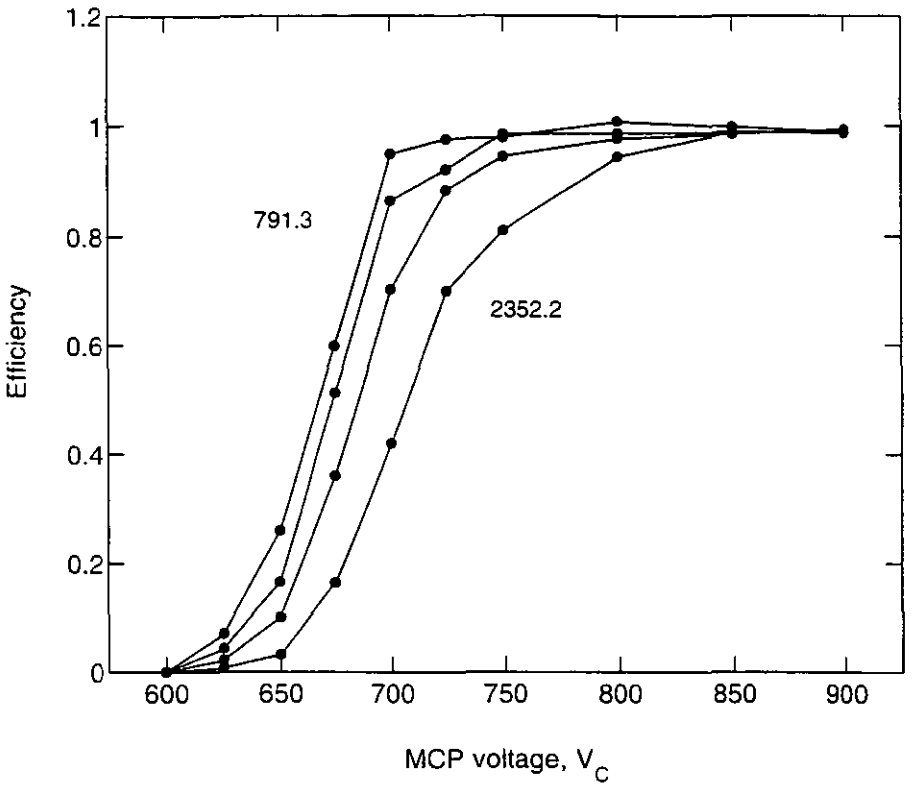

Fig 3 Effect of MCP gain voltage, V_C, on the detection efficiency of cationised PS oligomers with masses 791.3, 1103.5, 1519.8 and 2352.2.

of the steep efficiency gradient. The effect of ion mass on V_T for cationised polystyrene oligomers is shown in Fig 4. The higher voltage, V_N, required to increase the detection efficiency to 98% together with the values of V_T are shown in Fig 5. Straight line fits to these data give the necessary increase in voltage. The operating voltage, V_C, is now defined as a factor of 1.3 more than (V_N-V_T), for safety, in addition to V_T, such that

$$V_C = V_T + 29.1 + 0.0572\, m \qquad (3)$$

where m is the ion mass and V is in volts. To prevent damage and to reduce aging, the detector should not be operated at too high a voltage, so Eq (3) is limited to a maximum of 950 volts. To ensure that the efficiency is at least 98%, the MCP gain voltage should be set for the highest mass ion in the required mass range. As the MCP ages, the value of V_T, for a given mass, will increase and so the operating voltage should be calibrated at regular intervals and monitored using a control chart. The use of V_T allows one to do this with great precision so that the need to replace the MCP can be predicted in advance. For the remainder of this study V_C was set at 875 volts which gives approximately unity detection efficiency for all measured masses at ion impact energies of 20 keV.

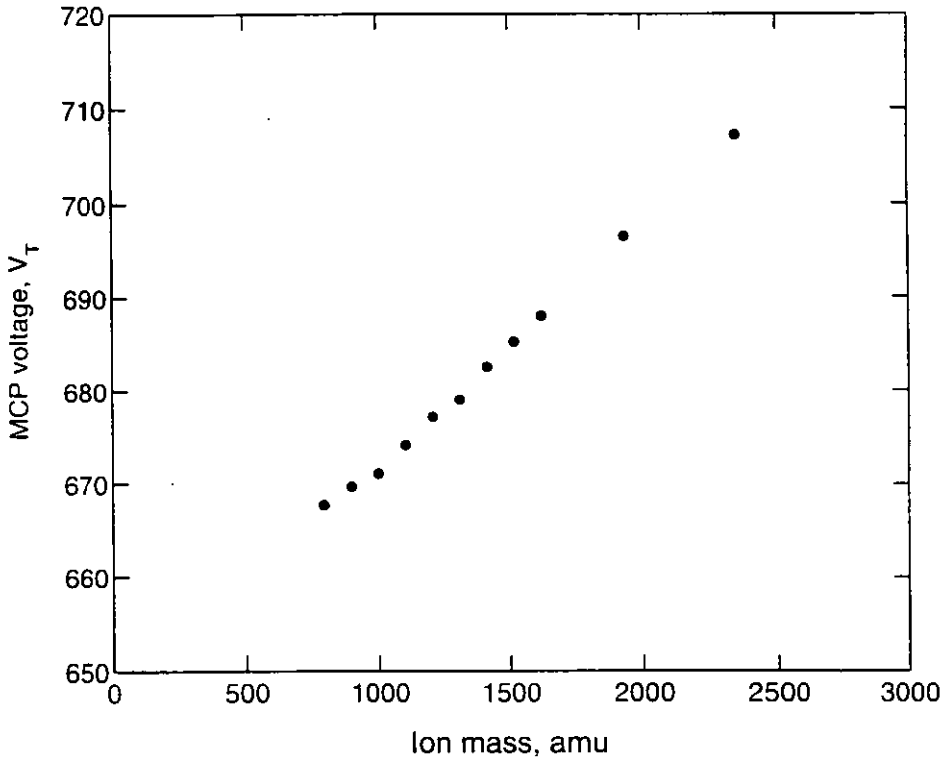

Fig 4 MCP transition voltage, V_T, required to give 50% of the plateau detection efficiency.

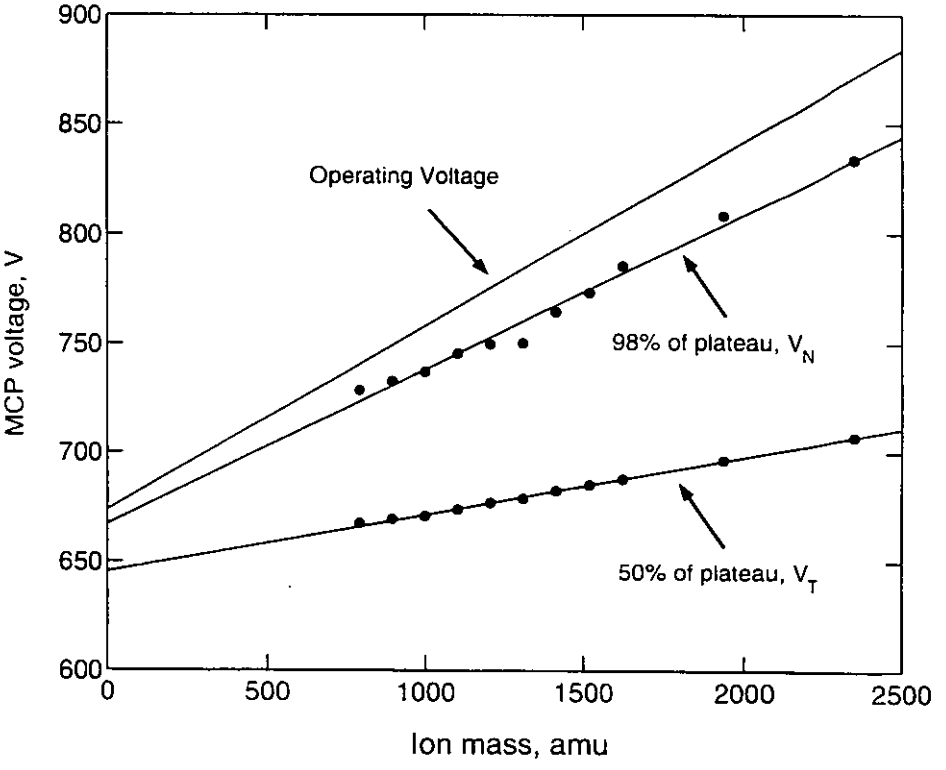

Fig 5 MCP operating voltage, V_C, together with V_T and V_N.

3.2 EFFECT OF ION MASS, ENERGY AND COMPOSITION

The positive ion static SIMS spectra from PS samples are shown in Fig 6(a) and (b) for detector post-acceleration voltages, V_D, of 2 kV and 20 kV. Whilst the low mass regions of 0-300 amu are similar, the intensities of the cationised PS oligomers are reduced by nearly two orders of magnitude for the lower energy. The effect of ion impact energy on the detection efficiencies for oligomers ranging in mass from 791.3 to 2352.2, are shown in Fig 7(a). The data are replotted in Fig 7(b) for the ion impact velocity. With this detector system it is not possible to measure the secondary ion current with a picoammeter for each mass in order to calculate an absolute efficiency. The currents are simply too small. Instead, the data have been normalised to unity efficiency at 20 keV. At energies greater than 15 keV, the peak intensities are relatively constant with impact energy. The families of curves in Fig 7 show how rapidly the detector efficiency falls as the ion impact energy is reduced or the mass is increased. Additionally, for a given ion impact velocity, the efficiency and consequently the yield is greater for the larger molecules than for the smaller ones.

Using a detector post-acceleration voltage, V_D, of 20 kV, it is only possible to extend the normalisation method, mentioned above, so far up the mass scale. Eventually, at a high enough mass, there will be no plateau in the energy range available. To analyse this effect, we fit a model to the data using a function to describe the ion-induced secondary electron yield and our knowledge of the behaviour of a continuous dynode detector.

Whilst the models, discussed earlier, for kinetic electron emission have provided much insight into the mechanisms of emission, they have limited applicability at the low velocities used in this study. Instead, we use a simple function in terms of velocity, v, with three independent variables, a scaling item A, the usual "straight line threshold" velocity v_0 and a power n, such that

$$\gamma = A\, v \left(1 - \left(\frac{1}{1 + (v/v_0)^n} \right)^{1/n} \right) \qquad (4)$$

At high velocities, this function reduces to the linear function of velocity as predicted by the theory of Sternglass. This function gives excellent fits to the data of Brunelle et al[15] for large

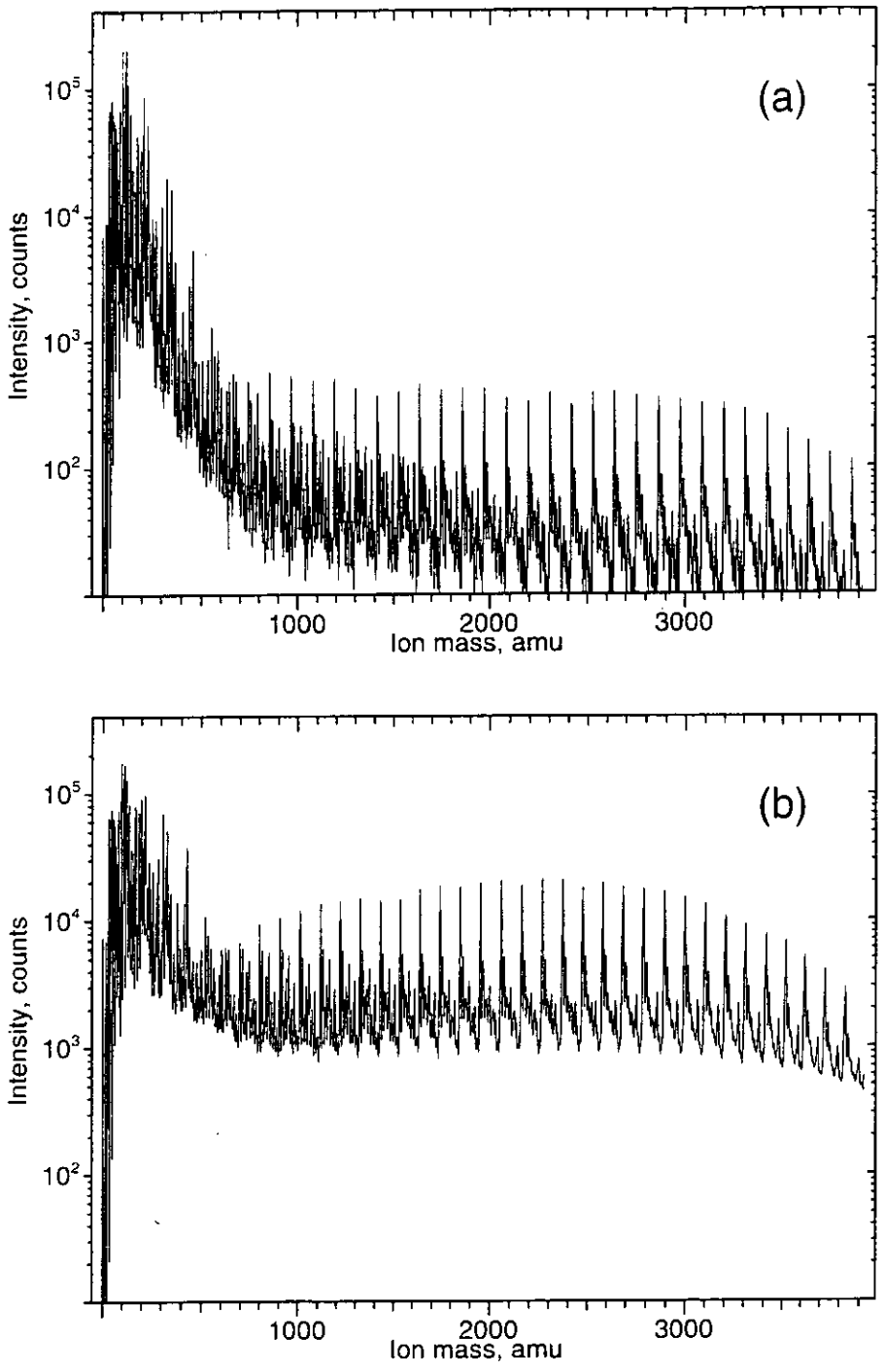

Fig 6 Positive ion SIMS spectra of Ag cationised PS (MW 2,500) with detector post-acceleration voltages of (a) 2 kV and (b) 20 kV.

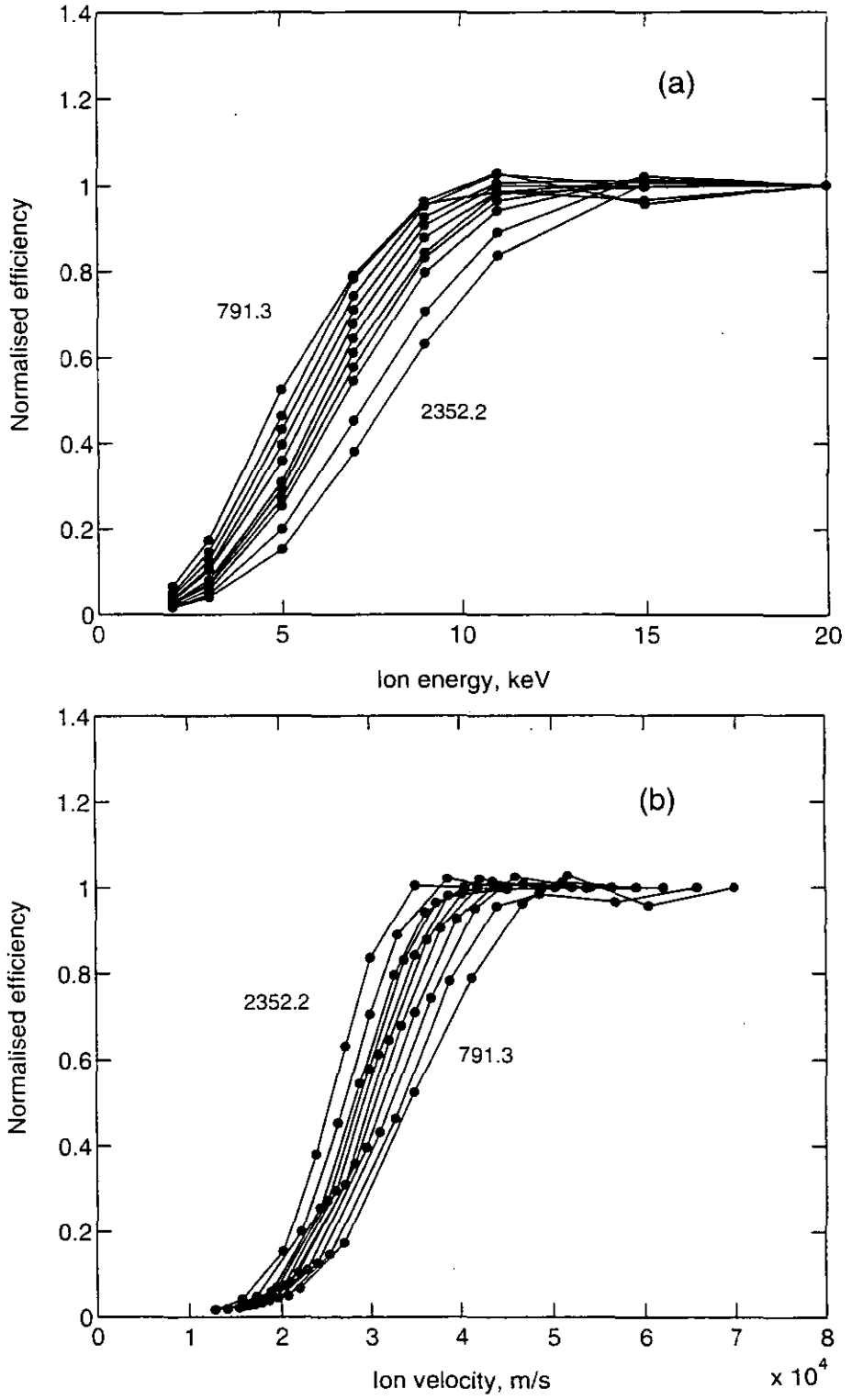

Fig 7 Normalised secondary ion intensities for cationised PS oligomers, with repeat units from 6 to 21 corresponding to masses between 791.3 and 2352.2, plotted against (a) ion impact energy and (b) ion impact velocity. The masses for the outer curves are shown.

organic molecules of bovine trypsin (MW 23, 295 amu) on a CsI surface with values for n and v_0 of 3.4 and 1.98 x 10^5 m/s respectively and also to the data of Hofer[32] for vanadium clusters incident on gold with values for n and v_0 of 4.7 and 1.71 x 10^5 m/s respectively. It also describes the general behaviour of Parilis and Kishinevski's model[23] and does not have the arbitrary change in behaviour, between each of the three regions of velocity dependence, often used in approximations to this model.

The theory for the efficiency of CEM detectors for electrons is already well established[2-6]. The emission of secondary electrons at each stage in the dynode has a Poissonian probability distribution. Therefore, at each stage in the amplification there is a finite possibility that the cascade will die. The detector efficiency is then calculated by summing the losses at each stage using Eq (6) of ref (2). This may be evaluated provided that the values for the secondary electron yield are known at each stage. In our system, the first emission stage is induced by ions and γ is given by Eq (1). The value of γ for subsequent stages depends on the potential difference along the dynode. Seah[2] found a value of 2 was acceptable and this value is used here.

In our model, we will assume that the yield for a polyatomic ion is simply the sum of the constituent yields, i.e. additivity is obeyed. For our series of cationised PS oligomers, where the composition of H and C is approximately constant, the yield is proportional to the number of repeat units and consequently the mass. The effect of the silver cation is always less than 1% of the composition and so is ignored here. We therefore replace the general scaling term A with a coefficient a multiplied with the ion mass. To evaluate the detector efficiency, the three independent variables a, v_0 and n of Eq (4) are required. These are found in the following way. Firstly, an approximate value for v_0 may be obtained from a survey of the literature. Table 1 gives the values of v_0 for a range of ion and target combinations, including polyatomic ions, from data over the last four decades. Notwithstanding the variety of experiments, the values are reasonably consistent with an average value, excluding the deuterium data, of 5.4 x 10^4 m/s. With this value as a first estimate of v_0 the variables a and n determined by fitting using a computer algorithm, to the efficiency curves of Fig 7 for each ion. The algorithm starts with trial values of 1 x 10^{-4} and 3.5, respectively, for the two parameters and calculates γ for each ion energy. This value is then input to the model by Seah[2] as the first emission event, which then gives an efficiency at each energy. The fitting minimisation proceeds using the least squares of the residuals. Excellent fits are found but

the values of the variables are rather scattered as they are correlated. As the mass of each oligomer is increased we are simply adding another unit of C_8H_8 and so the coefficient, a, would, therefore, be expected to remain constant. Values of a equal to 2 x 10^{-6} m/s and n equal to 4.9 are then taken as the average of the fitted values. Finally, the fitting is made with only one scaling parameter v_0. The fits and data for four of the ions are shown in Fig 8. The fitted results using Eq (4) are clearly excellent. Figure 9 shows values of v_0, which exhibit clear systematics with ion mass. The solid line in Fig 9 is a power law function fit with an index of -0.13.

Table 1 Values of v_0 found from a survey of the literature (in chronological order)

Impact ion	Target	v_0 10^4 m/s	Reference
Ar	Mo	10.7	24
Ne	Cu-Be	6.15	33
Ar		5.38	
C_7H_{16}	Cu	4.0	25
D	Ag	25.0	34
V	Stainless Steel	4.38	35
Nb		3.44	
$(H_2O)_n$ [n=320 to 3311]	Cu	4.14	27
$(H_2O)_n$ [n=320]	Cu	4.59	28
Xe	Au	8.49	36
$C_{16}F_{31}$	-	2.75	12

The systematic power law dependence of v_0 enables the detector efficiency for PS oligomers to be calculated for any mass and for any detector post-acceleration voltage. Figure 10 shows a family of such curves together with the data points and Fig 11 shows the deduced values of γ for two ions. The curves of efficiency fit the data excellently. Most modern TOF SSIMS spectrometers have a detector post-acceleration voltage of 10 kV. For this condition, beyond a mass of 1000 amu, the detector efficiency rolls off, falling to 80% at 2000 amu, 50% efficiency at 4000 amu and for ions of 10,000 amu has only 20% efficiency. In contrast, with a detector post-acceleration voltage of 20 kV the efficiency remains at unity to 4000 amu, slowly declining to 80% efficiency at 10,000 amu. By using a detector post-acceleration voltage of 20 kV, the relative spectral intensities are less sensitive to the precise instrument conditions used and have near unity detection efficiency. Many older TOF spectrometers

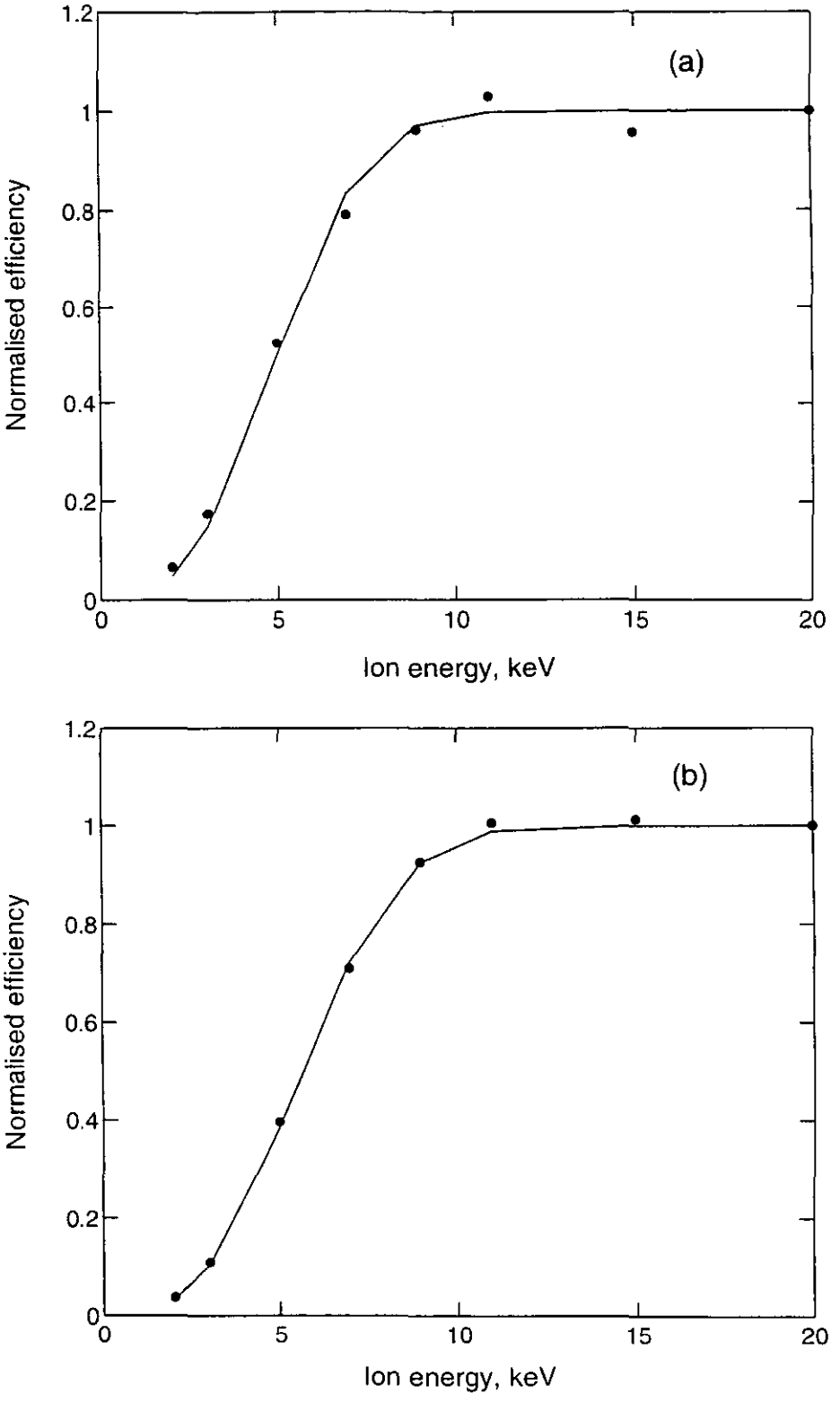

Fig 8 Fits to detection efficiency against ion energy (solid line) together with data values (●) for ion masses (a) 791.3, (b) 1103.5, (c) 1519.8 and (d) 2352.2.

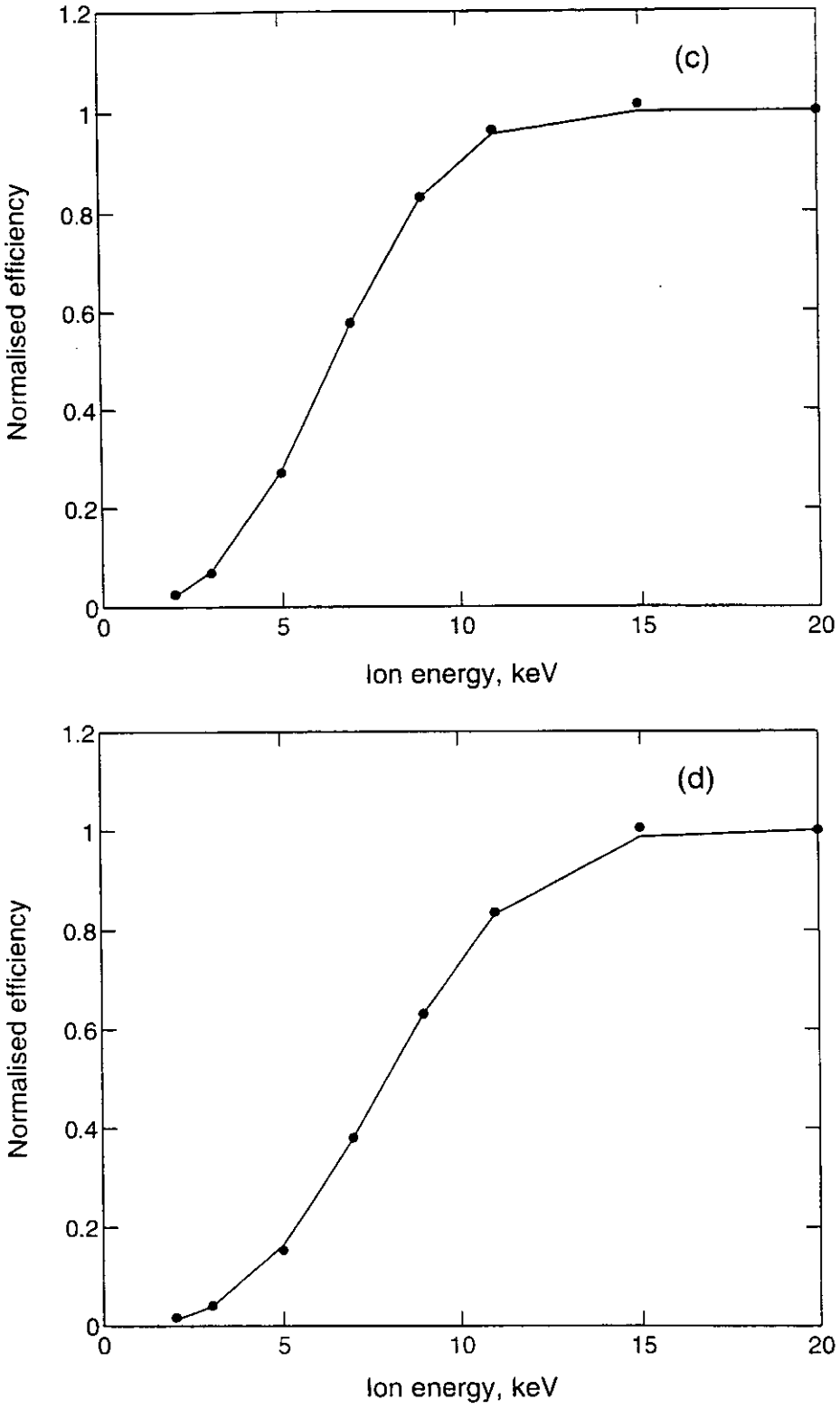

Fig 8 Fits to detection efficiency against ion energy (solid line) together with data values (●) for ion masses (a) 791.3, (b) 1103.5, (c) 1519.8 and (d) 2352.2.

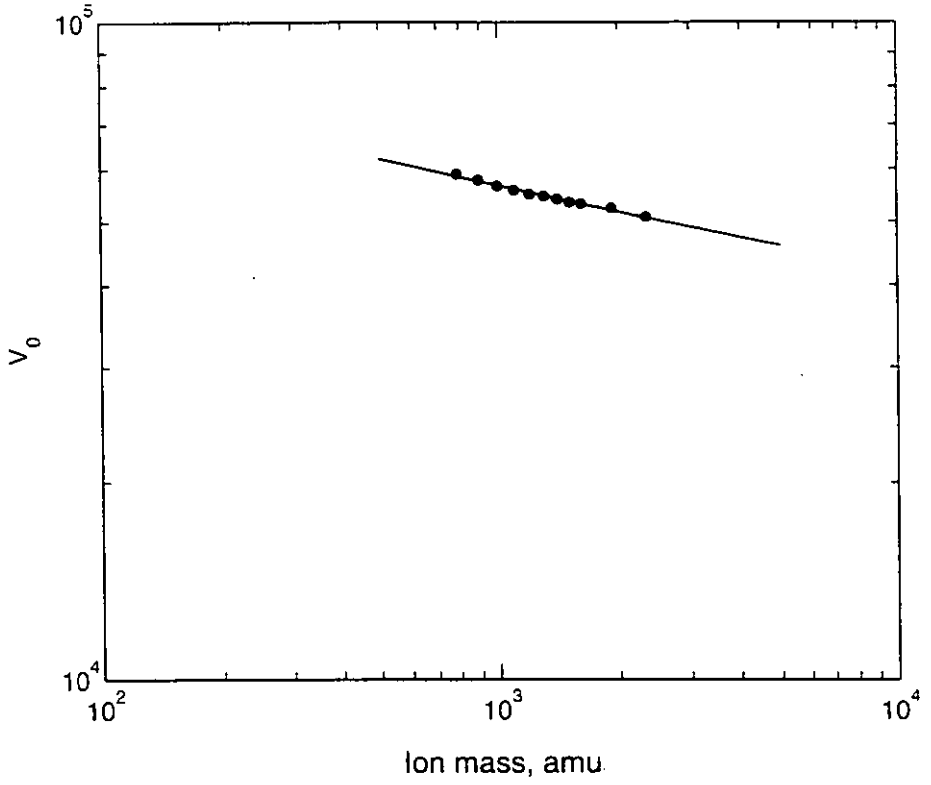

Fig 9 Values of the fitted velocity threshold v_0 against mass. The solid line is a power law fit to the data points.

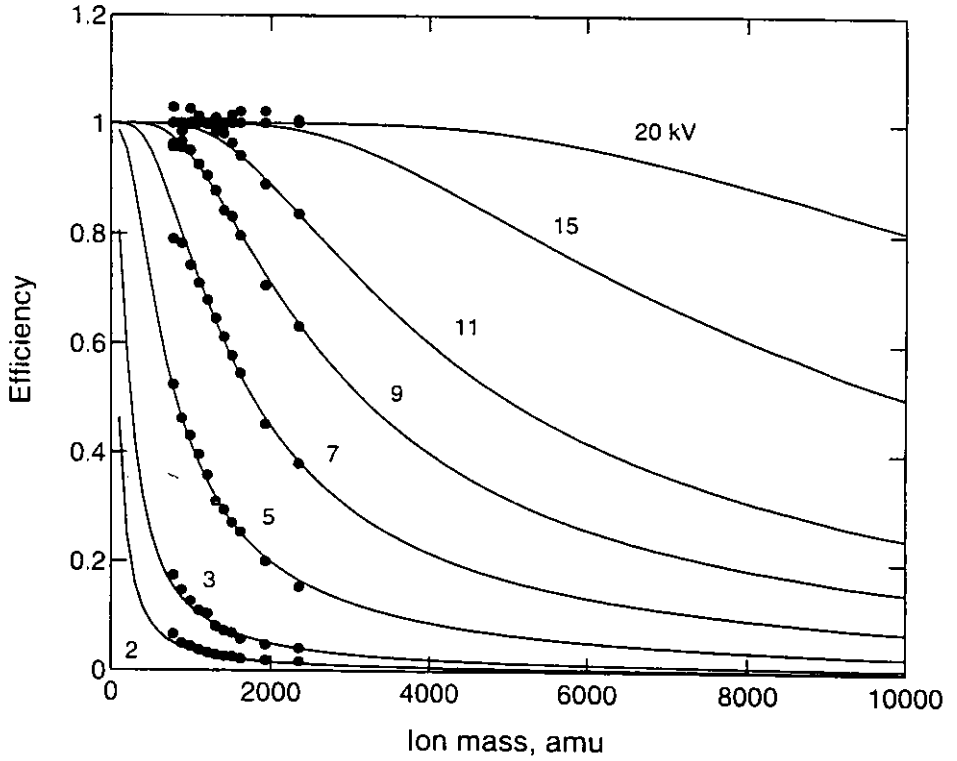

Fig 10 Calculated PS oligomer detection efficiency curves, for the different ion impact energies shown, together with measured values (●).

have a detector post-acceleration voltage of only 5 kV. In that case, the efficiency is already as low as 20% at 2000 amu. Quadrupole mass analysers using CEMs often use detector post-acceleration voltages as low as 3 kV. In that case, detector efficiencies fall rapidly with mass for masses above 100 amu. In comparisons of the transmission between quadrupole and time-of-flight mass analysers, this effect is generally not included and will add to the inherent differences of the mass spectrometers.

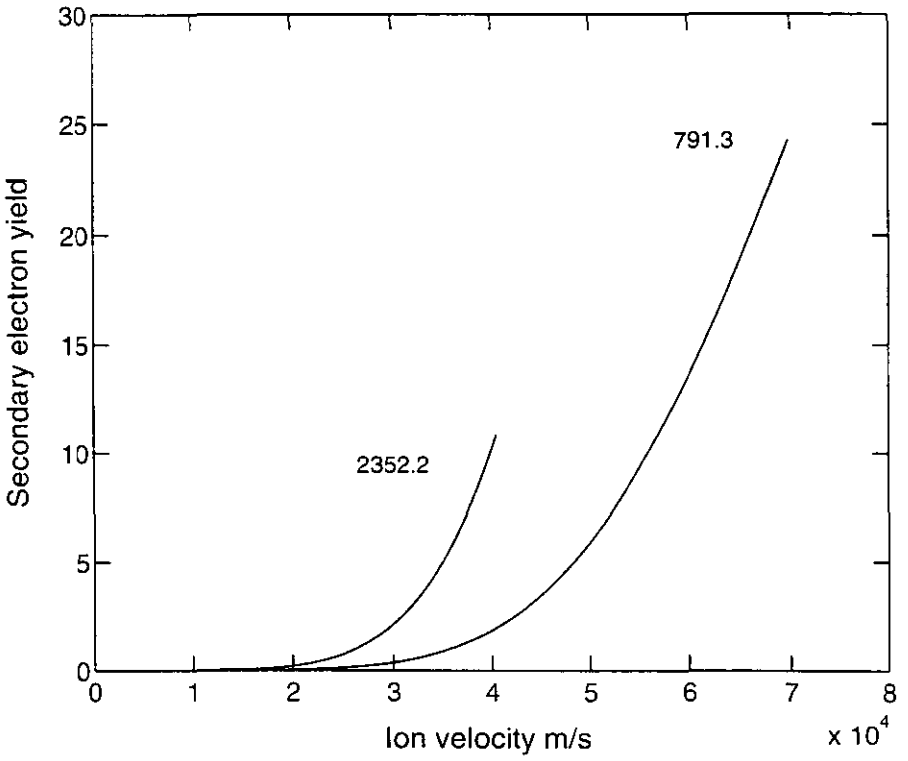

Fig 11 Secondary electron yield, γ, deduced from the fits of detection efficiency in Figs 8(a) and (d).

What we see in Fig 10 is the effect of δ_1 in Eq (2). As the fragment mass (number of constituent atoms) increases, the total secondary electron yield falls and the proportion of failed cascades increases. Thus, the efficiency falls. The reduction in yield has a secondary effect in that the successful cascades have a proportion with a slightly smaller pulse height distribution. This pulse height distribution thus also falls as the fragment mass (number of constituent atoms) increases and, this needs to be countered by an increase in the MCP gain voltage, V_C, as shown in Fig 5. If V_C is below the value set by Eq (3), the fall in efficiency in plots like Fig 10 becomes even more severe as the mass increases.

The efficiency curves are similar to those calculated by Niehuis[12] using Cr clusters which show a drop to an efficiency of 42% at mass 7488. This is somewhat lower than calculated

here. A cluster at this mass has 144 Cr atoms and the equivalent PS oligomer here would have one Ag, 568 C and 563 H atoms. In both cases, the impact velocity is the same for each component atom. Hydrogen has a rather small total stopping power and so its contribution to the overall electron emission will be small.

It is clear that the overall emission will depend on the composition of the ion. If the emission yield for C is greater than $\frac{144}{568}$ that of Cr, the detection efficiency would be higher. The curves shown in Fig 10 for PS would, in the more general case for any fragments, be bands which depend on the fragment composition. We study this behaviour below. The extent of these bands can be estimated by calculating the contribution to the total yield from each atomic species. Here we use Beuhler and Friedman's[25] model, based on the total stopping power, to calculate the electron emission yield for different atomic number ions relative to carbon. A cluster with a mass of 4000 amu and an energy of 10 keV impacts the detector at a velocity of 2.2×10^4 m/s. Each constituent atom has the same velocity. The electron yields are evaluated for elemental ions at this velocity impacting a target with an average atomic number of 20 and a secondary electron transport length of 1.04 nm[25]. The calculated secondary electron yields relative to C for H, N, O, Cr and Ag ions are 0.017, 1.321, 1.670, 11.123 and 29.952, respectively. Secondary electron yields may now be estimated, by summation of the component yields, for ions from four archetypal materials of different compositions; a chromium cluster, cationised polystyrene oligomers, a biological material based on Adenine and Thymine, and a saturated hydrocarbon. These ions have the following compositions of Cr_{77}, Ag $C_{300}H_{295}$, $C_{153}H_{168}O_{31}N_{107}$ and $C_{286}H_{572}$, respectively. Electron yields relative to the PS oligomers are then 2.56, 1, 1.04 and 0.88 for the chromium cluster, PS oligomer, biomaterial and hydrocarbon. These factors may be used to scale the term, A, in Eq (4), assuming that the relative scalings are approximately independent of velocity. Figure 12(a) shows a band covering the curves of Fig 10 recalculated for these different ion compositions. Each shaded area covers all 4 materials but is always limited by chromium cluster ions at the top of the band and saturated hydrocarbons at the bottom.

For analysts working with a wide range of compositions, the variation in detector efficiency with composition is surprisingly large. Using a detector post-acceleration voltage of 20 kV or above reduces this significantly, so that for ions below 4000 amu the efficiency is effectively unity. Figure 12(b) shows the case for an analyst whose work is generally

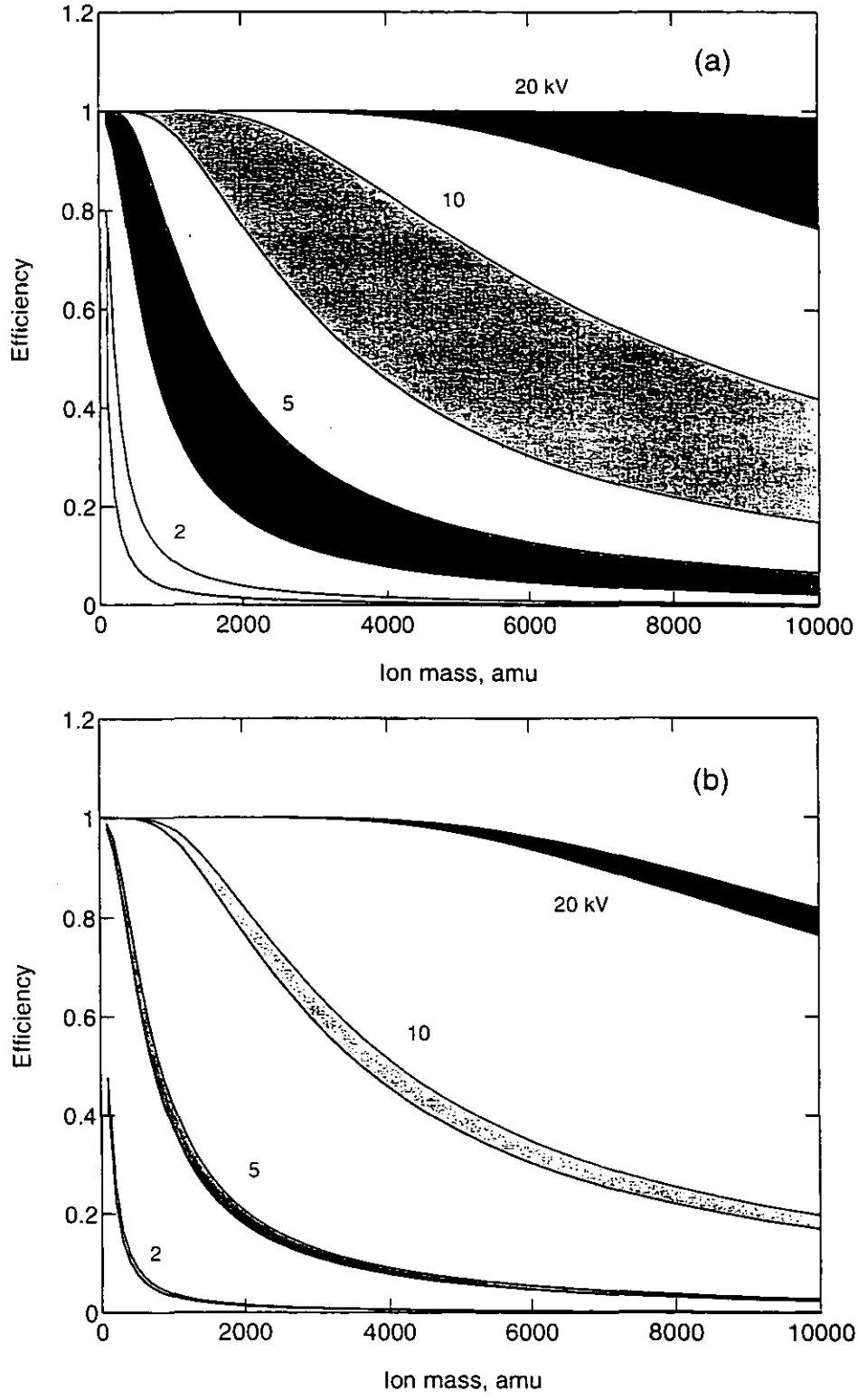

Fig 12 Estimated detection efficiency ranges of different ion compositions for detector post-acceleration voltages, V_D, of 2, 5, 10 and 20 kV for (a) chromium cluster ions and organics and (b) organics only.

restricted to organic ions. The limit at the top of each shaded area is now that deduced for the bio-material and at the bottom, again, for hydrocarbons. The variation with composition is now much smaller. These lower detection efficiencies arise from the higher hydrogen contents of the ions. To improve the detector efficiency for heavy ions and to reduce the variability from differing compositions, it is recommended that analysts use the highest value of detector post-acceleration voltage available to them.

We now return to the data and predictions for polystyrene. It is useful to know, for a given mass, what value of detector post-acceleration voltage is necessary to achieve a specified detector efficiency. Figure 13 shows such curves calculated from our model for PS oligomers. To work with a detection efficiency of 99% for ions of up to 10,000 amu requires a detector post-acceleration voltage of 35 kV. Such high voltages are not normally available in SIMS instrumentation. Many are limited to 10 kV and for these an efficiency of 99% is only achievable up to 850 amu.

The effect of detector ageing is an added effect of practical importance and may also be calculated using this model. Figure 14 shows, for the PS oligomer data of Fig 10, what happens as the detector ages and the secondary electron yield of the first event falls to half its original value. The original data are shown by a solid line and the aged data by the dashed line. This will lead to a relative loss of high mass intensity compared with low masses. The variations are more pronounced for lower values of detector post-acceleration voltage. For all purposes it is clear that high values of detector post-acceleration voltage are best.

4 CONCLUSIONS

The detection efficiency of a microchannel plate (MCP) for high mass cationised PS oligomer ions has been measured. The effect of the ion impact energy, between 0 and 20 keV, at the front of the MCP is studied and a model is developed based on a function to describe the ion induced electron emission and a general theory for CEMs[2]. For polyatomic ions, this function uses the additive nature of electron yields from the individual component atoms. Values of the "straight line threshold" velocity, v_0, are found to have a weak power law dependence on mass with an index of -0.13.

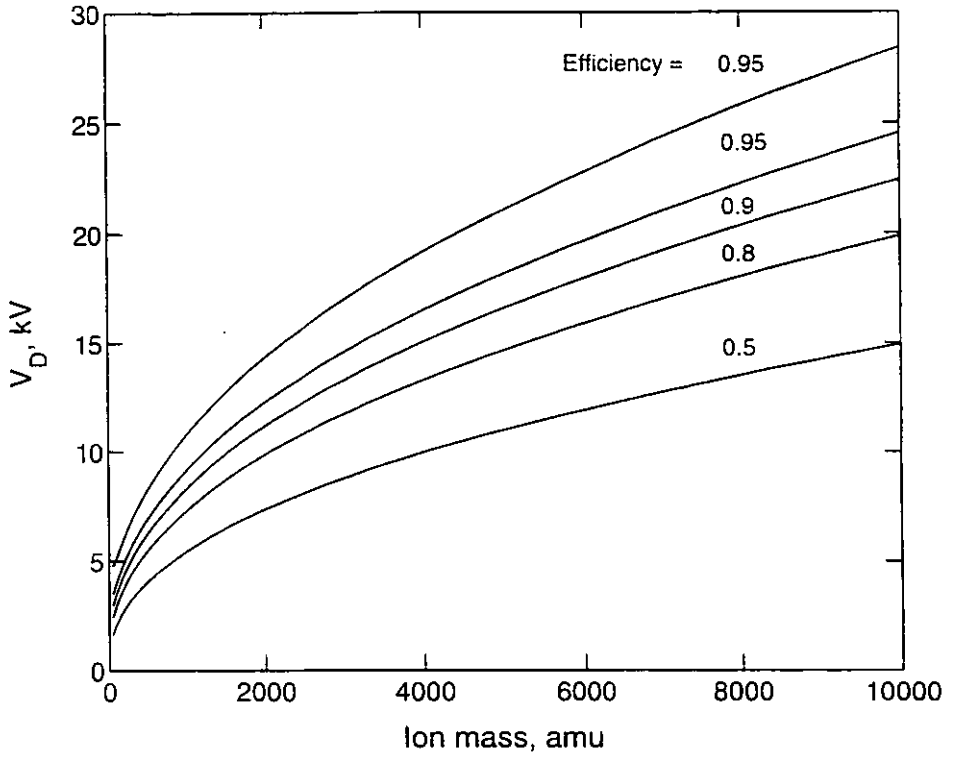

Fig 13 Value of detector post-acceleration voltage, V_D, required to attain detector efficiencies of 0.5, 0.8, 0.9, 0.95 and 0.99.

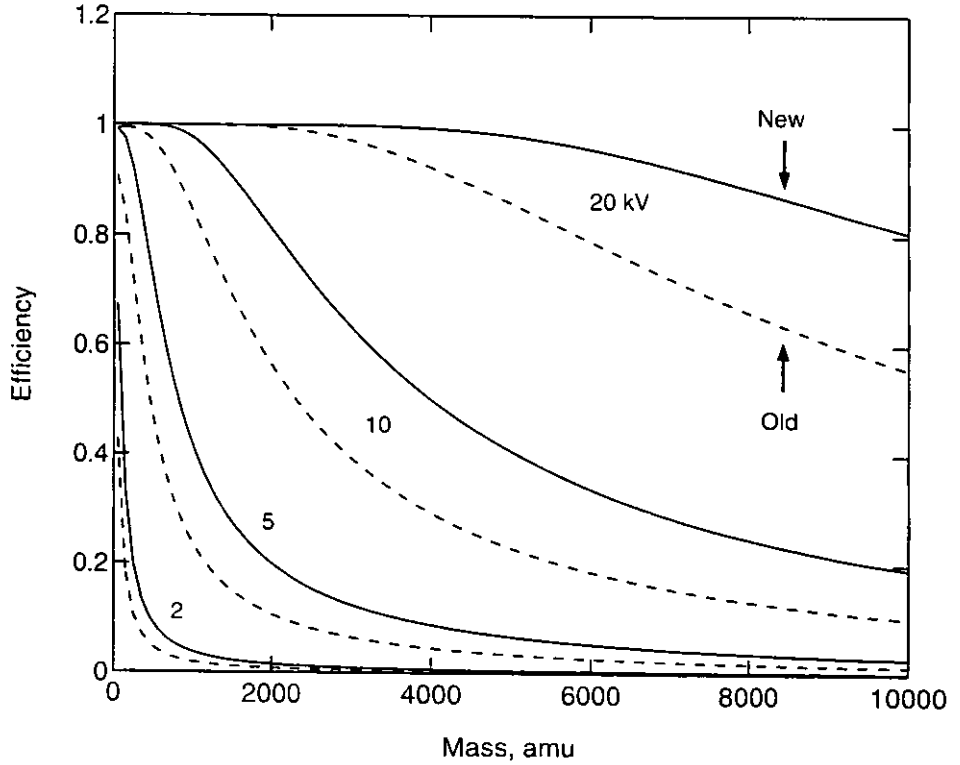

Fig 14 Detection efficiencies calculated for a new (_____) and aged (- - -) detector for post-acceleration voltages, V_D, of 2, 5, 10 and 20 kV.

The model is an excellent description of the data and shows how the efficiency falls away as the mass increases or the ion impact energy reduces. At a mass of 10,000 amu, the detection efficiency for 20 keV ions is 80%, falling to 25% for 10 keV ions. In a time-of-flight spectrometer the ion impact energy is controlled by the detector post-acceleration voltage, V_D. If this is set to 20 kV, approximately unity detection efficiency may be achieved for masses up to 4000 amu.

Estimates of the variation in detection efficiency with ion composition have been calculated for compositions ranging from hydrocarbons through biomaterials to elemental clusters. It is found that the effect of composition is strong. For low energy ion impacts, the spread in efficiency may be more than 100% of the mean efficiency. This effect reduces as the ion impact energy is increased. At an energy of 20 keV, the detection efficiency remains near unity for all clusters with masses of up to 4000 amu.

A method of setting the MCP gain voltage regularly, using an accurate and simple procedure is given. Here, the voltage at half the plateau intensity, V_T, may be quickly determined for the highest mass ion to be analysed. The MCP gain voltage should then be set to a voltage in excess of V_T, given by Eq (3), to give the best efficiency.

REFERENCES

(1) J. Ladislas Wiza, Nucl. Instr. And Methods B, **162**, 587 (1979).

(2) M P Seah, J. Electron Spectrosc., **50**, 137 (1990).

(3) M P Seah, C S Lim and K L Tong, J. Electron Spectrosc., **48**, 209 (1989).

(4) M P Seah and G C Smith, Rev. Sci. Instrum., **62**, 62 (1991).

(5) M P Seah and M Tosa, Surf. Interface Anal., **18**, 240 (1996).

(6) M P Seah, Surf. Interface Anal., **23**, 729 (1995).

(7) I S Gilmore and M P Seah, NPL Report CMMT(A)87 (1998).

(8) I S Gilmore and M P Seah, Appl. Surf. Sci. **144-145**, 113 (1999).

(9) I S Gilmore and M P Seah. In *SIMS XI*, Gillen G, Lareau R, Bennet J, Stevie F (eds). John Wiley: Chichester, 1998; 999.

(10) M A Rudat and G H Morrison, Int. J. Mass Spectrom. Ion Processes, **27**, 249 (1978).

(11) R Hinton, private communication (1997).

(12) E Niehuis, Doctoral thesis, Münster (1988).

(13) B Hagenhoff, A Benninghoven, H Barthel and W Zoller, Anal. Chem. **63**, 2466 (1991).

(14) A Brunelle, P Chaurand, S Della-Negra, Y Le Beyec and G B Baptisce, Int. J. Mass Spectrom. Ion Processes, **126**, 65 (1993).

(15) A Brunelle, P Chaurand, S Della-Negra, Y Le Beyec and E Parlis, Rapid Commun. Mass Spec. **11**, 353 (1997).

(16) V Tan Nguyen, K Wien, Nucl. Instr. and Methods B, **145**, 332 (1998).

(17) J Mootens, W Ens, K G Standing and A Verentchikov, Rapid Commun. In Mass Spec. **6**, 147 (1992).

(18) G Westmacott, W Ens, K G Standing, Nucl. Instr. and Methods B, **108**, 282 (1996).

(19) A Hedin, P Håkansson and B U R Sundquist, Int. J. Mass Spectrom. Ion Processes, **75**, 275 (1987).

(20) Y Le Beyec, Int. J. Mass Spectrom. Ion Processes, **174**, 107 (1998).

(21) K H Krebs, Fortschritte der Physik, **16**, 419 (1968).

(22) R A Baragcola, E V Alonso, J Ferron and A Oliva-Flino, Surf. Sci., **90**, 240 (1979).

(23) E S Parilis and L M Kishinevski, Soviet Phys.-Solid State, **3**, 885 (1960).

(24) U A Arifov and R R Rakhimov, Isv. Akad. Nauk SSSR, Ser. Fiz. Mat. **6** 49 (1958).

(25) R J Beuhler and L Friedman, J. Appl. Phys., **48**, 3928 (1977).

(26) E J Sternglass, Phys. Rev., **108**, 1 (1957).

(27) R J Beuhler and L Friedman, Nucl. Instr. and Methods B, **170**, 309 (1980).

(28) R J Beuhler, J. Appl. Phys., **54**, 4118 (1983).

(29) J. Schwietes, H-G Crammer, T Heller, U Jürgens, E Niehuis, J Zehnphenning and A Benninghoven, J. Vac. Sci. Technol., **A9**, 2864 (1991).

(30) I S Gilmore and M P Seah, to be published.

(31) M P Seah, The VAM Bulletin, **10**, 23 (1993).

(32) W O Hofer, Scanning Microscopy Supplement, **4**, 265 (1990).

(33) B L Schram, A J H Boerboom, W Kleine and J Kistemaker, Physica, **32**, 749 (1966).

(34) R A Baragiola, E V Alonso and A Oliva Florio, Phys. Rev. B, **19**, 121 (1979).

(35) F Thum, W O Hofer, Surf. Sci., **90**, 331 (1979).

(36) E V Alonso, M Alurralde and R A Baragiola, Surf. Sci., **166**, L155 (1986)

CHAPTER SIX

A Conductive Reference Material for the Evaluation of Instrument Response Functions for static SIMS

1	INTRODUCTION	128
2	PREPARATION OF REFERENCE MATERIAL	128
2.1	PREPARATION OF IRGANOX SOLUTION.	130
2.2	ETCHING THE SILVER.	130
2.3	DEPOSITION OF IRGANOX ON SILVER.	131
3	STATIC SIMS RESULTS	131
4	CONCLUSIONS	136
REFERENCES		137

1 INTRODUCTION

In chapters 3 and 4 we have seen that PTFE and PET are excellent reference materials for static SIMS. They are both insulators, which for some spectrometers can cause severe problems with charge control. For an inter-laboratory study, a conductive material is required to complement the others to assess the performance of charge control. Here we describe the procedure to prepare a conductive reference material for the evaluation of instrument response functions for static SIMS. The reference material comprises an ultra-thin layer of Irganox 1010, an anti-oxidant additive used in the plastics industry, on an etched silver substrate. Previously, conductive samples such as silicon and tantalum pentoxide have been considered. Unfortunately they need cleaning and so have to be sputtered to an equilibrium condition before reproducible static SIMS spectra can be acquired. Many static SIMS instruments are not designed to operate in this way and this leads to poor reproducibility[1]. The Irganox is deposited as a thin film which is sufficiently conductive not to cause charging problems. The surface of the Irganox samples is unreactive compared to metallic samples and can be analysed as received with no need to sputter to equilibrium.

Irganox is not a polymer but a large molecule with a carbon atom at the centre of four complex functional groups, with a nominal mass of 291, giving an overall molecular mass of 1176 amu. The structural formula of the Irganox molecule and the molecular dynamics representation are shown in Figs 1(a) and (b), respectively. The molecule is likely to lie on the silver surface so that the functional group perpendicular to the surface is only attached by one bond to the central carbon atom and will have a strong SIMS intensity[2]. Additionally, cationisation of the molecule with silver ions from the substrate allows whole molecules to detach under ion bombardment giving ions at very high mass in the SIMS spectrum, which is required to evaluate the instrument response function.

2 PREPARATION OF REFERENCE MATERIAL

The preparation of Irganox films for Static SIMS analysis requires a very clean working practice. To reduce surface contamination, clean glassware, tweezers and powderless gloves must be used. The equipment required is very simple, a 1 ml glass pipette, a 2 ml adjustable volume pipette filler (supplied by Volac) and a drying frame, which is a piece of copper sheet

bent to give a slope of 30° to the vertical, on which the samples rest to dry. The reference material is prepared in three stages which are described in order below.

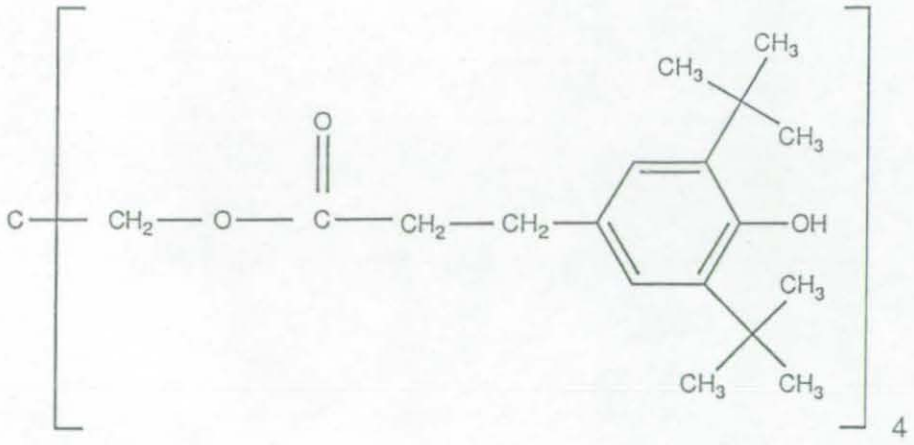

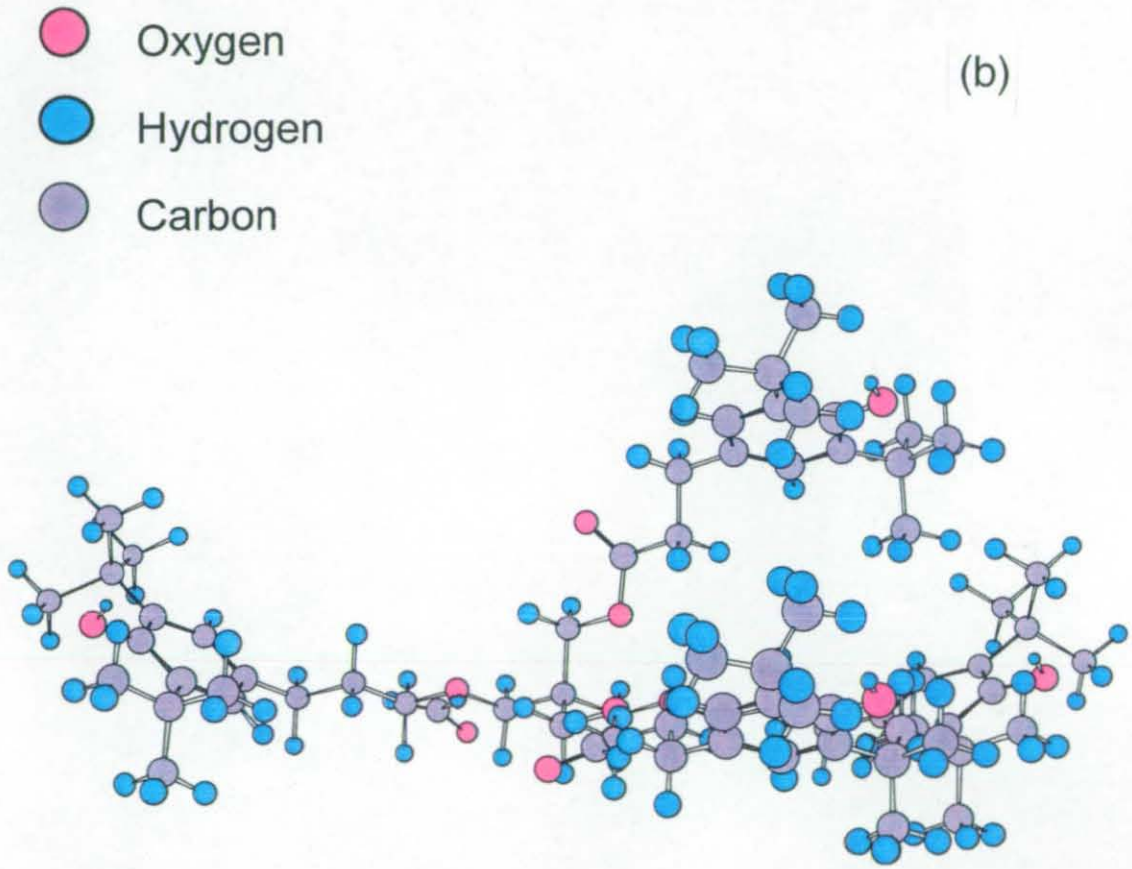

Fig 1 The structure of the Irganox 1010 molecule (a) structural formula, (b) molecular dynamics representation.

2.1 PREPARATION OF IRGANOX SOLUTION.

The Irganox, sample code SDP, was supplied by UMIST. It is non-hazardous. A solution of Irganox in chloroform (1 mg / ml) is prepared by weighing out 0.1 g of Irganox on a clean piece of aluminium foil. The Irganox is then introduced to a 100 ml, glass stoppered, measuring flask and chloroform, of Analytical Reagent quality, is added up to the 100 ml level line. The flask was then shaken to mix the Irganox. Chloroform is carcinogenic and appropriate safety precautions should be taken, such as using a fume cupboard.

2.2 ETCHING THE SILVER.

The silver must be etched before the Irganox layer is deposited to help the Irganox solution spread evenly over the surface. The silver foil used is of 99.97% purity, has a thickness of 0.125 mm and is supplied by Advent Research Materials Ltd. A piece measuring 105 mm by 80 mm is cut from the silver sheet. A 2 mm diameter hole is punched half way along the shortest edge. This hole allows the sheet to be suspended by a gold wire in a glass beaker for cleaning and etching. The silver is now immersed in a 2% solution of "micro" cleaning fluid[3] and distilled water. This process removes the oxide, exposing the silver surface. After ultrasonic agitation for five minutes the material is immersed in distilled water and ultrasonic agitation applied for a further five minutes. The silver is now removed and submerged in a solution of 20% by volume nitric acid (HNO_3) for ten minutes. Bubbles will begin to develop on the surface of the silver as the acid begins to etch, and so every two minutes the silver sheet should be given a sharp tap on one edge with a pair of clean tweezers to release these bubbles.

After etching, the silver is raised from the acid and flushed by pouring distilled water over both surfaces. The wet silver is then held with the lower edge touching a filter paper to remove excess water, whilst being dried by hot air from a sample dryer.

The dry, etched silver sheet is cut into four pieces of 52.5 mm by 40 mm. Two of the pieces will have half a hole in one corner. The silver is now ready to be coated with Irganox, which should be done without delay.

2.3 DEPOSITION OF IRGANOX ON SILVER.

The following is the procedure developed for depositing the Irganox. A fresh piece of Whatman filter paper 541 is attached to the drying frame with two paper clips. An etched piece of silver is then rested against the slope, with the long edge along the bottom. Shake the flask of Irganox. Depress the button on the pipette and dip the pipette tip into the Irganox solution, release the button to draw in 1 ml of the solution. Hold the pipette at about 30 degrees to the horizontal, with the tip pointing down. Press down the slow release lever and sweep the tip along the top edge of the silver back and forth until the flow comes to an end (there may be about .05 ml of solution left in the tip). Allow the sample to dry, it should dry evenly leaving only one narrow drying stain of around 1 mm width along the bottom of the sample. When the filter paper has dried, turn the sample upside down and repeat the covering process. The coated silver should now be cut into seven 7.5 mm by 40 mm strips and each strip placed in a clean glass bottle with an aluminium covered stopper.

3 STATIC SIMS RESULTS

The positive and negative static SIMS spectra of the reference material using a quadrupole instrument are shown in Figs 2(a) and (b) with a total dose of 3.2×10^{16} ions/m^2. The positive ion spectrum shows strong intensities extending over a large mass range. The repeatability of the Irganox sample was determined from the statistical scatter of Nij[4], (see Eq(7) of chapter 3) for the major peaks. A summary of these results is given in Table 1. The percentage scatter for the peaks at mass 57, 107, 203, 219, 259, 385 and 453 amu are 2.9, 9.8, 2.2, 3.4, 5.9, 3.8 and 7.5%, respectively, with an average scatter of 5.1%. Much of this scatter is due to the silver ion at mass 107, since the bare area of silver may be variable, and the fragments at mass 385 and 453 which are of low intensities. If these peaks are removed the average scatter reduces to the excellent value of 2.1%. The negative ion spectrum shown in Fig 2 (b) is not very detailed in the low mass range offered by the quadrupole spectrometer and is of a low signal intensity at high mass. Time-of-Flight (TOF) instruments with larger mass ranges and higher sensitivity can detect large fragments, as shown in Figs 3(a) and (b) for positive and negative ions.

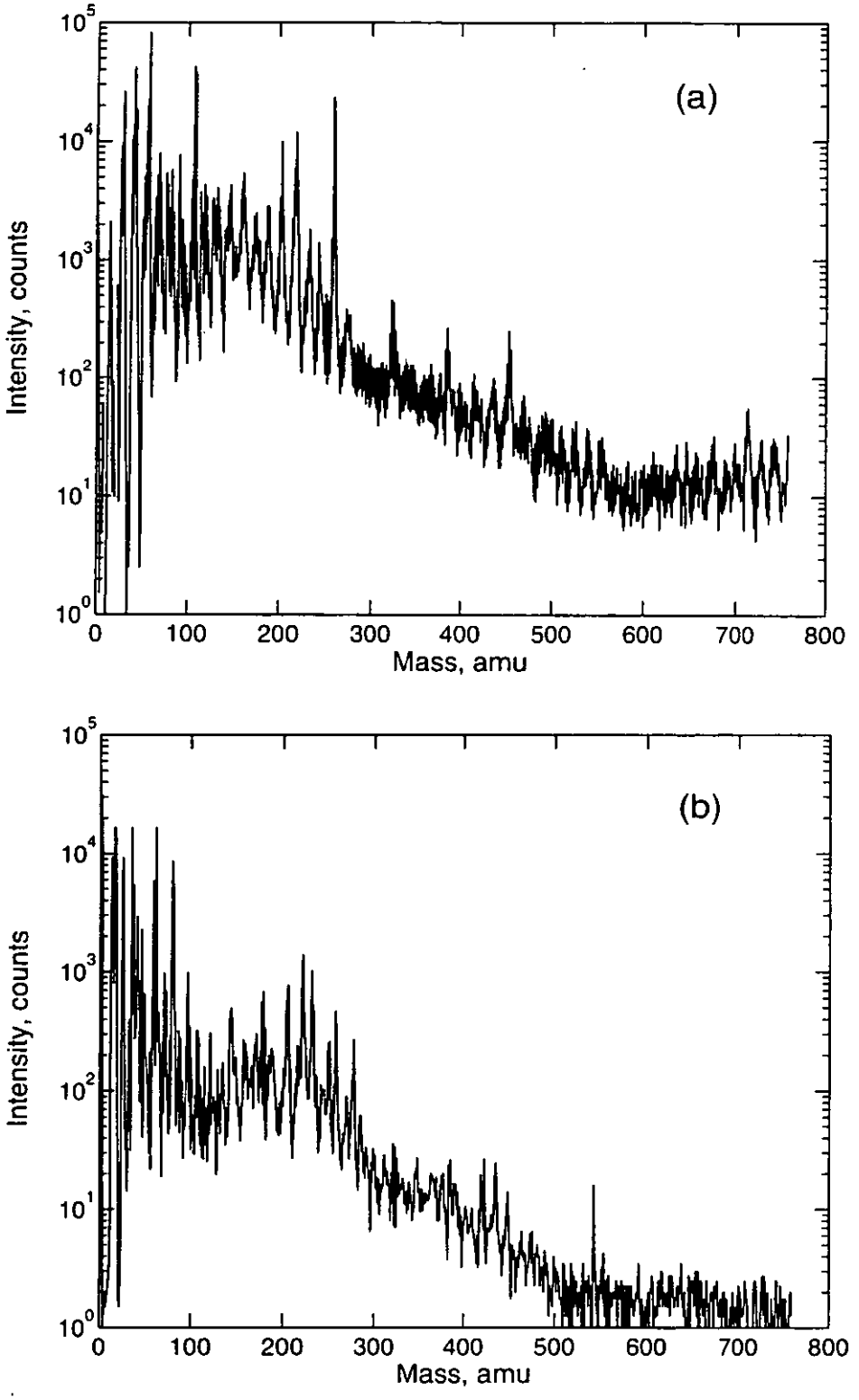

Fig 2 Quadrupole static SIMS spectra of Irganox reference material using 4 keV argon ions (a) positive ions, (b) negative ions.

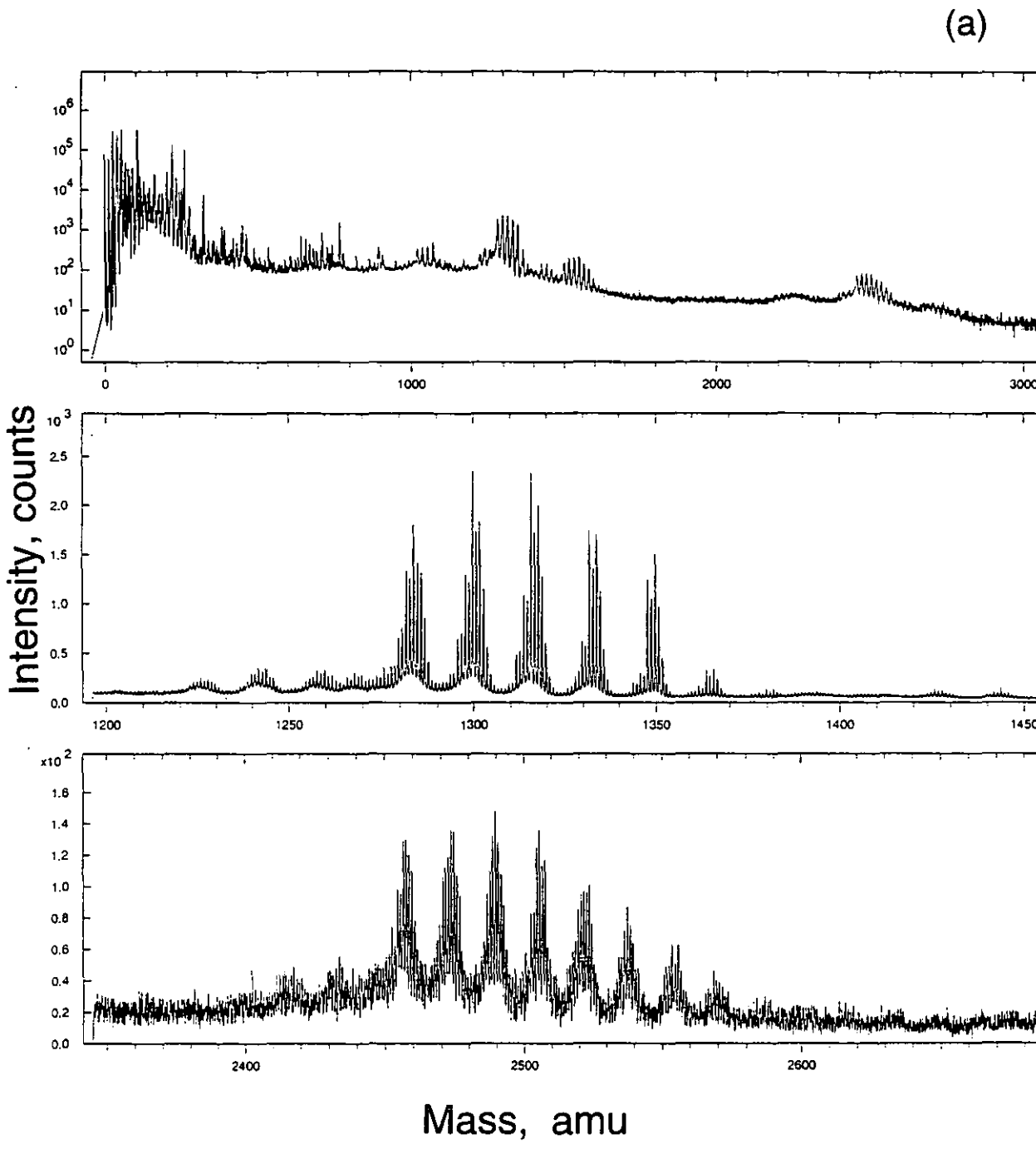

Fig 3 Time-of-Flight (TOF) static SIMS spectra of Irganox reference material with details on linear scales (a) positive ions, (b) negative ions.

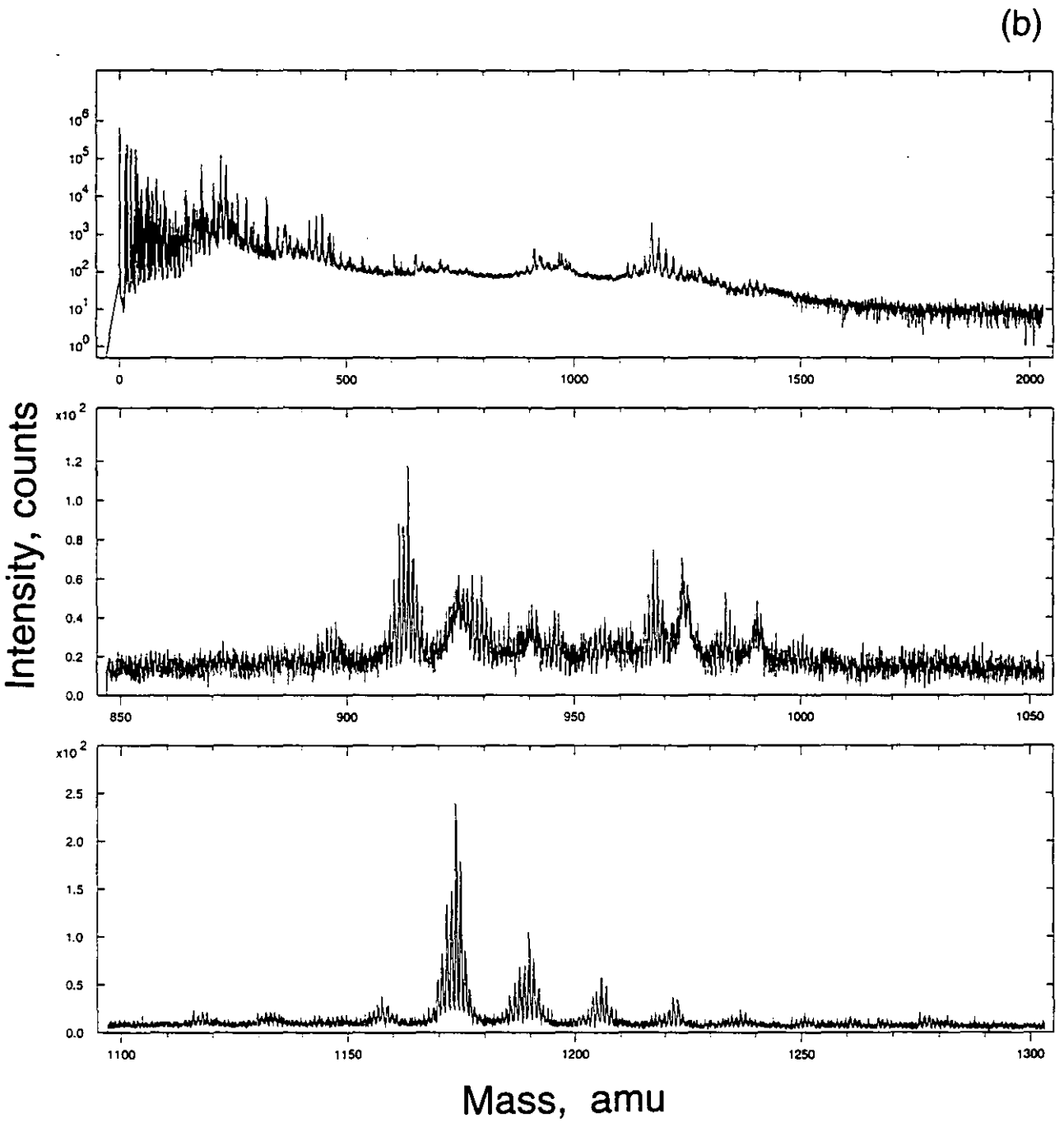

Fig 3 Time-of-Flight (TOF) static SIMS spectra of Irganox reference material with details on linear scales (a) positive ions, (b) negative ions.

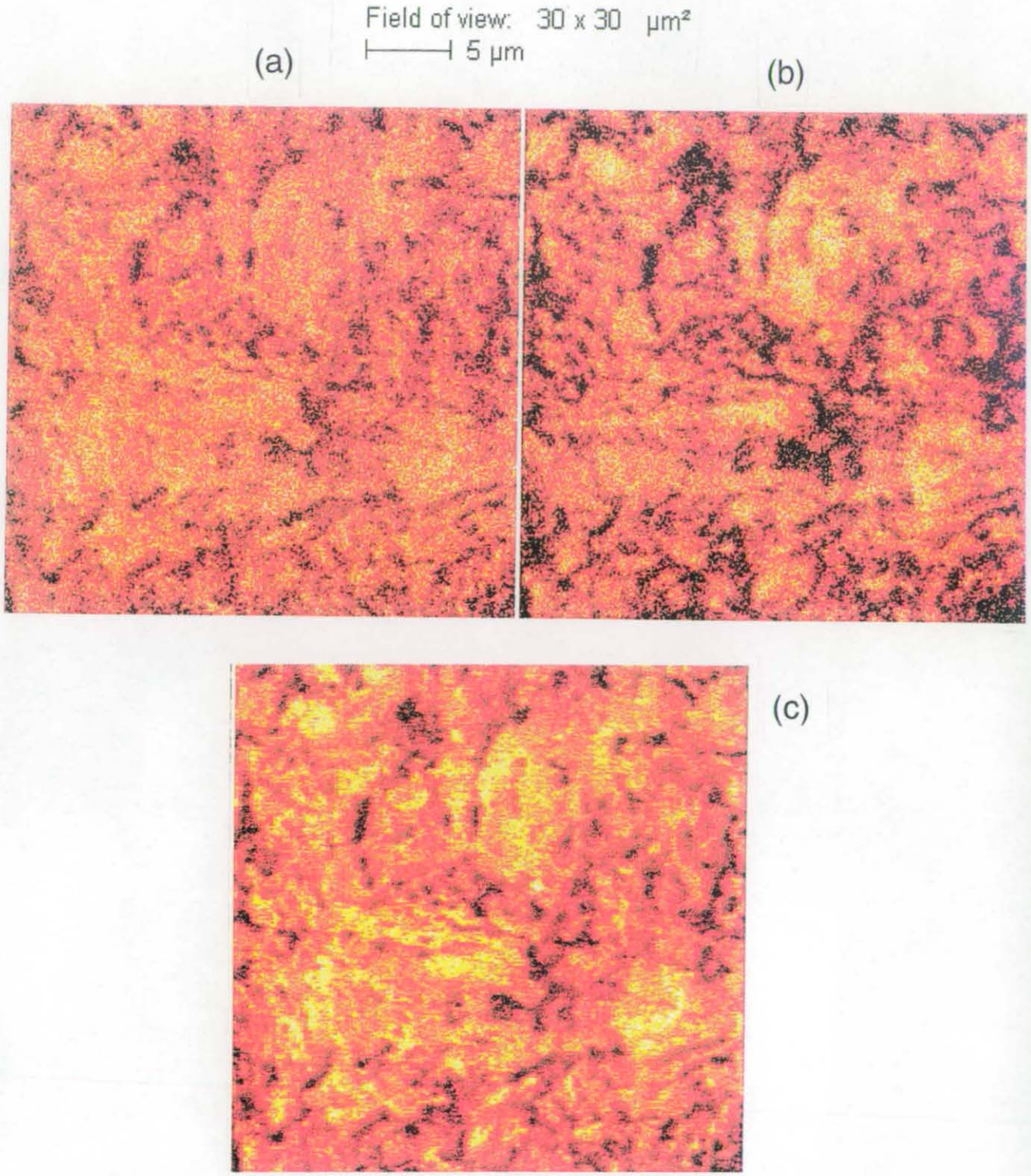

Fig 4 Static SIMS images of the reference material using a sub-micron gallium ion beam representing (a) Irganox coating (mass 57), (b) silver substrate (mass 107), (c) sum of all masses.

Table 1 **Repeatability measurements for four separate analyses of the positive ion intensities from Irganox 1010 using the NPL Quadrupole, with 4 keV Ar^+ and a total dose of $0.5x10^{15}$ ions m^{-2}. The table gives the scatter of the Nij values[4] as a standard deviation (%) for various mass peaks.**

	Mass of Peak							SD %
	57	107	203	219	259	385	453	
Full set	2.9	9.8	2.2	3.4	5.9	3.8	7.5	5.1
excluding Ag and peaks less than 500 counts	3.1	-	1.2	1.8	4.1	4.8	-	3.0
excluding Ag and peaks less than 1000 counts	3.0	-	1.1	0.7	3.8	-	-	2.1

A TOF SIMS instrument with a sub-micron gallium ion beam was used to study the spatial homogeneity of the reference material over an area of 30 μm x 30 μm. Static SIMS images of nominal mass 57, 107 and the sum of all masses are shown in Figs 4(a), (b) and (c), respectively. The ion at mass 57 represents the Irganox coating and the silver ion at mass 107 is from the substrate. It is clear that the thickness of the Irganox coating varies over the sample and , to ensure homogeneity, the SIMS instrument should be set to sample an area greater than 60 μm x 60 μm. It is usual in most quadrupole and TOF spectrometers to analyse an area of 100 μm x 100 μm for spectroscopy.

4 CONCLUSIONS

The Irganox coating on silver meets the requirements for a static SIMS reference material, it is conducting, has good repeatability, intense mass peaks in a wide mass range and is homogenous over an area as small as 60 μm x 60 μm. The sample can be analysed as received, it requires no cleaning and does not require sputtering to equilibrium.

REFERENCES

(1) I S Gilmore, M P Seah, D Briggs and M Hearn, NPL Report DMM(D) 228.

(2) I S Gilmore and M P Seah, *Surf. Inter. Anal.* **24** 746-762 (1996).

(3) "Micro" cleaning fluid, International Products Corporation, Chistlehurst, Kent, BR7 5PG, UK

(4) I S Gilmore and M P Seah, *Surf. Inter. Anal.* **23** 191-203 (1995).

CHAPTER SEVEN

A Static SIMS Inter-laboratory Study

1	INTRODUCTION	139
2	THE RESPONDEES	140
3	DATA	140
4	PROCESSING OF DATA	141
5.1	REPEATABILITY	141
5.2	RELATIVE INSTRUMENT SPECTRAL RESPONSE (RISR)	144
5.3	MASS RESOLUTION	160
5.4	DAMAGE STUDY	163
6	CONCLUSIONS	165
ACKNOWLEDGEMENTS		166
REFERENCES		167

1 INTRODUCTION

The surface analytical techniques of XPS and AES have matured to a sufficient level that calibration systems are now available[1] which allow spectral intensities to be related from instrument to instrument. Static SIMS must develop in a similar way if the spectral data libraries[2,3,4,5] required by industry are to achieve their full potential. Unfortunately, spectra are not yet consistent between different instruments and are often different between different operators of the same instrument. An inter-laboratory study has been completed in order to study the extent of the problem and to understand how to reduce instrument to instrument variability.

The objectives of this inter-laboratory study are (i) to determine the repeatability of instruments and the reproducibility of results between different laboratories, (ii) to evaluate variations in spectral response between different generic types of SIMS instruments, (iii) to establish the effectiveness of charge neutralisation and (iv) to evaluate ion beam damage rates in different instruments. These objectives are all important for obtaining reliable data, data that are transferable between instruments and laboratories, data that have the best mass resolution and data that are unaffected by excessive ion dose.

In this study, each respondee was sent a set of the three different reference samples developed in chapters 3, 4 and 6; PTFE, PET and Irganox 1010 on silver, together with the detailed instructions given in ref (6), on how to carry out the analyses and report the data. The PTFE was supplied as a full reel of tape, a sample from which had been removed and analysed at NPL to check that the batch to batch repeatability was better than 2%. Measurements of PET and Irganox 1010 gave values of 3% and 4% respectively. The PET was to be washed in iso-hexane by the respondee prior to analysis and the Irganox 1010 on silver was to be analysed in the "as received" condition. This sample needed no charge neutralisation.

The PTFE and PET samples are both insulators. The PTFE shows very repeatable results and so was included to define the instrument repeatability. The PET was included to see the extent to which conclusions drawn about the instrument response from the PTFE sample could be transferred to PET. PET is more complex than PTFE and, having a more reactive surface, is subject to greater problems of contamination. The Irganox 1010 sample, discussed

in chapter 6, was of a very thin layer on a silver foil specimen which would not require charge neutralisation. This sample was thus intended to study any charge neutralisation problems.

Compared with older instruments the newer time-of-flight, TOF, SIMS analysers are sufficiently sensitive that, for large area analysis, the total fluence is always in the static SIMS regime ($< 10^{16}$ ions/m^2). However, higher sensitivity permits a more focused beam to be used so that there will always be a resolution limit at which damage is no longer acceptable. Part of this study therefore, was to assess damage effects by significantly over-dosing samples with up to 10^{18} ions/m^2. This was designed to show to what extent damage thresholds may be transferred from instrument to instrument.

2 THE RESPONDEES

The acknowledgement details some of those responding in this inter-laboratory study and Tables 1 and 2 details of the instruments used. Data were supplied from twenty one instruments representing the following countries, UK, Belgium, Finland, Germany, Italy, Sweeden, Switzerland, USA and Japan. In Table 2 we also list the ion source conditions and the sets of data accumulated. The instrument letter given in the text refers to this Table 2. In some cases in the acknowledgements list, where there were two people involved from one instrument, they may refer to one or two instrument letters in Table 2 or one person in the list may operate more than one instrument and so may be allocated more than one letter in Table 2. In one case revised data were sent as the respondee, on reviewing their data, decided to improve their in-house procedures. The respondee shown as S is the revised data for respondee M. The difference between the results for S and M highlights the importance of good, documented working procedures.

3 DATA

The spectral data were returned to NPL in a variety of different formats including ASCII, binary, compressed data and proprietary formats. In general, each instrument had a different format. The data were sent on a number of different media including floppy disks, optical disks, CD ROM and data tapes for both PCs and SUN workstations. Data were also transferred by FTP and using e-mail attachments. The main problem encountered was with

the TOF data which, for ASCII files, could be as large as 10 Mbytes. There is, unfortunately, no standard data transfer format or media for handling large quantities of data. After some effort all data files could be loaded into NPL analytical software with the TOF mass spectra properly calibrated for mass. Each TOF spectrum requires calibration as the mass resolution is high and small changes in sample geometry lead to significant peak shifts.

Table 1 **The types of static SIMS mass spectrometers used in this study and the specific models**

Type of Analyser	Model
Quadrupole	VG MM 12-12 PHI 5600
Magnetic Sector	CAMECA IMS 3f VG IX70s
Time of Flight	VG IX23S ION TOF I, II, III and IV PHI 7000 and 7200 PHI TRIFT 1 and 2

4 PROCESSING OF DATA

Software was written to allow each different format to be read into a suite of software programs for processing the data. For determining the repeatability in each set of spectra the data were binned to one amu intervals to reduce the sensitivity to the exact peak position. This gives good counting statistics for each peak and makes the spectrum insensitive to the effect of ion beam pulse length and instrument resolution. The result of such a binning process is shown in Fig 1, the original spectrum is shown times a factor of 40. The original data are necessary for identifying each peak and for ensuring the absence of contaminating interferences but the binned data make the present analysis possible.

5 ANALYSIS OF RESULTS

5.1 REPEATABILITY

To measure the repeatability of a group of spectra, a set of nominated peaks which are the most characteristic components of the spectrum have been defined. A computer program is

Table 2 **The code given to each static SIMS instrument together with the primary ion source and energy for both positive and negative ions**

Instrument	Ion source	Ion energy (+ve)	Ion energy (-ve)
A	Ar^+	4	4
B	Cs	8	8
C	Ga	15	30
D	Cs	8	0
E	O_2^-	4.5	-
F	Ar	11	11
G	Ar	11	11
H	Ar	11	11
I	Ga	12	18
J	Ga	25	25
K	Cs	8	8
L	Ga	8	20
M	Ga	12	18
N	Ga	25	35
O	Ga	25	35
P	Ga	12	18
Q	Ar	2.5	2.5
R	Ga	12	8
S	Ga	12	8
T	Ar	11	11
U	Ar	25	-

then used to scan through all the data for each sample, from all of the contributors, in order to measure the repeatability of the characteristic peaks. This repeatability[7] was calculated using the method described in chapter 3. The scatter was also calculated for each peak in the unit mass spectrum. A typical spectrum of PTFE is shown in Fig 2. Figure 3 shows the results for the calculations for N_{ij} (see Eq (7) in Chapter 3) for the 17 peaks for the four spectra for instrument I. These show excellent repeatability, defined as the standard deviations of N_{ij}, of 1%. In Fig 2 these repeatabilities are indicated, for each peak, by a symbol at the top of the

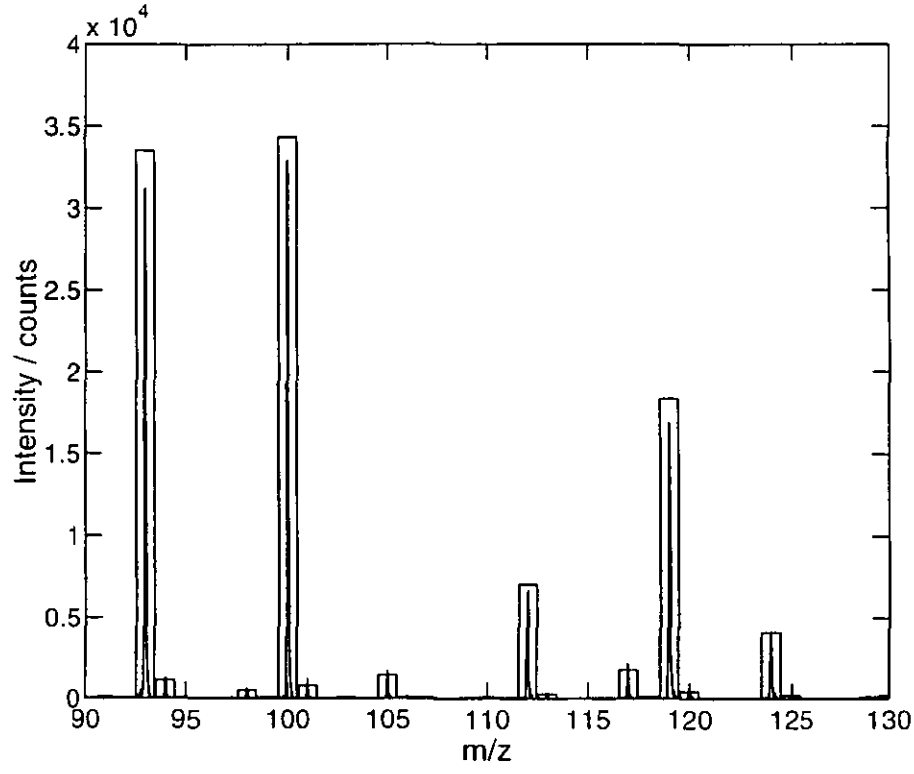

Fig 1 The mass spectrum binned to unit mass. The high resolution spectrum is shown magnified by a factor of 40 in intensity.

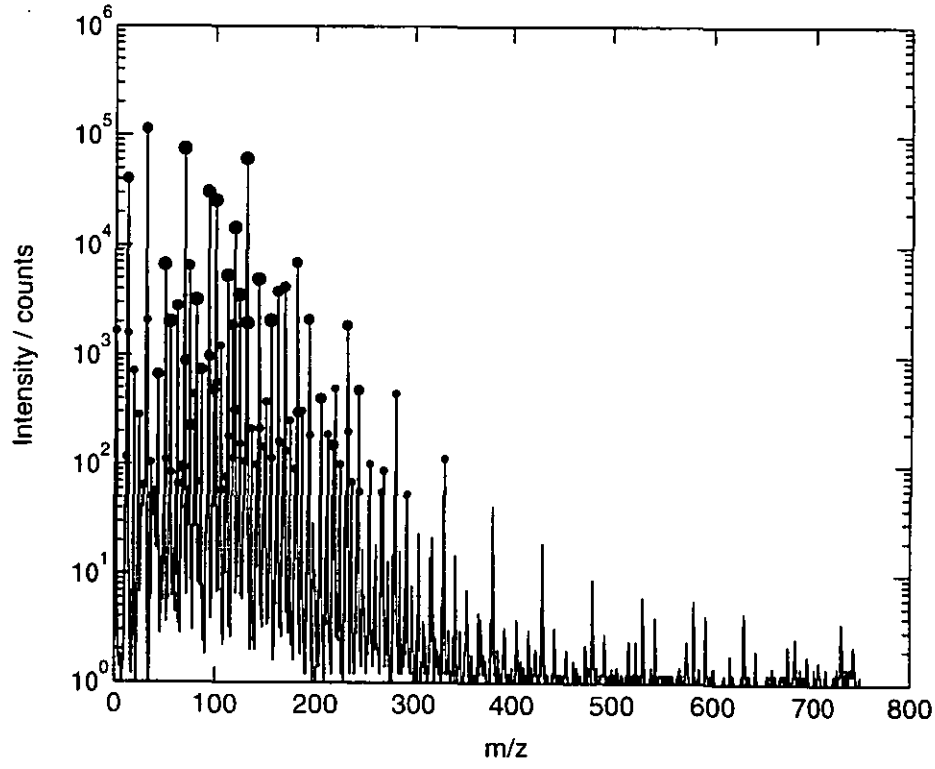

Fig 2 The unit mass spectrum of PTFE for positive ions from instrument A. The large dots represent peaks with a percentage scatter of better than 3%, medium dots a percentage scatter of between 3% and 5% and small dots for peaks with a percentage of between 5% and 10%.

peak. Those peaks with a scatter of less than 3% have a large dot, between 3% and 5% have a medium sized dot and those between 5% and 10% have a small dot. This enables the peaks which are strong in intensity and are of a good repeatability to be identified using the data of respondees that showed a good level of repeatability for the initial set of peaks. These new peaks were then added to the characteristic peaks of the nominated set to provide as large a nominated set of peaks as possible. The computer program then recalculated the repeatability for the new larger set. The sets of peaks for each material and ion polarity are summarised in Table 3.

Table 3 **The characteristic peaks for each material and polarity of ions, those in bold type were included in the calculation for repeatability. Mass peaks marked with an asterisk were measured for mass resolution.**

Spectrum type	Characteristic peaks
+ PTFE	**12,31,50,69,74,93,94,100,112,119,124,131*,155,162,181,193,231*,**281,331, 381*,431,481,531,581,631,681,731,781,831,881,931,981
+ PET	**50,57*,65,75,76,77,104*,121,149,191,193*,207,208,**385*,445,533,577, 621,681,769,917
+ Irganox	**40,57*,69,91,**107*,**147,161,203,219,259*,**305,**385,451,**520,**715*,**769,771
- PTFE	**19,38,69,93,119,131,169,231,281,331,381**
-PET	**16,25,49,76*,105,121*,165,191*,**209,313,357,401,475
-Irganox	**16,25,35,37,62,80,97,179,205,206,220,223,231,233,**419,**434,**655

The measurements of repeatability for the positive and negative ions for PTFE, PET and Irganox 1010 are shown in Fig 4. It is clear that positive ion repeatabilities, for all materials, can be less than 4% but that some instruments give poor results for all of the materials. The inherent repeatability of all three materials can be as low as 1%, but the overall average value for positive ions was 10%. Repeatabilities for negative ions are similar to those for positive ions for two of the reference materials, but those for PTFE are a factor of two worse. This caused the average value for negative ions to be 14%. Most instruments give similar values for both the insulators and the conductors, indicating that charge control is effective.

5.2 RELATIVE INSTRUMENT SPECTRAL RESPONSE (RISR)

To show how the spectral response from one instrument compares to that of another, a

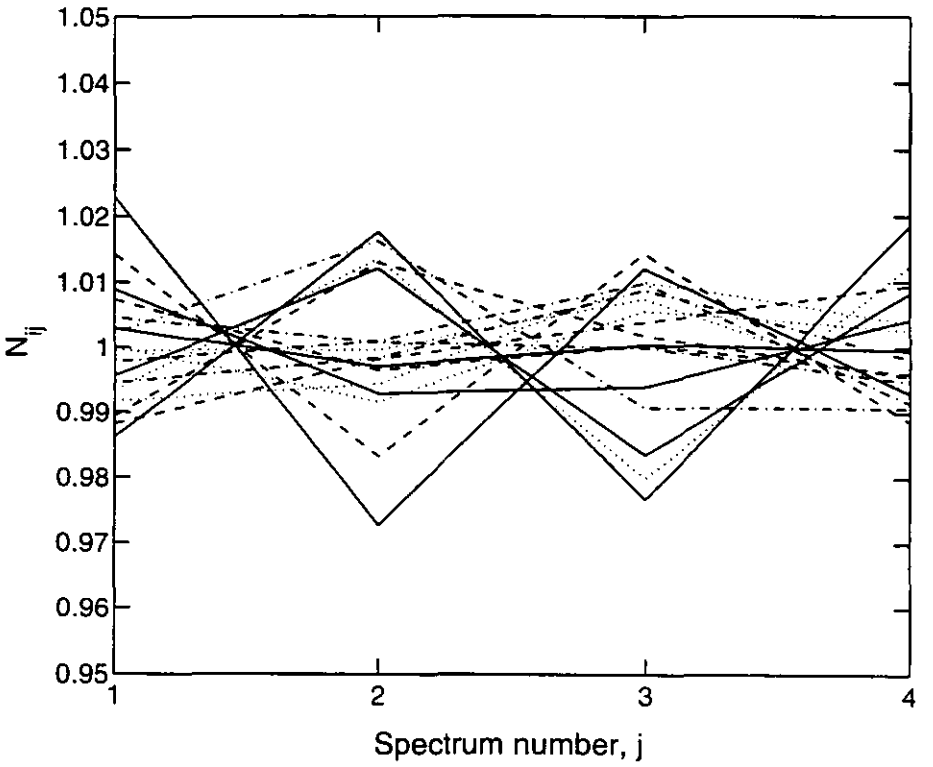

Fig 3 The N_{ij} repeatability values from four positive ion spectra of PTFE for instrument I.

relative instrument spectral response (RISR) functions was defined and calculated as follows. The average of the four binned unit mass spectra for each respondee for a given charge sign of secondary ions and for a given material, x, are formed into a matrix, I_{xmj}, where, m, is the mass of the characteristic peaks and, j, refers to a particular instrument irrespective of the type of ion in the beam and its energy. The spectra are truncated at mass 1500. First we calculate the approximate power, P_{xj}, in each spectrum:

$$P_{xj} = \sum_{m=1}^{1500} I_{xmj} \tag{1}$$

A matrix of normalised intensities N_{xmj} is then determined by dividing intensities in each spectrum by their respective P_{xj} value. This brings all spectra to roughly the same intensity and removes differences in the dose used and in the overall spectrometer efficiency. An average reference spectrum A_{xm} is next calculated from the I_{xmj} divided by P_{xj}, using only those instruments that gave data with a repeatability of better than 10%. The average reference spectrum is thus over k_0 instruments where k is a subset of j.

$$A_{xm} = \frac{\sum_{k=1}^{k_o} I_{xmk} / P_{xk}}{k_o} \tag{2}$$

The relative instrument spectral response (RISR) for the sample x is then determined by calculating, Q_{xmj} from the normalised intensities using

$$Q_{xmj} = \frac{N_{xmj}}{A_{xm}} \tag{3}$$

Q_{xmj} shows the relative intensity for a given mass, m, from material, x, for the spectrometer, j. The Q values will all be around unity.

It was found that some respondee's spectra exhibited significant contamination peaks or a high background signal but had a good repeatability and so had been included in the average reference spectrum, A_{xm}, above. We sought a method to determine which spectra were for relatively clean samples, and should therefore be included in creating the average reference spectrum, and those which were more contaminated and should have been omitted. We do this as follows. The Q_{xmj} plot for instrument S, for positive ions from PET, is shown in Fig 5(a). The stars represent data from the nominated peaks, given in Table 3. Additionally, the large dots represent peaks with strong intensities, medium dots represent medium intensity peaks and the small dots represent weak peaks. The straight line is a fit to the nominated peaks for the RISR which we shall discuss later. Here the straight line serves to guide the eye to the peaks representative of the PET spectrum. It is clear that the data fall into two clusters. The cluster of large dots at low mass, with a Q_{xmj} value a factor of 10 above the fitted line, do not correspond to any characteristic fragment from PET but arise from adventitious contamination (their intensities being weak in the average spectrum). Also plotted are large open circles at the mass positions for characteristic peaks of PDMS, a common contaminant. Here, the open circles circumscribe large dots clearly identifying that the sample is contaminated with PDMS or some similar silicone oil. A different contamination is evidenced by a vertical series of dots at approximate masses of 380 and 400 amu. This data set was considered to be too contaminated and was therefore deleted from the set used for calculating the average spectrum even though it had good repeatability. Figure 5(b) gives a further example Q_{xmj} plot, for instrument D, that whilst giving good repeatability was also rejected from the set for forming the average reference spectrum. Here, the small dots cluster in a band which rises above the line through the characteristic peaks. The cause of this is a much higher background signal than is found in our average reference spectrum. On discussion with the respondee concerned, the reason for this background was

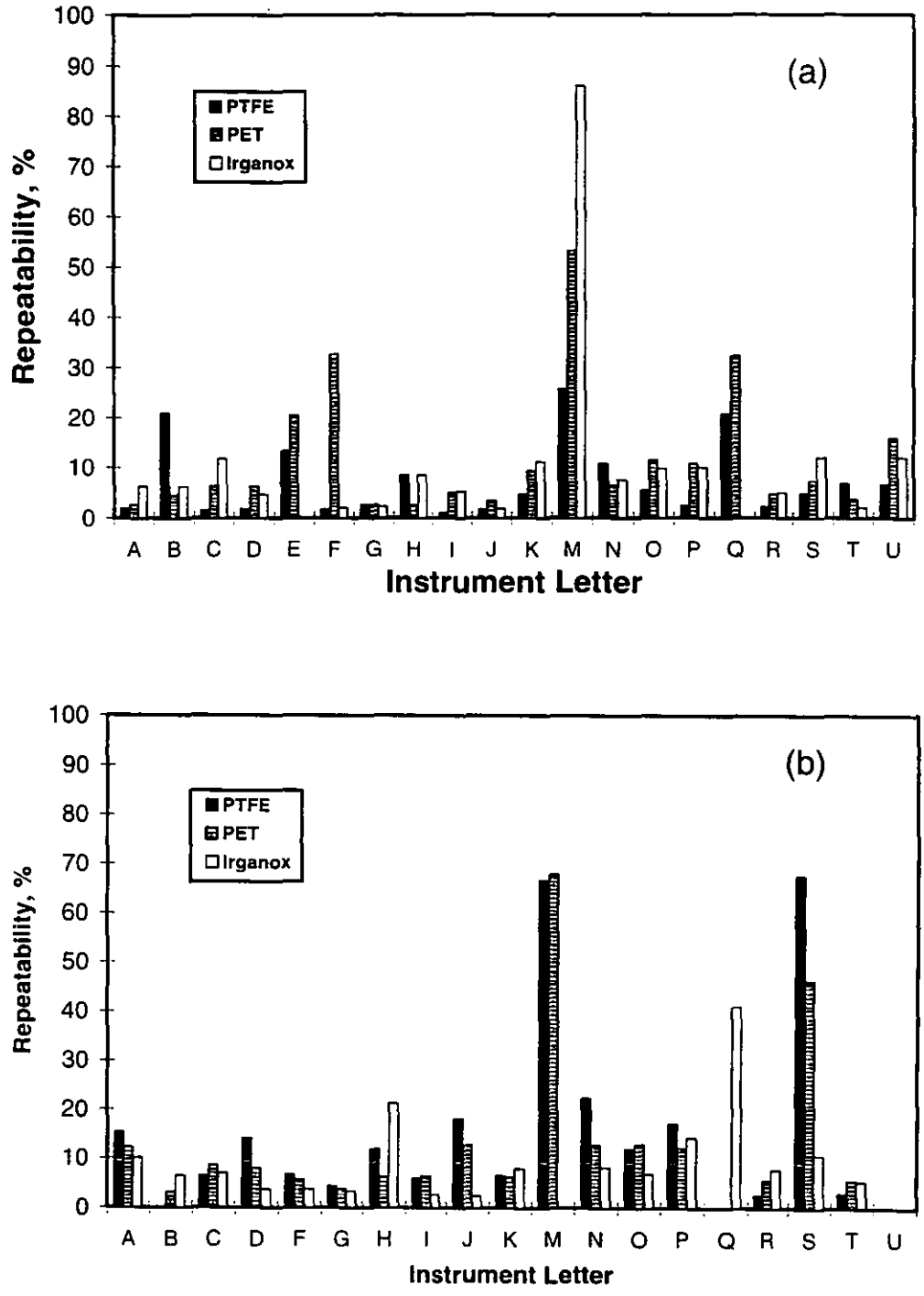

Fig 4 The repeatability, as a percentage, of spectra from PTFE, PET and Irganox 1010, (a) positive ions and (b) negative ions.

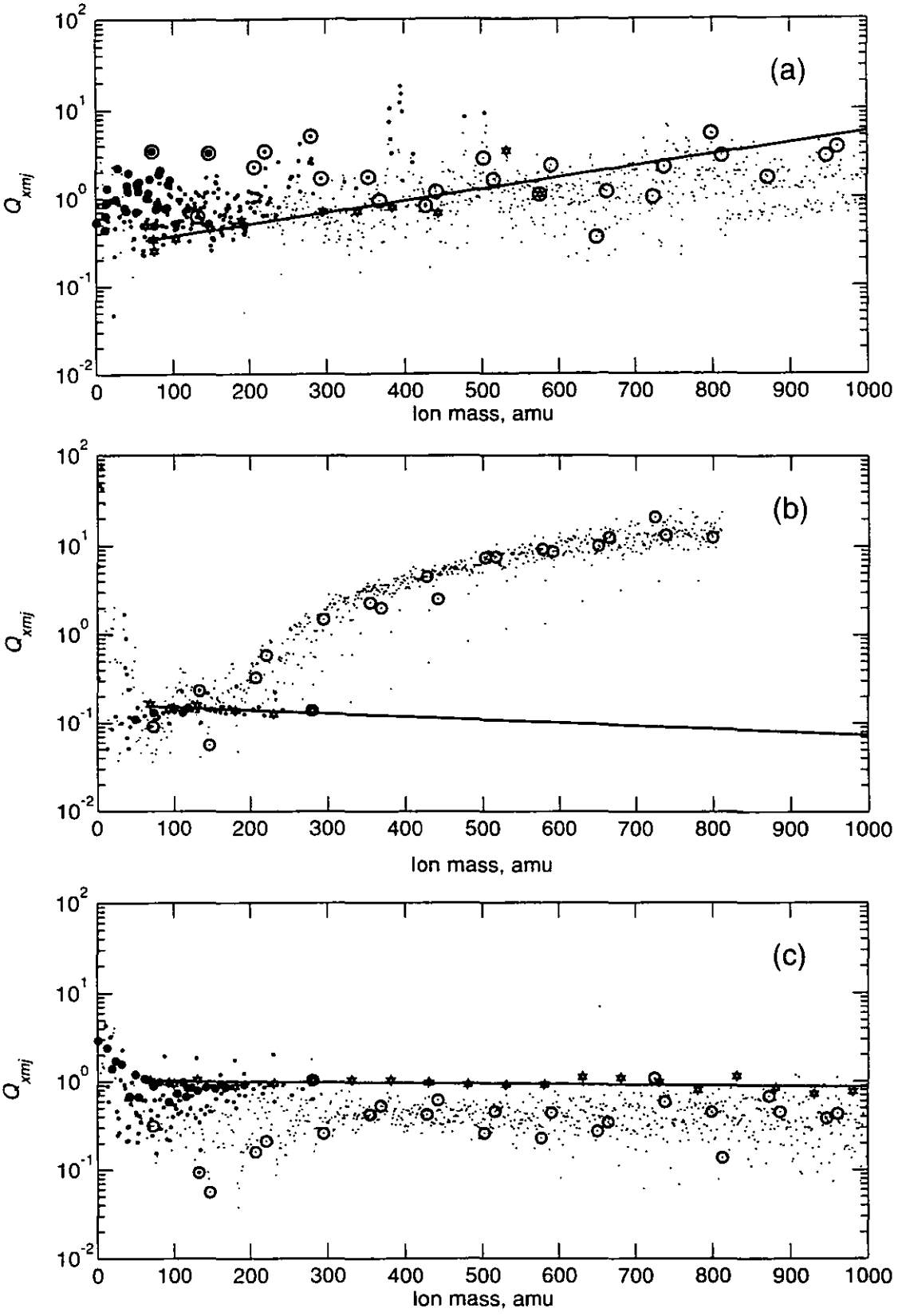

Fig 5 Examples of the positive ion Relative Instrument Spectral Response, RISR, evaluations for three instruments (a) S for PET, (b) D for PTFE and (c) R for PTFE. The dots represent different bands of intensity (see text). The straight line is to guide the eye to the nominated peaks.

discovered to be an incorrect timing sequence in the spectrometer. In TOF instruments, the electron neutraliser pulses synchronously out of phase with the extraction voltage. Ideally, there should be an interval of at least 5μs between switching off the electron gun and switching on the extraction voltage. This was not the case for instrument D where there was some time overlap when both the electron gun and extraction voltage were both on. Residual gas atoms, ionised by the neutralisation electrons, are accelerated by the extraction field into the spectrometer, giving rise to the observed background signal. Thus, the RISR evaluation can be used to distinguish contamination and give diagnostics of incorrect instrument behaviour.

The RISR for a "clean" spectrum from the well behaved instrument of respondee R is shown in Fig 5(c). There is no significant set of contamination data above the RISR line showing that the data were less contaminated than average data from the respondees. Note that, on average, half of the respondee results will have data for the contamination peaks above unity and half below unity as a result of our processing, no matter how low the average overall contamination level. This procedure simply allows us to select the least contaminated data reliably. The spectrum for the RISR plot of Fig 5(c) is typical of those included in the average spectrum. Using the above method of contamination detection and instrument diagnostics, the cleanest spectra were selected, from the respondees with an instrument repeatability of better than 10% and no instrument faults, to be included in the average reference spectrum. The selected instruments were A, B, K, I, R and T. All of these except A are TOF spectrometers. For consistency of instrument type, instrument A is dropped from the final set of instruments B, K, I, R and T used to calculate the final RISR values.

The calculated RISRs using the final nominated peaks for each instrument, are shown in Fig 6(a) for positive ions from PTFE and Fig 6(b) for positive ions from PET. The RISRs have been normalised to the value at lowest mass to aid visualisation. The line style has been kept consistent throughout the figures and so instrument A is always a solid line, instrument B a dotted line, etc. A summary of line styles and instrument letters is given in Table 4.

The data points for PTFE follow fairly smooth curves for most instruments and this is consistent with the good levels of spectral repeatability found earlier. The data points for PET are more scattered and this may, in part, be caused by sample contamination arising from washing in isohexane, or from impurities in the isohexane, or from contaminants in the

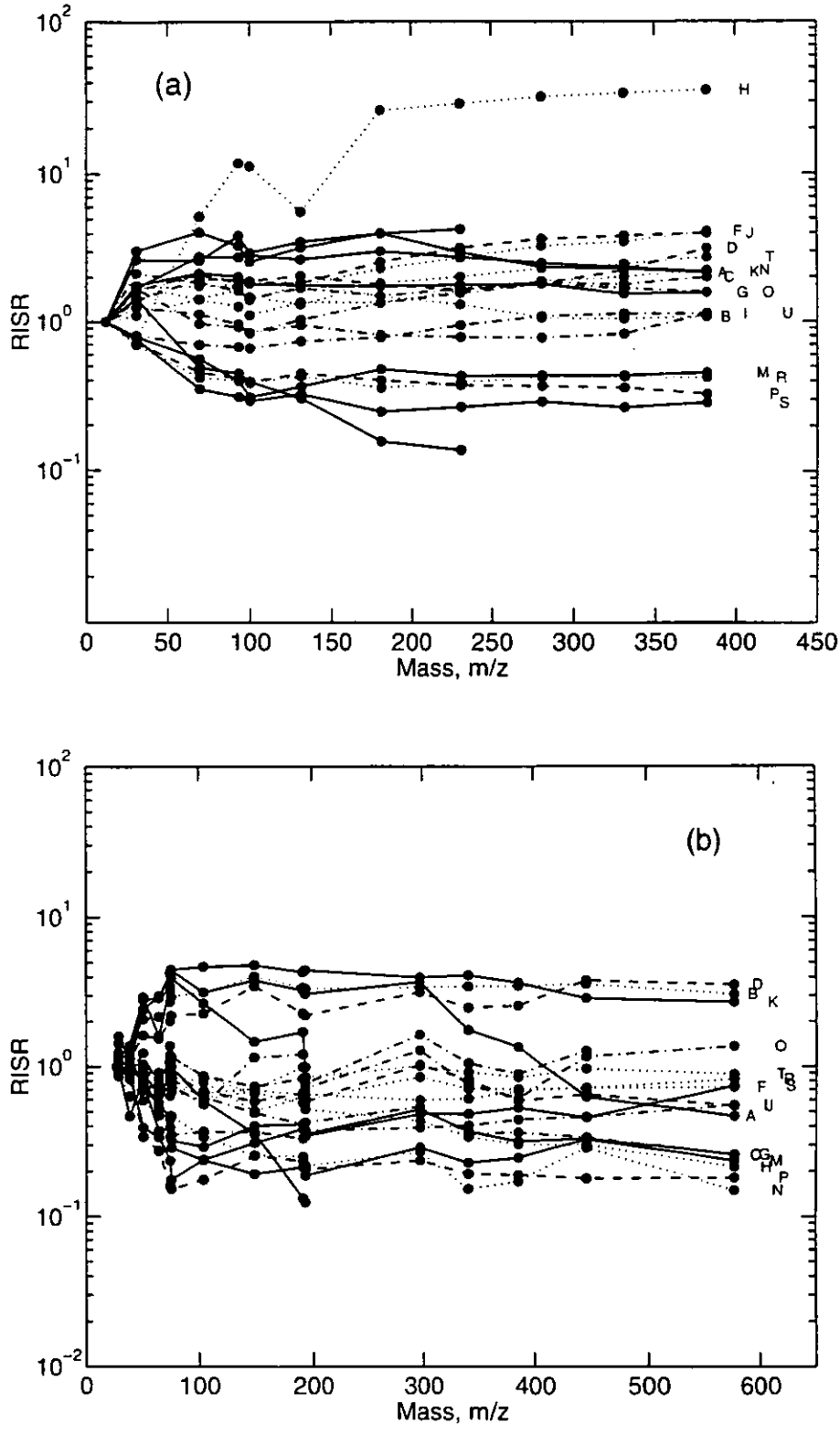

Fig 6 The RISRs for (a) and (c) positive ions from PTFE, and (b) and (d) positive ions from PET. The RISRs for (a) and (b) are normalised to the value at the lowest mass and that for (c) and (d) to a mass near 380 amu. Only the values for the nominated peaks are plotted.

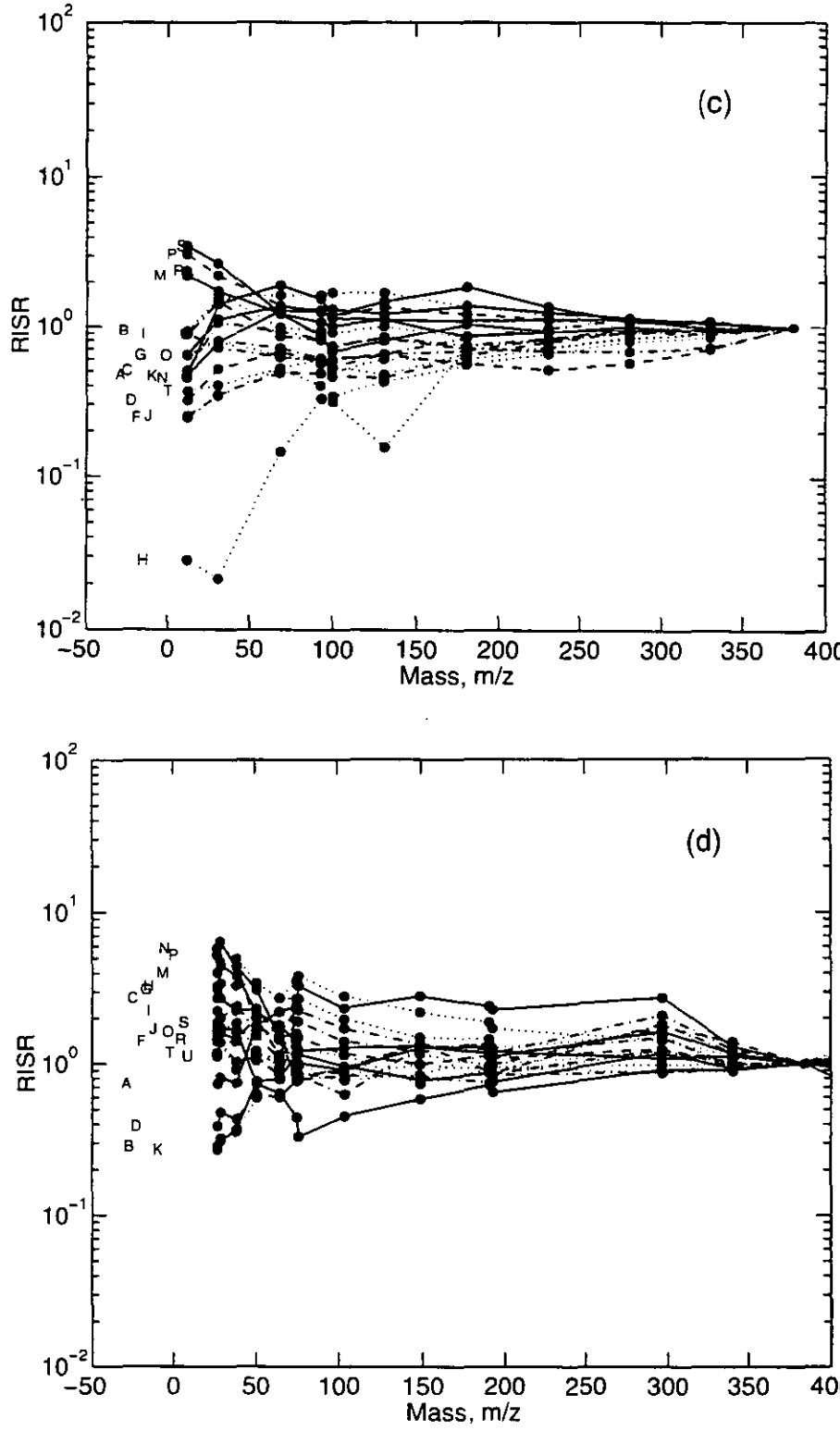

Fig 6 The RISRs for (a) and (c) positive ions from PTFE, and (b) and (d) positive ions from PET. The RISRs for (a) and (b) are normalised to the value at the lowest mass and that for (c) and (d) to a mass near 380 amu. Only the values for the nominated peaks are plotted.

vacuum chamber of the SIMS instrument. The use of isohexane to clean the PET was found to be necessary[8] and so was included in the sample preparation instruction to the respondees. Further effects are expected from differences in the fragmentation cascade produced by different ion beam energies, species and angle of incidence. The systematics of this are discussed in detail in chapter 8. The shape of each RISR curve for low mass depends on the energy band pass of the spectrometer. Instruments with a wide energy acceptance have a high transmission for the atomic and small molecular fragments which have broad energy spectra. These RISR curves initially fall. Figures 6(c) and (d) repeat Figs 6(a) and (b) but with normalisation at around 380 amu. It is clear from the data of Fig 6 that the instrument RISRs are reasonably well-behaved.

Table 4 **The line style used in Figs for each instrument.**

Line style	Instrument			
———	A	G	M	S
• • • •	B	H	N	T
- • - •	C	I	O	U
- - - -	D	J	P	
———	E	K	Q	
• • • •	F	L	R	

If we are to be able to transfer intensity data from one instrument to another we would need to use the RISR, it would need to be consistent between different materials and for both positive and negative ions. We cannot directly compare the RISRs for PTFE and PET as the data points are at different masses and so an analytic function must first be fitted to the data. It is clear from Fig 6 that the data points have some scatter and so the exact form of the function at this stage is not too critical. A simple linear function was therefore fitted to a plot of the logarithm of the normalised intensity, Q_{xmj}, versus mass for those characteristic peaks above 55 amu. We shall use this as the RISR function. The RISR below 55 amu is strongly affected by the energy band pass of the spectrometer and so will now be ignored. Examples of fits to the RISR for three instruments are shown in Fig 7. It is clear that the exponential function fits the data excellently in the required mass range. These examples are representative of the RISR functions calculated for most of the instruments. For some

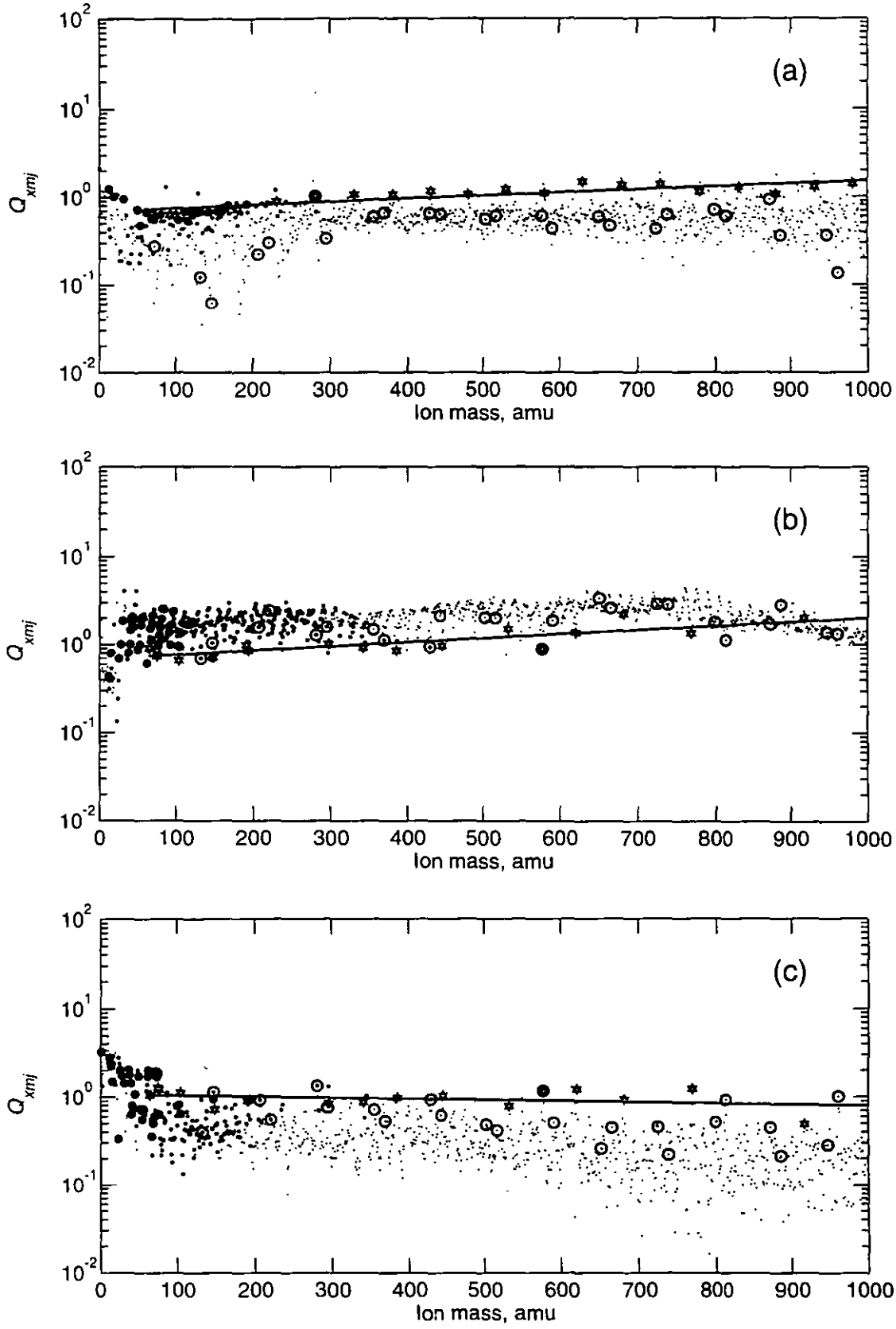

Fig 7 The RISR straight line fits for positive ions for three instruments (a) I for PTFE, (b) T for PET and (c) R for PET.

instruments, notably L and Q, the RISR data were rather more scattered. More examples of the RISR functions were shown earlier in Fig 5. The fits to the RISR data for negative ions from PTFE and positive and negative ions from PET were of a similar quality. Interesting systematics are observed in the positive ion RISR for instrument T from PET, shown in Fig 7(b). The data values shown by the small dots fall into a series of parallel groups of between approximately 5 and 10 points separated by 1 amu, with steep gradients. In chapter 8 we find that this effect results from slight differences in the fragmentation cascade of the respondee's instrument compared with the average reference spectrum. Here we will simply note that we are able to observe this from different instruments operated in different laboratories. The quality of these lines indicates that intensities are reproducible at a level better than 3% between laboratories. Figure 7(c) shows the positive ion RISR for instrument R, calculated from PET, to complement that shown in Fig 5(c) for PTFE from the same instrument. Both materials give similar RISRs, demonstrating that a general RISR is possible. Ideally the RISR function should be independent of the material and only depend on the instrumental parameters. We will now study these effects and the extent to which data can be transferred.

A new normalised RISR function, F_{xj}, is calculated from the fits Q_{xj} to the RISR, Q_{xmj}, limited to the mass range 55 to 400 amu, where

$$F^{+}_{xj} = Q^{+}_{xj}\left(\frac{P^{+}_{xj}}{P^{-}_{xj}}\right)^{0.5} \tag{4}$$

and $$F^{-}_{xj} = Q^{-}_{xj}\left(\frac{P^{-}_{xj}}{P^{+}_{xj}}\right)^{0.5}$$ so that $$\frac{F^{+}_{xj}}{F^{-}_{xj}} = \frac{Q^{+}_{xj}}{Q^{-}_{xj}}\,\frac{P^{+}_{xj}}{P^{-}_{xj}}$$

Here P_{xj}^{+} and P_{xj}^{-} are the power for positive and negative ions for one material, defined in Eq (1). This normalisation retains the correct ratio of intensities between the positive and negative ion spectra, but balances their errors to be equal.

The correlation of these weighted RISR functions, F_{xj}^{+} and F_{xj}^{-}, between PET and PTFE is

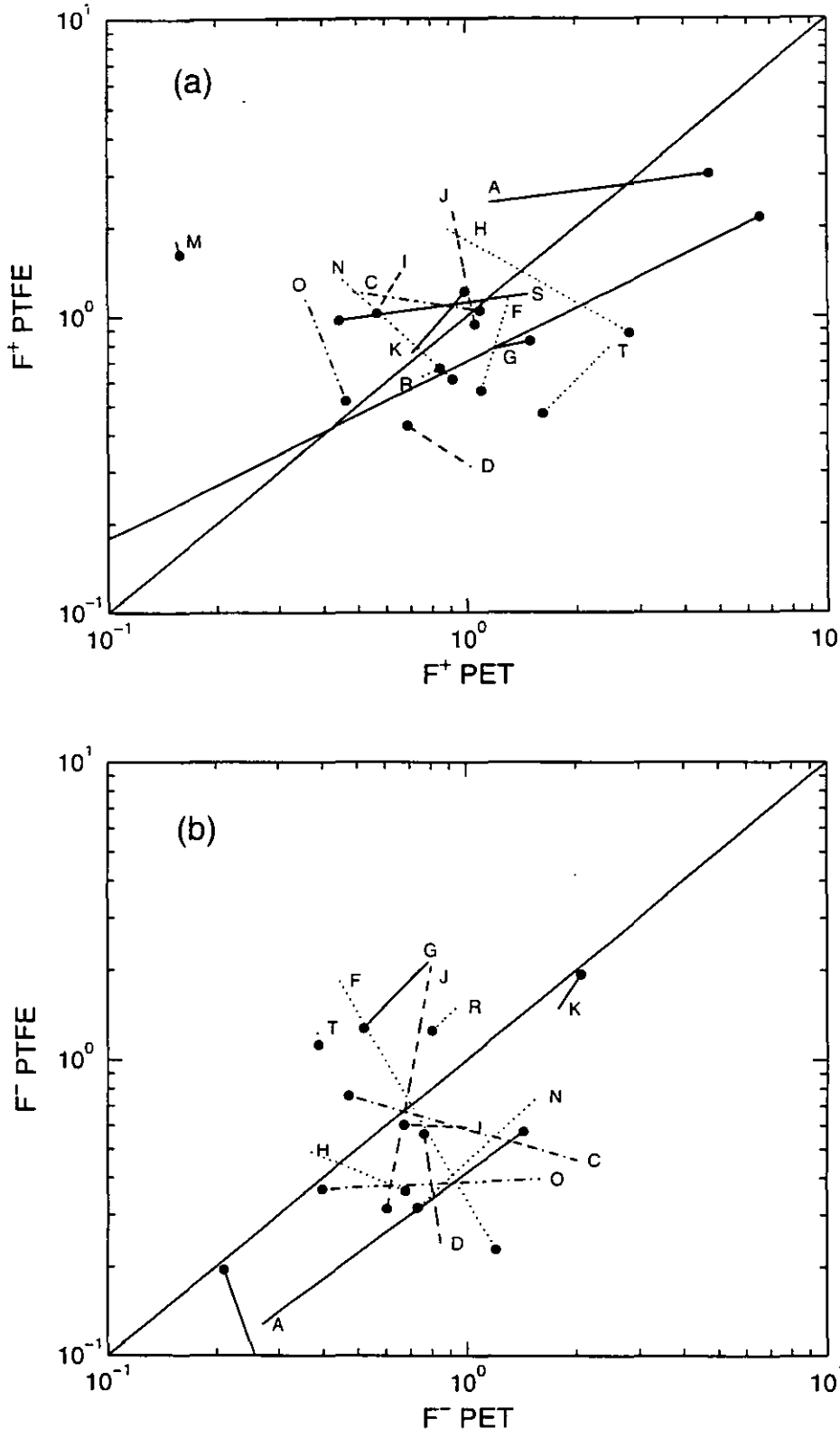

Fig 8 The correlation of F_{xj}^{+} and F_{xj}^{-} values between PTFE and PET for (a) positive ions and (b) negative ions and between positive and negative ions for (c) PTFE and (d) PET.

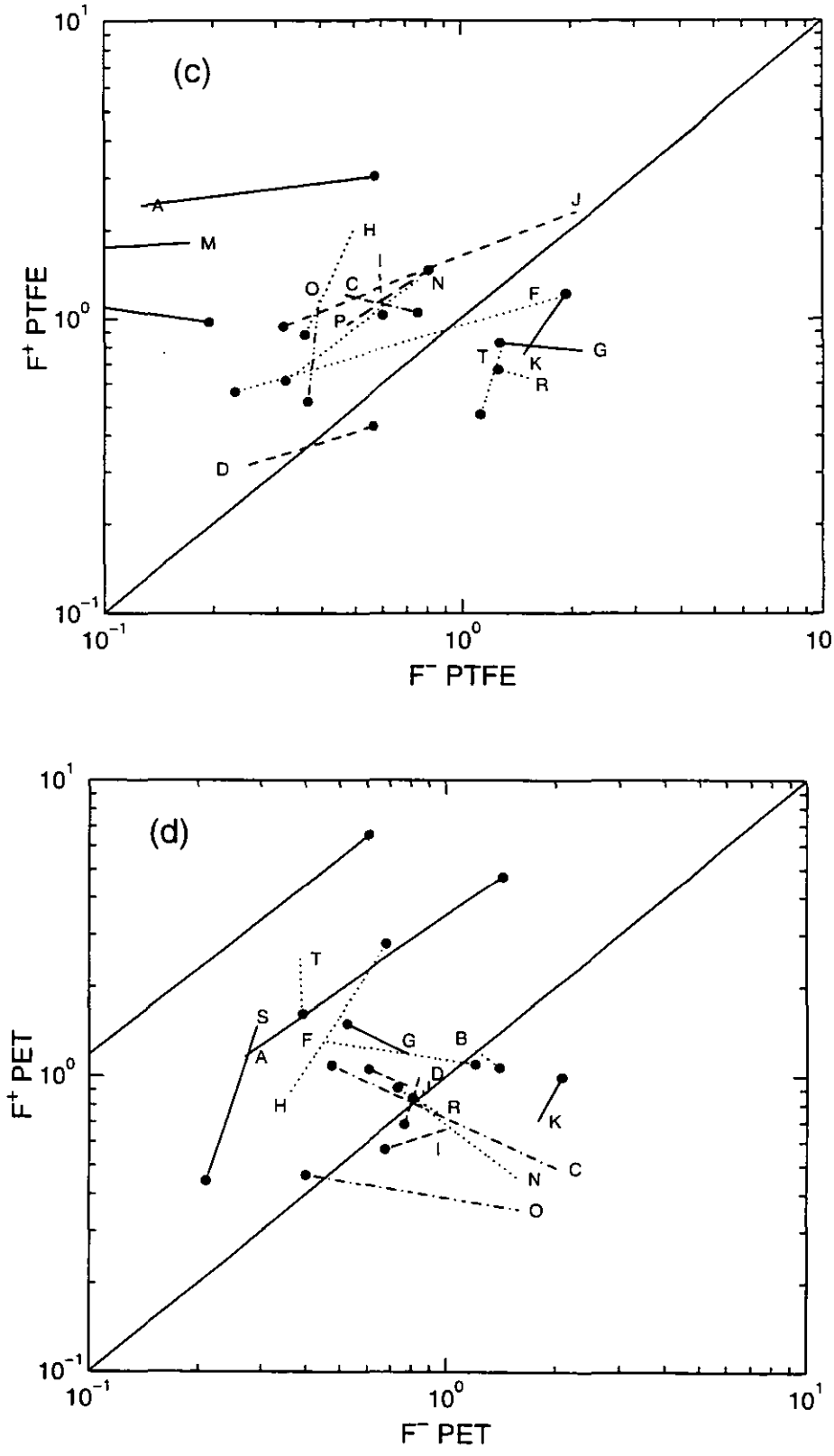

Fig 8 The correlation of F_{xj}^{+} and F_{xj}^{-} values between PTFE and PET for (a) positive ions and (b) negative ions and between positive and negative ions for (c) PTFE and (d) PET.

shown in Fig 8(a) for positive ions and 8(b) for negative ions. The point for the lowest mass end of the RISR data for each instrument is plotted with a large dot. The data in Fig 8 are plotted on logarithmic scales with a line of unity gradient to show the line of perfect correlation. An instrument for which the RISR has the same shape for PTFE and PET positive ions gives a line with a 45° gradient (the dot could be at either end). If the RISR has the same magnitude for both samples, the line will fall on the line of correlation. The instruments do cluster generally within an order of magnitude around this line. Instruments such as A, K, I, R, T and G with data along the line of correlation have well correlated behaviour between the two materials and those such as S, D, H, N and O that are perpendicular to the line are anti-correlated. The result for M, although perpendicular to the line of correlation, is so short that the data are very well correlated indeed. This overall grouping of correlations is similar for negative ions in Fig 8(b). For the instruments in Fig 8(a), ignoring instrument H, it is possible to exchange data with an average scatter of 20% over the mass range 55 to 400 amu.

The correlation of the weighted RISR functions, F_{xj}^{+} and F_{xj}^{-}, between positive and negative ions is shown for PTFE and PET in Figs 8(c) and (d) respectively, with the line of correlation plotted to guide the eye. If we are to be able to transfer data from one polarity to another, the figures should be independent of material. This behaviour is exhibited for instruments A, B, K, I, R and T but, for some instruments such as N, we see that the data change from being correlated to anti-correlated.

This analysis using the weighted RISR function, F_{xj}^{+} and F_{xj}^{-}, gives a good overall view of how the data for different respondees compare. What is now required is an estimate of the reproducibility of the RISR functions calculated from each reference material. In the simplest case, for any given instrument, the RISR would be the same shape for each material and ion polarity. The ratio of the RISR functions for PET to PTFE, and Irganox to PTFE for positive ions and the ratio for negative and positive ions for PTFE are shown in Fig 9 for each of the respondees. For all the RISR functions, the data for reference spectra are taken from the same suite of instruments and so the ordinate for each data line has an absolute value which, in the simplest case, would be unity, or at least constant. The reproducibility is then measured from the standard deviation of the RISR ratios, at 1 amu intervals from 55 amu to 400 amu, about constant values. Figure 10 shows the values of this reproducibility for each material and ion polarity ratio and the averaged values for each instrument. Values range from 60%

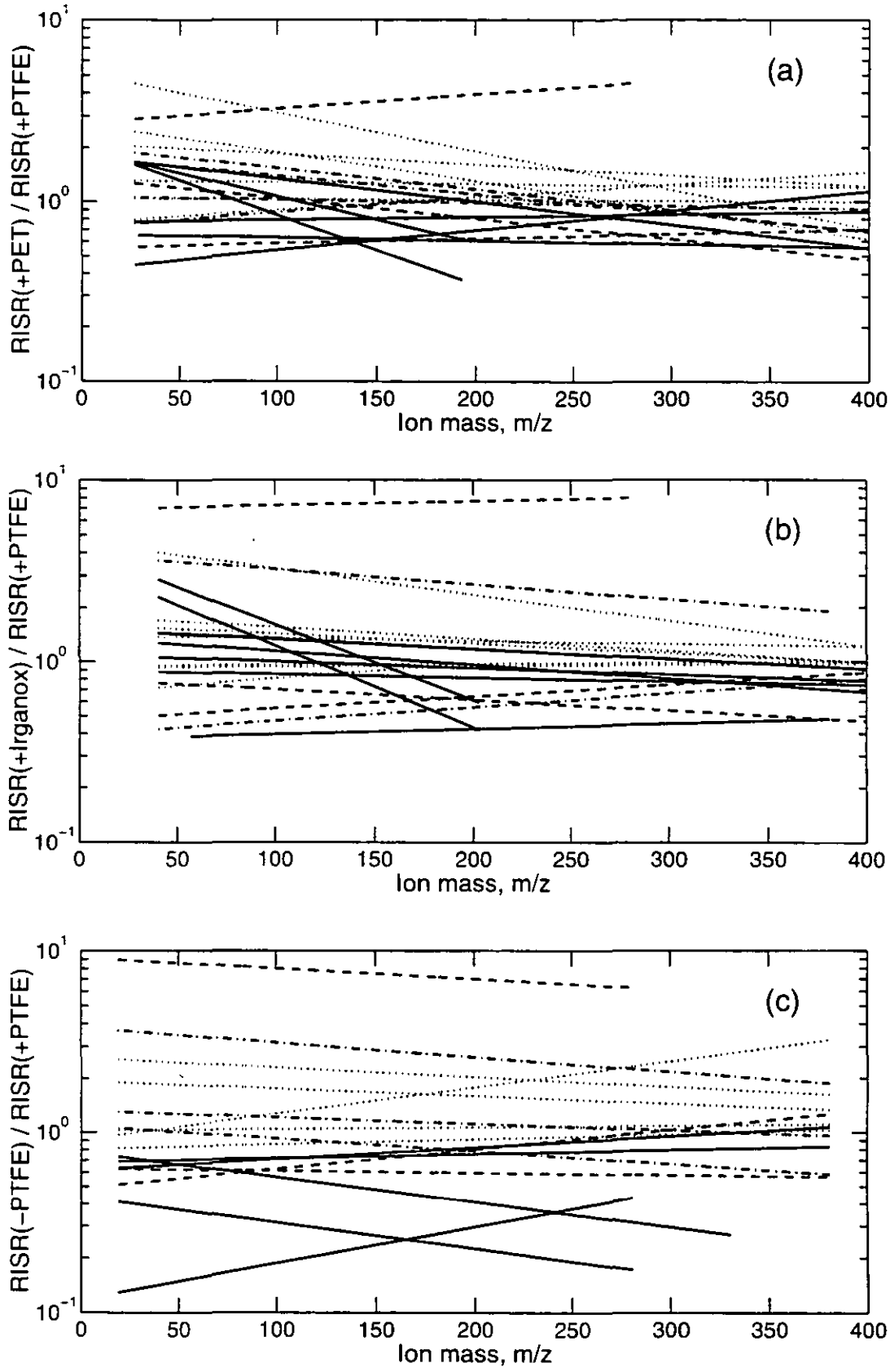

Fig 9 Ratio of RISR functions for positive ions from (a) PET and PTFE and (b) Irganox and PTFE and (c) negative and positive PTFE ions.

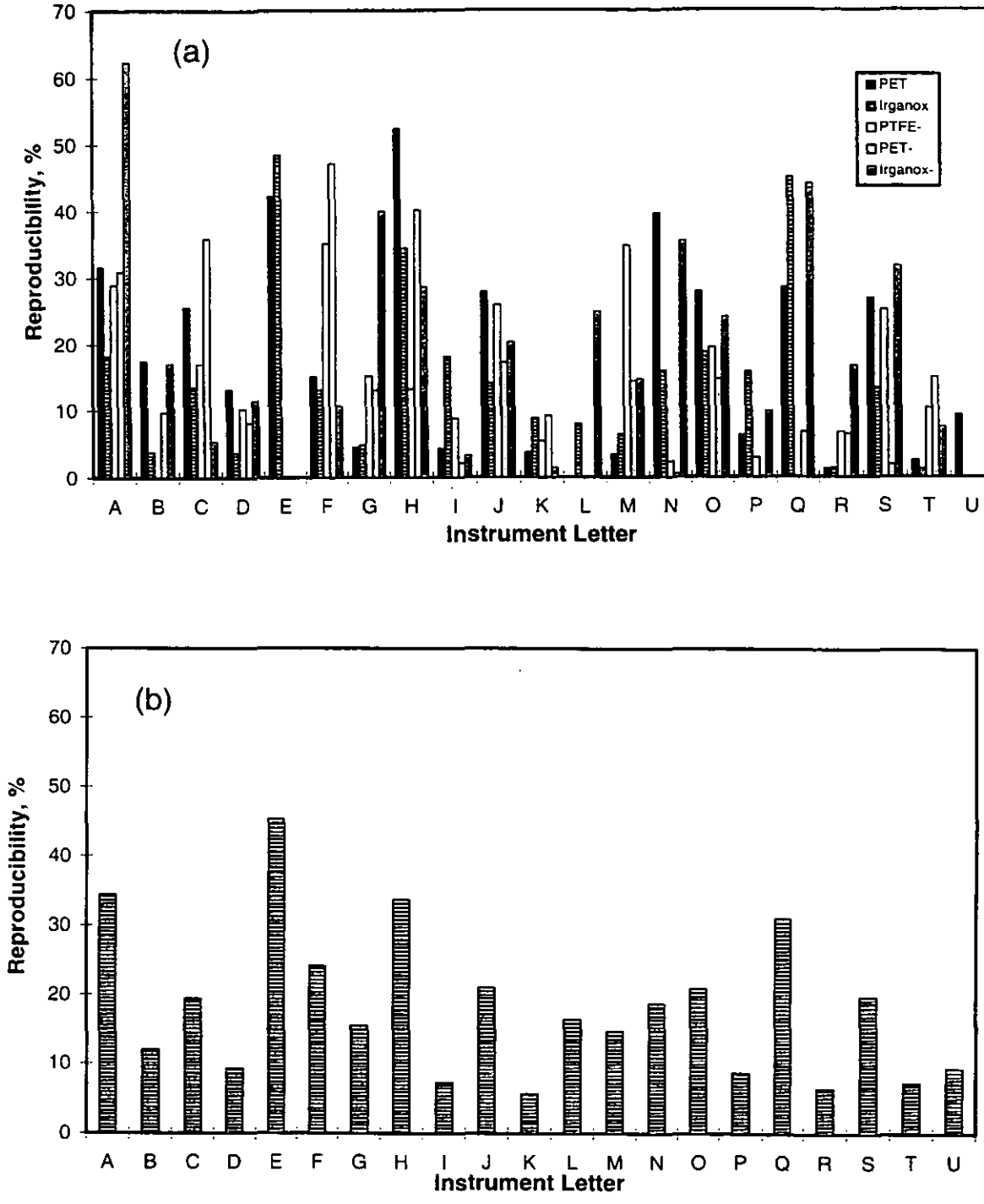

Fig 10 Reproducibility for each instrument (a) determined from the standard deviation of the ratio of the RISR for each material to the RISR for positive ions from PTFE for each material and (b) the average reproducibility for each respondee over all materials.

in the worst case but can be as good as 1% and on average are approximately 18%. From the material averaged values it is clear that instruments A,E,H and Q give the poorest reproducibility and, with these instruments removed, the reproducibility improves to the excellent values of 14% and 10% for positive ions from PET and Irganox relative to positive ions from PTFE values and values of 16%, 14% and 17% for negative ions from PTFE, PET and Irganox relative to positive ions from PTFE. The average value of 14% overall means that if a RISR function is determined using PTFE and that RISR function is used to correct the PET spectrum, the inter-laboratory scatter of intensities for the corrected spectra would be expected to be around 14%. For comparison, the equivalence of data between instruments, without correction for the RISR functions, for each material and ion polarity, is calculated from the average of the scatter factors of the Q_{xmj}, for each mass peak defined in Table 3 in the mass range 55 to 400 amu. Each spectrum is normalised to unity total intensity for all mass peaks. The scatter factor values for positive ions and negative ions of PTFE, PET and Irganox are $\times/\div$ 1.44, 1.36, 1.71, 1.46, 1.46 and 1.9 respectively, with an average value of $\times/\div$ 1.55. The correction of spectra with the RISR function significantly improved this reproducibility by a factor of 4 to $\times/\div$ 1.14. The chosen reference materials have clearly proved to be a good mechanism for the determination of the RISR function.

5.3 MASS RESOLUTION

A computer program was devised to determine the mass resolution and the peak centroid for selected peaks from each spectrum. The mass resolving power, R, is simply defined as

$$R = \frac{M_x}{W} \tag{5}$$

where M_x is the centroid of the peak and W is the full width at half maximum, FWHM. Often W is called the mass resolution and so, here, we have called R the mass resolving power for clarity.

The centroid is measured using the method described by Reichlmaier et al[9], and is given by the weighted mean of all the intensities, I_i, in the peak greater than or equal to half the maximum intensity. If M_i is the mass value of the ith channel number in the spectrum, the centroid mass M_x is given for the above intensity range by

$$M_x = \frac{\sum M_i I_i}{\sum I_i} \qquad (6)$$

A typical output from the program is shown in Fig 11 for an instrument of good mass resolution. The resolution for high, medium and low mass peaks were measured for all the spectra for each material and polarity; the average then being calculated. The mass peaks used for this are marked in Table 3 with an asterisk. Data for some instruments were supplied in a proprietary format using data compression. These spectra could only be processed using software supplied by that instrument manufacturer.

The mass resolving power was calculated using the method described above for each material for both positive and negative ions. The resolution may degrade between the conductor, Irganox, and the insulators, PTFE and PET for TOF instruments, if charge neutralisation is a problem. The extent of any degradation may indicate the need for control of the charge on the surface. If the surface potential fluctuates, the energy variation of the ions may become more than can be compensated by the analyser and the arrival times will vary. This leads either to broadening of the peak or, if the energy filter removes the ions, a reduction in the peak intensity. The mass resolutions cannot be directly compared between materials at a given mass because the characteristic mass peak values are different, and so a linear fit to a plot of mass resolving power, R, versus mass is used to make this comparison. A typical example of a fit to the data is shown in Fig 12 for instrument B. The fitted lines are, in general, better than 10% for masses above 100 amu, where the contribution of primary ion pulse width to the mass resolving power is small. The mean resolving power for the TOF instruments measured for PTFE and PET relative to that for Irganox is shown in Fig 13 for positive ions. If charging caused peak broadening we would see plots significantly below unity. At most, the drop is by 50% and this may arise as a result of material or instrument setting differences since we see more above unity than below! Since most instruments have a relative resolution around or above unity, it therefore appears that any charging problems are not strongly manifest by peak broadening but, of course, may be important in maintaining peak intensity.

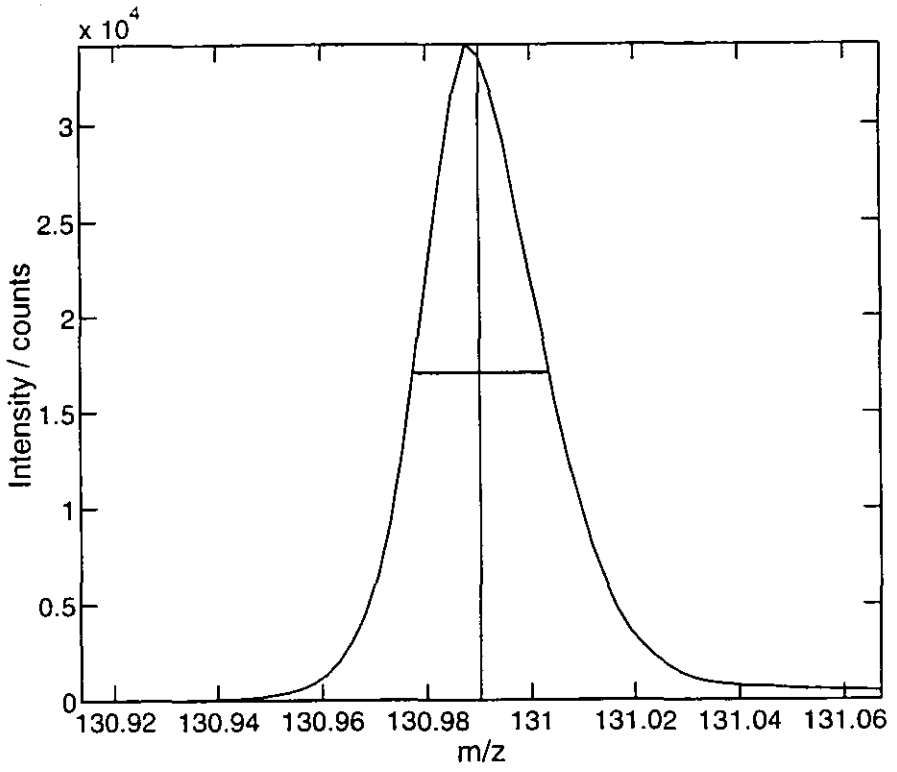

Fig 11 The measurement of mass resolution and peak centroid for a high mass resolution TOF instrument.

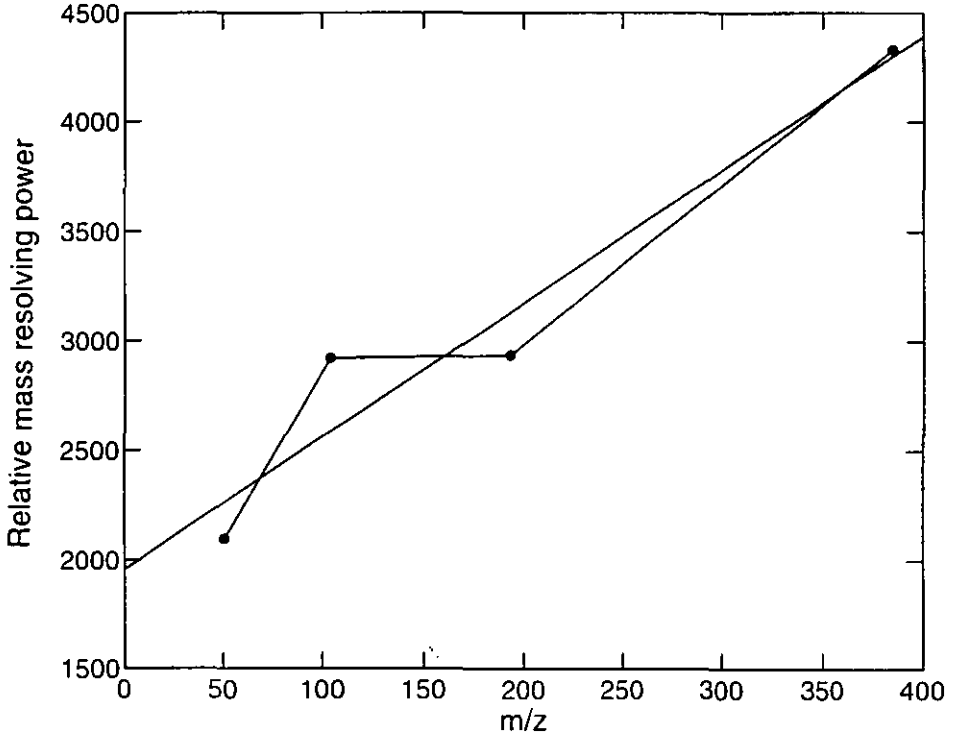

Fig 12 Example linear fit of the mass resolving power to mass for positive ions from PET for instrument B.

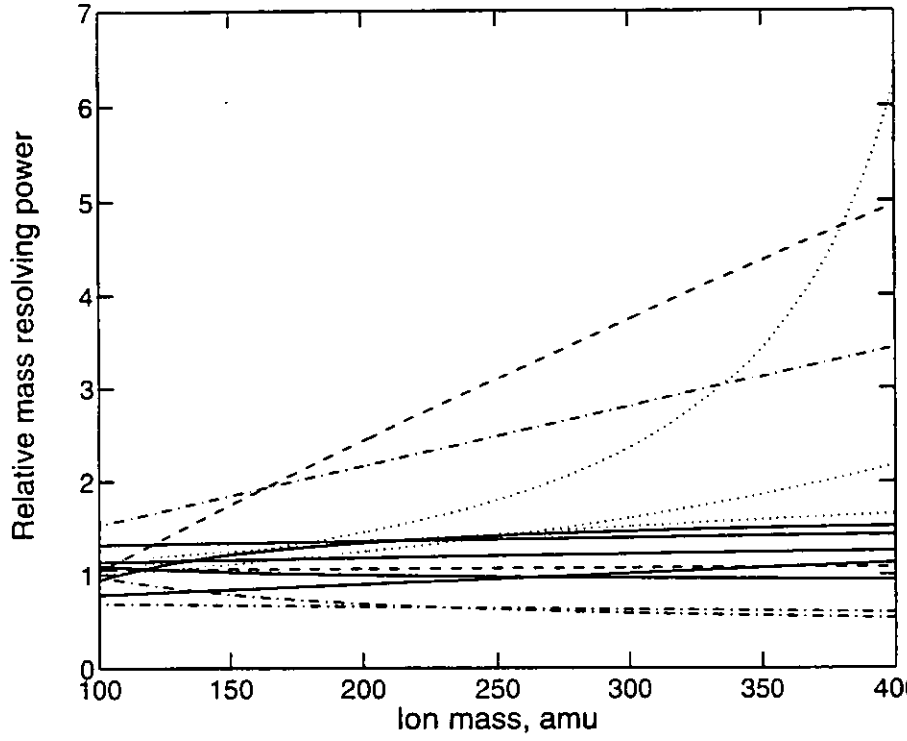

Fig 13 The relative mass resolving power of TOF instruments for insulators to conductors.

5.4 DAMAGE STUDY

Respondees were asked to follow the five main peaks for PTFE and PET defined in ref (5), for doses up to a total of 1 x 10^{18} ions/m^2. A detailed study of the effects of ion beam damage for these materials is given in ref(8). The PET is particularly sensitive to damage; the protonated monomer at a mass of 193 amu falls 10% in intensity after a dose of 0.11 x 10^{17} ions/m^2. The fragments from PTFE behave differently, with some fragment intensities reaching a plateau at a dose of 1.8 x 10^{17} ions/m^2. Therefore, the PTFE is useful for monitoring the control of the surface charge and the PET, which is very sensitive to damage, gives a measure of the ion fluence.

The dose at which the intensity of the PET $C_{10}H_9O_4^+$ ion (193 amu) had dropped by 10% and the dose at which the PTFE $C_5F_9^+$ ion (231 amu) peaked in intensity were measured for each instrument that supplied damage data. About 30% of the instruments were used and this reflected the difficulty in performing damage profile experiments using the older TOF instruments. The measured dose levels, for the intensity changes defined above for PET and PTFE, were then divided by the average values from the data set to determine the laboratory-

to-laboratory scatters. Instrument M was an outrider and was not included in this average. The scatter about the mean is shown in Fig 14. Data from respondees that supplied results for only one material are placed on the average value for the other material and are marked with a line to indicate the absence of that value. The relative standard deviations for the data for PET and PTFE are 41% and 35%, respectively. This is surprisingly good considering the difficulties of measuring the dose in these instruments. The average doses for the given damage levels are 73% and 100% of the values given in ref (8) for PTFE and PET, respectively. In ref (8) 4 keV argon ions were used whereas, here, the ion energies and ion masses are both higher so that damage is expected at lower thresholds. These results are, thus, excellent confirmation that damage limits may be set, may be effectively measured, and are transferable from material to material with a relatively small scatter. This means that any agreed static SIMS limit, i.e. the limit for damage free data, does not significantly depend on the instrument or the operating parameters and can be applied, equally, in all laboratories.

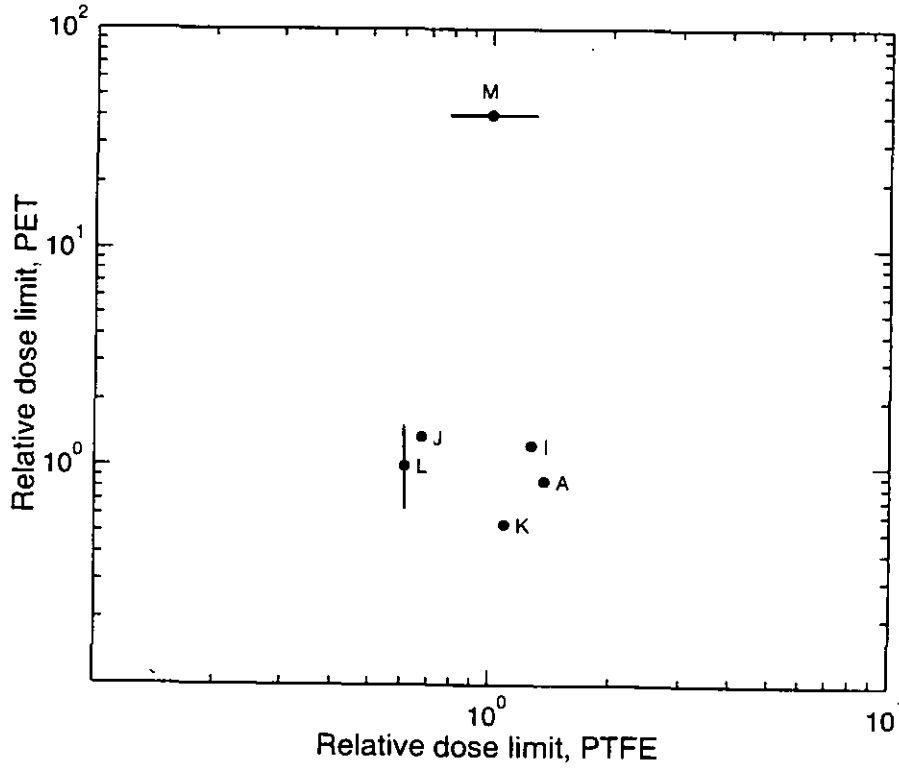

Fig 14 The scatter in the relative dose limits for PET and PTFE for six instruments. Instruments marked with a line supplied data for only one material, the missing data value is set to the mean for that material. The relative dose limit here is the measured dose divided by the average dose. The average here is 72% and 100% of the values found for PTFE and PET, respectively, using 4 keV argon in ref (8).

6 CONCLUSIONS

This work shows that static SIMS is developing as a reliable and reproducible technique. The repeatabilities of ion intensities, for all three reference materials, for both ion polarities, can be as good as 2% and for PTFE as low as 1%. Transferability of spectral data for comparison between one instrument to another or with library data is facilitated by use of the Relative Instrument Spectral Response, RISR. The reproducibility of the RISRs calculated from each reference material for both ion polarities can be as good as 6% for the best instruments with an average value, for 17 data sets, of 14%. This means that if the averaged RISR function is used to correct the spectra from a material for all instruments, the inter-laboratory scatter of intensity for the corrected spectra would be expected to be approximately 14%. Without this correction, the scatter on a log scale would be $\times/\div$ 1.55, i.e. approximately four times worse.

The three reference materials, of PTFE, PET and Irganox 1010 on silver, have proved to be good for understanding the behaviour of a very wide variety of static SIMS instruments. The use of PTFE, which has a low surface energy and is therefore easier to keep clean, but is an insulator, has shown that in most instruments the surface charge is controlled sufficiently for both positive and negative ion spectra. It would appear that some instruments can be very highly tuned to achieve high transmission and high mass resolution, so that each setable parameter can be very critical so that sample-to-sample repeatability degrades unless significant care is taken. The improvement between M and S shows this clearly. The PET reference material has shown that in some laboratories there are problems from PDMS contamination.

The damage study shows that instruments can be calibrated for ion beam dose to a scatter with a standard deviation of 38%. This is a major improvement from the large variability in the past and is sufficient to define the static SIMS limiting doses for imaging systems, where highly focused ion beams are used.

This study has met all of its initial aims with much superior repeatability than originally envisaged. This work forms a major platform for the development of static SIMS as an important analytical tool for accurate analyses and the detailed identification of molecules at surfaces.

ACKNOWLEDGEMENTS

The contributors to this inter-laboratory study are gratefully acknowledged. These include, in alphabetical order of first named:

D Briggs, M J Hearn and I W Fletcher, ICI Research and Technology Centre, UK.

R Canteri, Physics and Chemistry of Surface and Interface Division, CMBM, Italy.

G Egbers, D Lipinsky and A Benninghoven, Physikalisches Institut der Universität Münster, Germany.

B A Keller and P Hug, Swiss Federal Laboratories for Materials Testing and Research, EMPA, Switzerland.

F R Lang, D Leonard and H J Mathieu, Swiss Federal Institute of Technology Lausanne, EPFL, Switzerland.

J Likonen, Technical Research Centre of Finland, Chemical Technology, Espoo, Finland.

S J Pachuta and S G MacKay, 3M Corporate Research Laboratories, St Paul, Minnesota 55144, USA.

C Poleunis and P Bertrand, Université Catholique de Louvain, Unité PCPM, Belgium.

D Sykes and A Chew, ISST, Loughborough University, Loughborough, Leicestershire, UK.

REFERENCES

(1) M. P. Seah, P. J. Cumpson, R. E. Shawyer, *NPL AES and XPS intensity calibration software*, National Physical Laboratory, Teddington, UK (1997) .

(2) D. Briggs, A. Brown and J.C. Vickerman, *Handbook of Static Secondary Ion Mass Spectrometry (SIMS)*, Wiley, Chichester (1989).

(3) J.G. Newman, B.A. Carlson, R.S. Michael, J.F. Moulder and T.A. Hohlt, *Static SIMS Handbook of Polymer Analysis*, Perkin Elmer, Eden Prairie, MN (1991).

(4) *The Static SIMS Library*, Eds. J.C. Vickerman, D. Briggs and A. Henderson, Surface Spectra, Manchester, (1998).

(5) *The Münster High Mass Resolution Static SIMS Library*, B. C. Schwede, T. Heller, D. Rading, E. Niehuis, L. Wiedmann and A. Benninghoven, ION-TOF, Münster (1999).

(6) I S Gilmore and M P Seah, NPL Report CMMT(D)14.

(7) I S Gilmore and M P Seah, *Surf. Interface Anal.* **23**, 191 (1995).

(8) I S Gilmore and M P Seah, *Surf. Interface Anal.* **24**, 746 (1996).

(9) S Reichlmaier, J S Hammond, M J Hearn and D Briggs, *Surf. Interface Anal.* **21**, 739, (1995).

CHAPTER EIGHT

Towards Unfragmented Mass Spectra - the G-SIMS Procedure

1	INTRODUCTION	169
2	EXPERIMENTAL	170
3	RESULTS AND DISCUSSION	172
3.1	EFFECT OF ION BEAM ENERGY	172
3.2	FRAGMENT CASCADES	176
3.3	EFFECT OF ION BEAM SPECIES	178
3.4	THE GENTLE-SIMS (G-SIMS) PROCEDURE	180
4	CONCLUSIONS	191
REFERENCES		193

1 INTRODUCTION

In static Secondary Ion Mass Spectrometry (SIMS) the relative secondary ion yields are strongly influenced by the primary ion mass and energy. Development of the technique, particularly for dynamic SIMS, has provided a wide range of ion sources and energies for analysts to use. Gallium and similar sources give high spatial resolution, caesium and oxygen enhance the negative and positive ion yields, respectively, and argon and xenon are the traditional sources for ultra-high vacuum studies. As a consequence, the data reported from different laboratories may be expected to be significantly different and data in handbooks and libraries are only broadly comparable. These issues were recognised over a decade ago, but new sources have been developed to optimise the secondary ion yield of high mass fragments and to improve "finger-printing" analysis in the 20 to 200 amu range for identification. Briggs[1,2] and workers began a systematic investigation of polymer systems using He^+, Ne^+, Ar^+, Xe^+ and Ga^+ ions for energies in the range 1 keV to 10 keV. They concluded that the heavier ions gave a higher yield of large cluster ions and that this was enhanced by the use of low primary ion energies. Instrumentation at this time had inadequate charge compensation equipment, resulting in poor reproducibility for insulating samples. To circumvent this, Appelhans et al[3,4] developed an atom beam source using the auto-neutralisation properties of the molecular ion SF_6^-. They discovered that this polyatomic source gave ion yield increases of up to a factor of 20 for pharmaceutical compounds compared with the yields obtained with caesium at the same beam energy. More exotic ions such as ReO_4^- [5] are being used to improve analyses of environmental material. More recently, Benninghoven[6,7] has studied the improvements for a range of different polymers and also for Langmuir-Blodgett layers of arachidic acid. They reported that SF_5^+ gave a value for the figure of merit[8] of yield enhancement of up to a factor of 50, compared with the values for atomic ions.

To identify an unknown material using static SIMS, an analyst needs to be able to compare the measured spectrum with those available in libraries[9,10]. This may be done visually or, more recently, with the aid of computer search and matching algorithms. The variety of ion sources and energies in use, at present, makes this task more complex and, without understanding of the effects, the accuracy of the software matching algorithms is reduced. The present work aims to show the relation between the spectral intensities and the primary ion mass and energy and how this can be used to unify spectral data to facilitate the uptake

of spectral libraries and provide a simplification of the static SIMS spectra.

2 EXPERIMENTAL

The instrument used in this study, a CAMECA TOF SIMS IV, is of an open structure, single stage reflectron design[11]. The instrument is equipped with a high resolution Ga^+ focused liquid metal ion gun with an energy range between 12 keV and 25 keV, mounted at 45° to the sample surface normal. A dual source, electron impact and caesium, ion gun sharing a single focusing column, is also mounted at 45° to the sample surface normal. A 90° mass filter, following the electron impact source, allows the use of Ar^+, Xe^+ and SF_5^+ ions. Alternatively, Cs^+ ions produced from an in-line source may be used. For each analysis, the ion beam was digitally rastered with a 128 by 128 array over an area of 156 µm by 156 µm using a beam current of less than a picoamp. Total acquisition times were adjusted so that the ion dose did not exceed $1x10^{16}$ ions/m^2. To ensure the ion dose was uniform over the entire raster area, the spot size for each ion beam was defocused to be greater than 3 µm.

Three materials were analysed in this study, a bulk polymer of polytetrafluoroethylene (PTFE) together with spin cast films of polystyrene (PS), with a molecular weight of 2500, and polycarbonate (PC). Samples of PS were prepared from a 1mg/ml toluene solution and samples of PC from a 1.22 mg/ml tetrahydrofuran solution. Thin films were prepared on a clean 1 cm^2 silicon surface by spin coating in a modified centrifuge at 4000 r.p.m for 60 s. Prior to deposition, the silicon surface was cleaned of particulates using an argon jet followed by ultrasonic agitation in an ethanol bath for 5 minutes. To ensure that the coating was uniform, a number of repeat spectra were taken from the central 3 mm x 3 mm area. Analysis of these data gave a repeatability[12] relative standard deviation of 0.83%

A fresh sample was analysed for each different bombarding ion species. Spectra at different energies were taken from a square array with each analysis area separated by 900 µm. The order of acquisition was in ascending energy order, starting from right to left and top to bottom with the first middle and last spectra repeated at the same energy to give a check on the repeatability. Using this pattern, 16 analyses were possible for each sample. All spectra were at least 3 mm from the edge of the sample holder to prevent any effects of an uneven extraction field. To reduce any effects of sample inhomogeneity, for the spin cast samples,

two spectra were acquired from adjacent positions for each energy.

In this time-of-flight SIMS system, when analysing positive ions, the ion beam pulse is fired while the extraction voltage of +2 keV is applied. The primary ions are then deflected slightly away from the sample and towards the extraction electrode as they pass through this field. Even though the beam deflectors are adjusted so that the impact point is still aligned with the spectrometer axis, the angle of incidence of the ion beam is changed a small amount. The effect of ion energy on the angle of incidence at impact, calculated for the geometry of the sample region, is shown in Fig 1. The angle of incidence varies from 60° to 50° for energies between 5 keV and 20 keV. The small change in angle is expected to have a much weaker effect on the SIMS spectra than the effects of the energies and different source ions used here.

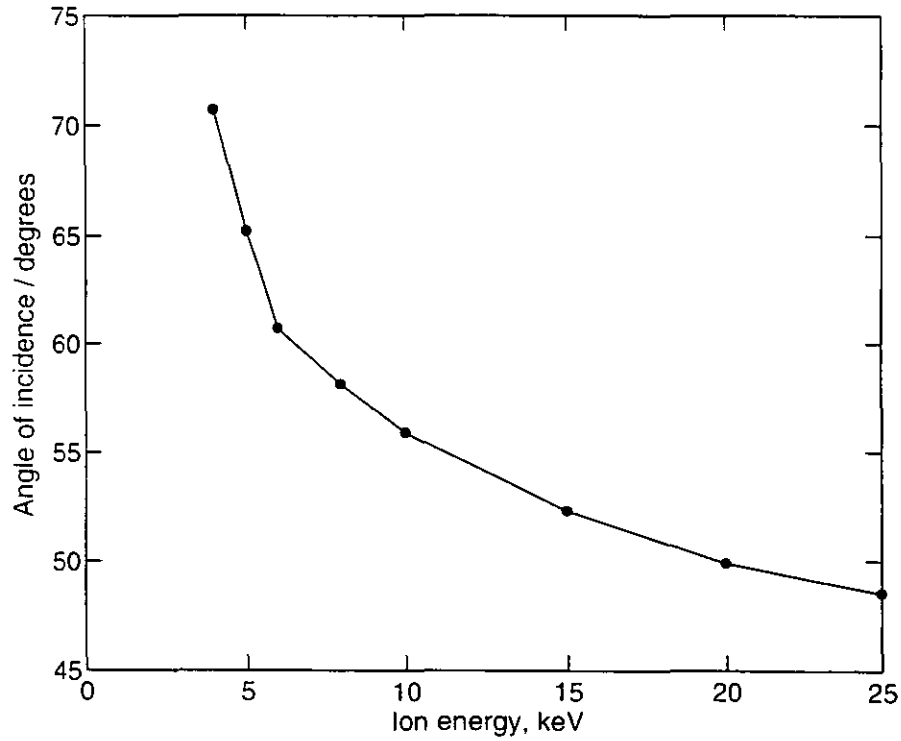

Fig 1 The effect of ion beam energy on the angle of incidence for the conditions used in the ION-TOF IV time-of-flight spectrometer, when analysing positive secondary ions.

For the insulating PTFE sample, charge stabilisation was achieved by using electrons from a low energy electron gun with the filament set well back from the sample to avoid damage by sample heating. Parameters were set as recommended by the manufacturer. This gave an excellent charge stabilization performance. On close inspection of the peak intensities

during this study, however, it was evident that electron beam damage was causing spectral changes at about the same level as those observed for different ion energies. As the sample was moved from one analysis position in the measurement array to the next, the total electron beam neutralisation dose increased. This caused spectra taken at the beginning and at the end of the array to differ by as much as 49%. The cause of this problem was an excessive electron current, measured at -13 μA. By reducing the filament current and shortening the time the gun was on between ion pulses, the current was reduced by three orders of magnitude. Charge neutralisation remained effective and further tests showed that the problem of electron beam damage had been eliminated.

3 RESULTS AND DISCUSSION

3.1 EFFECT OF ION BEAM ENERGY

In this study, spectra are acquired at high mass resolution with 200 ps time bins. Analysis for three materials with five different energies and five ion species generates an enormous volume of data. To reduce this to a manageable size, peaks are automatically identified using computer software incorporating a table with the peak centroid and width data. Typically, around 300 peaks are defined for each material.

After mass calibration of the spectrum, peak areas are measured for the defined peaks. This provides a matrix of intensities, $I_{x,y}$, with x_0 mass peaks at y_0 beam energies at mass M_x for each source ion. To analyse the effects of fragmentation, we proceed as follows. Each spectrum is normalised to give intensities $J_{x,y}$ by dividing by the geometric average intensity of its x_0 mass peaks. This removes any absolute yield or beam current drift from spectrum to spectrum. Thus

$$J_{x,y} = \frac{I_{x,y}}{\left(\prod_{x=1}^{x_0} I_{x,y}\right)^{1/x_0}} \qquad (1)$$

An average spectrum for all of the ion beam energies, A_x, is then formed from this

normalised set using

$$A_x = \frac{1}{y_0} \sum_{y=1}^{y_0} I_{x,y} \qquad (2)$$

This average spectrum is useful to assess the spectrum to spectrum variations. A new matrix of relative intensities, $F^*_{x,y}$, is produced by dividing each normalised spectrum, by A_x. This brings all intensities to near unity so that changes are clearly visible. Values of $F^*_{x,y}$ from the PS spectra for 10 keV argon ions are shown in Fig 2, together with a simple quadratic fit to the data. Whilst there is noticeable scatter about the fitted function, it does show the general behaviour. The fits for the whole data set, for energies between 4 keV and 10 keV, are shown in Fig 3. The overall effect of ion beam energy is weak over the mass range to 300 amu. Data acquired at 10 keV, compared with those at 4 keV, show a 50% increase in the intensity of low mass fragments but a corresponding decrease in high mass fragments.

Closer inspection of the data in Fig 2 shows the data values of $F^*_{x,y}$ fall into a set of parallel groups of points. Within each group, intensity changes between masses separated by a few amu are as large as the overall change in intensity over the mass scale. The relative peak intensities of neighbouring peaks vary surprisingly strongly for different energy beams. This is the reverse of the concept usually implemented in software for spectra identification. It is generally assumed, in these algorithms, that changes in the relative peak intensities of neighbouring peaks for different spectrometers will be weak compared to variations over the entire spectra.

The $F^*_{x,y}$ values of 4 keV and 10 keV argon ion data for PS are replotted in Fig 4 with any fragments identified as C_xH_y plotted as a filled circle. The largest fragment in each group is $C_nH^+_{n+2}$, followed (at lower mass) by a cascade of ions with successive losses of one hydrogen atom. We, thus, call this a fragment cascade plot. Fragments of the form $C_nH^+_{n+2}$ are more closely related to the polymer backbone whilst those with hydrogen loss are indicative of damaged fragments and contribute little extra information in the original spectrum. Fragments with the most hydrogen atoms for each group have higher $F^*_{x,y}$ values for 4 keV energy compared to 10 keV energy, by a factor of 1.9.

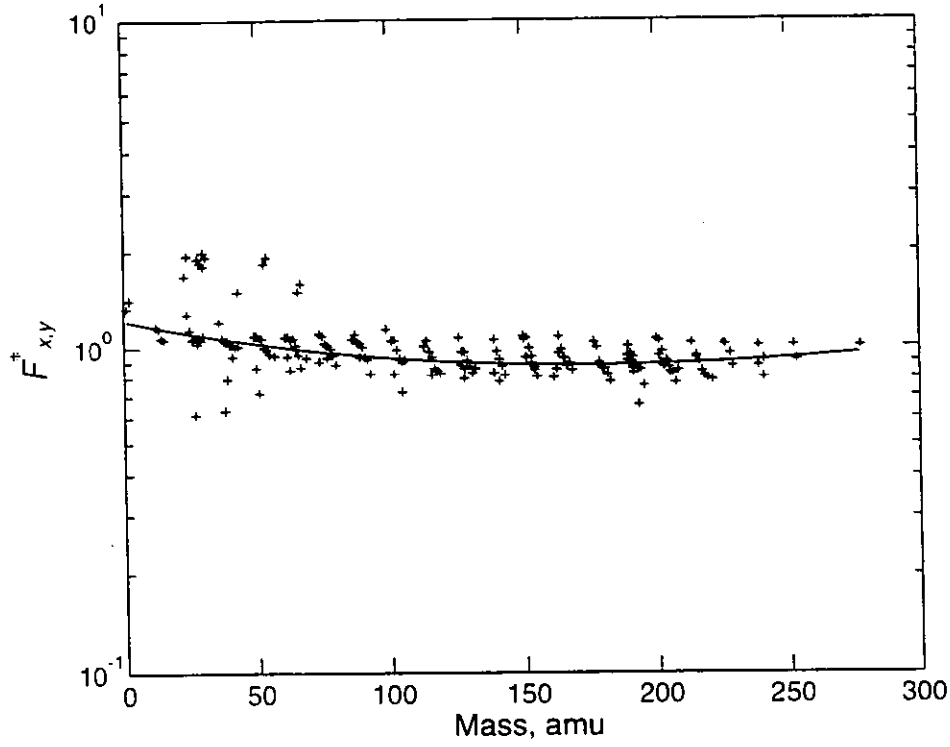

Fig 2 Values of $F^*_{x,y}$ for positive secondary ion data from polystyrene acquired with 10 keV argon ions.

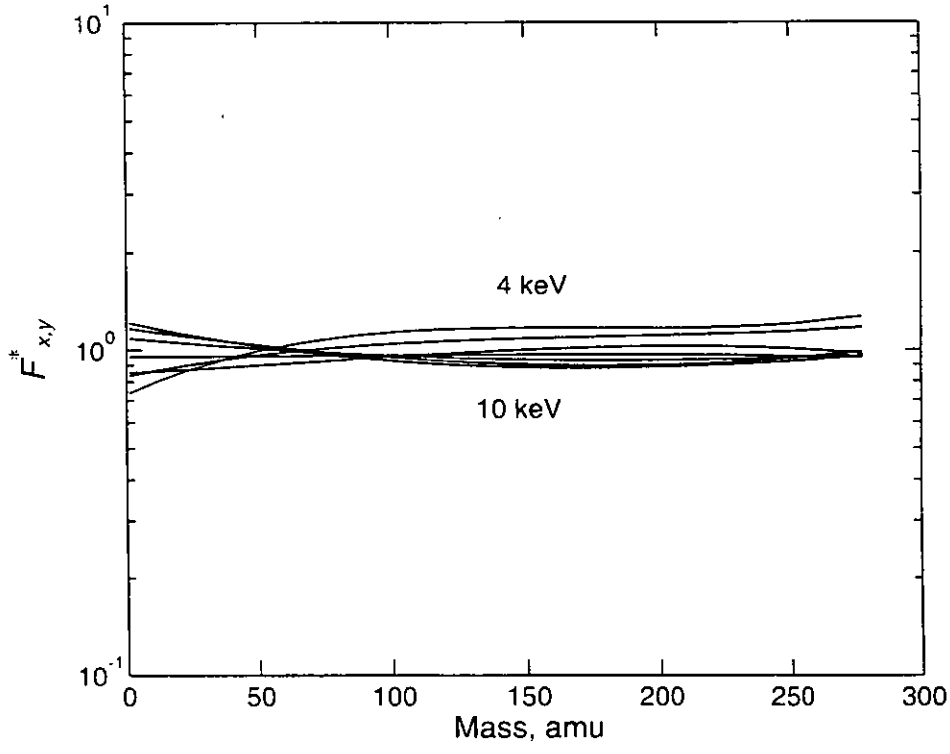

Fig 3 Fits to values of $F^*_{x,y}$ for polystyrene data acquired with argon ions of energies from 4 keV to 10 keV.

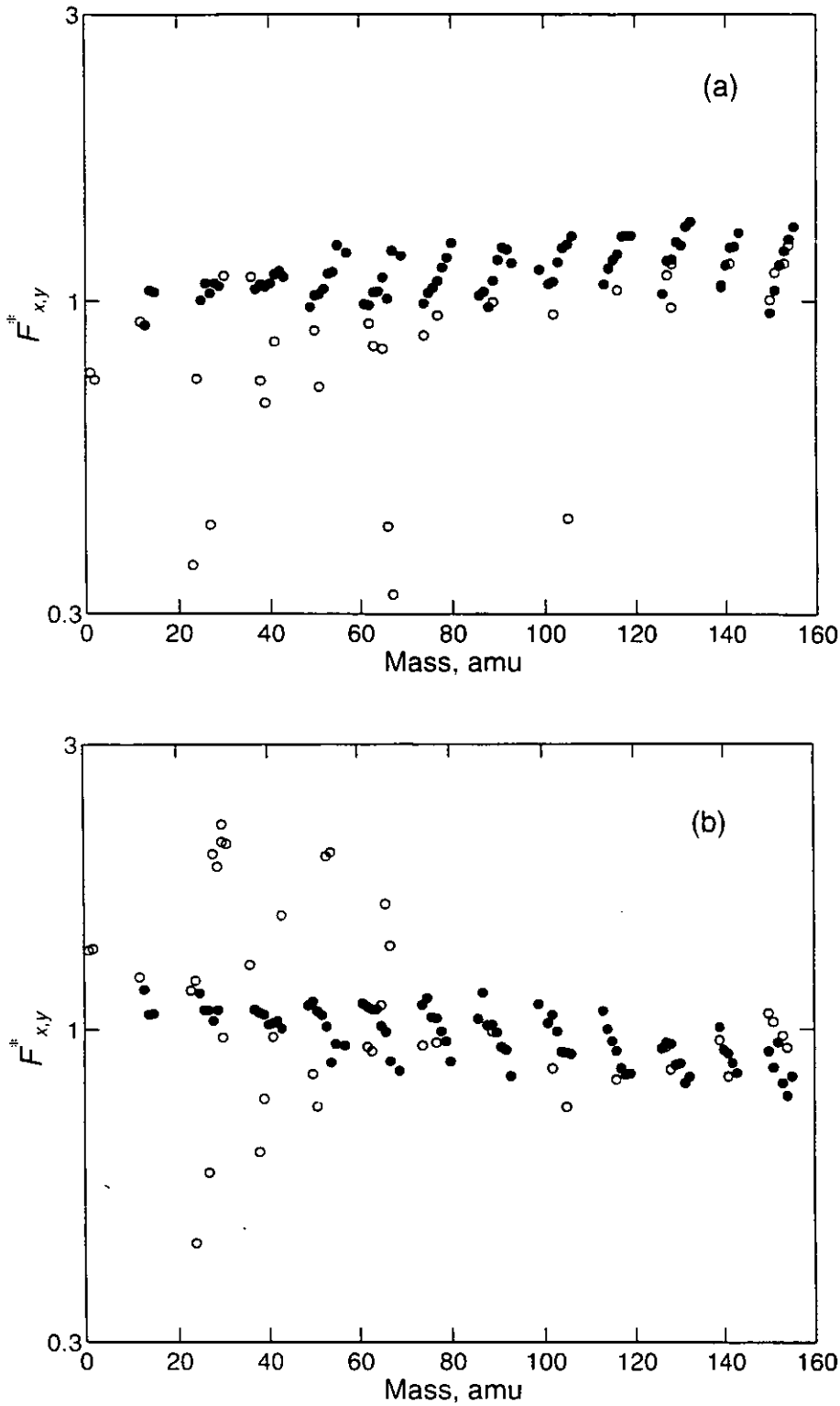

Fig 4 Fragment cascade plot showing polystyrene $F^{*}_{x,y}$ values for (a) 4 keV argon and (b) 10 keV argon ions. Data points identified as belonging to fragments of the type C_xH_y are plotted with a filled circle (●).

3.2 FRAGMENT CASCADES

In this section we consider how a fragment of the molecule leads to daughter products. For example, how the fragment C_nH_{2n-i} is obtained from C_nH_{2n}, and hence how their intensities are related.

We consider, in the recoil from the primary impact, that the surface zone may be characterised by a fragment surface plasma temperature, T, which, for a particular ion impact, will vary with the co-ordinates on the surface. Statistically, averaged over many impacts, one may write T as a function of the radius, r, from the point of impact. The plasma temperature is also a function of the bombarding ion species, S, and the impact energy, E. The total ion yield will be related to the integral of T over the sample but, for our purpose, we need the effective fragment surface plasma temperature, T_p, which is the average temperature characterising the emitted fragments. Thus, the total ion yield and our T_p will not be directly related. We envisage that the unreconstructed and undegraded parent fragment is given excess internal energy in the surface plasma and, as a result, has a probability of degrading or reconstructing between the time of the primary ion impact and the time of detection at the end of the flight path.

We now consider the series C_nH_{2n}, C_nH_{2n-1}, C_nH_{2n-2} and note that the energy, Δu, to remove each succesive hydrogen atom is approximately the same. Thus, the number of fragments, N_i, of composition C_nH_{2n-i}, derived from N_0 components of composition C_nH_{2n}, is given by the simple partition function relation:

$$N_i = N_0 \exp\left(\frac{-i\Delta u}{kT_p}\right) \tag{3}$$

In terms of the measured ion yields, if N_i^+ and N_0^+ are the relevant numbers of ions, then

$$N_i^+ = N_i \; Y_i^+(T_p) \tag{4}$$

and

$$N_0^+ = N_0 \; Y_0^+(T_p) \tag{5}$$

where $Y_i^+(T_p)$ is a factor which allows for the fraction of the particles that are ionised and which are subsequently detected. Thus,

$$N_i^+ = N_0^+ \frac{Y_0^+(T_p)}{Y_i^+(T_p)} \exp\left(\frac{-i\Delta u}{kT_p}\right) \quad (6)$$

If we now consider these ion yields at the two ion beam energies E_1 and E_2, with associated fragment surface plasma temperatures T_{p1} and T_{p2}, we get

$$\frac{N_i^+(E_2)}{N_i^+(E_1)} = \frac{N_0^+(E_2)}{N_0^+(E_1)} \frac{Y_0^+(T_{p2})}{Y_0^+(T_{p1})} \frac{Y_i^+(T_{p1})}{Y_i^+(T_{p2})} \exp\left[\frac{-i\Delta u}{k}\left(\frac{1}{T_{p2}} - \frac{1}{T_{p1}}\right)\right] \quad (7)$$

The partitioning of the neutral and ion species will depend exponentially on the surface plasma temperature and so Eq (7) reduces to

$$\frac{N_i^+(E_2)}{N_i^+(E_1)} = \frac{N_0^+(E_2)}{N_0^+(E_1)} \exp\left[\frac{-i\Delta u'}{k}\left(\frac{1}{T_{p2}} - \frac{1}{T_{p1}}\right)\right] \quad (8)$$

where $\Delta u'$ now incorporates the effects of both the fragmentation and the ion yields, $Y_i^+(T_p)$.

The intensity ratio on the left of Eq (8) is $F_{x,i}$ where

$$F_{x,i} = F_{x,0} \exp(-\beta i) \quad (9)$$

and $-\beta i$ is given by the items in square brackets on the right of Eq (8). Thus, an intensity ratio plot of $F_{x,i}$ versus mass, with a $\log_e$ ordinate scale, will show a straight line with gradient β per increment in i. In the case used here, where the increment in i is a hydrogen atom, the gradient is simply per amu. If $\Delta u'$ is positive and if the surface plasma temperature, T_{p1}, at energy E_1 is greater than the surface plasma temperature, T_{p2}, at energy E_2, β will be positive and vice versa. Note that the energy to remove a hydrogen atom from $C_{12}H_{24}$ will be very similar to that from C_6H_6 so that the gradients, β, will be same for all hydrogen loss series in the intensity ratio plot. This intensity ratio plot shows clearly the fragmentation cascades and so will be termed a Fragment Cascade Plot in the rest of this paper.

We may see positive gradients in Fig 4(a) and negative gradients in Fig 4(b) where $F_{x,i}$ is plotted with the E_1 spectrum being an average spectrum over all of the data for all energies. This average is equivalent to a spectrum for argon of about 7 keV. Where this average Ar spectrum is used we denote $F_{x,i}$ as $F^*_{x,i}$.

The intensity ratio of Fig 4 is replotted in Fig 5 against the number of hydrogens lost, i, for the C_6 series (n = 6). The data are accurately characterised by the exponential function of Eq (9). Note that, in order to obtain plots of this precision, the repeatability of the intensities, when changing from one beam energy to another and back again, needs to be considered. The scatter in Fig 5 is 1% and mainly arises from the E_2 spectrum since that for E_1 is summed over many spectra. In this work the spectral intensities for the relevant peaks were from 2000 to 20000 and the shot noise statistics were the main contribution to the 1% scatter. The instrument and sample repeatabilities were, therefore, significantly better than 1%.

Observation of the parallelism of the gradients in Fig 4 shows that, for $n > 3$, a single value of $\Delta u'$ or β may be used to describe the fragmentation process. The averaged gradient, β, is plotted in Fig 6 against the argon ion beam energy. The dependency is, to a good approximation, linear and shows that fragmentation increases with increased beam energy. The higher the surface plasma temperature, the greater the degree of successive fragmentation, and hence the more negative the value of β at higher beam energies.

3.3 EFFECT OF ION BEAM SPECIES

Measurements of β provide a framework to build an overall understanding of the effects of different primary ion mass and energy. To do this, the matrix, $F^*_{x,y}$, is formed with the common overall normalisation based on the average energy argon spectrum $A_{x,Ar}$. Values of β, determined for each species and energy, are plotted in Fig 7(a), (b) and (c) for the polystyrene, PTFE and polycarbonate data, respectively. Note that the ordinate range in each plot is the same but that the PTFE values are more negative. The data for Figs 7(b) and (c) are obtained from plots like Fig 4 but for PTFE and PC.

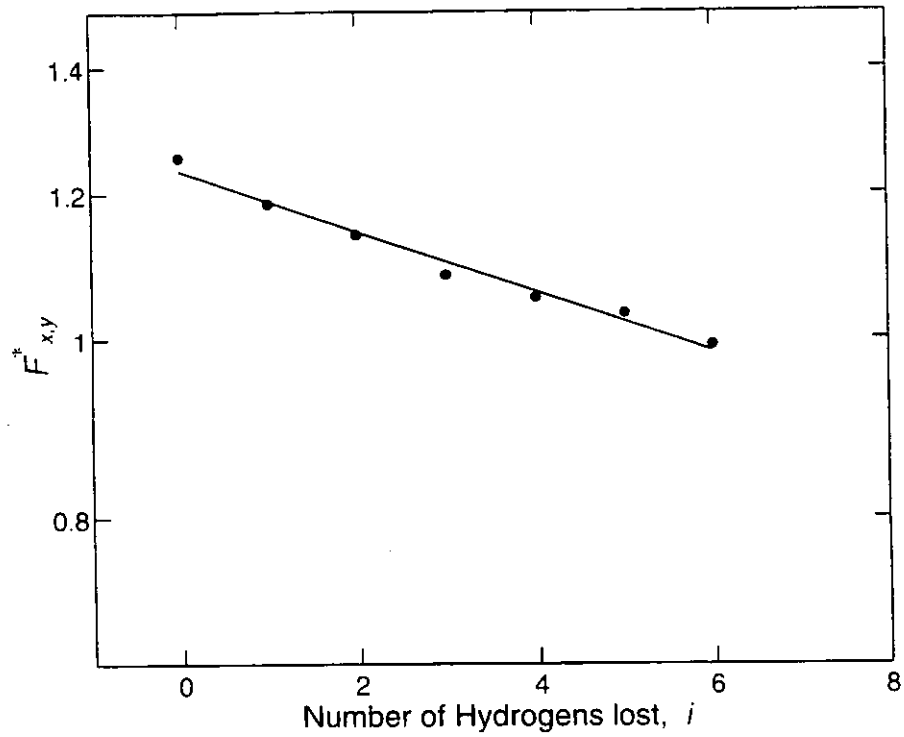

Fig 5 Detail of Fig 4(a) for the C_6 fragments replotted against number of hydrogen atoms lost.

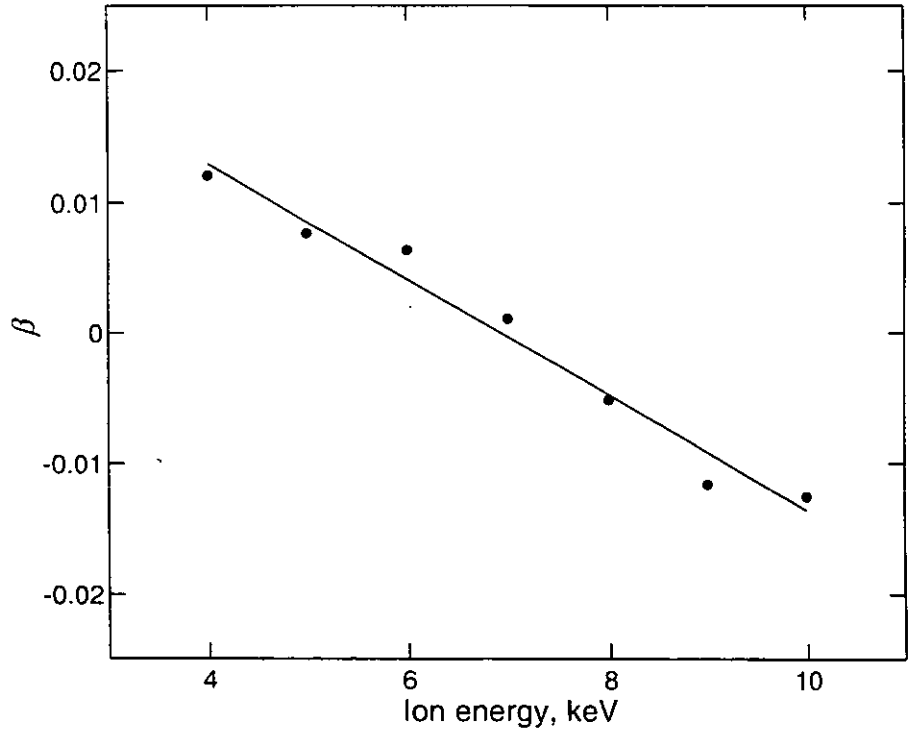

Fig 6 Average cascade gradient, β, for argon energies from 4 keV to 10 keV for polystyrene.

Since the fragmentation behaviours in Figs 7(a) and (b) are linearly dependent on energy, data at only two energies were acquired for polycarbonate. The cascade gradient plots for each material unify all of the fragmentation behaviour for the five different sources and the various beam energies. The behaviour shown for PC and PS is similar. The primary ions of higher mass create less fragmentation (higher β values) and, for monatomic ions, the fragmentation increases with energy. The similar behaviour of Cs^+ and Xe^+, which are of different chemistry but similar mass, indicates that there is no effect of ion chemistry. The linear energy dependence is found for all of the primary ions in this study. The polyatomic ion, SF_5^+, retains the linear dependence on energy but now the fragmentation reduces with increasing energy. This result is consistent for all three materials.

The behaviour of PTFE, shown in Fig 7(b), is different from that of the other two materials. Here, the benefit of increased primary ion mass is lost. Significantly more fragmentation is produced by the polyatomic ion than the monatomic ions. This may arise from the higher mass density of PTFE (average Z = 8) compared with PS (average Z = 2.67) or PC (average Z = 4.06). A further effect may be the unusual surface morphology of PTFE. A high resolution scanning electron microscope (SEM) image of PTFE (coated with a thin layer of gold to reduce charging) is shown in Fig 8. PTFE is formed by compression of a colloidal suspension. The tape, used in this study, is skimmed from a drum which causes stretching of the colloid particles, seen as vertical lines in the figure. Further topography is seen as islands of colloid particles produced by separation at the surface. In a previous study of damage in polymers[8] it was also found that there was a loss in efficiency for PTFE when using xenon rather than argon, but a gain in efficiency for PET.

3.4 THE GENTLE-SIMS (G-SIMS) PROCEDURE

Identification of a material from the static SIMS spectra is not straightforward. Currently this is achieved by pattern recognition and comparison with library spectra. We have seen, in the earlier part of this work, that the patterns may change significantly for different ion beam species and energies. The wide variety of ion beam sources and energies in use at present

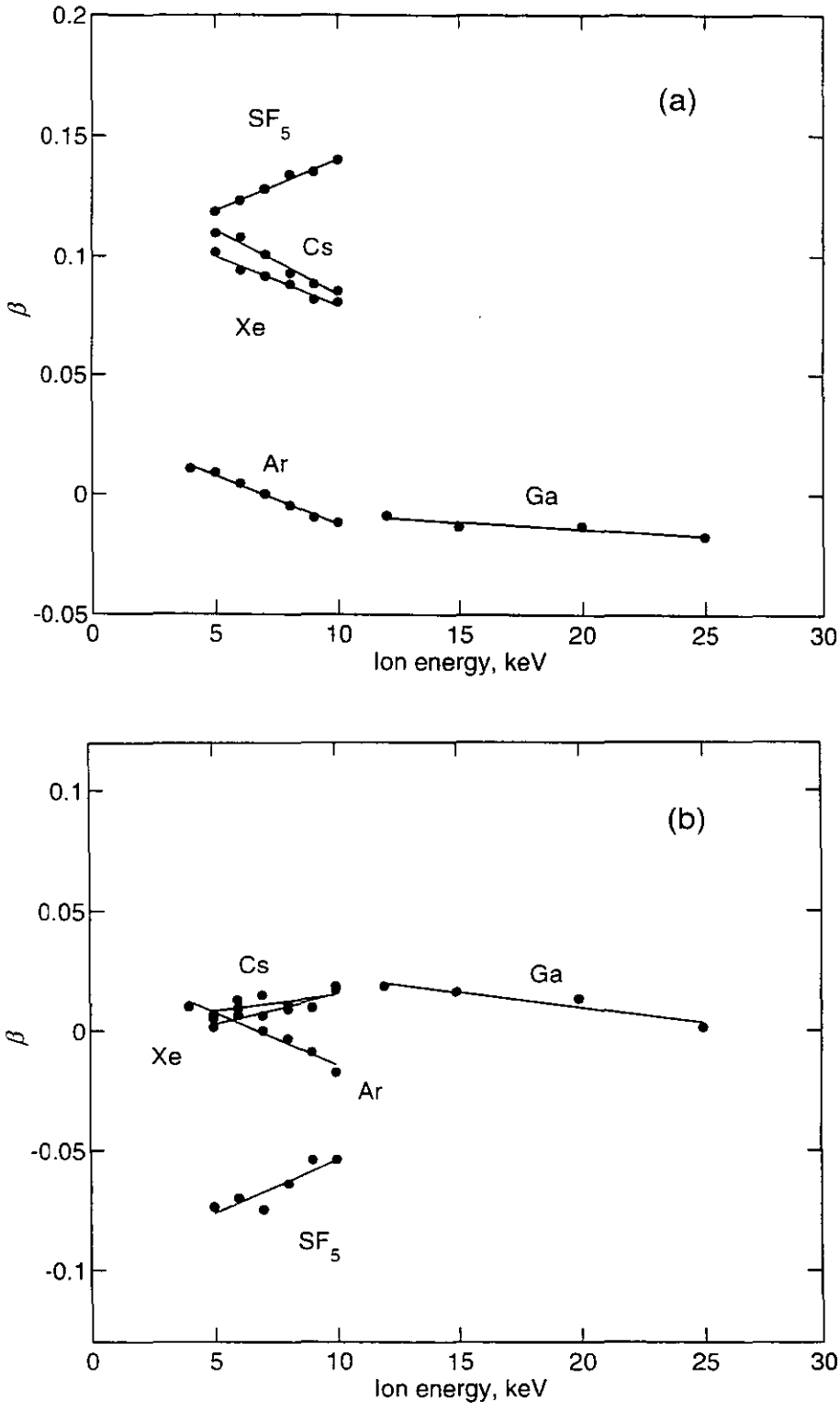

Fig 7 Unified cascade gradient plots for Ar^+, Ga^+, Xe^+, Cs^+ and SF_5^+ for energies between 4 keV and 25 keV (a) polystyrene, (b) PTFE and (c) polycarbonate.

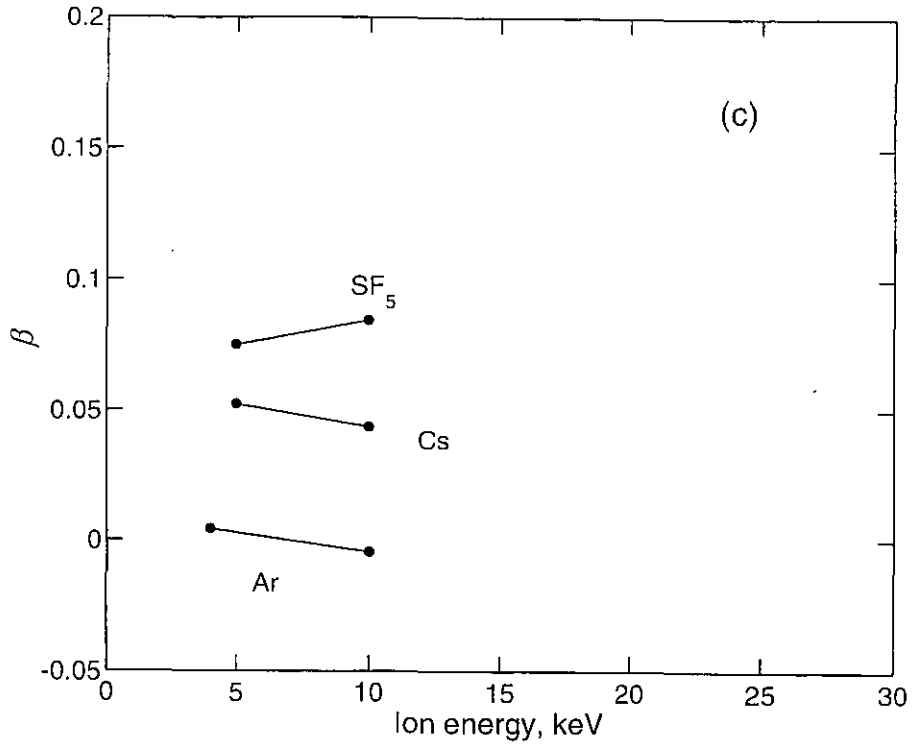

Fig 7 Unified cascade gradient plots for Ar^+, Ga^+, Xe^+, Cs^+ and SF_5^+ for energies between 4 keV and 25 keV (a) polystyrene, (b) PTFE and (c) polycarbonate.

Fig 8 SEM image of PTFE coated with a thin gold layer. (Field of view 7.5 μm x 5.8 μm).

means that spectral matching and identification with libraries is complicated. Quantification of mixtures is also impaired. Usually a characteristic peak is identified for each material. In many cases this is a subjective choice. For example, one might, with good reason, choose the tropylium ion for PS but, as we shall see later, this would have been a poor choice.

A method is required to reduce the large number of peaks in the static SIMS spectra produced by excessive fragmentation but to leave those peaks of ions which are more clearly diagnostic of the material. We require those fragments ejected from the surface characterised by a low surface plasma temperature (i.e. a high value of β). Ideally one would like to move to a state where only unreconstructed fragments are observed - at the same time one would prefer to retain some useful intensity. We do this as follows. First, for a monatomic ion species, the ratio of the intensities, $N_i^+(E_2)$, for low energy (E_2) to those at high energy, $N_i^+(E_1)$, gives a factor, F_x. This term is related to the effective surface plasma temperatures T_{p1} and T_{p2} from Eqs (8) and (9). Since T_{p1} and T_{p2} are of a similar magnitude and T_{p2} is less than T_{p1} by ΔT, we may first consider the factor F_x^2 which would be the F_x value for surface plasma temperatures T_{p2}-ΔT and T_{p1}. Thus, one could use F_x^{13} or some high power to deduce the result at a significantly lower surface plasma temperature than that relevant to any of the recorded spectra. A plot of this function would look just like Fig 4 except that the ordinate, instead of being one order of magnitude would be 13 orders of magnitude.

We may now generate a low surface plasma temperature static SIMS spectrum by multiplying an existing spectrum, N_x, with the factor F_x^{13}. This forms the G_0-SIMS spectrum with intensities $I_{0,x}$ given by

$$I_{0,x} = G_{0,x} \; N_x \tag{10}$$

and

$$G_{0,x} = M_x \; F_x^a \tag{11}$$

where a, as given above, is taken as 13. The additional factor M_x, the mass of the emitted fragment, is found useful to enhance the natural fall in emission with mass. The exact number of 13 for a is not critical but has been found to be a useful value. Figure 9(a) shows

the static SIMS spectrum, N_x, for polystyrene acquired using 10 keV argon ions and Fig 9(b) the G_0-SIMS spectrum, $I_{0,x}$, where F_x is derived from the ratio of a spectrum using 4 keV argon ions to that at 10 keV. The G in G-SIMS is used to denote the intention of developing an approach that extracts data only from the most gentle part of the process (gentle SIMS) so that structures may be deduced directly from the spectra.

The G_0-SIMS spectrum is directly based on the above surface plasma theory. Users can retain the essential aspects of the theory, whilst not completely suppressing fragments which may be strong in the N_x spectrum, by using a slightly different equation which is very similar for F_x above unity but does not attenuate peaks as strongly for $F_x <$ unity. This function is given by the G_1-SIMS spectrum, $I_{1,x}$, where

$$I_{1,x} = G_{1,x} N_x \tag{12}$$

and

$$G_{1,x} = M_x \, 10^{F_x^2} \tag{13}$$

Figure 9(c) illustrates the G_1-SIMS spectrum. The factor $10^{F_x^2}$ is arbitrary but is a mathematically convenient form which gives a similar result to F_x^{13} for enhancing the upper data points in Fig 9(a) but does not attenuate the lower data points as quickly. Thus, Figs 9(c) also includes the weaker peaks which may yet prove to contain useful information.

The strong power dependence in Eqs (11) and (13) creates arbitrarily high intensity values and so, for convenience, the peak area of the most intense peak is normalised to unity. What we have done in the G-SIMS procedure is to blend information from the fragment cascade with the original spectral intensities. Those fragments which have little degradation are boosted in intensity and those with significant degradation are suppressed. This is what would be observed if one could do static SIMS with a low T_p value. In Fig 9 we show the original static SIMS spectrum for PS acquired with 10 keV Ar^+ together with the two options of the gentle SIMS spectra. Whilst the two G-SIMS spectra are nearly identical, the original and the two G-SIMS spectra are clearly very different. The dominant peak in the G-SIMS

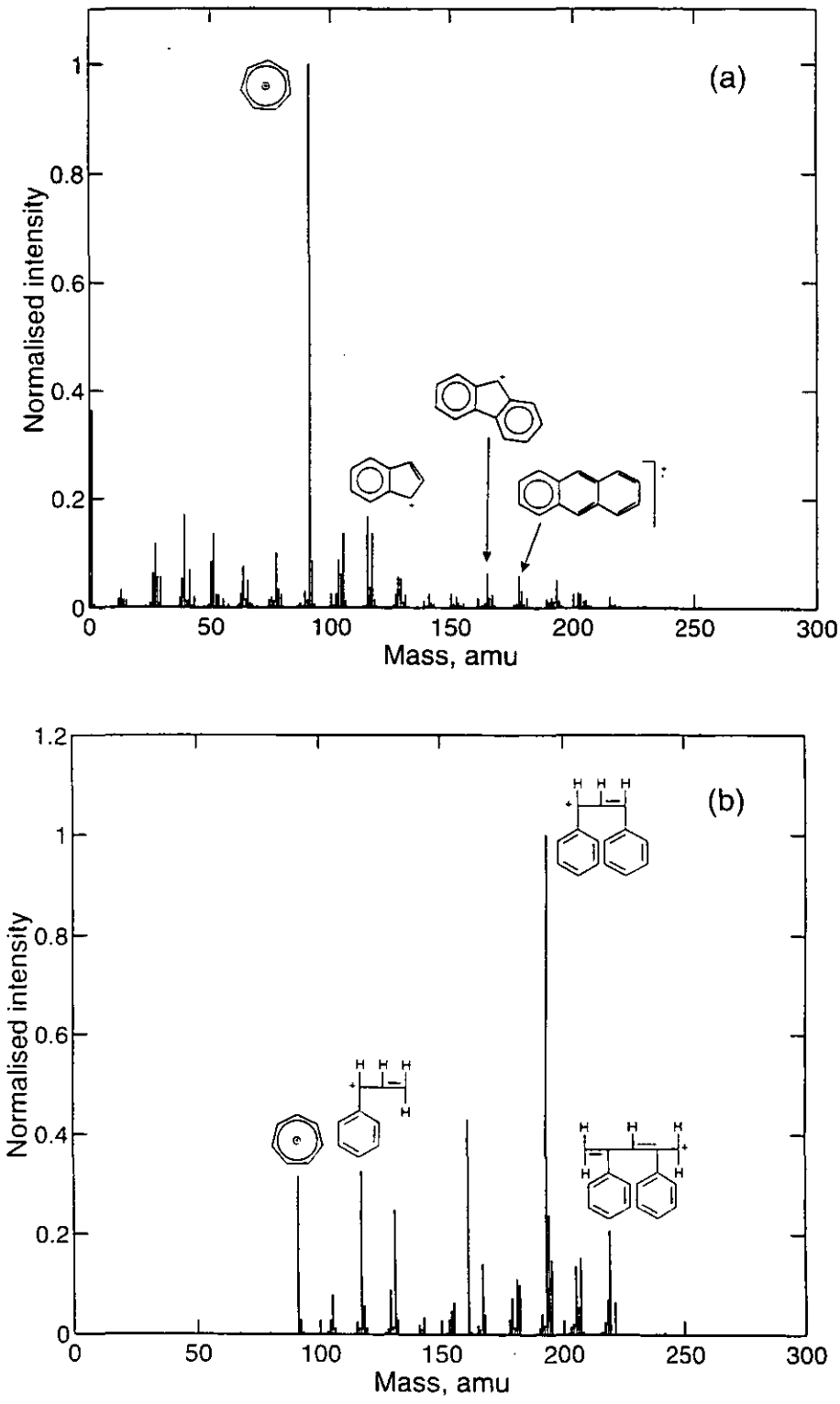

Fig 9 Positive ion spectra of polystyrene using 10 keV argon ions (a) Static SIMS, (b) G_0-SIMS and (c) G_1-SIMS.

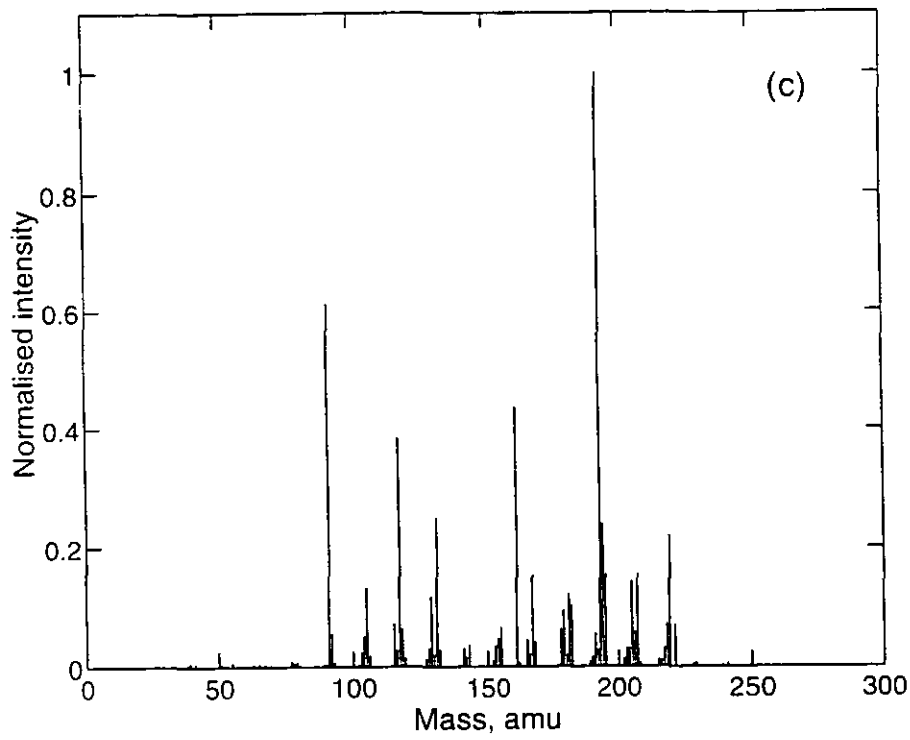

Fig 9 Positive ion spectra of polystyrene using 10 keV argon ions (a) Static SIMS, (b) G_0-SIMS and (c) G_1-SIMS.

spectra is the $C_{15}H_{13}^+$ ion followed by ions at nominal mass 91, 105, 117, 131, 161, 193 and 219 amu attributed to $C_7H_7^+$ (tropylium), $C_8H_9^+$, $C_9H_9^+$, $G_{10}H_{10}^+$, $C_{12}H_{17}^+$, and $C_7H_{15}^+$. Each of these ions, except tropylium, are simply derived from the polystyrene backbone. The pendant phenyl group in their structure makes them easily recognisable as originating from PS. In contrast, the original spectrum has a dominantly intense tropylium ion followed by ions at mass, 115, 128, 165 and 178. Structurally, these ions have a complex linked cyclic arrangement which exhibits little direct resemblance to the polystyrene structure. The polycyclic aromatic structures are very stable ions produced from the high energy fragmentation cascade, either as recombination events or the end result of a decay process for a molecule originally with excess internal energy. These ions are misleading as they appear to be very characteristic but, when used in quantification, give poor results. The G-SIMS spectra has overshadowed these peaks with those that are truly characteristic. The static and G-SIMS spectra for PTFE are shown in Fig 10 for 10 keV argon ions. Here, again, F_x is derived from spectra using 4 keV and 10 keV argon ions. It is evident, from the static SIMS spectra, that the fragmented pattern is unusually simple, most peaks have the formula C_nF_{2n-i} for $1 \leq i \leq 5$ and $i > 2n\text{-}1$. The G-SIMS procedure works well here but, unfortunately there

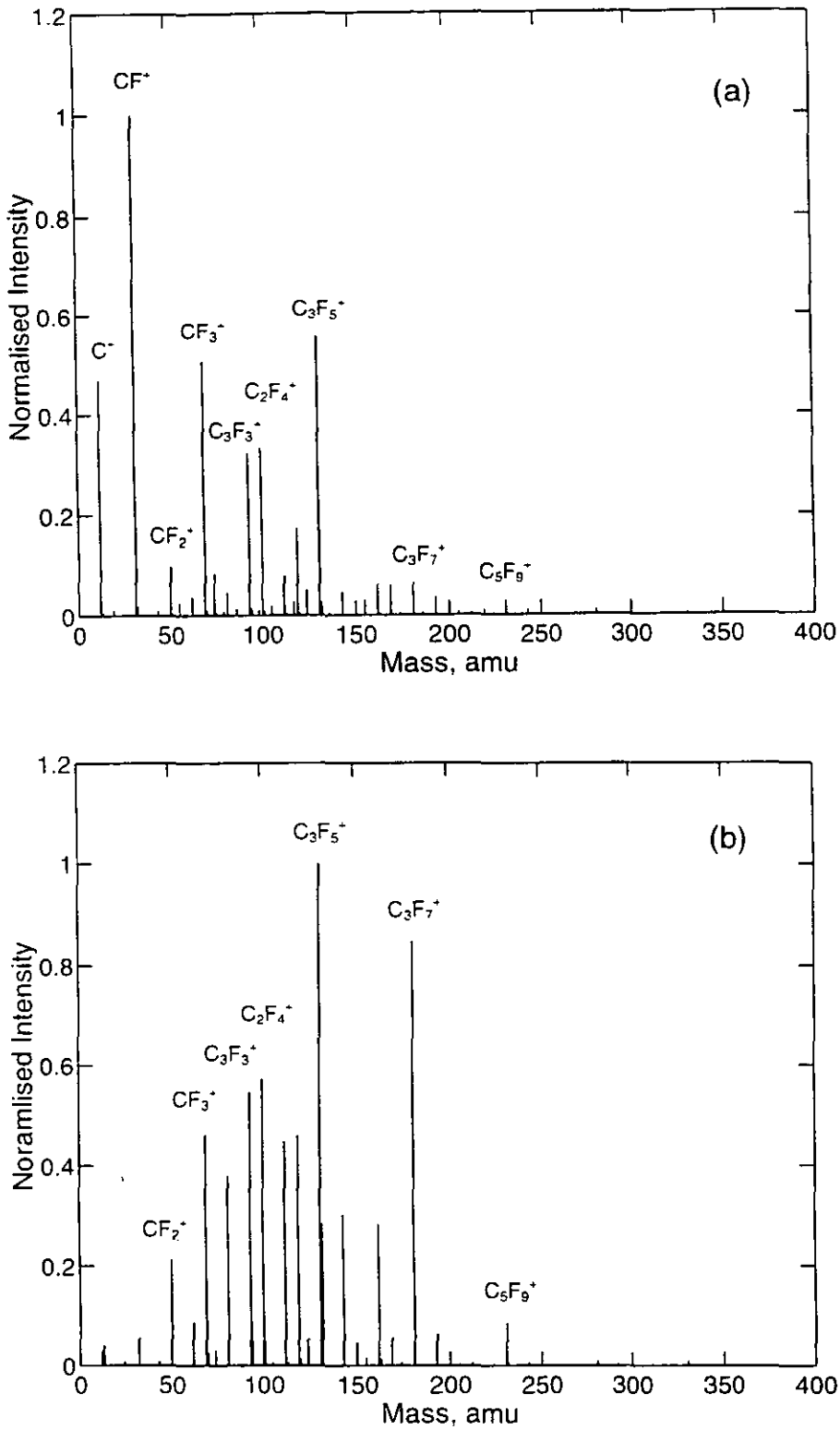

Fig 10 Positive ion spectra of PTFE using 10 keV argon ions (a) Static SIMS acquired with 10 keV argon, (b) G_0-SIMS and (c) G_1-SIMS.

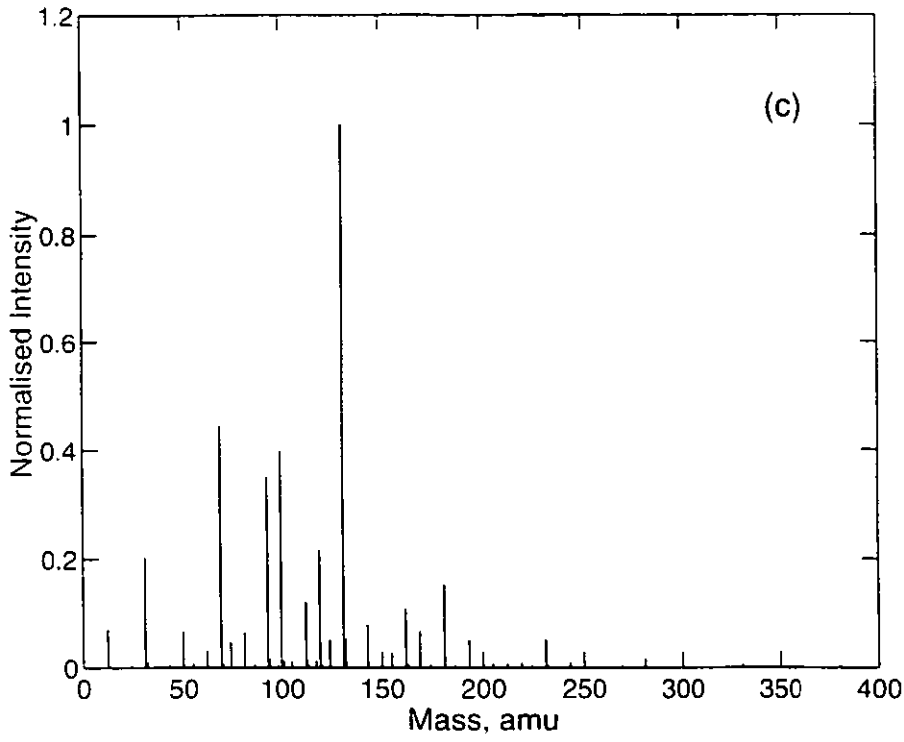

Fig 10 Positive ion spectra of PTFE using 10 keV argon ions (a) Static SIMS acquired with 10 keV argon, (b) G_0-SIMS and (c) G_1-SIMS.

is little more that can be done to simplify the spectrum further, the result being similar to the static SIMS spectrum. Polycarbonate has a more complex structure than the previous samples, additionally incorporating oxygen, and so provides a good test for the effectiveness of the G-SIMS procedure. Here, we investigate the effectiveness of a slightly different approach. It is evident from Fig 7(c) that we can increase the strength of the term F_x using the ratio of spectra acquired with high and low mass ion beams rather than by varying the energy for one ion. For PS there is a gain of a factor of 7 by using the ratio of the spectra for caesium and argon at 10 keV. There is a further advantage here for time-of-flight systems because it is easier to operate high energy beams to give the small pulse widths necessary for good mass resolution. To resolve the C,H,O containing ions in the PC spectrum, a mass resolution of at least 5000 is required. The analogue of Fig 4 is shown in Fig 11 for the ratio of the positive ion spectra for 10 keV caesium and 10 keV argon. Fragments identified as belonging to C_xH_y groups are plotted with a filled circle and fragments additionally containing oxygen are plotted as open circles. By using different bombarding ion masses, we have introduced a general mass dependence into the ratio values. This is removed by a simple cubic fit to the data using a least modulus minimisation, as shown by the line in Fig 11. It is clear that the

oxygen containing fragments follow a series of lines parallel to the C_xH_y groups and that the least damaged fragments are at the head of each parallel group. This means that these oxygen containing fragments will be emphasised in the G-SIMS spectrum and the hydrocarbons will be reduced. The effect of applying the G-SIMS procedure to PC is shown in Fig 12 together with the original static SIMS spectrum acquired with 10 keV caesium for comparison.

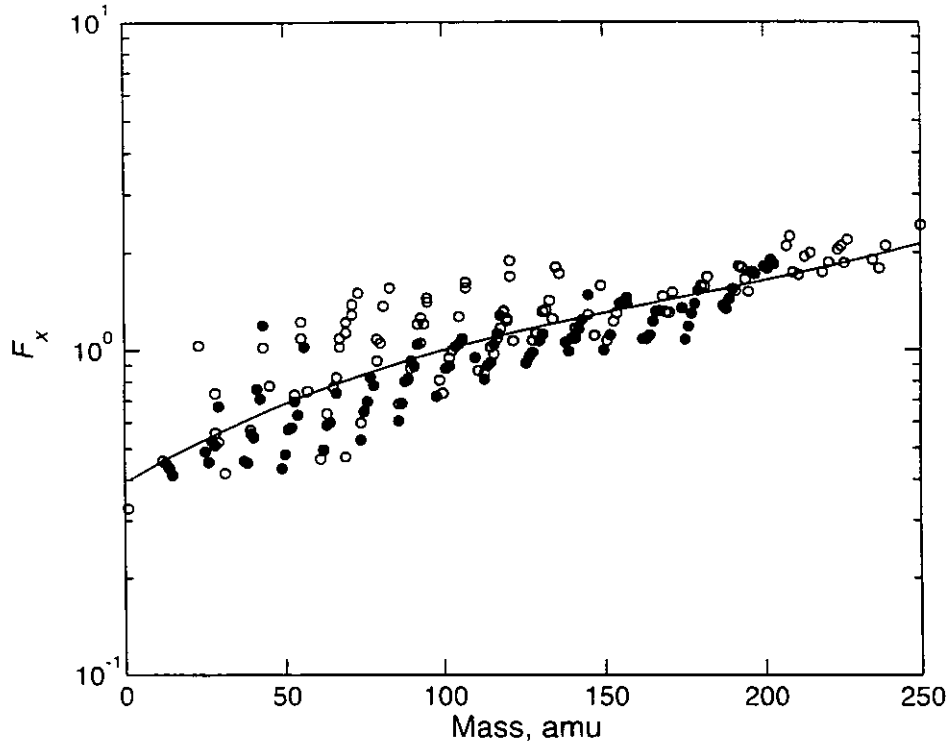

Fig 11 Ratio of positive ion intensities from polycarbonate spectra acquired with 10 keV Cs^+ to those for 10 keV Ar^+. The solid line is a cubic function fitted to the log ratio data using a least modulus minimisation routine.

The static SIMS spectrum of Fig 12(a) is populated by intense hydrocarbon peaks. Fragments at masses 91.062, 103.03, 115.053, 152.055, 165.056 and 189.043 are identified as $C_7H_7^+$, $C_8H_7^+$, $C_9H_7^+$, $C_{12}H_8^+$, $C_{13}H_9^+$, $C_{14}H_{10}^+$, and $C_{15}H_{19}^+$. These ions have a polycyclic aromatic structure not directly related to the PC structure. Additionally, these peaks were also found in the static SIMS spectrum of PS and so cannot be used as unique identifiers. The lower mass region of the spectrum contains simple hydrocarbon ions usually seen for aliphatic

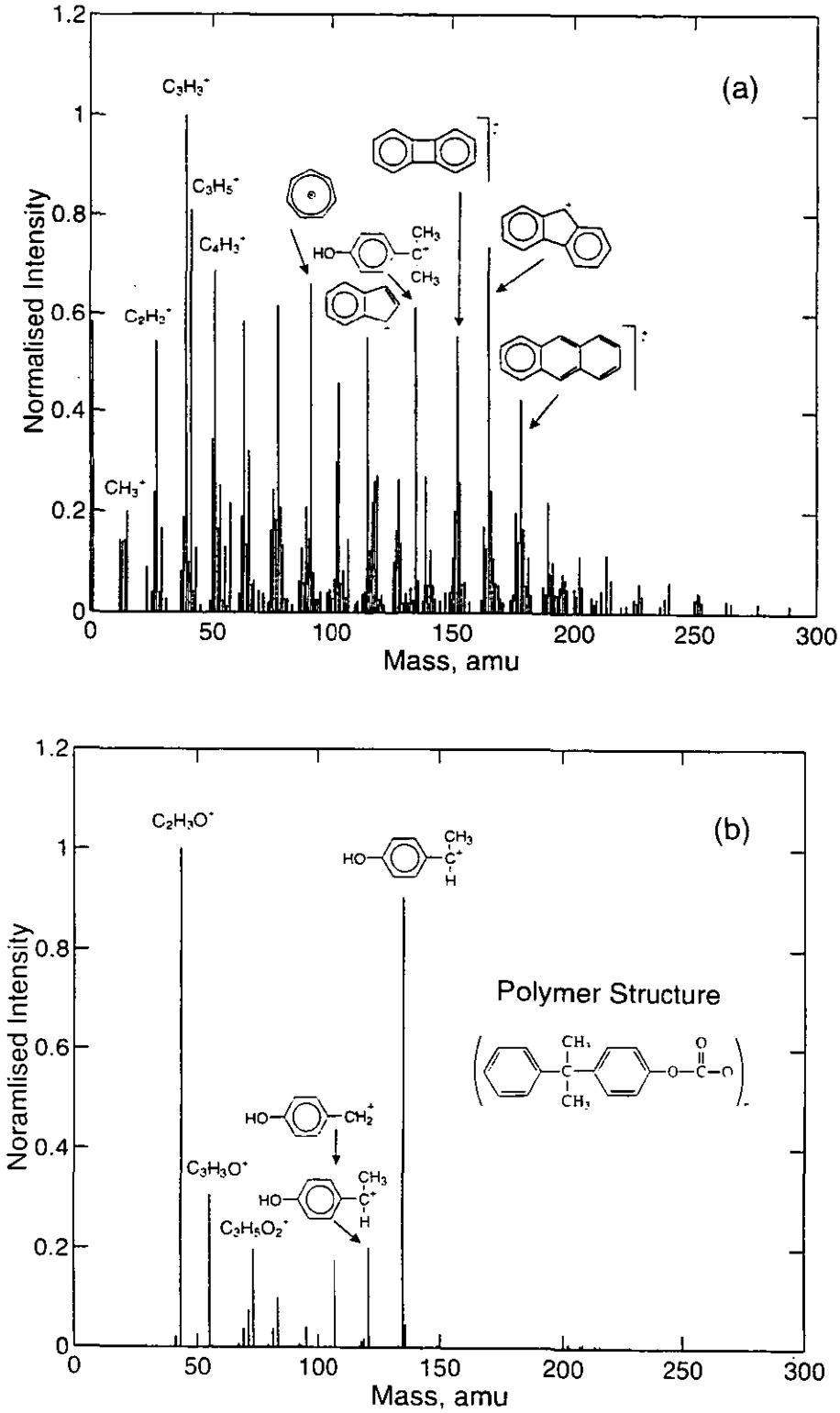

Fig 12 Spectra of polycarbonate (a) Static SIMS spectra acquired with 10 keV Cs^+, (b) G_0-SIMS and (c) G_1-SIMS.

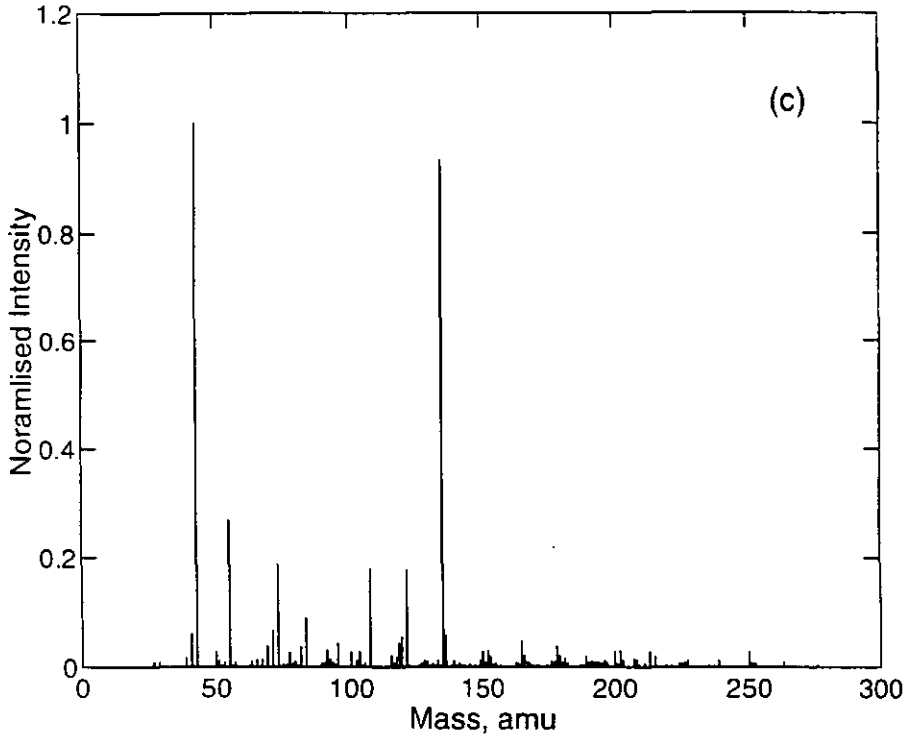

Fig 12 Spectra of polycarbonate (a) Static SIMS spectra acquired with 10 keV Cs^+, (b) G_0-SIMS and (c) G_1-SIMS.

hydrocarbon polymers. Amongst all of these ubiquitous peaks is one at mass 135.099 corresponding to $C_9H_{11}O^+$ which is representative of the polycarbonate structure. In contrast, in both of the G-SIMS spectra, all of the confusing hydrocarbon peaks have been significantly reduced and other peaks enhanced. The enhanced peaks are simply related to the PC structure and the highly characteristic fragment $C_9H_{11}O^+$ is the most dominant. Figure 12(b) shows the PC structure and the structural components deduced from the main peaks. The advantage gained by using primary ions of different mass has completed suppressed the tropylium ion, in the G_0-SIMS spectrum, along with the other polycyclic ions to the baseline. This new spectrum is much simpler for interpreting and identifying the molecular groups than a traditional static SIMS spectrum.

4 CONCLUSIONS

A methodology is developed which describes the fragmentation in static SIMS spectra in terms of a surface plasma temperature, T_p, and exponentially decaying populations of degradation products from each parent fragment. These exponential decays have the same

characteristic parameter, β, independent of the mass of the parent fragment. This concept is used to unify the effects of primary ion energy and species in a single unified cascade gradient plot for each material. It is shown that there is a linear relationship between the cascade gradient parameter, β, and the incident ion energy and that there is least fragmentation for high mass projectile ions at low energies. The polyatomic ion SF_5^+ creates less fragmentation than the equivalent mass atomic ion and that fragmentation, for this ion, decreases with increasing energy. No effect of primary ion chemistry is seen, as shown by the equivalent behaviour for caesium and xenon.

An extension of the analysis provides a simplification of the static SIMS spectrum known as gentle SIMS or G-SIMS. The G-SIMS spectra are equivalent to the spectra that would be obtained from a very low collision cascade surface plasma temperature. The G-SIMS spectra therefore exhibit peaks which are more directly related to the material structure. All that is necessary to generate a G-SIMS spectrum is to acquire two spectra, either at different ion beam energies or, more effectively, using two different primary ion species. In modern instrumentation this is very easy to accomplish. From these spectra we form the ratio F_x which is used with one of the spectra via either Eq (10) or (12) to form the G-SIMS spectrum. Identification of molecular groups in, and interpretation of, G-SIMS spectra are much simpler than for traditional static SIMS spectra, as illustrated by examples for PTFE, PS and PC.

REFERENCES

(1) D. Briggs and A. B. Wootton, Surf. Interface Anal. 4 (1982) 109.

(2) D. Briggs and M. J. Hearn, Inter. Journal Mass Spec. and Ion Proc. 67 (1985) 47.

(3) A. D. Appelhans, J. E. Delmore and D. A. Dahl, Anal. Chem. 59 (1987) 1685.

(4) A. D. Appelhans and J. E. Delmore, Anal. Chem. 61 (1989) 1087.

(5) G. S. Groenwold, A. K. Gianotto, J. E. Olson, A. D. Appelhans, J. C. Ingram, J. E. Delmore and A. D. Shaw, Inter. Journal. Mass Spec. and Ion Proc. 174 (1998) 129.

(6) F. Kötter, A. Benninghoven, Appl. Surf. Sci. 133 (1998) 47.

(7) D. Stapel, O. Brox, A. Benninghoven, Appl. Surf. Sci. 140 (1999) 156.

(8) I. S. Gilmore and M. P. Seah, Surf. Interface Anal. 24 (1996) 746.

(9) *The Static SIMS library*, Eds. J. C. Vickerman, D. Briggs and A. Henderson, Surface Spectra, Manchester, (1998).

(10) *The Münster High Mass Resolution Static SIMS Library*, B. C. Schwede, T. Heller, D. Rading, E. Niehuis, L. Wiedmann and A. Benninghoven, ION-TOF, Münster (1999).

(11) J. Schwieters, H.-G. Cramer, T. Heller, U. Jürgens, E. Niehuis, J Zehnphenning and A. Benninghoven, J. Vac. Sci. Technol. A 9 (1991) 2864.

(12) I. S. Gilmore and M. P. Seah, Surf. Interface Anal. 23 (1995) 191.

CHAPTER NINE

Conclusion and Outlook

This thesis establishes a framework to provide a measurement base for static Secondary Ion Mass Spectrometry. Individual components in the measurement chain, identified as contributing to poor repeatability and reproducibility, are studied, characterised and solutions and recommendations provided to improve measurement reliability.

At a fundamental level, ion beam currents and current densities must be calibrated to enable comparability and validity of data. The design of a simple compact Faraday cup is provided and recommendations provided which give accuracies for current and current density measurements better than ± 2% and often as good as ± 1%.

One very significant problem in static SIMS has been the charging of insulating material. This has resulted in widely different spectra being obtained from a given material from one spectrometer and also between spectrometers. A lack of control here, has impeded progress in the understanding of the fundamental processes in SIMS. An entirely new method of charge stabilisation is developed utilising secondary electrons emitted from an electrode in front of the sample. This is combined with a modulation of the sample potential with a triangular waveform, effectively broadening the acceptable energy window of the spectrometer. This new method now enables insulating samples to be routinely analysed with repeatabilities of better than 2% in quadrupole mass spectrometer based instruments which are very sensitive to the absolute value of the surface potential. Two UK manufactures have now incorporated this design in their quadrupole mass spectrometer based SIMS instruments. This is important since these quadrupole based systems are much cheaper that TOF mass spectrometers. If static SIMS is to become a routine quality control analytical technique, it is these quadrupole based systems that will be used.

These developments give excellent stability and control which enabled a precise and systematic study of the effects of ion beam damage in polymers to be conducted. This work resolved much of the conflicting information in the literature. A simple bond breaking model

describing the effects of damage is developed explaining the different shapes of observed damage profiles. From this, it is possible to gain additional information about the polymer structure which is not possible from the regular static SIMS spectrum.

The ion detection efficiency, a final link in the measurement chain, has a strong effect on the relative intensities in the static SIMS spectrum and the detection sensitivity for very high mass ions. It is recommended that the secondary ions impact the detector at as high an energy as possible and a procedure is given to set the detection voltage. For an impact energy of 20 keV the detection efficiency is unity for ions with a mass of up to 4000 amu. This greatly simplifies procedures for quantitative analysis.

The results of an inter-laboratory study conducted with twenty one instruments worldwide shows the range of repeatability currently achievable. Some laboratories are as good as 1%, but many are at 10% and a few as poor as 80%. The reference materials PTFE, PET and Irganox have performed excellently. Transferability of spectral data for comparison between instruments or with library data is facilitated by use of the Relative Instrument Spectral Response, RISR. Excellent reproducibility of the spectra after correction using the RISR is found with an average of 14% for most instruments. Without this correction, scatter factors rise to $\times/\div$ 1.55.

The diverse variety of primary ion beam species and energies presently in use complicates the transferability of spectra from one spectrometer to another. A methodology is developed which describes the fragmentation in static SIMS spectra in terms of surface plasma temperature. This concept is used to unify both the effects of ion beam energy and species to a single plot for each material. This provides, for the first time, a way of conceptualising the behaviour of different primary ions. Recommendations are provided to give the optimum use. A development of this method gives a totally new spectroscopy, known as G-SIMS or gentle-SIMS. Here, a static SIMS spectra equivalent to a low surface plasma temperature is calculated. The great advantage here, is that the peaks truly representative of the analysed material are increased in intensity whilst the majority of peaks caused by additional fragmentation and re-arrangement mechanisms are suppressed. The resulting G-SIMS spectra are much simpler, easier to identify and give a more direct interpretation.

Successive parts of this thesis have built on the previous parts. It has only been possible to do the work in the final stage because of the high precision and repeatability developed in the early stages. It is the whole that provides a measurement base.

The development of the G-SIMS procedure may alter the way all static SIMS analyses are conducted. The advantages are many-fold; selection of characteristic fragment ions for quantification, simpler procedures for material identification and de-skilling of the technique. Expert SIMS analysts are able to read a static SIMS spectrum and, through their extensive experience, deduce the type of material and identify common contaminants. However, it is not yet possible to accumulate these inferences and codify them to provide an expert system. One of the greatest limitations of static SIMS is the acknowledged barrier of the complexity of the spectra, many of the most intense peaks are ubiquitous and are therefore not suitable for unique material identification. Often, this limits analysts to simply recognising the major contaminant, if it is relatively common. G-SIMS provides the opportunity to simplify the spectra directly and permits a framework for deducing the structures and molecules present at a surface. We are no longer required to have the relevant spectrum in our library. This will open the technique to a wider audience with stronger industrial acceptance. More work is required to test G-SIMS with different materials including pharmaceuticals and biomaterials. Many developments of SIMS have emerged only to die because of a limited user base, but for G-SIMS this user base may be large. G-SIMS may become the routine method for analysis providing more automated and direct interpretation. Secondary Ion Mass Spectrometry, may then, become the dominant surface analytic tool in industry.

Libraries of digital static SIMS spectra are now growing rapidly, these are required by industry and will assist the increased industrial use of the technique. For these libraries to realise their full potential and deliver the full benefits to analysts, the data must be of high quality and have equivalence between different instruments. At present, for some libraries, the data is compiled from a wide range of different instruments operating under different conditions with different procedures for data acquisition. Consequently, comparability of spectra between libraries is often poor. Further work is required, building on the foundations laid here, to improve the internal consistency so that the maximum valid information can be extracted by analysts and that data is equivalent between instruments. At present, only rudimentary computational methods are employed to search and identify an unknown spectrum from those stored in the library. Work, at NPL, is now being developed, using

modern information theory such as neural networks and multivariate analysis, to provide a digest of library data. This work will allow much more powerful searches for material identification with higher reliability and the ability to assign an unknown spectrum to a material class even if an exact material match is not contained in the library.

Over recent years there, has been a rapid expansion in the application of static SIMS to areas relating to more complex organic molecules such as pharmaceuticals and biomaterials. Figure 1 gives a schematic of the increased use of static SIMS for the analysis of complex molecules, firstly in leading edge research and then in advanced products. At NPL, work is now progressing to develop the measurement base to support measurements in this important and extensive area of applications which include, drug delivery systems, surfaces of body implants, protein compatibility, boron neutron capture therapy for cancer treatment as well as DNA biosensor chips for genetic disease diagnosis and drug detection.

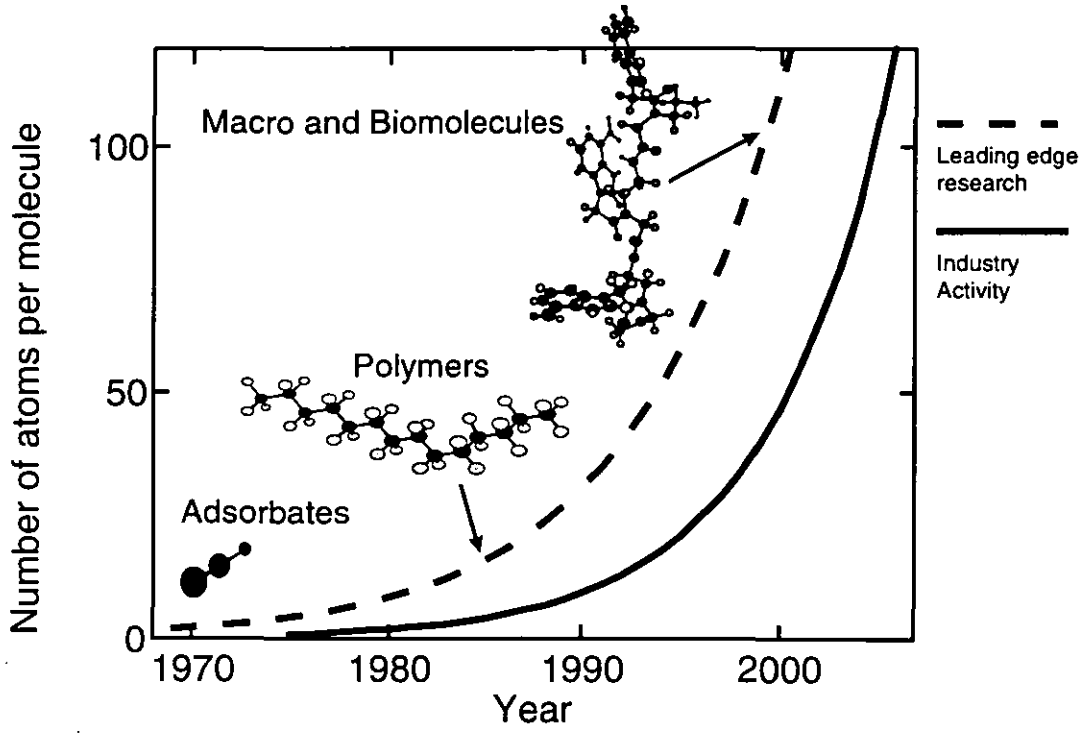

Fig 1 The development of molecular complexity in surface analysis by static SIMS

Additionally, there is now a growing demand for static SIMS analyses for forensics, law and litigation. Here, the need for accurate, traceable analysis is critical. Examples in these areas range from identification of product liability, analysis of prohibited drugs in athletes to advanced materials to prevent fraud and counterfeit banknotes.

Static SIMS is recognised as a powerful technique to solve a gamut of industrial problems. Measurement repeatability has improved enormously and confidence in the technique to solve real problems has grown concomitantly. The measurement base provided here will help ensure this growth in static SIMS.